An Investigation of Behavior and Modeling of Bond for Reinforced Concrete

Jingjuan Li

A dissertation submitted in partial fulfillment of
the requirements for the degree of

Doctor of Philosophy

University of Washington

2010

Program Authorized to Offer Degree: Department of Civil and Environmental Engineering

University of Washington
Graduate School

This is to certify that I have examined this copy of a doctoral dissertation by

Jingjuan Li

and have found that it is complete and satisfactory in all respects,
and that any and all revisions required by the final
examining committee have been made.

Chair of the Supervisory Committee:

_____

Laura N. Lowes

Reading Committee:

_____

Laura N. Lowes

_____

John F. Stanton

_____

Gregory R. Miller

Date: _____

In presenting this dissertation in partial fulfillment of the requirements for the doctoral degree at the University of Washington, I agree that the Library shall make its copies freely available for inspection. I further agree that extensive copying of this dissertation is allowable only for scholarly purposes, consistent with "fair use" as prescribed in the U.S. Copyright Law. Requests for copying or reproduction of this dissertation may be referred to Proquest Information and Learning, 300 North Zeeb Road, Ann Arbor, MI 48106-1346, 1-800-521-0600, to whom the author has granted "the right to reproduce and sell (a) copies of the manuscript in microform and/or (b) printed copies of the manuscript made from microform."

Signature_____

Date_____

University of Washington

Abstract

An Investigation of Behavior and Modeling of Bond for Reinforced Concrete

Jingjuan Li

Chair of the Supervisory Committee:
Associate Professor Laura N. Lowes
Department of Civil & Environmental Engineering

This research investigates *bond* between concrete and steel in reinforced concrete (RC) using X-Ray tomography image data and nonlinear analysis, with the objective of developing recommendations for modeling bond in RC structures. RC is a composite material that combines concrete, which is strong in compression and weak in tension, with reinforcing steel, which is strong is tension and buckles in compression. Bond is necessary to maintain the composite action and realize the full utility of the material. However, bond-zone response data are not easily collected and the mechanics of bond are not easily assessed using traditional experimental test methods, as traditional instrumentation may interfere with the bond mechanism and can not provide high-fidelity data. Recently, X-ray computed tomography (CT), which is non-invasive and provides high resolution data, has been used to monitor bond tests. In this study, state-of-the-art image processing techniques are applied to 3D X-ray images of bond-zone specimens to characterize bond behavior. Bond-zone response data generated from X-ray CT images are used to verify nonlinear high-resolution finite element (FE) modeling of bond-zone specimens. These FE models are used to further investigate bond-zone response and the impact of modeling parameters on predicted response. The results of this research provide high-fidelity data characterizing bond-zone response, improved understanding of bond-zone mechanisms and recommendations for design and modeling of bond behavior in RC structural components.

Table of Contents

List of Tables

List of Figures

Glossary

BOND STRESS: stress on the bar surface in the direction parallel with the bar.

BAR-SLIP: relative displacement between bar and concrete in the direction parallel with the bar.

FE: finite element

IN-PLANE: in the section plane of bond specimen which includes direction parallel with and perpendicular to the bar axis.

PULL-OUT TEST: bond test to simulate bond behavior in anchorage zone

RADIAL DISPLACEMENT: relative displacement between bar and concrete in the direction perpendicular to the bar.

RADIAL STRESS: stress on the bar surface in the direction perpendicular to the bar.

RC: reinforced concrete.

SECONDARY CRACKING: the local bond-zone conical cracks with an inclined in-plane angle to the bar axis.

SPLITTING: the longitudinal cracking parallel with the bar axis.

TRANSVERSE CRACKING: in tension test, the major cracks perpendicular to the bar axis.

UNIFORM TENSIONS TEST: bond test to simulate bond behavior in flexural response zone

Acknowledgments

I would like to express my deepest gratitude to my advisor, Professor Laura N. Lowes for her rigorous academic instructions, constant encouragement, and tremendous patience and help. This dissertation would not exist without her exceptional guidance and continued financial support. I have learned so much from her and most important, she is my role model for being an excellent researcher and wonderful teacher.

I would like to thank Professor John Stanton for taking time being my dissertation committee and providing instructions. John has not only provided helpful suggestions for my research, but also patiently helped me with my presentation skills and English writing.

I would like to thank Professor Miller for his excellent academic education, which has built me a strong engineering mechanics foundation, for being my dissertation committee and providing instructions on numerical modeling.

I would like to thank Professor Mark Ganter for serving as gradate school representative and providing guidance.

Special thanks to Professor Peter Mackenzie and Professor Steven Seitz, from whom I have taken classes that built the academic foundation for this dissertation.

I want to express my sincere appreciation to my family, my husband Genmiao and my son Henry, for the sacrifice and understanding. You are always my spirit support for working hard. My brothers and sisters, Jing lie, Jing xian, Jing yue, Jing lian, Jing ping, Jing run, thank you for giving me a happy childhood with so many beautiful memories. My friends and colleagues, Anna, Amanda, Kelly, Laila, John, Ingimar, Olafur and Shawn, thank you for chatting with me and pleasant cooperations when we worked together.

Finally, I would like to express my sincere appreciation to the University of Washington, where I have the opportunity to pursue my PhD study. I would also like to thank the National Science Foundation, the department of Civil & Environmental Engineering, and College of Engineering for providing financial support for finishing this dissertation.

Dedication

To my parents: Li, Hongzhong and Guan, Yongfang

Chapter 1

Introduction

1.1 Motivation

Reinforced concrete (RC) is a classic composite material widely used in civil engineering applications. The utility of RC lies in the combination of two materials: concrete, which is strong in compression and weak in tension, and reinforcing steel, which is strong in tension and buckles in compression. Composite action is maintained through load transfer between concrete and steel. This load transfer occurs via *bond*. In the design of RC structures, perfect bond between concrete and steel and strain compatibility between these two materials is commonly assumed. Figure 1.1 shows this assumption employed to compute the flexural strength of an RC beam.

If bond stress demands are large, concrete may be damaged in the vicinity of the concrete-steel interface. This allows reinforcing steel to slip relative to the surrounding concrete and increases the flexibility of the structure. For performance-based seismic design, in which accurate assessment of strength and stiffness under earthquake loading is critical, modeling the structural response including bond-zone damage may be necessary. If bond demands are severe, bond-zone damage may result in loss of bond strength, loss of composite action, and failure of a structure. Figure 1.2 shows an idealization of a RC frame sub-assemblage in which loss of bond strength and slip of reinforcing steel result in wide cracks and increased flexibility of the structure. Figure 1.3 shows wide cracks at a

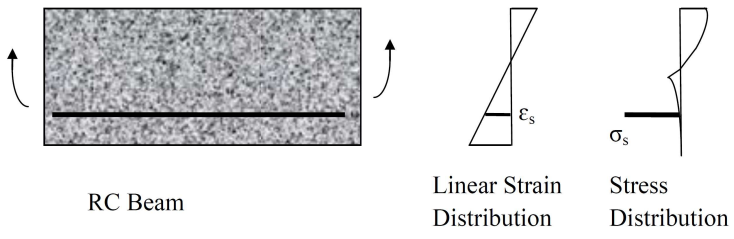

Figure 1.1: Strain Compatibility Assumption for RC Component Strength Calculation

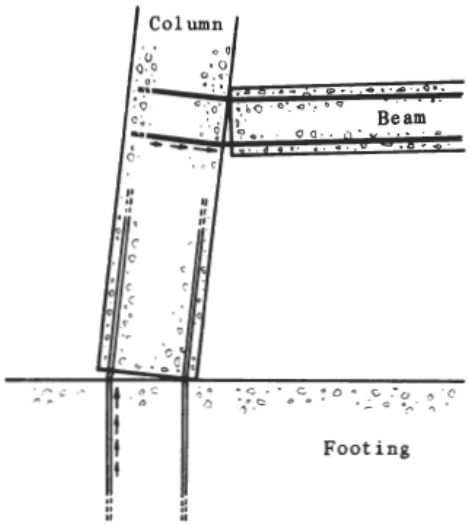

Figure 1.2: Example of Reinforcing Bar Slip Due to Bond Failure [137]

beam-column interface in a lab specimen due to the slip of reinforcing steel.

To advance design and analysis of RC structures to accurately account for the impact of bond and bond-zone damage, improved understanding of bond-zone mechanisms and high-resolution data characterizing local bond-zone behavior are required. This study seeks to develop this understanding and these data. Specific issues motivating the study include the following:

1. Current bond strength models define bond strength based on parameters such as the thickness of concrete cover over the steel and the volume of reinforcing steel provided to confine the bond-zone. However, data show that current strength models are imperfect. More accurate models that better represent the effect of fundamental bond mechanisms are necessary. Thus, one motivation for this study is to better understand bond-zone mechanisms and damage patterns to advance the assessment of bond strength for design.

2. In analysis of RC components or sub-assemblages, bond may or may not be explicitly represented. Some models assume perfect bond (displacement compatibility) between

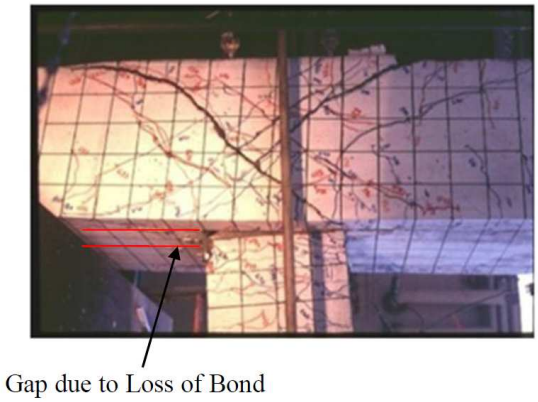

Figure 1.3: Loss of Bond in a Bridge Beam-Column Joint [95]

concrete and steel; some models use interface bond elements between concrete and steel to simulate slip between concrete and steel. Variety of approaches exist for modeling bond; these approaches employ different constitutive bond models, geometric representations and modeling scales. The best approach for incorporating bond behavior into an analysis is not known. Thus, a second motivation for this study is to evaluate different approaches and identify one or more preferred approaches.

3. Finally, experimental data, recently developed by researchers at the University of Washington characterizing bond response, include X-ray CT images of bond specimens at various load steps in the laboratory tests. These images can potentially provide previously unavailable information about bond-zone damage as well as 3D deformation fields. Thus, a third motivation for this study is to analyze X-ray CT images of bond test specimen to improve understanding of bond-zone behavior and use these data to evaluate FE analysis results.

1.2 Current Understanding of Bond-zone Behavior

Investigation of bond behavior, including bond-zone load transfer mechanisms, bond stress versus bar slip relationships, and the factors that affect bond response have been the focus of numerous previous studies. The majority of these studies have been experimental

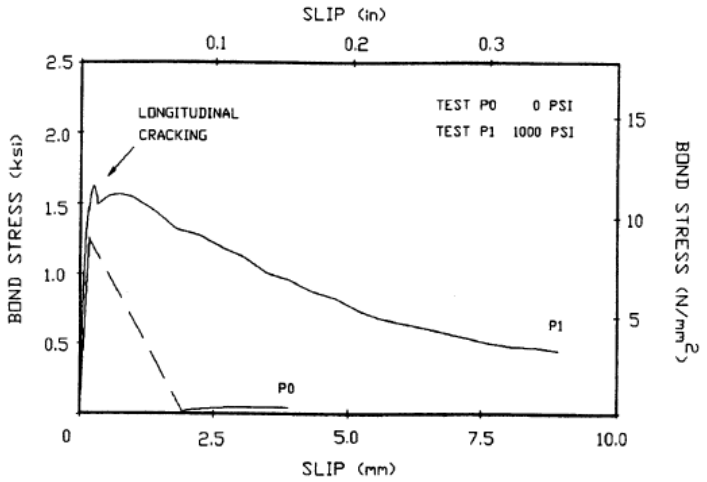

Figure 1.4: Bond Stress versus Slip by Malvar [107]

investigations focused on defining the average bond stress versus bar slip relationship and the impact of parameters, such as geometric configuration and material properties, on this relationship. Figure 1.4 shows the average bond stress versus bar slip response determined by Malvar [107] through experimental testing of bond specimens subjected to different levels of confining pressure. As is done typically, Malvar defines bond stress as the applied load divided by the nominal surface area of the bar embedded in the concrete:

$$\tau = \frac{P}{\pi d_b L} \tag{1.1}$$

where τ is the bond stress, P is the applied load, d_b is the nominal bar diameter and L is the bonded length. Slip is defined as the relative displacement between concrete and steel bar at the free end of the bar.

For a deformed bar, the bond stress is developed through initial chemical adhesion at small load levels, mechanical interlock between reinforcing steel ribs and the surrounding concrete as the load increases, and friction after the mechanical interlock fails [50, 73, 107, 147]. The mechanical interlock between concrete and reinforcing steel ribs leads to a concrete stress state in which the concrete directly in front of the ribs carries compression and the concrete above the ribs carries primarily shear, as shown in Figure 1.5. Experimental tests of

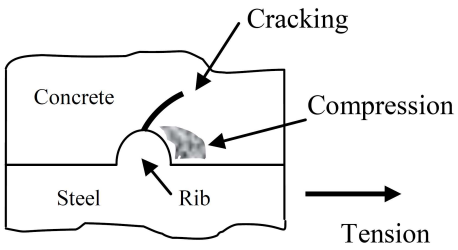

Figure 1.5: Bond-zone Stress Field

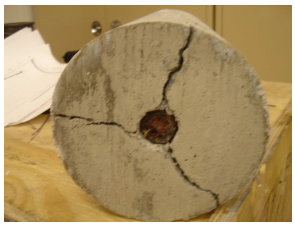

Figure 1.6: Splitting of Bond Test Specimen [108]

unconfined pull-out specimens result is a splitting type failure, such as shown in Figure 1.6. This failure mode suggests that radial compressive stress develops at the concrete-steel interface due to mechanical interaction between concrete and steel. These radial stresses produce tensile hoop stress and splitting cracks in the surrounding concrete [147].

The splitting behavior and the internal cracking observed in the laboratory tests [18, 65, 73, 108] suggests the multi-directional response of bond-zone under tensile or compressive loading of the bar. The bonds stress versus slip response history is fundamentally controlled by the local multi-directional response of the bond-zone concrete. Global load-displacement response of bond-test can be measured by traditional instruments. However, measuring interior response of bond-zone without interrupting the bond performance or destruction of the bond specimen can capture the full history of both global and local bond response.

Monitoring the local 3D bond-zone response is challenging using traditional instrumentation (i.e. strain gauges and displacement transducers). If strain gauges are placed on the reinforcing bar at multiple locations to measure the steel strain, from which the bond stress distribution can be estimated, the multiple gauges and wires can reduce bond strength. It

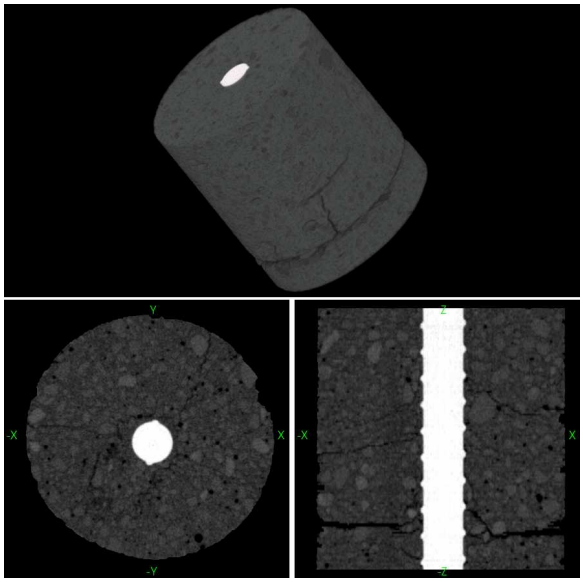

Figure 1.7: X-ray Images of Bond Test Specimen

is possible to use special hollow bars or make grooves on the bar and gauge the interior, but this is extremely expensive and may not have same behavior as the construction bars. Thus most studies have opted to collect average bond stress data, with average bond stress calculated by the applied load divided by bonding surface area, although research show that this average bond stress is a function of anchorage length [137]. Similarly, deformation of the specimen especially radial deformation near bond-zone is rarely monitored as the possible interruption of bond behavior.

Recent advances in X-ray CT technology have wide applications in medical field, mechanical system and civil engineering materials. High resolution images and emergent image processing techniques make it possible to visualize the interior bond response and verify results from analytical models. To address the limitations of traditional bond test methods and instrumentation, researchers at the University of Washington recently applied X-ray computed tomography (CT) to investigate the local bond-zone behavior. Extensive pull-out tests and uniform tensions tests were conducted and High-energy X-ray CT facilities were used to generate 3D X-ray images for part of these test specimens. Figure 1.7 is an example of three-dimensional X-ray image of a bond test specimen.

To address the limitations of traditional experimental tests, researches have also employed numerical analysis to investigate the local bond-zone behavior including bond-zone damage evolution and the relationship between the local damage and global load-displacement response [19, 120, 133]. For the investigation of bond-zone damage patterns, techniques and software for high resolution three-dimensional (3D) nonlinear analysis are available to model the bond-zone. However, the modeling methods are very different from each other as different assumptions on geometry, material and boundary conditions exist. Evaluation of these models and data to verify these models are needed to advance the understanding and modeling of the bond behavior.

1.3 Contributions of the Dissertation

A review of previous investigations of bond, both experimental tests and numerical simulations, shows that consensus exists regarding many aspects of bond behavior, including properties of global load displacement response, failure modes, existence of radial expansion. However, there are still a number of questions that remain unanswered about bond-zone behavior and the modeling of this behavior. These include

1. What are the internal damage and deformation patterns in vicinity of the concrete-steel interface, and how do they evolve during the load history?

2. What are the bond-zone mechanisms of load transfer, and how to they change through the load history?

3. How are the bond-zone damage patterns, deformation patterns, and the bond mechanisms affected by various design parameters?

4. Can local bond-zone response be simulated using high-resolution nonlinear FE models?

5. To what extent can X-ray CT images and state-of-the-art image processing techniques be used to generate data to answer the above questions?

6. Can X-ray CT image analysis and high-resolution FE analysis provide data to support simplified analysis?

Answers to these questions were sought through the research activities presented in this dissertation. Specifically,

1. State-of-the-art image processing techniques were applied to X-ray CT images of bond-zone specimens and the resulting data were evaluated to improve understanding of bond. A three-dimensional optical flow algorithm was implemented to estimate the motion (displacement) field in local bond-zone. The motion (displacement) data was used to determine the local strain field and strains were used to assess cracking and crushing of concrete. A parallelized domain-decomposition solution method was developed and used to analyze the image data, this solution algorithm was necessary due to the large size of image files. Results of image analysis include local strain and displacement fields, global bar slip and radial deformation data.

2. Nonlinear finite element analysis was used to model bond-zone test specimens and the results were evaluated to improve understanding of bond-zone behavior and the performance of different modeling approaches. An extensive investigation of nonlinear FE analysis of bond-zones was accomplished. The FE modeling approaches considered included rib-scale modeling with contact analysis to simulate mechanical interlock between concrete and bar ribs, rib-scale models with displacement compatibilities, as well as different bar-scale models commonly used for structural component analysis. The FE study also evaluated material models, geometric models, and numerical solution procedures in modeling the post-peak residual strength of bond.

3. Through image analysis and FE modeling, correlation between local bond behavior and global bond response was established. This understanding of local bond response mechanisms will provide a basis for advancing RC structural design and analysis. An analytical model was developed, based on the understanding of bond behavior developed from previous research and the image and FE analysis activities described above.

1.4 Organization of the Dissertation

The remainder of this dissertation is organized as follows:

- Chapter 2 summarizes previous experimental and numerical research in investigating bond, identifies critical bond mechanisms and parameters affecting bond mechanisms.

- Chapter 3 presents X-ray images of bond tests and the state-of-art image processing methods that are appropriate for application to these images to extract qualitative and quantitative damage or deformation data.

- Chapter 4 presents the implementation of a motion estimation method to extract the displacement field for the bond test specimens at different stage of loads.

- Chapter 5 presents models for finite element analyses of the bond-zone and evaluation of different modeling procedures.

- Chapter 6 presents the results of finite element modeling of specimens tested at the University of Washington and comparisons of simulation and experimental results.

- Chapter 7 summarizes bond mechanisms found from image analyses and FE analyses as well as development of an analytical model explaining the bond behavior.

- Chapter 8 summarizes findings from the current study and provides recommendations for future work.

Chapter 2

Current Understanding of Bond Behavior

2.1 Introduction

Bond has been the focus of numerous research efforts, given the importance of concrete-steel bond to the strength and performance of RC structures. Experimental studies sought to determine bond strength, develop simple mechanical models for predicting bond strength and define one-dimensional bond stress versus slip relationships [50, 65, 73, 137]. As the complex stress-state and confinement level near bond-zone, more recent studies have sought to refine strength and mechanistic models as well as develop multi-dimensional bond models [62, 107, 108]. Some experimental tests also tried to explore the interior damage in local bond zone [18, 65, 73, 108]. To explain the bond behavior, some analytical studies [114, 147, 156] formulated the bond mechanism using fundamental mechanics of materials, such as Timoshenko's [151] elastic thick wall theory. Additionally, numerous studies were focused on numerical finite element (FE) modeling to account for both spatial and temporal evolution of bond strength, to accurately estimate the strength of bond or the RC structural component under different load stages.

Experimental results found that a number of factors affecting performance of bond, such as confining pressure, anchorage length, properties of concrete, and state of concrete and steel stress strain near bond-zone. As the goal of this study is to investigate fundamental bond mechanism and its correlation with global bond strength, review of previous experimental results provides current understanding of characteristics of global bond behavior and local bond mechanism, and identifies factors that may contribute to bond behavior but are not available from the experiments.

Along with experimental test, numerical simulations of bond tests repeat the test procedure and may provide more information than measurements of experimental test. In addition, more and more analysis of RC structures or components has taken the bond effect into the modeling procedures to improve the results accuracy especially under severe earthquake load. The strategies in considering bond effect into the modeling depend on the

specific goal and scale of RC structures models. A number of models applied additional interface model for bond between concrete and steel. These interface models were from calibrations of experimental data to best reflect the actual bond behavior. Another goal of this study is to analyze bond using high resolution FE modeling. Previous research on modeling bond-zone provide information on characteristics and performance of each model. This chapter reviews previous research with the objectives of:

- Characterizing bond-zone response.
- Identifying strength, load-displacement, and damage data that can be used to validate analysis results.
- Establishing the state-of-the-art procedures in bond-zone modeling.

Section 2.2 summarizes experimental research investigating bond and presents typical bond tests. Section 2.3 summarizes bond mechanism found from experimental tests. Section 2.4 introduces previously proposed analytical bond models. Section 2.5 provides detailed summaries of different FE modeling procedures.

2.2 Experimental Investigation of Bond Behavior

2.2.1 Significant Experimental Bond Tests

Experimental studies conducted to investigate bond [18, 50, 65, 73, 107, 108, 137] sought to define bond strength, load-displacement response, and the impact of design parameters on both, as well as to improve understanding of the mechanisms that control both. These tests are reviewed with the objective of identifying data for use in evaluating and validating numerical models. Most bond tests may be classified as either pull-out or tension-type tests.

Pull-out tests are intended to simulate anchorage bond-zone conditions, such as might occur where beam column or wall longitudinal steel is anchored in a well-reinforced elements or anchorage element such as a foundation. In this case, reinforcing steel stress is maximum at the surface of the anchorage element and drops to zero, if bond strength is adequate,

within the anchorage zone. Bond strength is defined as bond stress at peak load in a pull-out test. The bond stress is calculated as the load divided by the perimeter of the bar and embedment length along the bar.

Eligehausen [50] tested 125 pull-out reinforced concrete block specimens to simulate the confined region of beam-column joint (Figure 2.1 and 2.2). The parameters studied include loading history, confining reinforcement, bar diameter, concrete compressive strength, bar spacing, active transverse pressure and loading rate. The test specimens have short anchorage length and transverse confinement to simulate bond performance when bar was in elastic state. Test results showed more brittle splitting failure when transverse restraining reinforcement is not enough, however, once the restraining reinforcement reach the minimum value that prevents the specimen from splitting failure, more restraining reinforcement did not improve the bond behavior. The influence of bonded bar diameter and transverse bar spacing on the bond stress-slip is small, increasing bar spacing from 1 bar diameter to four times bar diameter increase bond peak strength by 20%. Concrete compressive strength has influence both on bond strength and slip at peak bond strength. Bond strength increases proportionally to the square root of concrete compressive strength, and slip at peak bond strength decreases proportionally to the square root of concrete compressive strength. Bond strength is larger when loading rate is higher. Bond strength deteriorated larger when when the cyclic load is more than 80% of bond strength.

Hungspreug [73] tested 54 standard concrete cylinder pull-out tests (Figure 2.3) with short embedment bar to investigate the impact of parameters, such as confinement, bar geometry, load history, internal and surface cracking. The test results show that confining pressure increases the peak bond strength, but not initial stiffness. The bond slip and deterioration propagates from ribs near the load end to the free end. The first rib near the load end experiences largest slip and carries most of the load. Test specimens include bar with one rib, two ribs and three ribs. Two ribs bar and three ribs bar have similar behavior, both have higher bond strength than one rib bar. Under cyclic load, deterioration of bond mainly happens during first cycle load. Only an insignificant amount of bond damages happened for additional cyclic loading. For specimens with one rib bar, by injecting ink into the pre-set holes 3/8" to the bar surface, the internal cracking was observed with optical

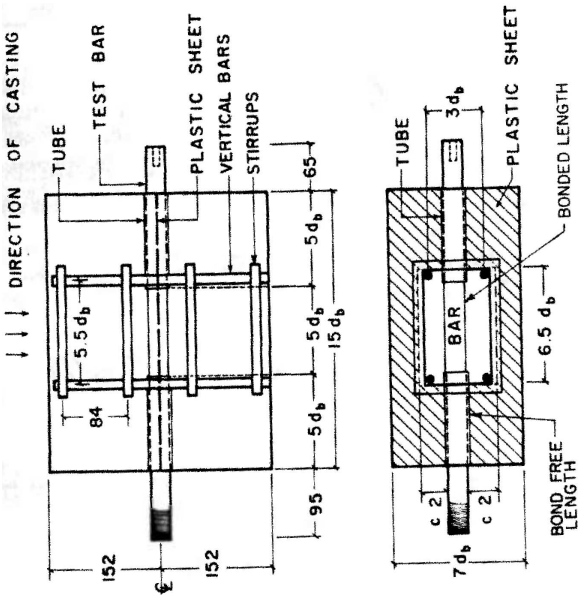

Figure 2.1: Test Specimen by Eligehausen [50]

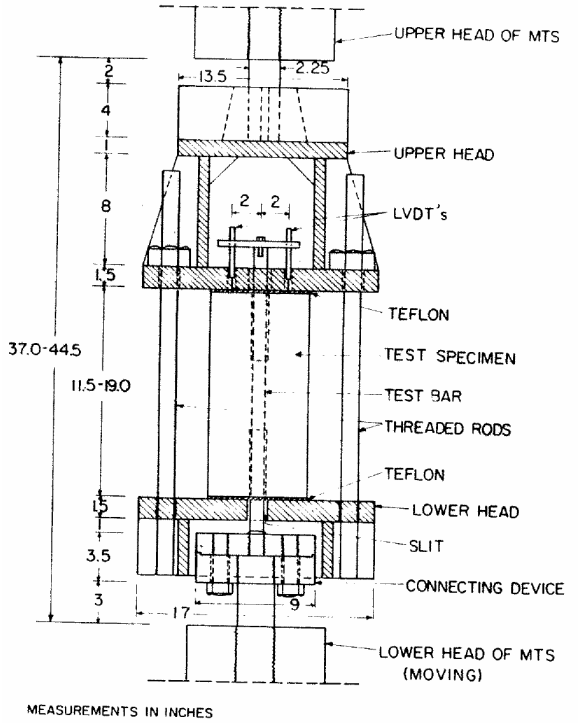

Figure 2.2: Pull-out Test Setup by Eligehausen [50]

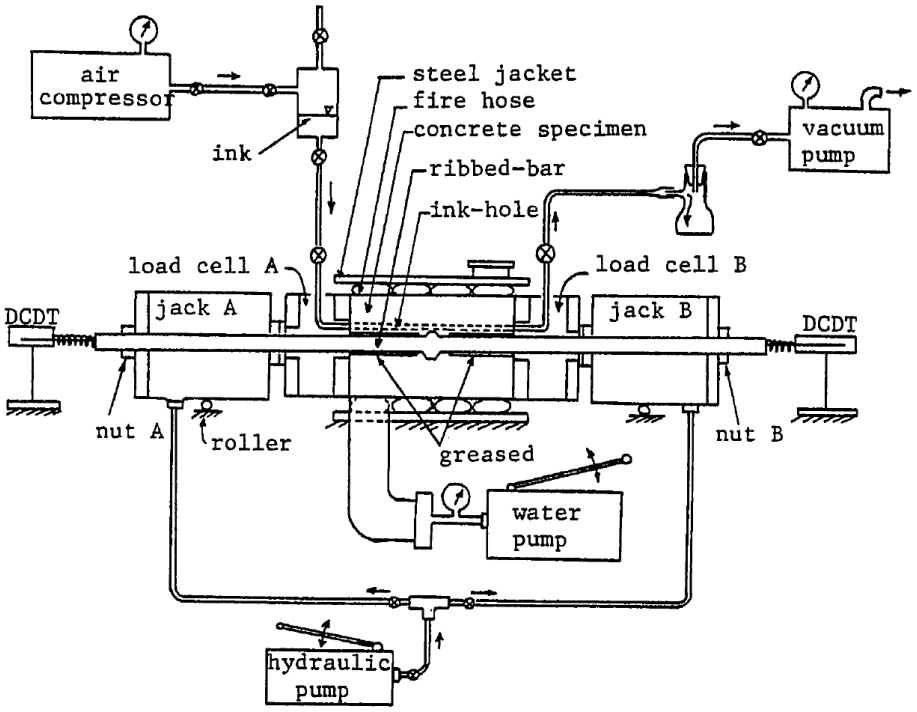

Figure 2.3: Pull-out Test Setup by Hungspreug [73]

microscope. This procedure was used when the specimen was under 5 kips of load, which is about 50% of peak load, and under 10 kips of load, which is about peak load. Two types of cracking was found: transverse radial cracking and longitudinal splitting. The splitting cracks propagate from bar surface to the outer surface of the specimen. The transverse cracking happens near bond zone and does not propagate to the outer surface. At 5 kips load, only splitting cracks were observed, which means either transverse cracking is not developed or in region very close to bar surface where no injection holes. Hungspreug's test results were consistent with Eligehausen's in dependency of bond strength to the compressive strength of concrete, the bond strength is proportional to square root of the compressive strength of concrete.

Malvar [107] conducted concrete cylinder pull-out tests (Figure 2.4) to investigate the radial expansion in pull-out tests under different confining pressure. The specimens are 3 inch diameter, 4 inch long concrete cylinder with one 0.75 inch diameter bar in the

center. The specimens were first loaded as pull-out test until splitting made the specimen into several individual pieces. The longitudinal cracking and transverse cracking can be observed after splitting of the specimen. After splitting, a range of active pressure were applied to test the bond behavior and radial expansion under different confinement levels. The active pressure was applied after the specimen splitting so as to reduce the confinement due to concrete and accurately control the active pressure. Malvar also concluded that confining pressure increase bond strength. The peak bond strength is increased by 200% when increasing confining pressure from 500 psi to 4500 psi at the bar surface. After reaching a high confinement level, bond strength is not significantly improved any more. Measured average radial displacement showed that before peak bond strength is reached, the radial expansion is insignificant. After the peak bond strength, the radial deformation measured on the outer surface increases sharply, and the radial deformation depends on the confinement level. Specimen with lower confinement has larger radial deformation than specimen with higher confinement. Bars with ribs normal to bar axis have better performance than bars with inclined ribs.

Shima [137] conducted pull-out tests (Figure 2.5) with short bar embedment and long bar embedment to study the stress strain distribution along the bar and the bond behavior after the bar yields. The pull-out concrete cylinder had large diameter of 50 cm (20 inch), with a 19 mm (0.75 in) diameter bar in the center. After bar yielded, the bond stress had sudden decrease and slip was increased. Results showed that the bond stress-strain relation after bar yielded depends on the properties of steel.

Martin [108] conducted a series of pull-out test to investigate the impact of a variety of parameters and the internal damages in bond-zone using X-ray CT images. Results showed that the bar end load-displacement was linear until about 90% of peak load. The failure modes (pull-through, splitting or bar yielding) were decided by confinement or bar bonded length. In specimens with very short embedment length, the bar pulled-through the concrete, with no sign of cracking. The concrete in front of ribs were crushed off. In specimens with heavy confinement, the bond failed by pull-through with local splitting along the bar surface. In specimens with moderate confinement, bond response was more brittle than specimens with heavy confinement. The failure modes were also pull-through accompanied

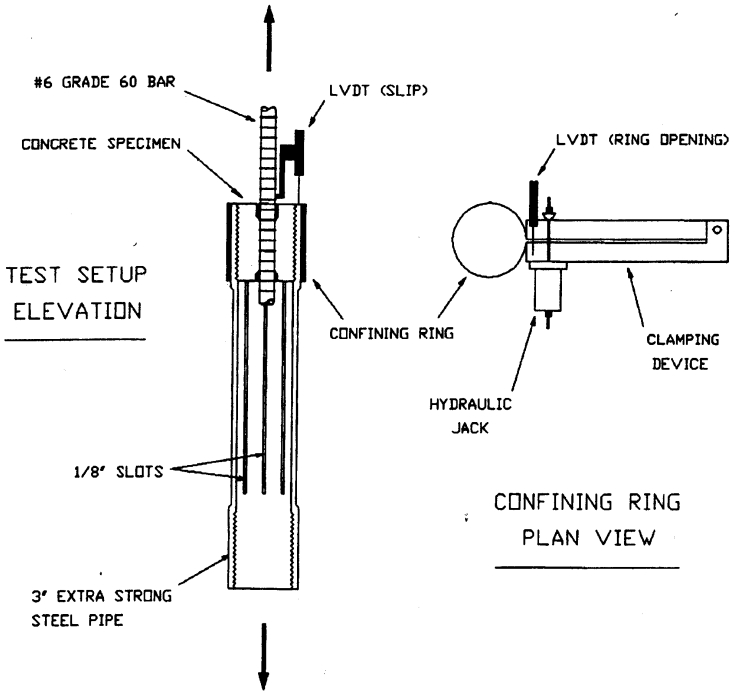

Figure 2.4: Pull-out Test Setup by Malvar [107]

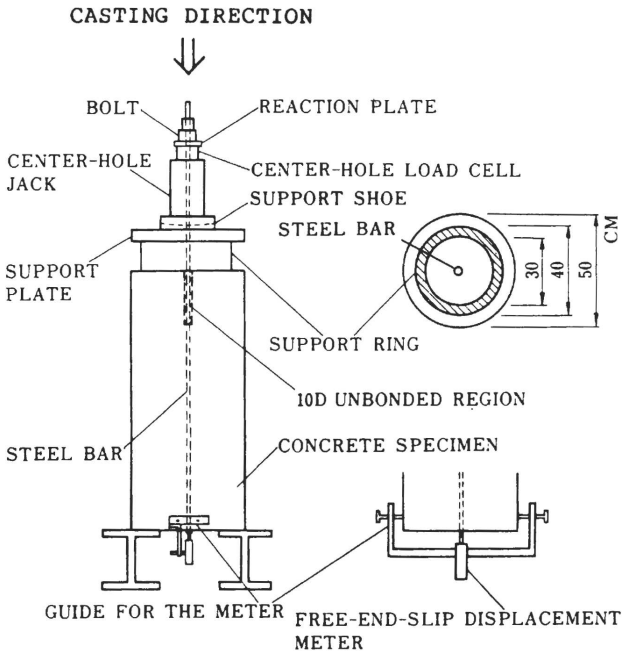

Figure 2.5: Pull-out Test Setup by Shima [137]

by splitting. For unconfined specimens, the response was extremely brittle. The bond failed by longitudinal splitting through the concrete outer surface and the specimen was broken into several pieces.

Tension tests are intended to simulate bond-zone conditions within the tension zone of a flexural element such as might occur at mid-span of a beam. In this case, reinforcing steel carries maximum stress at both ends of a reinforced concrete element and lower stress within the element. If steel stress demands are large enough and bond strength is adequate, tension transfered to the concrete will cause the concrete element to crack. In testing tension specimens, the focus is on the cracking damage patterns on the specimen.

Broms [18] tested a series of long and short tension specimens with different cross sections to investigate the crack spacing and width. One small hole was designed near bar surface and along bar axis (Figure 2.6). During test, resin was forced into the hole by a pressure system. The observation was by a microscope. Major transverse cracks were observed crossing the whole section, secondary transverse cracks were found close to bar region when stress in reinforcement reached 20∼30 ksi. Longitudinal splitting cracks were found starting at existing primary or secondary transverse cracks and propagate along the reinforcement. For major transverse cracking, the surface crack was wider than cracks near bar surface. The observed major crack spacing decreased with increasing stress in the reinforcement until a critical stress was reached after which the crack spacing was stabilized.

Goto [65] tested the tension specimens with square cross-section and different ribs configuration to investigate the internal cracking pattern. During test, ink was injected into 4 holes parallel with bars at the four corners of the cross-section (Figure 2.7). After test the specimen was cut open and photographed. Goto has similar findings with Broms, such as existence of the three types of cracking and the major cracking is wider at the specimen surface. In addition, results show regular secondary cracking pattern which is inclined about 60 degree to the reinforcing bar axis.

Martin [108] investigated tension tests using specimens 24 inch long, 4 inch diameter, with one 0.5 inch diameter bar in the center. The specimen was long enough to develop multiple transverse cracks. Tests showed that the transverse cracks happened simultaneously at location of crack initiator. The internal cracking were observed by injecting UV-sensitive

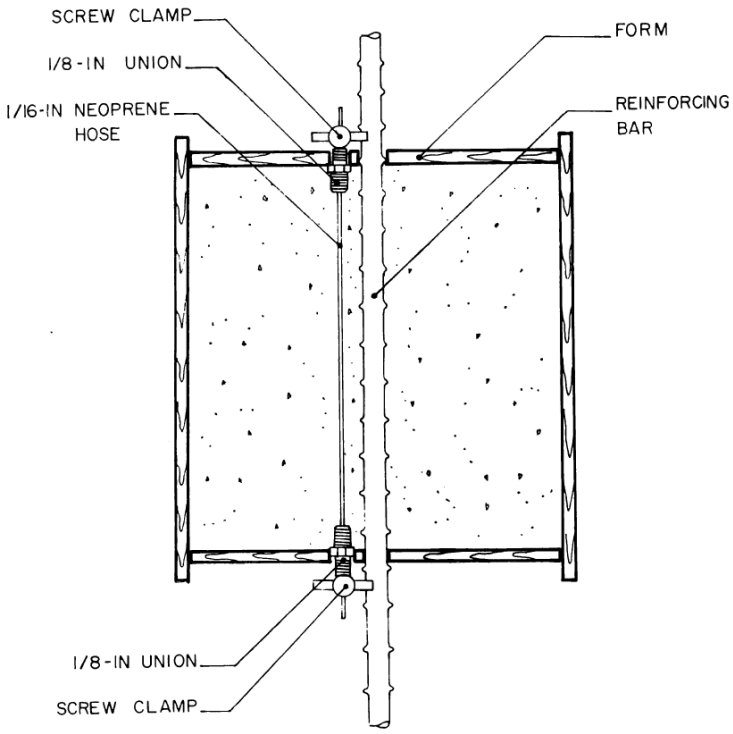

Figure 2.6: Tension Test Setup by Broms [18]

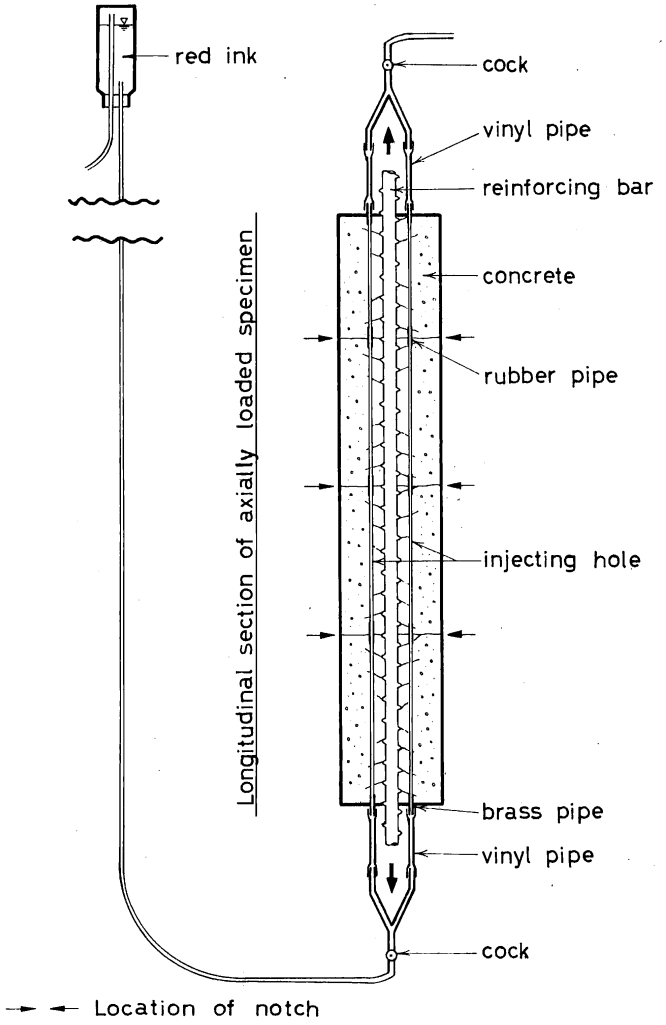

Figure 2.7: Tension Test Setup by Goto [65]

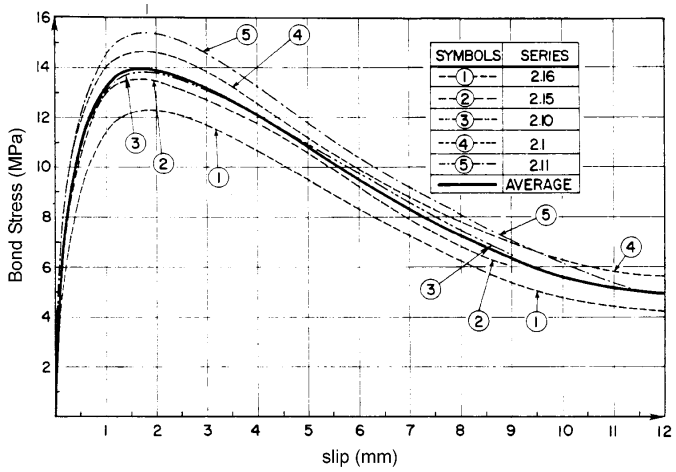

Figure 2.8: Bond Stress Versus Slip Under Monotonic Load [50]

epoxy and cut in half along longitudinal axis. The major transverse cracking and slip on the bar surface were observed. No regular secondary radial cracks as observed by Goto [65] were found. Lowes [96] tested tension specimens to investigate the internal damage in bond-zone. During the test, high energy X-ray CT facilities were used to generate high resolution gray scale images of the specimen.

2.2.2 Characteristics of Pull-out Test

Bond Stress versus Slip Response: For pull-out tests, the most direct and significant test results are bond stress versus slip data. Figure 2.8 shows monotonic load-displacement data for specimens with different levels of active confinement pressure. The load-displacement data is from anchorage bond pull-out tests representing a well-confined beam-column joint in a building frame [50].

The results of experimental studies show that initial bond response is relatively stiff and linear, followed by nonlinear response with reduced stiffness. Once maximum strength is reached, bond-zone damage resultS in rapid strength loss.

Bond Failure Modes and Parameters Affecting Bond Strength: Failure of bond is shown globally as either longitudinal splitting of the specimen or pull-through of the bar

(a) Splitting (b) Pull-through

Figure 2.9: Failure of Pull-out Test [108]

from concrete (Figure 2.9). For unconfined concrete, the bond response is brittle with rapid loss of bond after longitudinal splitting happens (brittle failure). For well confined concrete, the bond response is more ductile (ductile failure) with typically higher strength and loss of the strength is less rapid [50, 108]. Splitting cracks are prevented due to active confinement or restrained from opening due to passive confinement provided by reinforcing steel.

Corresponding to the failure mode, the major parameter affecting bond strength is confinement. Higher level confinement significantly increases bond strength and post peak response, but not initial response [73, 107]. It was also found that specimen size will affect bond strength, bond strength decreases as specimen size increases [11]. Under cyclic loading, bond strength is lost significantly under the first cycle of load, with very low bond capacity under additional cycles of load [73]. Parametric studies about effects of rib height, rib shape, concrete cover, bar lead length, bar embedded length and transverse reinforcement were also investigated [73, 19]. Results show that for unconfined specimens, rib height and shape have little effect on bond peak response, but have some influences on bar slip. Concrete cover has positive effect on both peak response and slip. Bar lead length and embedded length have positive effects on bond response. For specimens with confinement, the rib geometries have great effects on bond response, especially the rib height.

Correlating the bond damage mechanism with the global bond strength versus displacement curve, after the short initial linear elastic part in load displacement curve, nonlinearity

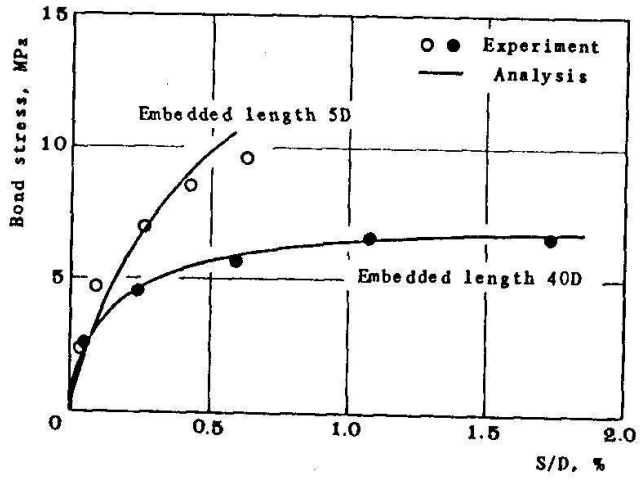

Figure 2.10: Bond Stress vs. Slip for Short Embedment and Long Embedment [137]

occurs as a result of bond-zone local damage, such as cracking of concrete. At peak load, major failure events occurred. The major events are either longitudinal splitting of specimen under low confinement, or pull-through of bar from specimen under high confinement pressure. Splitting always happens, but for high confinement specimen, splitting may not propagate to out edge of specimen. Confinement has positive effects on bond strength. The higher the confinement is, the higher the peak load is.

Bond Force Distribution Along Rebar: Experimental results show that the average bond stress is larger with short bar embedment length than that with longer embedment length [137]. This is due to the non-uniform distribution of bond stress along the bar. Figure 2.10 shows the comparison of bond stress vs. slip for short bar embedment length and long embedment length. Tests of specimens with two ribs bar and three ribs bar show that under monotonic loading, load distributions between ribs are similar for bond with two ribs and bond with three ribs. The third rib carries insignificant amount of load [73].

Multi-dimensional Bond Response (Radial Expansion): As suggested by the significant impact of confinement on bond response, bond is a three-dimensional phenomenon, and the stress-strain field in the radial and hoop directions affect performance of bond. A primary cause of bond strength loss is splitting, the opening of several longitudinal cracks

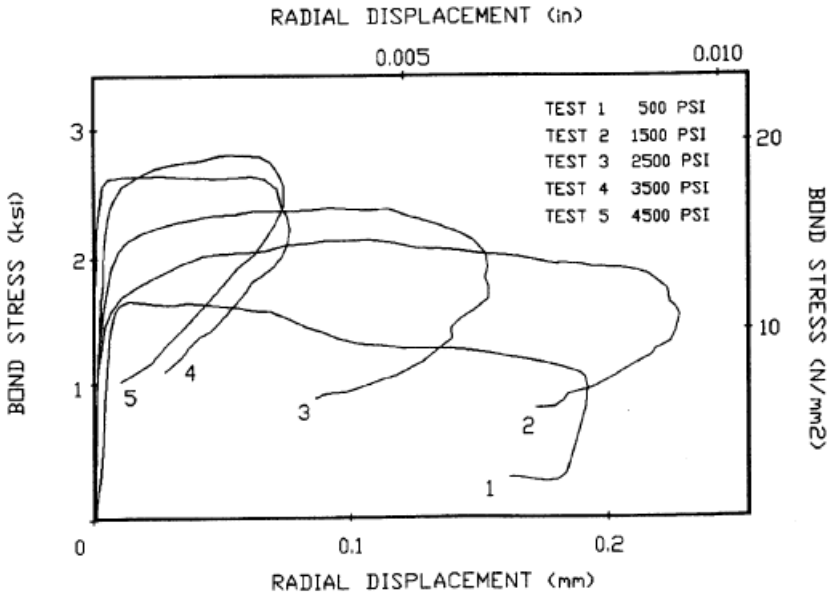

Figure 2.11: Radial Deformation in Pull-out Test [107]

parallel to the anchorage bar. Splitting results from high tensile hoop stress which is accompanied by radial deformation. Figure 2.11 shows the outer radial deformation of an confined concrete cylinder measured during pull-out tests [107]. The data show very slight radial expansion until, approximately, the bond strength is reached. At this point, significant radial expansion is observed. Once bond strength loss exceeds 10$\sim$ 20%of of maximum strength, this expansion diminishes, the radial expansion evolves to radial contraction (unloading). The higher the confinement pressure, the larger the radial contractions becomes. This is due to more local damage under radial cracking near bond zone and crushing of concrete in front of lugs for higher confinement. All specimens show both radial and longitudinal cracking. Under small to medium confinement, the bond failure is controlled by longitudinal splitting. Under high confinement, the transverse radial cracking and shear-compression of concrete in front of ribs causes the major failure of bond: pull-through of bar from concrete.

Behavior under Cyclic Loading: Bond behavior under cyclic loading depends on the intensity of the load. Bond zone deterioration happens mainly in the first cycle of load [73]. More deterioration in bond-zone will happen if the cyclic bond stress is close to the peak

bond strength [50].

2.2.3 Characteristics of Tension Test

For tensions test, three types of cracking were observed [18, 65, 108]: primary transverse cracking, secondary cracking inclined to bar axis, and longitudinal splitting (Figure 2.12 and 2.13). The primary cracking propagates from the bar surface to the concrete outer surface, and the spacing of primary cracks near bar surface is closer than that observed on outer surface of the specimen. Close to primary cracking, secondary cracks form a cone shape near the exposed surface of concrete, where longitudinal splitting was observed. Martin [108] tests showed that all primary cracks happened simultaneously after loading. This is different from numerical simulation results in which the primary cracks are in sequential order. It was unclear if it is because the propagation of cracks is too fast to capture in the laboratory.

2.2.4 Bond-zone Damage Patterns

Bond strength shows nonlinearity before peak strength due to local damages in bond-zone. Given that a bond-zone test specimen is necessarily a reinforced concrete element, few measurement techniques allow for monitoring the interior of the RC elements since using too many embedded strain gauges could affect the bond behavior. Early methods include investigation of concrete cracking pattern after the bond test. Resin or color ink were used to inject into the specimen [18, 65, 73]. Figure 2.12 shows the cracking pattern observed after an uniform tension test of rectangular specimen. Regular secondary (transverse) cracks were observed with average angle of 60 degrees to the bar axis. These transverse cracks were first initiated after loading from the first rib near the load end of specimen and propagate to the free end of specimen [73].

Recent advancement in investigation of local bond behavior includes high resolution X-ray CT imaging of bond test utilizing the high-energy X-Ray facilities [142]. Figure 2.14 shows the cracking information extracted from the images.

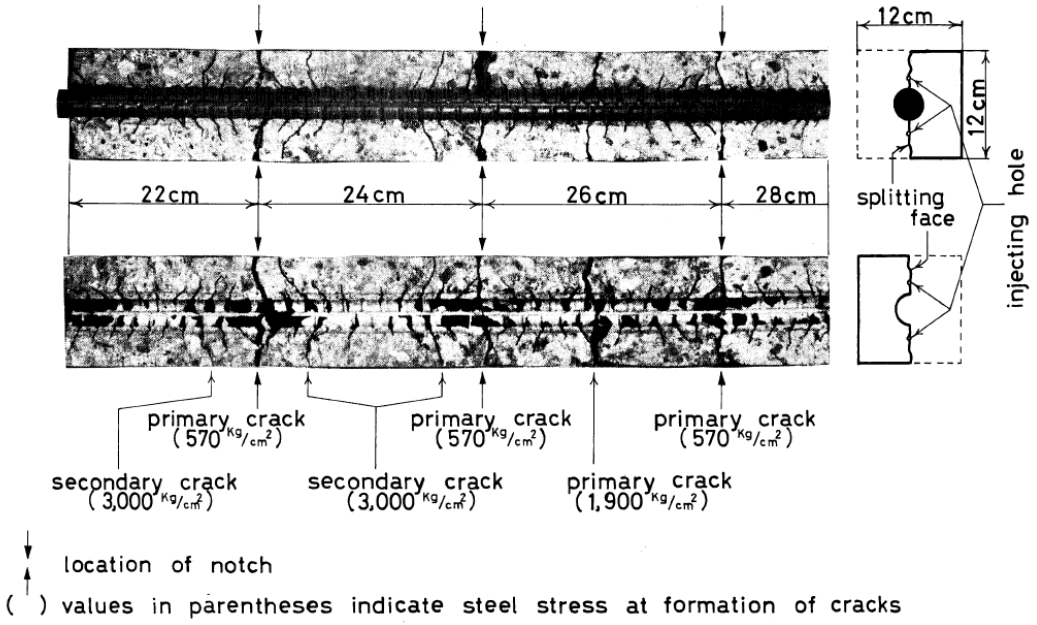

Figure 2.12: Internal Cracking for Uniform Tension Test [65]

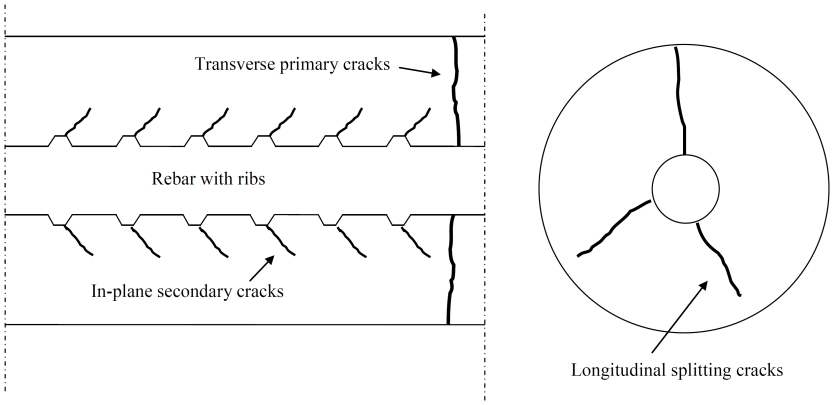

Figure 2.13: Description and Definition of Cracking near Bond-zone

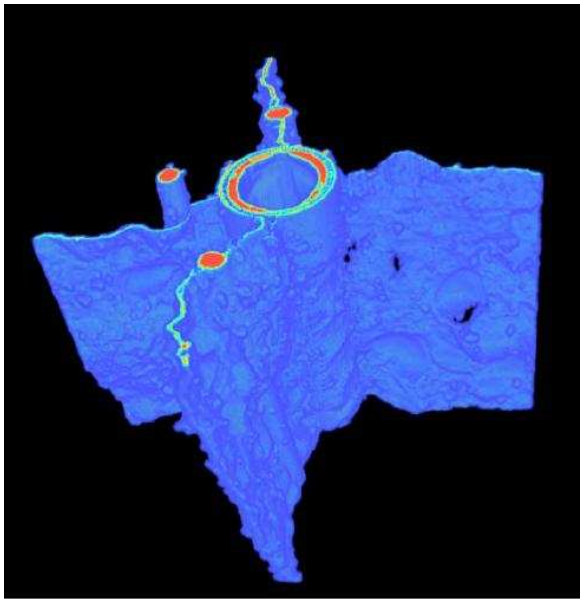

Figure 2.14: Cracking Extraction from Pull-out Test [142]

2.3 Mechanism of Bond

Lutz [103] concluded that load transfer between concrete and steel, i.e. bond, occurs through chemical adhesion, friction and mechanical interlock between concrete and deformed bar ribs. Chemical adhesion and friction are primary source of bond load transfer for a smooth bar but secondary to mechanical interlock for a deformed bar. For a deformed bar, chemical adhesion is active at initial load and represents a relatively small portion of the total bond strength. Mechanical interlock is the primary source of bond-strength for deformed bars. Friction takes effect once mechanical interlock strength is lost, providing strength at large slip demands and prior to reloading for cyclic loading. These three mechanism can be related to the measured load-displacement curves (Figure 2.15). The solid line represents the mechanical bond phase.

Further evaluation of the typical bond stress versus slip history provides insight into local bond-zone damage patterns. Initial response is stiff and elastic. Some stiffness is lost and nonlinearity introduced when chemical adhesion is lost. However, continued stiffness loss is observed up to peak strength. This is commonly attributed to initiation of cracks at the bond

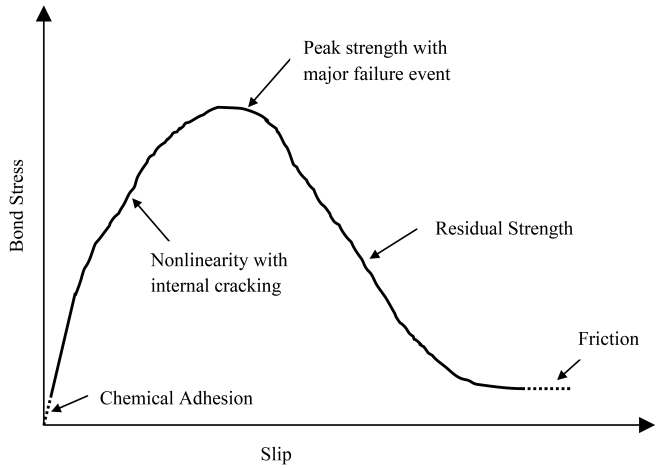

Figure 2.15: Bond Mechanism on Load-displacement Response

interface and propagation of the cracks, as found by test data in Goto and Martin [65, 108]. Crack propagation continues until maximum bond strength is achieved and the failure mode is exposed. Three major types of cracking associated with bond were observed. They are transverse cracking perpendicular to bar axis, longitudinal cracking along the bar axis due to splitting, and secondary in-plane cracking in local bond zone (Figure 2.12 and 2.13). Besides cracking, crushing of concrete in front of ribs also contributes to nonlinearity and local damages in bond-zone [50].

Bond strength loss and failure result from the development, propagation and opening of splitting cracks or pull-through. The opening of splitting cracks is accompanied by radial dilation of concrete in bond zone [107]. Pull-through happens when splitting cracks can not be propagated to the outer fibers of concrete due to active or passive confinement provided by reinforcing steel or large volume of plain concrete. Local damages in bond-zone including internal secondary (radial) cracking and crushing of concrete in front of ribs accompanies the pull-through failure [50].

The above responses are typically observed in a pull-out type test. It could be observed in a tension type test. However, typically tension test specimens have such a small volume of concrete surrounding the steel bar that radial cracks, which form prior to splitting cracks, propagate to the concrete surface. Thus the major event in a uniform tension test is the

development of primary transverse flexural cracking. After this major event, additional load results in the formulation of additional transverse cracks and the widening of existing ones. These cracks limit the load transfer to concrete [65, 108].

As the primary mechanism of load transfer after post-peak stage is friction, post-peak residual strength is dependent on confinement levels. Unconfined specimens show brittle failure with rapid loss of bond strength. For well confined specimens, bond strength shows more ductile behavior, with residual strength diminishing gradually.

In summary, the primary characteristics of bond-zone response are as follows:

1. Bond response is nonlinear with respect to the relative slip of bar with respect to concrete. The nonlinearity is due to the cracking and crushing of bond-zone concrete.

2. The stress field in the concrete surrounding the bar is three-dimensional. Loss of bond strength is attributed to damage in the plane of the bar as well as direction perpendicular to the bar. Pull-through failure is in-plane (cutting section along bar axis) stress dominant which contributes to the in-plane local cracking and crushing of bond-zone concrete , while splitting failure is radial stress dominant which contributes to the longitudinal splitting of the specimen.

3. Bond stress has nonuniform distribution along the bar axis. The ribs close the load end contribute most to the bond force.

4. Confinement level has significant effects to peak and post-peak bond strength.

5. Radial expansion and contraction of concrete accompanies the longitudinal slip of the bar.

These previous research conclusions provide a qualitative understanding of bond-zone behavior and the mechanism that determine this behavior. Results of the current study could be expected to further quantify the understanding.

2.4 Simplified Analytical Bond Models

Bond mechanism is summarized by the observations of global bond behavior and micro-structural observation in bond tests. The experimentally observed bond mechanisms were also explained by simplified analytical analyses. The bond splitting behavior has been explained by previous research using the Timoshenko's thick-walled cylinder theory [114, 148]. The splitting of concrete in bond zone is closely related with the cracking properties of concrete. Tepfers [148] assumes concrete will lost tensional capacity immediately after the cracking in developing bond strength associated with radial splitting. Nielson [114] applied fictitious cracking theory and used an exponential softening theory to account for the post cracking tensional capacity of the quasibrittle concrete material. The number of longitudinal splitting cracks is a preassumed parameter.

These existing analytical models result in peak bond strength only, not full bond development as a function of bar slip, and major focus is on longitudinal splitting. In modeling reinforced concrete structures especially considering earthquake effects, post-peak structural response has been counted to fully evaluate the structural behavior after loading. When considering bond effect in modeling RC structures, it is also important to account the post-peak bond response. Numerical analysis of bond describes not only the post-peak response, but also the local behavior near bond-zone.

2.5 Numerical Analysis of Bond

In developing models for analysis of reinforced concrete structures or components, consideration of bond behavior can provide more accurate structural response. Including bond is by adding numerical models that describe the bond behavior. A variety of modeling procedures for bond exist. Both discrete crack models [19, 165, 73, 74] and smeared crack models [133] have been used to simulate the response of bond-zone concrete to tensile loading. To accurately simulate the response of confined bond-zones, plasticity models for compressive response combined with tension softening [134, 130], the microplane model [120], and plastic-damage model [94] have been used. Review of these models identifies critical issues in these models and contributes to the development of high resolution FE models presented

in Chapter 5 in this study.

Numerical modeling of the bond-zone includes modeling the geometry of the region, which includes the concrete and steel that compose the region and the concrete-steel interface. This section introduces different approaches of modeling bond-zone on the bases of geometric formulation of the bond-zone. The material constitutive models and the concrete-steel interface constitutive models are discussed along with the geometric formulations.

2.5.1 Scale of Numerical Modeling

Modeling of bond-zone geometry is typically characterized as member-scale, bar-scale or rib-scale (Figure 2.16). Member-scale modeling treats reinforced concrete structural member as a single element member. Simulation of the impact of bond on member response is accomplished by modifying steel material response or adding additional flexibility to the element response. An example is the nonlinear bar-slip spring introduced at the base of a bridge column model to simulate additional column flexibility due to slippage of reinforcement out of a foundation [12]. This type of model is ideal for system level analysis but requires multiple assumptions about bond-zone response. This type of model is not appropriate for continuum analysis.

Bar-scale models treat concrete and steel as different material and introduce bond as a third, interface material. The level of mesh refinement is significantly greater than for the member-scale models, but reinforcing steel is typically modeled using line elements. The bond interface material is then calibrated to provide an idealized simulation of complex load-deformation response associated with steel bar and surrounding concrete. This type of model is ideal for continuum analysis of RC components. However, calibration of the interface element to capture the complex phenomena at the interface is challenging. Additionally, most interface models have been one dimensional, neglecting radial bond-zone response, which may be critical to accurately simulate component behavior.

Rib-scale modeling represents a more fundamental approach to modeling the bond-zone. A highly refined mesh is employed for concrete and steel; steel is modeled using continuum elements such that ribs on the bar are represented. An interface model may or may not be

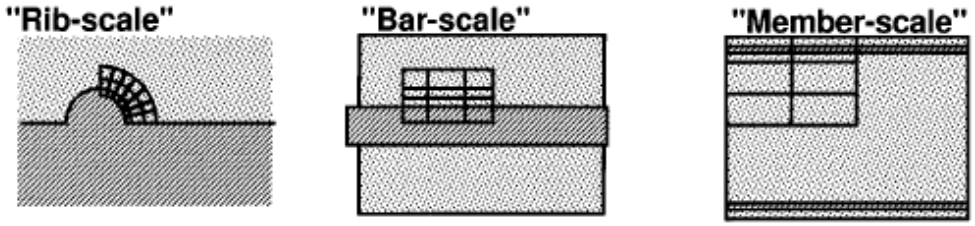

Figure 2.16: Different Scales of FE Model of Bond [38]

employed between the concrete and steel elements.

As member scale models are derived from mix formulation of concrete, steel and bond interface model. The bond interface models are same with the interface models employed in bar-scale models. The following two sections will review previous research on bar-scale models and rib scale models.

2.5.2 Bar-scale Modeling Using Bond Interface Model

In bar-scale models, the geometry of the ribs on the reinforcing steel is not specifically modeled; bond behavior is represented by the interface elements [90, 94, 101, 134, 165]. The interface element is either discrete or continuous, such as discrete link or spring element [134] or continuous zero depth four nodes plane elements [90, 94, 101, 165]. In describing these interface models, the term normal stress is the in-plane stress perpendicular to the bar axis in concrete bond-zone. The normal stress is accompanied with radial dilation or expansion, which is the relative displacement of concrete to the bar in direction of perpendicular to bar axis. The shear or friction stress (bond stress) is referred to the average bond stress in bond-zone in direction parallel with the bar axis. The shear stress is accompanied with slip, which is the relative displacement between concrete and steel in the direction parallel with bar axis.

Cox [38] employs plasticity theory to establish the relationship between bond stress and bond zone displacement. The bond stress is in direction of parallel and perpendicular to bar axis (normal stress and shear stress). And the bond zone displacement is bond slip and radial dilation. The model assumes axisymmetric behavior of bond-zone. The coupling

of normal stress and shear stress is reflected in the elastic constitutive relation of stress strain and is a function of slippage and elastic modulus of concrete. The yielding criteria and non-associate flow rule are calibrated from two groups of pull-out test with data of slip and radial dilation, and bond stress and normal stress [61, 107]. The model needs four parameters including concrete tensile strength, concrete elastic modulus, rebar diameter and rib spacing. The interface model can be implemented using four nodes continuum elements. By including radial dilation and normal stress, the proposed model was assumed to simulate average bond strength and longitudinal splitting of concrete. The validation of the model on five groups of independent pull-out tests indicated some improvements needed for this model. First, the radial dilation from the model results was much smaller than experimental data, especially for high confinement specimens. This was explained as there are not enough radial expansion experimental data to calibrate the model. Second, the accuracy of the model reduces as the confinement level increases. Third, the magnitude of longitudinal splitting can not be simulated without appropriate model for concrete to simulate the splitting.

Lowes [94, 95] presented a concrete-steel interface constitutive model including mechanical and friction mechanism of bond. The model (Figure 2.17) assumes that the radial stress is proportional to bond shear stress in developing constitutive relationship between the shear stress, radial stress and rebar slip, radial expansion. In addition, the model includes parameters such as confining pressure, slip history, concrete damage state and rebar strain rate. The bond strength is also dependent on an nonlocal formulation of concrete stress state. The constitutive model was developed to use together with a plastic damage model on surrounding concrete. This model has a good representation of the bond mechanism under confinement. For unconfined specimen with brittle splitting failure, this model gave more ductile results. In modeling load history, the model could be improved to count the bond strength increases as slippage larger than past history under cyclic loading.

Lundgren [101] presented a 2D/3D plasticity-based interface model with the elastic stiffness proportional to the elastic modulus of concrete. The elastic stiffness relates the stress along the bar axis (friction or shear stress) and along the direction perpendicular to the bar (normal stress) with slip and dilation. The 2D interface model is used for axisymmetric

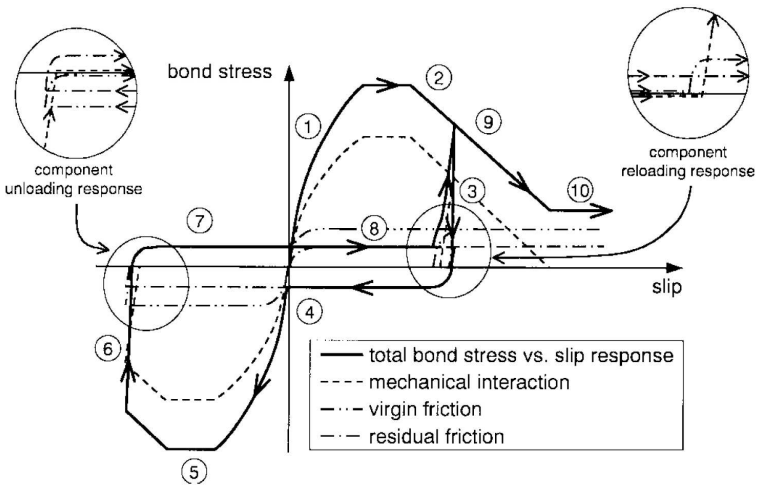

Figure 2.17: Bar-scale Bond Stress versus Slip Model by Lowes [94, 95]

modeling of RC members and the 3D model has same properties with 2D model except that the 3D model adds additional stiffness to constrain the rotation of concrete along the hood direction of bar. Yield functions include a friction model related with normal stress and an upper limit function that describes the pull-out failure. For yielding happens in the range of friction model, a nonassociate flow rule function is used. For yielding happens in the upper limit function, an associate flow rule is assumed. A hardening parameter was defined combining radial plastic deformation and slip plastic deformation. Three pull-out tests with pull-out failure, concrete splitting and steel yielding are simulated to test the model. In modeling the pull-out test, Lundgren adopted three different models for concrete, Rankin model, fixed crack model and rotating crack model. It was found that different concrete models gave different bond performance on predicting radial dilation.

Yu [165] applied cohesive fracture theory on the discrete crack modeling of RC structures (Figure 2.18). A perfect plastic bond-slip law and contact friction law is used to represent the steel-concrete interface, and cohesive theory of fracture to model concrete. When the bond stress reaches critical stress, the interface element with bond-slip law is inserted between concrete and steel is activated. contact friction law is activated when radial compression happens between concrete and steel on the interface. Both load displacement curve and

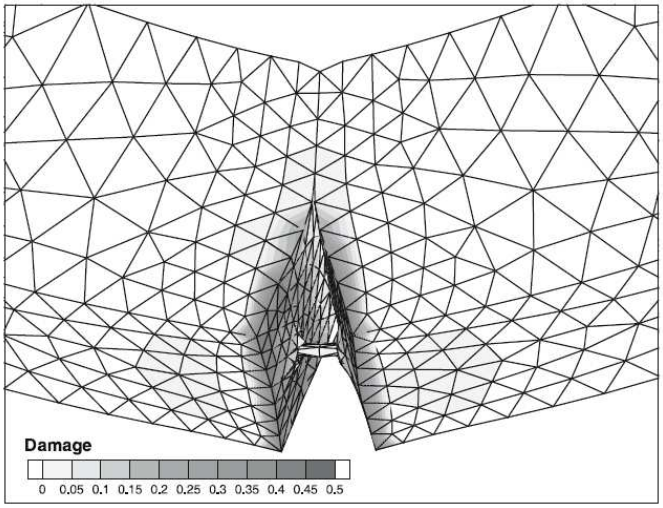

Figure 2.18: RC Beam Model by Yu [165]

cracking propagation results were presented for a reinforced concrete flexural bending beam model. The interface model was implemented with discrete crack model of concrete to simulate a reinforce beam bending. Results for members with deformed bar and smooth bar are compared. Local splitting cracking were found around deformed bar, while only slips occur around smooth bar. Results also showed that members with deformed bar have the most ductility, while smooth bars exhibit rapid strength loss. The perfect plastic bond-slip law in this model didn't address the evolution of bond strength as observed in global load-displacement response. Also, the normal stress and bond stress is decoupled.

Salem [134] applied two-dimensional joint element to model the bond slip and radial response. The geometry of ribs is modeled with one or two rectangle element. The normal stress and shear stress of the interface elements are un-coupled and different bilinear functions of radial strain and bond slip (Figure 2.19). The bilinear functions represent relation of normal stress versus radial dilation or shear stress versus slip when concrete and steel are in open and close condition. The concrete model is plastic and fracture model. The constitutive relationship between equivalent elastic strain and equivalent stress of concrete is a function of concrete fracture. The compression strength of paste near bond zone was assumed to be twice of that in concrete and stiffness is half of concrete. Stiffness adjustment

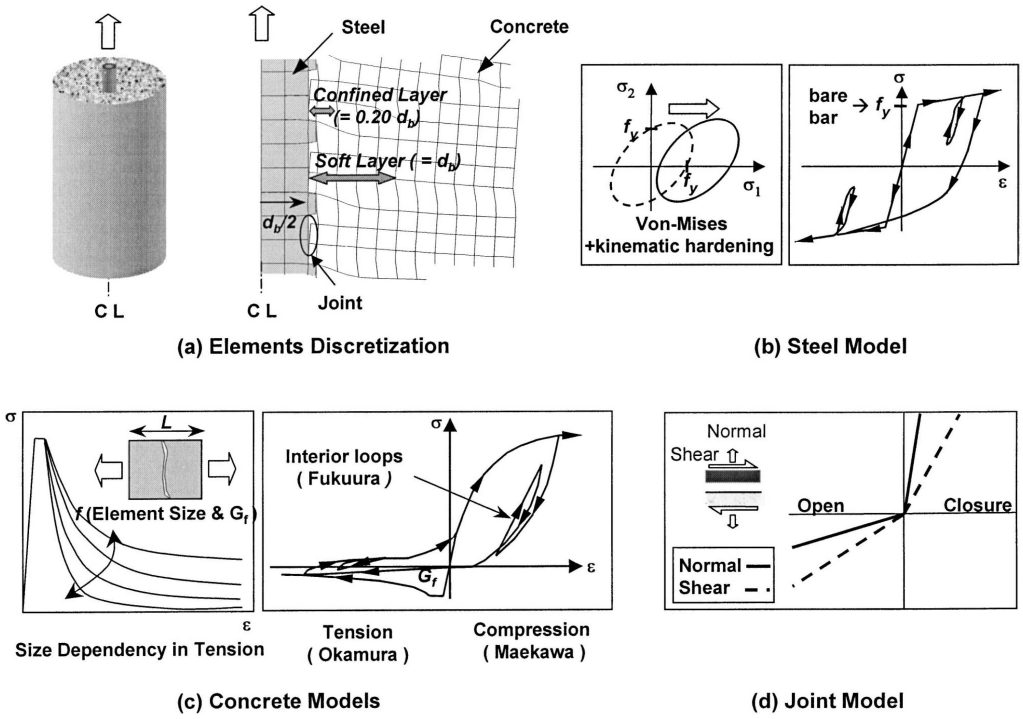

Figure 2.19: Bar-scale Model by Salem [134]

at this zone was used to model the material behavior. The adjustment was calibrated and verified by the test results. Using same model, Salem also checked the bond performance assuming complete displacement compatibility between concrete and steel without using link elements, no drastic change of bond performance was found. The model was implemented to simulate experimental test conducted by Shima [137]. The analysis results showed that at near bond-zone with layer thickness of about one bar diameter, the effect of soft porous concrete should be counted. If the stiffness of this soft layer was assumed to be one half of concrete, the analysis results matched with experimental results very well. By comparing results from using gap element or using full displacement compatibility, it was concluded that it is not necessary to use gap element between concrete and steel.

Lettow [90] presented implementations of an interface model in a three-dimensional analysis of pull-out test. The interface was modeled with finite-length and zero-width four nodes element. The constitutive model for interface (Figure 2.20) is one-dimensional model

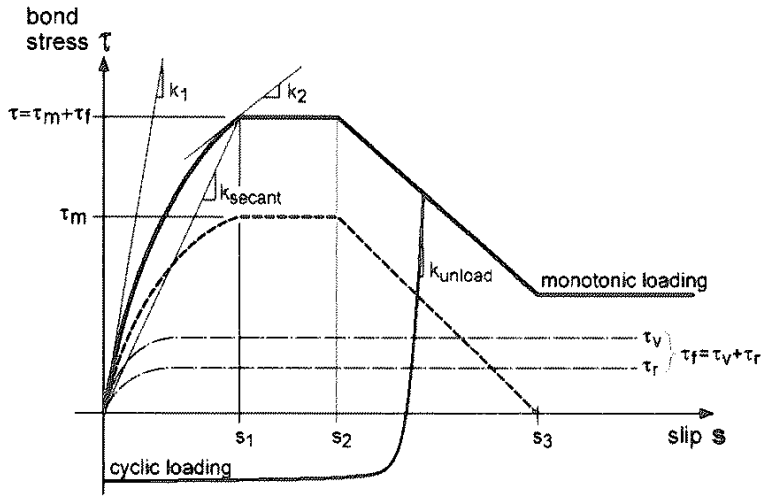

Figure 2.20: Bar-scale Model by Lettow [90]

which counted the steel strain state, concrete stress state and cyclic loading history as the parameters deciding the bond strength. The one dimensional model represents the experimental relationship between bond stress and bar slip. In radial direction, nodal displacement compatibility between concrete and steel was assumed. The radial component of bond stress (normal stress) is reflected in the concrete model near bond zone. The one-dimensinal interface model was implemented in three-dimensional modeling of pull-out tests with short bar embedment and long bar embedment. The concrete was modeled by 3D brick element and microplane model [121], the steel was modeled as truss element. Splitting and pull-out failure were identified in short bar embedment and long bar embedment specimens.

Above summaries of different interface models show that variation in developing and implementing the interface models exist. Due to limitation of experimental data, quantifying radial expansion in the interface model is not accurate [38]. Even with interface model considering normal stress and radial expansion, an accurate concrete model is still needed to simulate the component failure [101]. A one dimensional interface model together with a full three-dimensional model of concrete can simulate radial response. With a better concrete material model, interface element seems not necessary [134].

2.5.3 Rib-scale Modeling of Bond Zone

Bar-scale modeling seeks a simplified approach to simulate the load-displacement of the concrete steel interface and the impact on this response from numerous parameters such as confining pressure and concrete damage. Rib-scale modeling seeks to explicitly simulate the impact of these factors on bond response through detailed modeling of bond-zone geometry and materials. In a rib-scale model, loss of bond stiffness and strength results primarily from concrete in the vicinity of the concrete steel interface. This modeling approach is particularly appealing for investigation of bond-zone behavior as it minimizes the assumption that must be introduced in creating the model.

2.5.3.1 Brown and Darwin Model

Brown and Darwin [19] analyzed the pull-out splitting failure of beam end specimens using nonlinear fracture mechanics model (Figure 2.21). The rectangle specimens were between 7 in and 9 in high, 9 in wide and 12 inch long. One square bar of 1 in width and hight was placed in horizontal center of the specimen cross section, with top cover from 1 to 3 inch. The bar has trapezoid shape of rib with hight of 0.06 and 0.09 inch, and center spacing of 0.64 inch. The fictitious crack model was adopted to model the splitting cracks along the center line of the specimen. Stress across the cracks was modeled using nonlinear rod elements. The concrete-steel interface was modeled with interface link elements. The Mohr-Coulomb failure surface was used to model of concrete-steel interface: contact \ stick, contact \ slip or separation. Constitutive models for these three modes were established separately. Concrete and steel were both modeled with brick elements and assumed to be elastic. The geometry of ribs were modeled with fine meshes of brick element. To improve the computing efficiency, the interface elements were applied only on the compression sides of the interface between ribs and concrete.

The model results included a series of parameter analysis such as :

- The effect of rib geometry to bond behavior. As rib hight is increased, there is slight

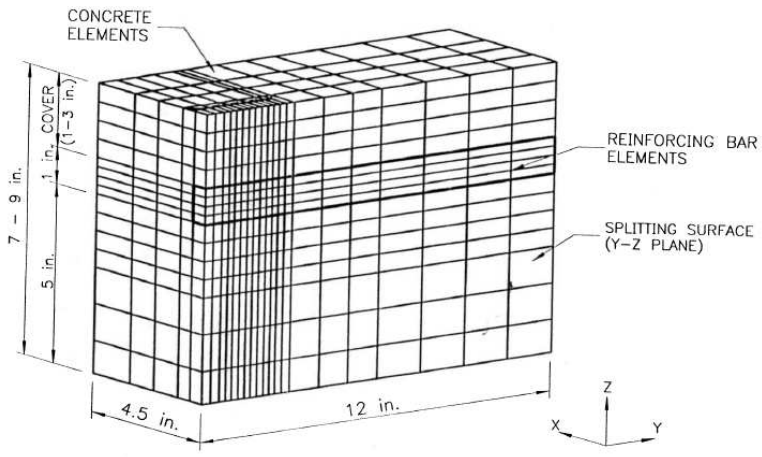

Figure 2.21: FE Model of Pull-out Test by Brown and Darwin [19]

decrease of bar slip at peak load, but the magnitude of peak load is not affected by the change of rib hight. The bond strength calculated from model with 45 degree rib side face is same with that from model with rib faces having multiple angles. However, the slip at peak is larger for multi-angle rib faces.

- The effect of transverse reinforcement confinement and concrete cover. Bond strength and slip at the peak increase as increasing transverse reinforcement or concrete cover.

- The effect of lead length and embedded length. Increase in bond strength was observed when increasing unboned lead length. Similarly, increasing embedment length will increase longitudinal splitting length. However, the amount of concrete splitting at peak load does not increase proportionally with the increase of embedded length, which means bond strength does not increase proportionally with embedded length.

- Lateral displacement. Before peak load, Lateral displacements measured at the face of the specimen do not vary with rib hight or rib shape. Once peak load is reached, increasing rib hight will increase lateral displacement.

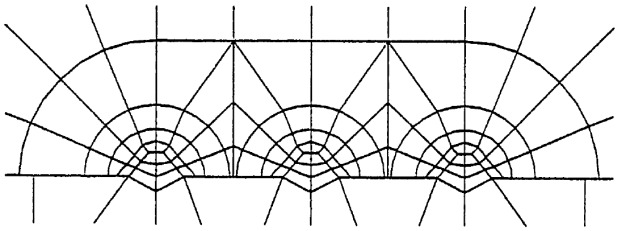

Figure 2.22: FE Model of Pull-out Test by Hungspreug [73]

2.5.3.2 Hungspreug Model

Hungspreug [73] presented a parametric finite element analysis of pull-out tests (Figure 2.22). The specimen was 6 inch long, 6 inch diameter and a 1 inch diameter bar with 3 ribs in the center. The trapezoid shape ribs were modeled geometrically with finer four nodes quadrilateral elements and triangle elements. Different bar and concrete boundary condition include radial constraint of concrete and radial free movement of concrete. Different ribs and near rib concrete interaction conditions include free contact, contact with interface element. Linear fracture model was used to model concrete cracking.

Results for all cases of analysis show much stiffer load-slip curve than the experimental results. The reasons were explained as neglecting of splitting cracks and nonlinearity of concrete, particularly in front of ribs. Transverse secondary cracking happens before longitudinal splitting crack. The analyzed results are much stiffer than the test results also show that the overall bond behavior of concrete is not affected by the transverse secondary cracking alone, other nonlinearity of concrete as well as splitting cracks contribute to the overall bond response. The analysis also found that the boundary conditions at the ribs did not affect the overall behavior or the strain distribution along the bar, but affect the local stress magnitude. Although the initial crack direction in front of ribs are affected by different boundary conditions between rib and concrete, the slight change of cracking angle did not have significant impact to the overall behavior. The approximate angles of the secondary cracking are 50, 60 and 70 degrees for first, second and third ribs.

2.5.3.3 Ozbolt Model

Ozbolt [120] modeled one of the pull-out tests conducted by Eligehausen [50] using microplane model [120] to simulate concrete response in bond-zone. The test specimen was a 8 inch diameter, 7 inch long concrete cylinder, with 1 inch diameter bar embedded in the center. The ribs have hight of 0.06 inch and spacing of 0.5 inch. An axisymmetric model of the specimen was created using 4-node element for concrete and steel (Figure 2.23). The shape of ribs was modeled. The displacement compatibility between steel and concrete was assumed.

The modeling results show shear failure of concrete between ribs. Under monotonic loading, at about 30% of peak load, cracks were initiated at ribs and propagate at an angle of around 65 degree to the bar axis. At about 60% of the peak load, much high nonlinearity induced by splitting cracking happened. The splitting cracks activated the confining reinforcement. At the same time, the high nonlinearity was also caused by significant compression stresses in front of ribs. Ozbolt also concluded that peak load, displacement peak load and descending branch of the load-displacement curve strongly affected by lateral confinement.

Analysis results showed that the bar slip displacement at peak load is much smaller than experimental data observed in the lab. The reasons were explained as:

1. For confined specimen, the small volume of concrete near rib-zone is under high compression and shear stresses state with large volume dilatancy. The exact modeling of this phenomenon with current model may have problems.

2. The analysis was based on small strain formulation, which is different from the actual large deformation of concrete near rib-zone.

3. The axisymmetric model was used instead of a full 3D model.

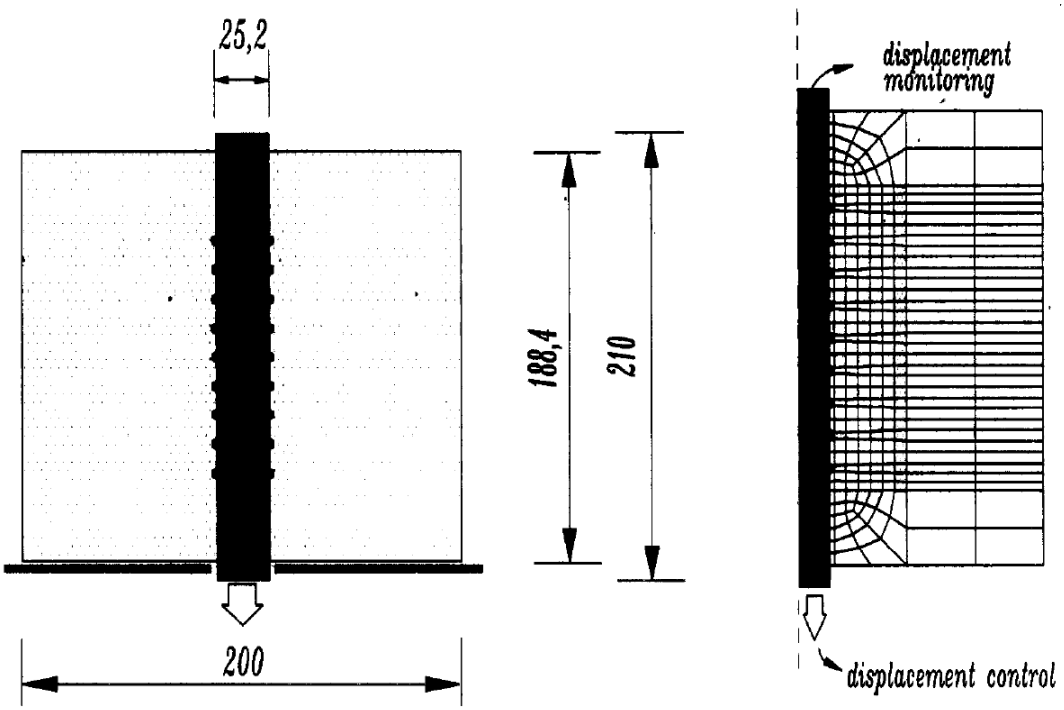

Figure 2.23: FE Model of Pull-out Test by Ozbolt [120]

2.5.3.4 Reinhardt Model

Reinhardt [130] modeled a pull-out test by using axisymmetric model with a nonlinear slip layer around the deformed bar. The nonlinear behavior in this special layer of elements was modeled by Mohr-Coulomb model with tension cut-off with smeared cracks, steel and concrete outside this layer are linear elastic homogeneous body. The geometry of rib zone concrete was modeled as continuum elements. And the slip layer of 2.9 mm near ribs have material properties of mortar with lower Young's modulus than surrounding concrete, but slip layer far from ribs are around 10 times thicker than the mortar layer and have properties of concrete. The trapezoid shape of bar ribs in the mortar layer is meshed with 2∼3 small elements. The reinforcing bar is not modeled but boundary condition is used along the bar/ribs mortar interface. The boundary is set to allow displacement parallel with bar direction but fixed in the direction perpendicular to the bar. In addition, the boundaries between ribs addressed adhesion and friction due to the bar slippage. concrete outside the rebar zone are represented by linear elastic springs. The stiffness of the spring elements was calculated by elastic solution of internal loaded thick wall cylinder [151].

The analysis was focused on bond peak strength and pre-peak behavior. Results show that the normal stress in the slip layer increase almost linearly with the bar slip. And high strength concrete model also has a higher normal stress. The model was used to test the dependence of bond stress and normal stress to confinement by adding additional radial pressure on the outer surface of the slip layer. Both bond stress and normal stress increase as the radial pressure increases.

The concrete plastic deformation happened in front of the ribs. The cracking patterns were presented by using the orientation of the principal tensile stress. The in-plane secondary cracking emerged from the plastic zone in front of the ribs into concrete forming a cone shape cracked zone. At the same time, the longitudinal splitting cracks happen at entire slip layer. Higher strength concrete specimen showed smaller plastic zone, while only slight differences were found for the cracking patterns from normal strength and high strength concrete. For analysis under different radial pressures, the results showed that the higher the radial pressure, the larger the plastic zone and the smaller the cone shaped cracks

zone.

2.5.3.5 Rots Model

Rots [133] analyzed a uniform tension specimen test in which a 1 inch diameter reinforcing bar was embedded in a 6 inch diameter concrete cylinder. The specimen was long enough to develop the primary transverse cracking. The geometry of specimen was modeled as axisymmetric and mirror-symmetric, which means one quarter of the specimen was modeled. The bar was modeled using four-node rectangle elements; and concrete was modeled using three-node triangles. The element size is 0.25 inch. The space of ribs is 0.5 in. the geometry of rib was not modeled specifically. The concrete was modeled as material with nonlinear softening with secant unloading stiffness. A fixed crack model was used for longitudinal cracking and rotating crack model was used for transverse crack modeling. Steel was linear elastic. In the first model, mechanical interlock was modeled by enforcing displacement compatibility between concrete and steel at the location of ribs. Between ribs, displacement compliance was enforced only in the radial direction for the overlapping nodes between steel and concrete. Adhesion and friction along the steel-concrete interface were neglected to emphasize the impact of mechanical interlock provided by the ribs. Geometric imperfection was applied to pre-identified locations along the longitudinal direction and perimeter of the specimen as the crack initiator. The cracking propagation was in the sequence of initial secondary cracking stage, transverse primary cracking stage and final secondary cracking. Longitudinal splitting cracking was modeled assuming two or four cracking along the perimeter of the specimen. Sudden softening in the global load-displacement response due to the longitudinal splitting cracking was found. Rots also explained the limitation of axisymmetric model in modeling the longitudinal cracking due to the ring stress effect from smearing the cracks along the perimeter of the cylinder.

The second model was essentially the same as the first one with the exception that the interface truss element was assumed between steel and concrete. For the interface truss element, 1D bond stress versus slip relation is used, the interface normal stress and shear-normal coupling were ignored. The radial component of bond-zone stress is reflected by

stress in concrete elements. A tri-linear shear-slip relation was adopted for the interface elements. Material imperfection was adopted by assuming material strength random distribution. The primary cracking was formed reasonably at several locations. To compare the effect of using interface element or not, a bending beam model subjected to flexural loading was analyzed. Results showed that with interface model, the primary cracking was located at several discrete locations, which is similar as experimental results. The first model with displacement compatibility between concrete and steel resulted transverse cracking diffusion along the beam without localization of the cracking.

2.5.3.6 Ingraffea Model

Ingraffea [74] applied discrete nonlinear fracture mechanics to the FE modeling of two uniform tension specimens (Figure 2.24). The investigation was focused on secondary cracking in flexural bond zone. The models were axisymmetric and displacement compatibility was assumed between concrete and steel nodes. The geometry of steel rib was not modeled. The first model is a 6 inch diameter concrete cylinder with a 1 inch diameter reinforcing bar in the center, and specimen length is 12 inch. The second model is a 12 inch diameter concrete cylinder with a 0.6 inch diameter reinforcing bar in the center, and specimen length is 24 inch. The objective was to investigate the secondary cracking and if the secondary cracking is independent of the overall specimen size.

Modeling results showed that propagation of secondary cracking is consistent with the experimental observations from Goto [65]. The first secondary cracking was initiated under very low load, and at location where the bar exits concrete (end of specimen or at location of primary cracking). Even the second model has a larger concrete cover, results showed that the secondary cracking was confined to a region where reinforcing bar exits concrete. It was concluded that the bond-slip behavior is a local phenomenon independent of the overall structural geometry.

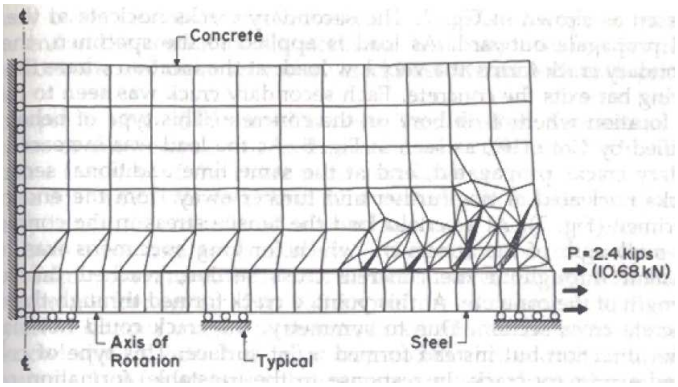

Figure 2.24: FE Model of Tension Test by Ingraffea [74]

2.5.3.7 Summaries on Rib Scale Modeling

The benefit of rib-scale models is the availability of local bond cracking or crushing behavior, which is critical on global bond behavior. Additionally, rib-scale models have the potential to investigate bond in full three-dimensional scale as as to fully quantify the radial responses. Early rib-scale models can be improved both on geometric refinement and material complexity. To capture the stress field in the local bond-zone, the finite element mesh size should be fine enough, and the interaction between concrete and ribs should reflect as realistic as possible the physical phenomenon. In material aspect, both tension cracking and compression plasticity need to be addressed to fully capture the damage process. Chapter 5 presents the FEM modelings considering above factors that will improve the rib-scale modeling.

Chapter 3

Investigation of Bond Using X-ray Tomography Data

3.1 Introduction

Knowledge of the deformation and stress-strain field in the vicinity of the concrete-steel interface is fundamental to understanding the behavior of bond. Measuring the local bond-zone deformation during a bond test using traditional instrumentation is difficult. The use of traditional steel strain gages disrupts the concrete-steel bond, unless bars are machined to place gages inside the bar or within a groove on the bar. The use of embedded concrete gages also may disrupt bond, and such gages can only provide average strains in a few locations and orientations. Additionally, in the past only destructive methods were available for monitoring concrete crack patterns within the bond-zone [65, 18]. Given the limitation of traditional instrumentation, high-energy computed tomography (CT) imaging provides an ideal tool for monitoring progressive bond damage to the local bond-zone.

The researchers at University of Washington (UW) completed the first of a series of bond tests in which specimen response was monitored during loading using high-energy CT [96, 108, 142]. At different load levels, 3D images of the specimens were generated by combining stacks of two-dimensional gray scale images. The 2D images represent slices of the specimens, with gray-scale values for each pixel represents the amount of energy penetrating the material at that particular location [142]. Thus, air voids and cracks show up at black pixels while concrete paste and aggregate are various shades of gray and the reinforcing steel is represented by white pixels. Figure 3.1 shows a typical image specimen. The resolution of the images is typically 0.2x0.2x0.5 mm. Applying image processing algorithms to these image data, it is possible to identify progressive cracking as well as determine deformation fields. This chapter introduces high-energy CT imaging of the bond specimens and the algorithms used to analyze these data to improve understanding of bond-zone behavior.

Section 3.2 introduces high-energy imaging technologies applicable to investigation and

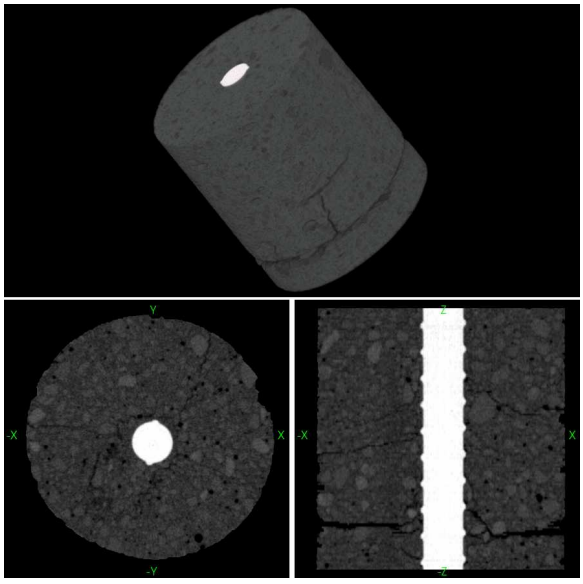

Figure 3.1: Typical Image Specimen

monitoring of RC concrete structures.

Section 3.3 presents information on the facilities used to accomplish high-energy CT of the bond test specimens.

Section 3.4 presents the image data collected by researchers at UW including the bond tests employed and the image data available for use in the current study.

Section 3.5 provides a review of algorithms in processing/analyzing the image data.

Section 3.6 reviews previous research of investigating concrete and bond using X-ray images.

Section 3.7 summarizes the methodologies identified to analyze the bond test X-ray CT images.

3.2 High-energy Imaging

Detecting flaw or damages in interior of structures or materials is significant to investigate the materials or monitor the structural health. Energy-based imaging techniques used for engineering materials are appealing because they are non-destructive and can quickly obtain the material defects information. Buyukozturk [25] and Pla-Rucki [126] presented detailed

summary on technologies imaging concrete structures. The imaging technologies include material density-based Radioactive Computed Tomography (CT), material temperature-based Infrared Thermography, material dielectric property-based Microwave Tomography and elastic wave propagation-based Acoustic Tomography.

Radiography imaging utilizes the X-rays or gamma rays emitting from radio-active isotopes as the energy resources. As the X-ray passes through the object, the energy intensity is reduced due to the absorbing of some X-ray photons by the object. The X-ray energy loss is a function of material density as indexed by attenuation coefficient of material, which is proportional to material density. Attenuation coefficient for steel is 1, for concrete is 0.3, and for air is 0 [126].

Imaging by X-ray CT requires an X-ray source, specimen to be imaged, and a detector to receive signal and generate images. Sprague [142] presented very detailed information of X-ray CT imaging process. Either specimen or X-ray source needs to be rotated to obtain transmitted signals in all directions. The image is constructed by solving the attenuation coefficients at the intersection of X-ray beams on the specimen from different directions according to source energy and reduced energy intensity, as from equation 3.1.

$$\int_0^t \mu(x,y,z)dt = -ln(\frac{I}{I_0}) \tag{3.1}$$

where I_0 is the source energy intensity, I is the transmitted intensity measured, μ is attenuation coefficient of material at location (x,y,z). Once the attenuation coefficient is calculated, the material density is known. Depending on the X-ray source configurations, a single-pencil-beam emitting a small amount of straight ray , a single-plane-fan-beam emitting a number of straight and fan-shape rays, or multiple-plane cone beam emitting multiple rays in 3D cone shape can be generated. The resolution of the image is dependent on the number of ray paths, which is dependent on the number of views in imaging and the material slice thickness in 2D imaging. Other variables influencing the quality of images are pre-calibration of the detector, integration time for detector to receive the signals and filtering [142].

The advantage of X-ray CT technology is it can generate high accuracy images. The

disadvantages are that the equipment is expensive and the imaging is limited for laboratory use due to the hazardous nature of X-rays.

Infrared Thermography utilizes the nature infrared (IR) radiation of the object as the energy source. The radiation emitted from an object is dependent on surface temperature of the object and can be measured by IR cameras. As the heat flow within the object is affected by the internal anomalies, the distribution of subsurface temperature within the object can indicate the defects in the objects.

The IR thermography has low hazard and the equipment is portable. However, the image construction is difficult as the surface temperature of the object is affected by surrounding environment. Wind, cloud cover, surface moisture and surface roughness are parameters that need to be corrected when constructing the images. Besides the problem of accuracy, IR imaging does not provide information about depth of object flow and has limitation on detecting deep flaw.

Microwave Tomography Groudn-penetrating radars (GPR) can send short electromagnetic microwave pulses into the detecting object. Due to the different dielectric properties of different materials, the pulses are reflected at the interfaces of different materials and the echoes are monitored by the receiver. The depth of the interface is estimated by the travel time when the pulse velocity is known. The advantage of GPR is its ability to penetrate deep members, so it is widely used in geotechnical engineering for locating buried pipes, cables or hazardous-waste containers. The main disadvantage with GPR is the wavelength of the microwave is dependent on the object's dimensions. This increase the difficulty in reconstruction of the images and the accuracy.

Acoustic Tomography (AT) generates images according to the different elastic wave propagating properties of materials under an impact source. The elastic wave can be ultrasonic pulse, surface wave, impact-Echo wave and impulse response wave. Recent development of acoustic tomography is summarized in Zhu [171]. In imaging concrete structures, the AT technologies are mostly used to detect defects such as voids and cracks in concrete.

Figure 3.2: UT Austin X-ray Facility [96, 142]

3.3 Imaging Facilities

Two high-energy CT facilities were used to investigate imaging of reinforced concrete components and improve understanding of bond-zone behavior: the NSF-Supported High-Resolution X-ray CT Facility at the University of Texas at Austin and the industrial CT Facility at YXLON International in Hattingen, Germany.

The UT Austin facility (Figure 3.2) includes two imagining sub-systems, one that can be used to produce ultra high-resolution (∼250 m to ∼5 m) images of small, moderately dense specimens (diameter less than ∼20 mm) and one that can be used to produce high-resolution (∼5 mm to ∼0.25 mm) images of larger, denser specimens (diameters less than ∼200 mm). For this project, the second system was used. This second system employs a 420-kV tungsten X-ray source and a 512-channel cadmium-tungstate solid-state linear array. The cadmium-tungstate detector provides superior sensitivity because of its high absorption efficiency. This detector has a vertical aperture (slice thickness) ranging from 5 mm down to 0.25 mm and a horizontal channel pitch of 0.31 mm. This system can accommodate specimens up to 50 kg in weight and 1500 mm in height. For this project, imaging resolution was typically 0.3 mm by 0.3 mm in the 2D plane with a slice thickness of 0.5 mm.

The YXLON International facility in Hattingen, German includes three imaging systems with different energy sources and different detectors: A 200-keV x-ray source with a panel detector (YXLON Panel Detector XRD01620 Universal). A 450 keV x-ray source (YXLON Y.TU 450-D09 biploar metal-ceramic x-ray tube) with a cadmium-tungstate linear detector array (YXLON Y.LineScan 250-16-65). For the specimens imaged as part of this study, this system provided a maximum resolution of approximately 0.2 mm in the plane with a slice thickness of 0.5 mm. A 9 MeV linear accelerator with a linear diode array (LDA Detector). For the specimens imaged as part of this study, this system provided a maximum resolution of approximately 0.2 mm in the plane with a slice thickness of 0.5 mm. For this project, the 450 keV and the 9 MeV systems were used.

3.4 Bond Test Specimens for the Imaging Study

Three types of test were used to investigate high-energy CT imaging of reinforced concrete: single-ended pull-out tests, double-ended flexure tests, and controlled cracking tests. These tests are described below.

3.4.1 Single-ended Pull-out Tests

The single-ended pull-out test is the type of bond test described in section 2.2 previously, as shown in Figure 3.3. These tests are intended to represent an anchorage bond zone, such as where a column longitudinal bar is anchored in a foundation or where a beam longitudinal bar is embedded in a joint.

A test specimen consisted of a plain or reinforced concrete cylinder of variable height (such as 12 inch) and diameter (such as 6 inch) in which a single reinforcing bar of variable diameter (No.6 or No.8) is embedded with a variable anchorage length. Concrete cylinders were typically reinforced using a spiral of small-gage steel wire. Spiral pitch, wire diameter, and wire material properties were varied to achieve different levels of confinement. Spiral diameter was typically 1 inch less than the diameter of the concrete cylinder. Some specimens were reinforced by casting the concrete cylinder in a thick-walled aluminum tube, which was not removed. The embedded reinforcing bar was placed at the center of the

cylinder, extended the entire length of the cylinder and protruded from one end of the cylinder to enable tensile loading of the bar. To reduce the length along which the concrete was bonded to the reinforcing steel, the embedded steel bar was placed inside a thin-walled PVC tube of variable length. The bonded region of the reinforcing bar was located at the end of the concrete cylinder opposite from the protruding end of the bar. Figure 3.3 shows a typical specimen.

Testing of the pull-out specimens was accomplished using a self-equilibrating test rig in which tensile load was applied to the protruding end of the embedded reinforcing bar to achieve a monotonically increasing displacement history and reacted as compression on the surface of the concrete cylinder. Figure 3.3 shows a typical specimen in the test rig, additional details are provided by Martin [108].

The behavior of single-ended pull-out specimens was typically characterized by an initially stiff load-displacement response up to a peak load beyond which two, three or four splitting cracks formed in the cylinder and the specimen rapidly lost strength. For very well confined specimens (e.g., specimens confined by a thick-walled aluminum tube), specimens did not exhibit splitting cracks and specimen strength was determined by yielding of the embedded reinforcing bar. Figure 3.4 shows a typical load-displacement response for a specimen that exhibited a splitting-type failure; the points at which CT imaging was done are identified by black circles.

3.4.2 Double-ended Flexural Bond Tests

The double-ended flexural bond test is a tension test, as introduced in section 2.2 and Figure 3.5. These tests are intended to represent a flexure bond zone, such as develops in the vicinity of a longitudinal reinforcing bar at mid-span of a beam or mid-height of a column.

A test specimen consisted of a plain or reinforced concrete cylinder of variable length and diameter in which a single reinforcing bar of variable diameter was embedded. Concrete cylinders were reinforced using a spiral of small-gage steel wire. Spiral pitch, wire diameter, and wire material properties were varied to achieve different levels of confinement. Spiral diameter was typically 1 inch less than the diameter of the concrete cylinder. The embedded

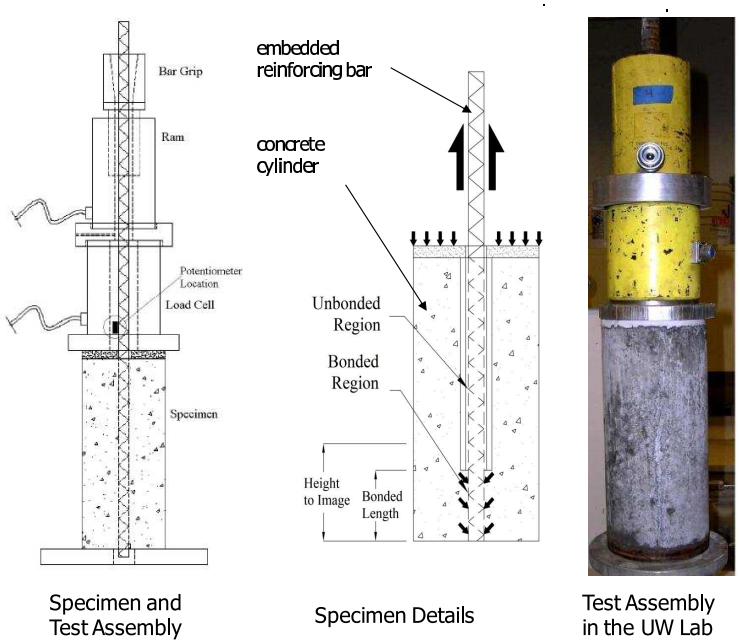

Figure 3.3: pull-out Test Setup [108]

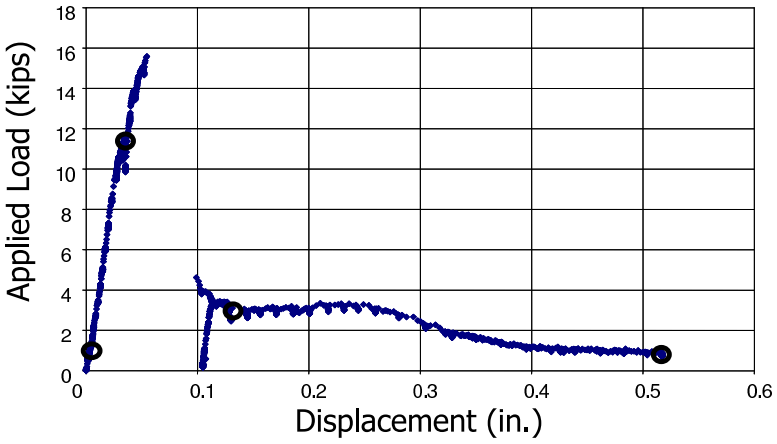

Figure 3.4: Pull Out Test Load-displacement Response [96, 108]

reinforcing bar was placed at the center of the cylinder and protruded approximately 2 ft. from each end of the cylinder to enable tensile loading of the bar. The bar was bonded to the concrete cylinder along the entire length of the concrete cylinder. Crack initiators were used to locate cracks that formed perpendicular to the axis of the specimen. For some specimens, these crack initiators were relatively large gauge (0.25 inch diameter) wire rings with diameters 0.5 in. to 1.0 inches less than the outer diameter of the concrete cylinders; for other specimens, crack initiators were 0.25 inch grooves ringing the exterior surface of the cylinder. Crack initiators were spaced at 4 in. to 8 in. intervals along the length of the cylinder.

Testing of the flexural bond specimens was accomplished at UW using the Baldwin Universal testing machine and at both UW and YXLON Int. using a self-equilibrating test rig. Figure 3.5 shows the self-equilibrating test rig in which the bottom end of the embedded bar is attached to the base plate of the test rig and tensile load is applied to top end of the embedded bar via a hydraulic ram that reacts against the top plate of the test rig. Ultimately, the test rig induces tension in the reinforced concrete cylinder and compression in the acrylic tube surrounding the test specimen. Flexure bond specimens were loaded in tension to induce monotonically increasing elongation of the specimen.

Flexure-bond specimens typically responded with an initially stiff load-displacement response followed by simultaneous opening and widening of multiple cracks perpendicular to the axis of the specimen and located at the embedded crack initiators. Figure 3.6 shows the load history of a typical flexure-bond specimen.

3.4.3 Controlled Cracking Tests

Figure 3.7 shows a drawing of a controlled cracking test specimen and the testing apparatus. Controlled cracking tests were not intended to represent a specific region within a reinforced concrete specimen, but were instead intended to provide data for use in evaluating high-energy CT imaging of reinforced concrete components.

In the controlled cracking tests, a mechanical device was used to subject a hollow reinforced concrete cylinder to monotonically increasing internal expansive deformation. This

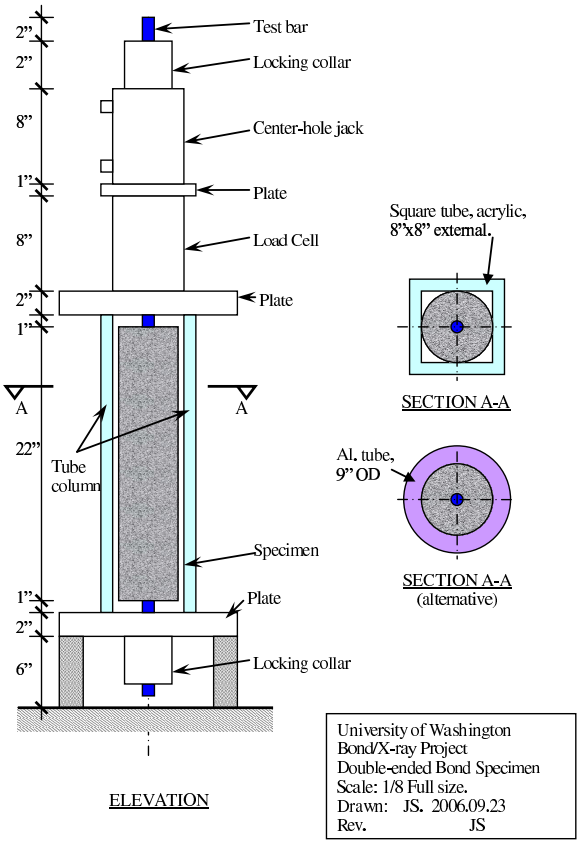

Figure 3.5: Flexural Bond Test Setup [96]

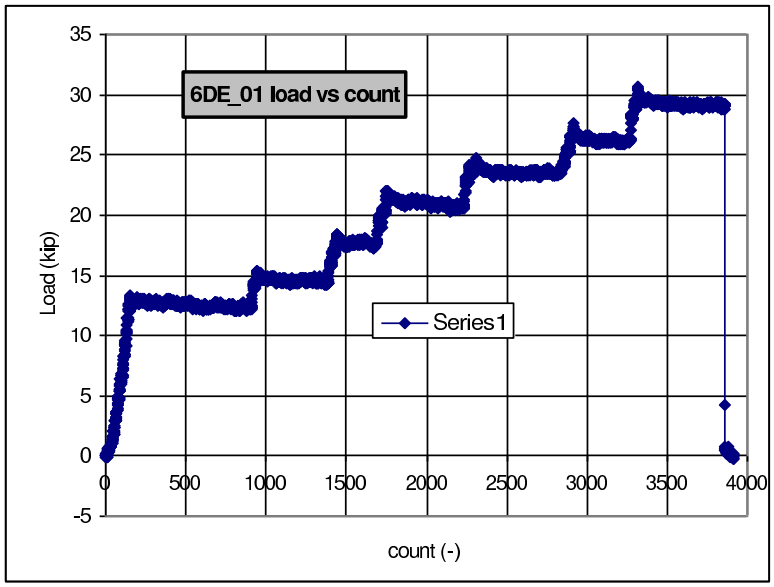

Figure 3.6: Flexural Bond Test Load-displacement [96]

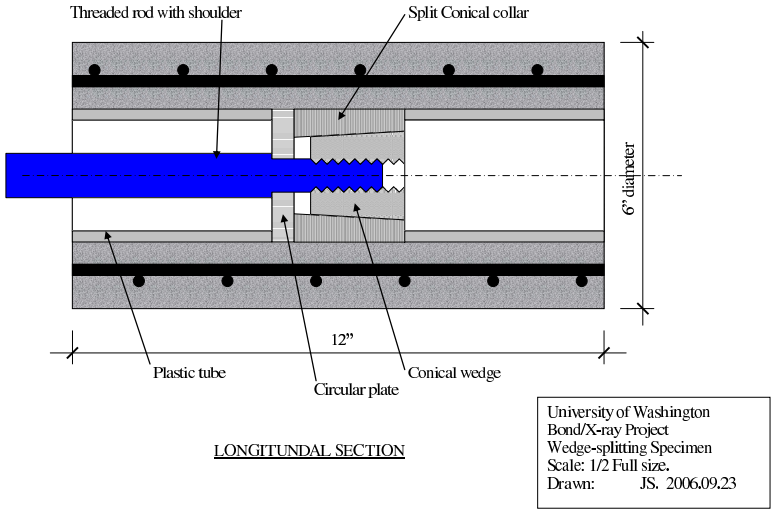

Figure 3.7: Controlled Crack Setup [96]

results in the development of splitting cracks in the concrete cylinder that initiate at the inner surface of the cylinder and propagate towards the outer surface and along the length of the cylinder. By controlling the rate of internal expansion, it is possible to control the width of the concrete cracks.

3.4.4 Laboratory Test Program

As suggested by the above discussion, many individual laboratory tests were conducted to investigate bond-zone behavior and high-energy CT imaging of reinforced concrete specimens [108, 142]. As a result of this project, 14 specimens were imaged at either the UT Austin or YXLON facility. Table 3.1 provides details of the image data sets generated as part of this study. Specimens were imaged in a variety of conditions. Two specimens were imaged in their original un-damaged state. Five specimens were imaged following application of load at UW. Two specimens were imaged at multiple points during an increasing load history but not under load (this was done by subjecting the specimens to an increment of load to increase specimen damage, removing them from the loading apparatus, imaging them, returning them to loading apparatus and repeating the process). Six specimens were imaged at multiple points during an increasing load history, while under load.

Table 3.1: Bond Test Images [96]

Test Series Name	Date of Testing	Type of Specimen and Loading	Imaging Facility and Imaging System	Image Resolution	Length of Specimen Imaged
Martin-Series 1	Oct. 2004	Two pull-out specimens (SA*-B, SA*-D). Specimens were tested at UW and imaged following testing.	UT Austin: 420 keV system	0.3 mm x 0.3 mm x 1 mm	Approx. 3 in. of bond-zone at base of specimen
Martin-Series 5A	March 2006	Four pull-out specimens (SF 0612-08-03* OR 4, 6, 9, 16). Specimens were tested at UW and imaged following testing.	UT Austin: 420 keV system	0.3 mm x 0.3 mm x 0.5/1 mm	Approx. 3 in. of bond-zone at base of specimen
Martin-Series 5B	May 2006	Five pull-out specimens (SF 0612-08-03* OR P1, P3F, P3W1A, P3W1B, P3W2). Specimens were imaged under load. Imaging was done at four points during the test	UT Austin: 420 keV system	0.3 mm x 0.3 mm x 0.5/1 mm	Approx. 3 in. of bond-zone at base of specimen
Series 6	March 2008	Three specimens: Predamaged flexure-bond specimen (6DE00). Undamaged flexure-bond (6DE02) and controlled cracking specimens.	YXLON Int.: 9 MeV system	0.2 mm x 0.2 mm x 0.5/1 mm	The entire 22 in. length of specimen 6DE00 was imaged. Approx. 3 in. lengths of specimens 6DE02 and CC were imaged.
Series 7	April 2008	Three specimens imaged:Predamaged flexure-bond specimen (6DE00). CC and pull-out specimens imaged, not under load, but at points of increasing damage.	YXLON Int.: 450 keV system	0.2 mm x 0.2 mm x 0.5/1 mm	Approx. 3 in. lengths of specimens are imaged.
Series 8	June 2008	One specimen: flexure-bond specimen (6DE02) imaged under load at seven load levels	YXLON Int.: 9 MeV system	0.2 mm x 0.2 mm x 0.5/1 mm	The entire length (22 in.) of the specimen was imaged.

3.5 Previous Research on Image Processing

The goal of collecting X-ray CT images of bond test specimens is to extract information from the images to identify changes of material state during the test. There are two major areas in image processing that contributes to extracting information from images: segmentation and motion estimation. Segmentation is a method to group objects in images that have same properties, such as extracting cracks, aggregates or steels in concrete images. Motion estimation involves estimating feature displacements between two sequences of images.

Image segmentation is to identify different objects (Figure 3.8) within an image so that additional processing of these objects (e.g. calculation of volume, centroid, surface area) can be accomplished. Image segmentation is an active research area, the most common algorithms can be categorized as simple intensity frequency based (threshold segmentation), gradient based (edge detections [31]), statistical clustering (k-mean clustering [36]) and variational optimization method (such as active contour or level sets [77]). Detailed summaries on the segmentation methods can be found in dissertations of Brox [20] and Zhang [169].

The bond test X-ray images are in gray scale, with gray value of each pixel representing the material density at the pixel point. For the bond test specimen it is desirable to detect concrete, steel, voids and developed cracks. Threshold method is most direct and simple method of segmentation. It is accomplished using predefined threshold intensity values which are based on histogram of the image intensity. For a gray scale image, if the intensity value of a pixel falls into the threshold range, then it is considered as one type of object. For example, in a gray scale image with 8 bits integer data type, where 0 represents color white, and integer 255 represents color black. The integers in between representing different gray scale transmitting from white to black. The disadvantage of threshold segmentation is that the result may be sensitive to the chosen threshold values and to noises in the images. For concrete specimen, in which the intensity of pixels covers a wide range and air voids in the concrete continuum have the same intensity as cracks, this means that the crack volume

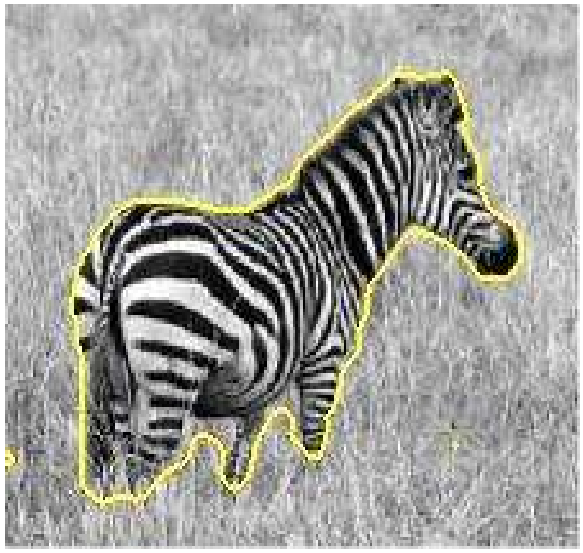

Figure 3.8: Segmentation of Zebra [20]

is highly sensitive to the threshold chosen as the cutoff between concrete and cracks, and calculation of crack volume must address the fact that some void pixels are air voids that existed in concrete continuum prior to testing. Figure 3.9 shows the cracked specimen and extracted cracking, voids and noises using threshold segmentation.

The application of other several segmentation methods (such as edge detection, clustering or active contour) to bond images are also not preferred as these segmentation methods are highly dependent on the texture of images. Concrete material is heterogeneous and bond specimen X-ray images are highly textured data with omnipresent discontinuities. Figure 3.10 shows recent development on concrete damage detection [35] applying active contour segmentation method. The image was taken by camera and has low texture of concrete comparing with X-ray bond images.

Given that multiple images of bond specimens were taken during testing, motion estimation algorithms provide a means of enhanced image processing beyond segmentation. This is especially meaningful when using image processing on mechanics of materials problems. By computing the motion field, the strain field can be derived from the motion displacement

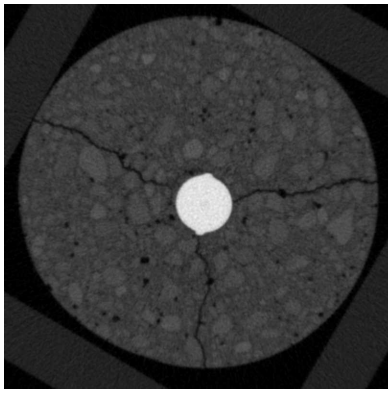

(a) concrete specimen image

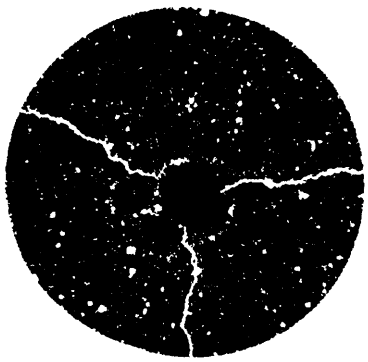

(b) segmented concrete specimen image

Figure 3.9: Segmentation of A Uniform Tension Specimen Section

(a) Test Setup with Cameras

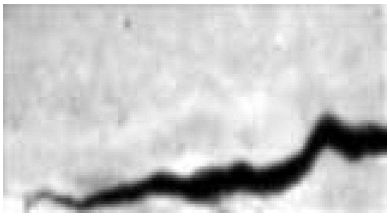

(b) Concrete Crack Region

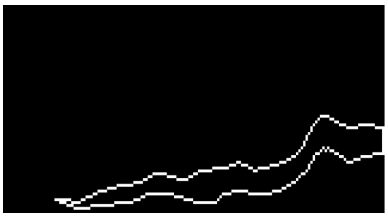

(c) Segmented Cracks

Figure 3.10: Segmentation of Concrete Cracks from Camera Image [35]

data. The strain field will be used to compare with FE analysis results and identify the bond mechanism. Ultimately, the goal is to use the motion field data to i) identify large, many-voxel cracks, ii) potentially identify fine, sub-voxel, cracks that may not be immediately identifiable from visual inspection, and iii) compute strain fields, radial displacement and bar slip. Large gradients in the motion field could be expected to signify discrete cracks or zones of crushing and smaller gradients could be expected to indicate the validity of a continuous strain field. Motion estimation includes estimation of concrete deformation and rigid motion during loading from image data.

The motion estimation can be categorized as feature based and optical flow. Feature based method is suitable to estimate rigid motion of specimen, such as image registration or alignment. Features in specimen such as aggregate corners are compared from temporally different images to estimate the spatial movement of the features points. Optical flow is an method to estimate dense motion field. Each pixel in two images is treated as a feature point, the estimated motion is at each pixel location. For the goal of cracking extraction, feature based method is more efficient. However, dense motion field from optical flow estimation has the benefit of estimating deformation and strain field of the specimen. In addition, the basic assumption in optical flow is that the change of pixel intensity is due to motion not lighting [20, 69, 99]. Optical flow is suitable to analyze bond images as the X-ray CT bond images are generated according to density of materials. The gray scale intensities of the images are material properties related, but not lighting conditions of cameras.

The basic formulation for optical flow is: Let $I_0 = I_0(X) = I_0(x, y, z)$ represents undeformed reference image function and $I_1 = I_1(X) = I_1(x, y, z)$ represents deformed image function, position vector X=(x,y,z), find displacement vector W=W(x,y,z)=(u,v,w) that ideally makes $I_1(X + W) = I_0(X)$. Assume small displacement from deformed image to reference image, i.e. W is small enough to use Taylor series on I_1:

$$I_1(X + W) = I_1(X) + \nabla I_1 \cdot W \tag{3.2}$$

where ∇I_1 is gradient of image I_1 at X. The goal is to find displacement vector W(x,y,z) to minimize the absolute difference $|I_1(X+W)-I_0(X)|$. In implementing the sum of absolute error, the sum of square of the errors are used to keep the function continuous, which change the goal to minimize

$$E = \int_{\Omega} (I_1(X+W) - I_0(X))^2 \tag{3.3}$$

Insert equation 3.2 into equation 3.3, and use:

$$I_t = I_1(X) - I_0(X) \tag{3.4}$$

The objective function E becomes:

$$E = \int_{\Omega} (I_t + \nabla I_1 \cdot W)^2 \tag{3.5}$$

Minimize E by taking the derivative of E with respect to W, get:

$$(I_t + \nabla I_1 \cdot W)\nabla I_1 = 0 \tag{3.6}$$

As can be seen from equation 3.6, when ∇I_1 has zero numbers, this equation is singular, which means no single solution of W(x,y,z).

To solve this ill-posed objective equation, the popular methods for optical flow computation includes statistical correlation formulation [169], robust motion estimation [14], local methods [99] and global optimization [69] based on variational formulation. The former three are based on local constant flow field within a preselected region. Assume within this region, the flow field is constant, this reduces the number of unknown displacement to one vector W for the local region. The objective functions becomes: find W to minimize:

$$E = \int_{\Re} (I_t + \nabla I_1 \cdot W)^2 \tag{3.7}$$

where $\Re$ is a small local region. Equation 3.7 is well-posed as the usage of sum of ∇I_1. It can be solved using least square method [14] or direct derivative with respect to W [99].

The variational calculus based global optimization of E was originally published by Horn and Schunck [69]. To solve the ill-posed objective equation 3.3, the assumption of small displacement is implemented into the objective equation as:

$$E = \int_{\Omega} [(I_1(X+W) - I_0(X))^2 + (|\nabla W|)^2] \tag{3.8}$$

The two terms in equation 3.8 mean the basic assumptions in optical flow: the constancy of image intensity and the small displacement flow field.

Besides the high accuracy of variational formulation, for applying optical flow method to mechanics of material, the differential methods from variational formulation are fundamentally similar to finite element formulation in solving engineering differential equations. Formulations of local method minimizes the difference between reference image and deformed image by assuming constant motion for the local region. Thus it provides a region-based discontinuous flow field. This is not consistent with the properties of bond specimen, which is a continuous deformation body with some isolated cracks. On the other hand, global optimization minimize the total difference between reference image and deformed image. The flow field is continuous displacement at image pixel level. Recent development on the variational optical flow algorithm has been advanced to reserve the discontinuous displacement (such as cracks in concrete) in the images and robust to image noise.

Image processing methods introduced is this section have a number of applications, such as medical field, transportation and auto industry, as well as vision entertainment areas. The advancements are also made on the investigation of civil engineering structures, concrete material and reinforced concrete structures, such as building damage detection under earthquake [143], structural displacement and deformation measurement [33], concrete surface cracking analysis [4, 34, 35], concrete particle shape modeling [63]. Camera images are mostly used for surface cracking or deformation measurement. X-ray CT images used for

this study include high-resolution data for the whole specimen in four dimensions.

3.6 Previous Work of Investigating Concrete and Concrete Damage Using X-ray Image

As early as 1963, Floyd [58] has published observation of concrete using three-dimensional X-ray images. Images were taken by X-ray tubes with energy rating of 150 Kv. The images were fine enough to identify the concrete aggregate arrangement, internal voids distribution. To test the accuracy of X-ray images, concrete cylinder was cut into thin pieces and painted with carmine drawing ink. After ink penetrated to voids and cracks and dried, the piece was observed by microscope. Although the test showed that X-ray images obtained had no enough resolution to show cracks in the paste as observed from microscope, Floyd stated the potential of using X-ray images on concrete due to the non-destructive nature of the method.

Landis [86] published research on investigating concrete internal cracking using X-ray image data obtained from a compression concrete cylinder. A series of image slices were obtained to construct the three-dimensional specimen data, the images were taken at different load stages from 35%, 75%,100% peak load and 65% post-peak load to observe and quantify the progressive cracking of concrete. Threshold method was used to extract cracks and voids from the specimen. Although the threshold was chosen subjectively, as the goal was to compare crack area and volume between load stages, using one threshold on all images wouldn't generate significant errors. Differentiation of cracks and voids are made by computing perimeter to area ratio for each detected blob, any objects with ratio greater than 2 are considered cracks. After cracks are extracted, crack surface area and volume are computed by adding up numbers from all slices. Results showed that crack area was largest at peak load. At the post load, there were more increases in crack volume than crack area.

Sprague [142] investigated cracking extracting from gray scale X-ray bond images using threshold segmentation method. As the cracking surface and volume were parameters used to calculate fracture energy of concrete. The threshold has significant influence on fracture

energy results. A series of threshold were selected to separate cracks, voids and background from other portion of image. As crack, voids and image background are all black due to the zero X-ray energy absorbing coefficient of air, higher threshold will lead to decrease of specimen volume but increase of internal cracking, vice verser. From the plot of cracking volume as a function of threshold, the threshold corresponding to maximum crack volume was identified as the final threshold in calculating fracture energy of concrete.

Zhang [169] applied statistics-based motion estimation algorithm on specimen images used by Landis [86]. Normalized cross-correlation of reference image and deformed image in a small region (Equation 3.9) was used as the similarity criteria to be maximized. The method is similar as the local method introduced in section 3.5. After computing the motion optical flow and ignoring the continuum displacement within specimen, the cracks are found by clustering the estimated motion according to minimum description length method [91]. The major parameters for the description length was rigid translation and rotation. Regions have similar rigid motion and translation belong to same cluster. By doing this, the motion segmentation ignored small displacement field. Pixels belong to same cluster are extracted as one object using marching cube algorithm [92], a method to extract three dimensional object from image pixels. Cracking surfaces were identified as interfaces of the extracted objects.

$$\rho(R_0, R_1) = \frac{cov(R_0, R_1)}{\sigma_{R_0}\sigma_{R_1}} = \frac{E[(R_0 - \overline{R_0}) \cdot (R_1 - \overline{R_1})]}{\sigma_{R_0}\sigma_{R_1}} \tag{3.9}$$

where R_0 and R_1 represent local small region of reference image and deformed image, $\overline{R_0}$ and $\overline{R_1}$ are mean, σ_{R_0} and σ_{R_1} are standard deviation of R_0 and R_1.

Sprague [142] investigated the motion estimation by finite element method. For uncracked specimens, small strain elastic finite element formulation provided good motion estimation. Each pixel is a finite element node. The objective function to be minimized was the sum square difference of two images analyzed plus the strain energy term (Equation 3.10).

$$E = \int_{\Omega} [(I_1(X + W) - I_0(X))^2 + W^T \cdot K \cdot W] \tag{3.10}$$

where K is the stiffness matrix and function of material properties. Equation 3.10 is essentially same with Horn and Schunck formulation in equation 3.8 if K is constant, which is elastic case. The problem of elastic registration is over smoothing of displacements thus cracks are not represented. To estimate the motion including cracking, the displacement field is enriched by a heave-side additional term to represent the displacement discontinuity across the crack (Equation 3.11) when cracking condition was satisfied. The cracking condition was decided by maximum principal strain in each element. The detection of cracking initiation and direction was achieved by checking the maximum principal strain from elastic analysis.

$$u(x) = \sum_{i \in I} \varphi_i(x) u_i + \sum_{j \in J} \varphi_j(x) H(x) a_j + \sum_{k \in K} \varphi_k(x) (\sum_{l=1}^{4} \phi_l(x) c_k^l) \tag{3.11}$$

where the first term is the elastic formulation of displacement function, the second term is the enrichment term for element with full cracking, the third term is the enrichment term for elements with partial cracking. H is Heaviside function, which is used to keep displacement on the same side of cracks used in displacement function. More detailed information for the enriched displacement equation 3.11 is presented in thesis [142]. The difficulties encountered in this discontinuous motion field formulation was the singularity at crack corners, separation of individual cracks and the identification of boundary from cracks.

3.7 Image Processing-Analysis of Bond Image Data

3.7.1 Investigation of Bond-zone Cracking Propagation by Image Segmentation

To facilitate preliminary review of bond-specimen image data and visualize crack propagation under increased loading, threshold segmentation was applied to automatically detect the edge of the concrete specimen and to isolate and extract cracks in the test specimens. After the crack volume is isolated from rest of the specimen, the internal cracking can be visualized in 3D. Using the threshold segmentation method, the primary cracks developed at increasing load levels for a flexural bond test specimen were extracted. The gray inten-

sity threshold chosen for segmentation was based on a histogram of gray scale value in the images. As the goal is to visualize cracks instead of calculating quantities, the threshold based on histogram is enough to give reasonable results.

To accomplish threshold segmentation, for a typical set of images for a typical specimen, the following tasks are performed using Matlab software.

1. Raw 2D images are cropped to isolate the region of interest (Figure 3.11(b)). This can significantly reduce computation time.

2. Thresholding of the cropped image is performed. The chosen threshold is based on gray intensity histogram of the image. The threshold values for voids is 44. Figure 3.11(c) shows the segmented image where concrete is white and all others are black.

3. Since the background, air voids in concrete, noise and crack volume are all color black, additional processing is required to find the border of the concrete cylinder. This is accomplished by filtering the segmented image to set the entire cylinder to white (cracking and noises are filtered into concrete), then the cylinder border is the boundary between white and black region (Figure 3.11(d)).

4. Setting the outside border region and concrete region to black but cracking and noise white, and erase noises with small areas.

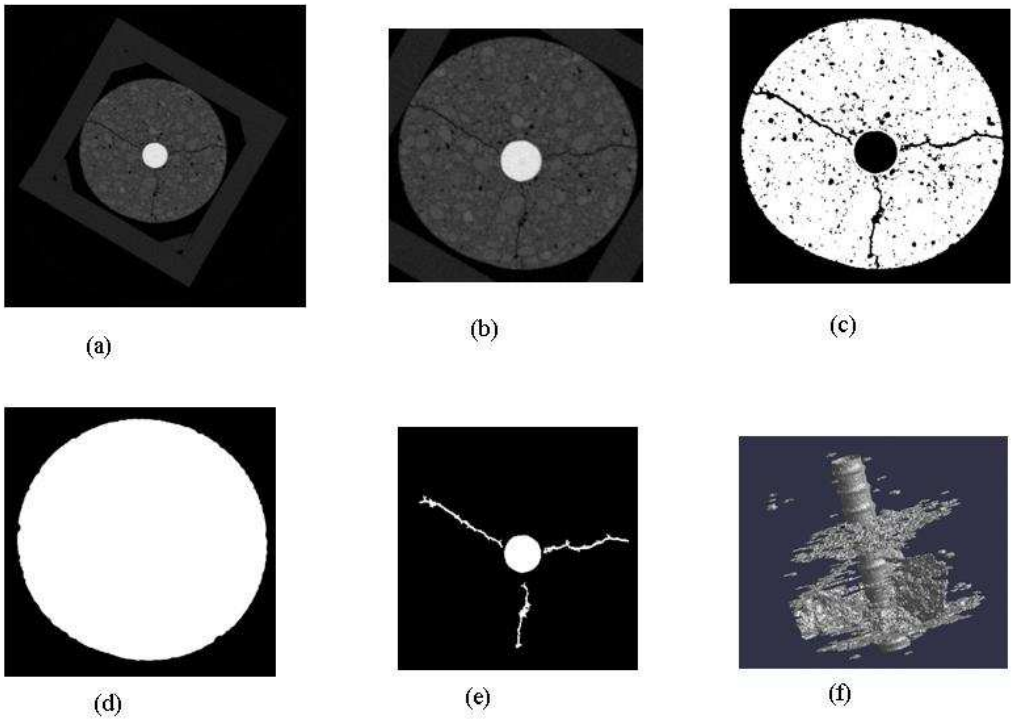

Figure 3.11: Segmentation Procedures

The above procedure was applied to image series 8 in Table 3.1 at increasing load level (0, 2400 lbs, 6000 lbs and 8400 lbs load). Figures 3.14, 3.16 and 3.18 show the extracted cracking of flexural bond test specimen under three load levels. From Figure 3.18 it can be seen the splitting behavior and secondary cracking near the major transverse cracking zone. In load level 2400, no local secondary cracking is extracted. This could be explained that the initial cracking is very fine, even with current resolution, it is very difficult to extract the initial fine cracking. Initiation of secondary cracking under load level 6000 is extracted in Figure 3.16. The segmentation process has isolated and exposed the full internal cracking which is not easy to visualize from the raw images.

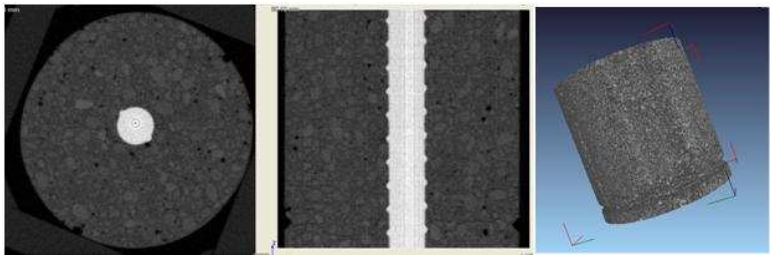

Figure 3.12: Specimen Images at Load Level 0

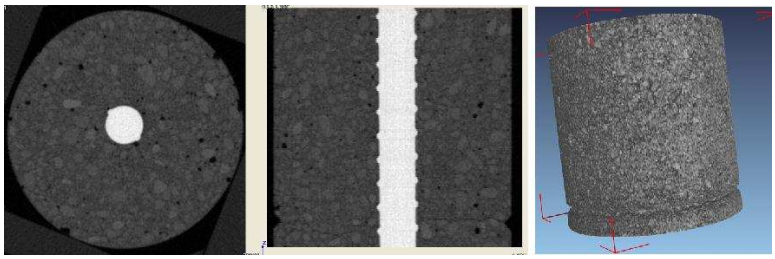

Figure 3.13: Specimen Images at Load Level 2400

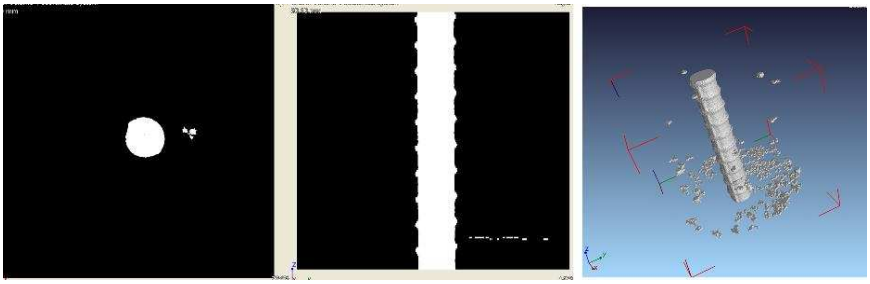

Figure 3.14: Internal Cracking at Load Level 2400 lbs

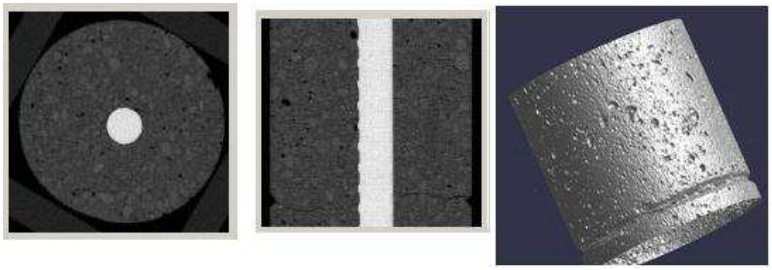

Figure 3.15: Specimen Images at Load Level 6000 lbs

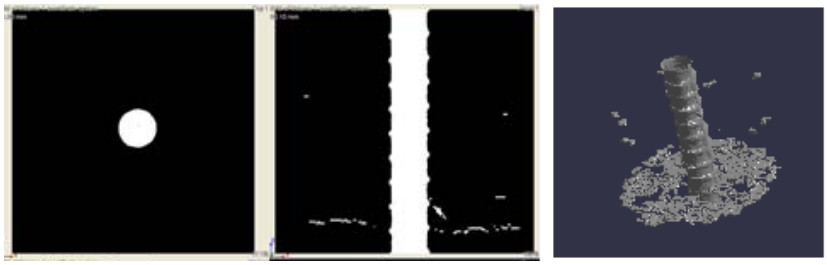

Figure 3.16: Internal Cracking at Load Level 6000 lbs

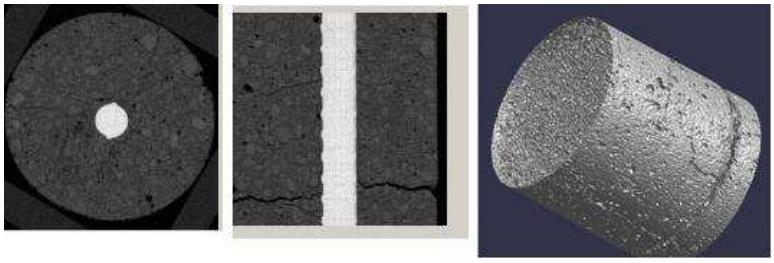

Figure 3.17: Specimen Images at Load Level 8400 lbs

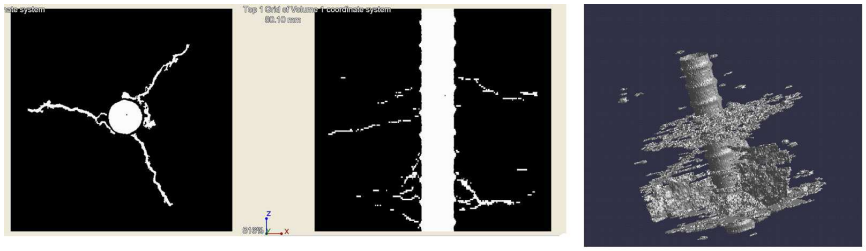

Figure 3.18: Internal Cracking at Load Level 8400 lbs

3.7.2 Motion Estimation Method for Bond Specimens

The challenge in estimating motion field using optical flow algorithm is reserving the discontinuous displacement field, as stated in section 3.5 and previous research by Sprague [142]. The original formulation of Horn and Schunck [69] algorithm or elastic registration presented by Sprague [142] have difficulties in representing cracks in bond specimen due to over-smoothing of the displacement field. Addressing this problem using discrete formula-

tion of displacement [142] was not successful due to the complexity in embedding cracks in displacement function. Noise sensitivity of the algorithm is also a concern as the noise level in bond specimen images.

Recent advancements in optical flow computation made significant contributions in overcoming these difficulties [21, 135, 160, 167]. Beyond accuracy, there are more challenges in considering applications of the algorithms on bond specimen images: efficiency and memory capacity due to the size of the 3D volumetric images. All these factors lead to the decision of choosing an algorithm that is the combination of state-of-the-art accuracy and complexity.

The optical flow algorithm developed and applied here is a modification of the algorithm proposed by Brox and Bruhn [21] for application on spatially three-dimensional images. This algorithm framework is used because of its excellent performance on Middlebury web-site [159], a well-known algorithm evaluation web-site developed by Microsoft Corporation.

The objective function in original Horn-Schunck formulation was sum of square, i.e. the function is in the form of $f(x) = x^2$. This significantly increases the sensitivity to noise and displacement discontinuity. If the objective function to be minimized is dominated by noise and the displacement gradient at cracks, the ultimate optimized results will not be the global minimum and the displacement discontinuity at cracks will be smoothed out. Brox and Bruhn used a new energy function that is also continuous and concave but reduced the sensitivity to noise outliers and large gradients. In addition, to reserve the displacement discontinuity, an additional gradient term was added to the objective function. The objective energy function includes three terms: the gray scale difference of the reference and deformed images, the gradient of the gray scale difference, and the gradient of the displacement field.

The basic assumption in optical flow is small displacement. Capture of large displacements is by the multi-resolution image pyramid method. The original image is resampled to coarser scale with smaller image size, but low pixel resolution. Since the displacement unit is pixel, in coarser scale, small displacement is actually large displacement in finer scale

images. The motion field at coarser scale is used as the initial displacement at the next finer scale. Use of this initial displacement from last resolution level also avoids the problem of trapping into local minimum due to random guess of initial solution.

Detailed introduction of the algorithm and inplementaion results are presented in Chapter 4.

Chapter 4

Motion Estimation of Bond Test Specimens Using X-ray CT Image Data

4.1 Introduction

This chapter is focused on implementing motion estimation optical flow algorithm identified and application to bond test specimen images. One pull-out specimen, P3W1A from Martin Series 5B, and one uniform tension flexural bond test specimen from Series 8 (Table 3.1) were analyzed.

Using the displacement field calculated, two deformations particular interest to this this study were computed: the slip of the reinforcing bar relative to the concrete and the radial expansion of the concrete around the bar. The bar slip is computed as the movement of the bar, in the direction of the bar axis, with respect to the concrete surface at a distance of 0.2 inch from the surface of the bar. Radial expansion is the radial motion of concrete away from the center of the specimen and is computed for three concrete cylinder surfaces that located at a radius of 0.2 inch, at approximately middle of the concrete cylinder surrounding the bar and at the surface of the specimen. Also using the 3D displacement field, the 3D strain field was calculated assuming small displacement.

The principal strains were calculated by solving for the eigen values of the strain tensor. Finally the equivalent total strain was calculated according to equation 5.4a.

Section 3.7 introduces in detail the motion estimation algorithm used for the bond test images.

Section 4.3 presents the test results of the motion estimation algorithm.

Section 4.4 introduces the parallel domain decomposition on the large set of volumetric image data.

Section 4.5 and 4.6 presents the results of application of the optical flow algorithm and

processing of the displacement field data for the flexural bond and pull-out specimens.

4.2 Theoretical Background

As discussed in section 3.7.2, the optical flow algorithm is defined by an objective function to be minimized. The objective function consists of two primary parts, a data part and a smoothing part, as in equation 4.1. The data part is a function of the gray-scale difference and the gradient of the gray-scale difference (Equation 4.2) between reference image and deformed image. The smoothing part is a function of the gradient of the displacement flow (Equation 4.3). The energy function is a truncated rising concave function as equation 4.4 and Figure 4.1. This function is continuous and on the order of L1 optimization, which will keep the unique solution for the minimization problem, and the penalty on larger numbers will keep the discontinuity (no unexpected over-smooth on cracks) in flow field.

$$E(W) = E_{Data} + \alpha E_{Smooth} \tag{4.1}$$

$$E_{Data}(W) = \int_{\Omega} \psi(|I_t|^2 + \gamma|\nabla I_t|^2)dX \tag{4.2}$$

$$E_{Smooth}(W) = \int_{\Omega} \psi(|\nabla W|^2)dX \tag{4.3}$$

$$\psi(x) = \sqrt{x^2 + \epsilon} \tag{4.4}$$

where,

$$I_t = I(X + W) - I_0(X) \tag{4.5}$$

$$\nabla I_t = \nabla I(X + W) - \nabla I_0(X) \tag{4.6}$$

$I_0(X) = I_0(x, y, z)$ is a reference image function at time t0, $I(X + W)$ is a deformed image function (deformed specimen) at time t, ∇ is the gradient operator corresponding to x,y, and z, W is displacement vector [u,v,w] for each image pixel, γ is a weight factor for image gradient term, α is a weight factor for displacement smooth term, and $\epsilon = 0.001$ is a

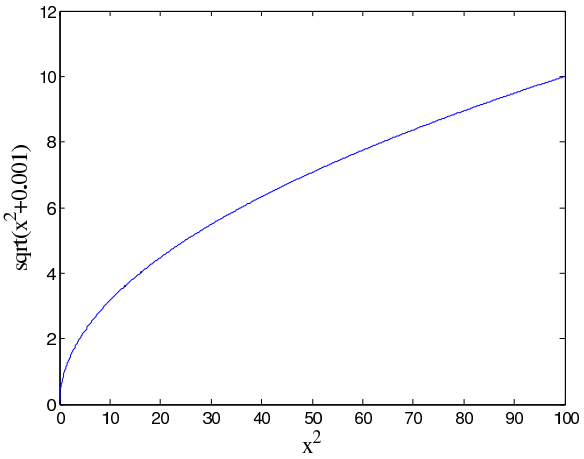

Figure 4.1: The Energy Function ψ(x)

small positive number to avoid singularity in derivative of the function.

$$|\nabla W|^2 = |\nabla u|^2 + |\nabla v|^2 + |\nabla w|^2 \tag{4.7}$$

The objective function is a spatially three-dimensional partial differential equation in the form of:

$$E(u(x,y,z), v(x,y,z), w(x,y,z)) = \int_\Omega f(x,y,z,u,v,w,u_x,u_y,u_z,v_x,v_y,v_z,w_x,w_y,w_z)dxdydz \tag{4.8}$$

Using variational calculus, minimization of this function leads to a series of Euler-Lagrange partial differential equations, i.e. $\frac{\partial E}{\partial u} = 0$, $\frac{\partial E}{\partial v} = 0$, $\frac{\partial E}{\partial w} = 0$, following strong form of equilibrium equations can be derived [51]:

$$\frac{\partial f}{\partial u} - \frac{\partial}{\partial x}(\frac{\partial f}{\partial u_x}) - \frac{\partial}{\partial y}(\frac{\partial f}{\partial u_y}) - \frac{\partial}{\partial z}(\frac{\partial f}{\partial u_z}) = 0 \tag{4.9a}$$

$$\frac{\partial f}{\partial v} - \frac{\partial}{\partial x}(\frac{\partial f}{\partial v_x}) - \frac{\partial}{\partial y}(\frac{\partial f}{\partial v_y}) - \frac{\partial}{\partial z}(\frac{\partial f}{\partial v_z}) = 0 \tag{4.9b}$$

$$\frac{\partial f}{\partial w} - \frac{\partial}{\partial x}(\frac{\partial f}{\partial w_x}) - \frac{\partial}{\partial y}(\frac{\partial f}{\partial w_y}) - \frac{\partial}{\partial z}(\frac{\partial f}{\partial w_z}) = 0 \tag{4.9c}$$

Insert the data term in equation 4.2 and smoothing term in equation 4.3 into the objective function of equation 4.1, f() in equation 4.8 is defined as:

$$f = \psi(|I_t|^2 + \gamma|\nabla I_t|^2) + \alpha\psi(|\nabla W|^2) \tag{4.10}$$

This function represents the gray scale difference between the volumetric reference image and deformed image, and the scale of the flow field. Insert f() in equation 4.10 into equations in 4.9a, and using following derivatives:

$$\frac{\partial I_t}{\partial u} = \frac{\partial I(X+W)}{\partial (X+W)} \cdot \frac{\partial (X+W)}{\partial u} = I_x \tag{4.11}$$

$$\frac{\partial \nabla I_t}{\partial u} = \nabla I_x \tag{4.12}$$

Use similar derivatives with respect to v and w, and define $\nabla I = \nabla I(X+W) = [I_x, I_y, I_z]$ and substituting Equation 4.10 into 4.9a results in following system of nonlinear partial differential equations satisfied at each image pixel.

$$\psi'(|I_t|^2 + \gamma|\nabla I_t|^2)(I_t I_x + \gamma \nabla I_t \cdot \nabla I_x) - \alpha div(\psi'(|\nabla u|^2 + |\nabla v|^2 + |\nabla w|^2)\nabla u) = 0 \text{ (4.13a)}$$

$$\psi'(|I_t|^2 + \gamma|\nabla I_t|^2)(I_t I_y + \gamma \nabla I_t \cdot \nabla I_y) - \alpha div(\psi'(|\nabla u|^2 + |\nabla v|^2 + |\nabla w|^2)\nabla v) = 0 \text{ (4.13b)}$$

$$\psi'(|I_t|^2 + \gamma|\nabla I_t|^2)(I_t I_z + \gamma \nabla I_t \cdot \nabla I_z) - \alpha div(\psi'(|\nabla u|^2 + |\nabla v|^2 + |\nabla w|^2)\nabla w) = 0 \text{ (4.13c)}$$

The partial differential equations 4.13 are nonlinear equations used to solve for three unknowns: u, v, and w. Solution of these equations is by introducing following assumptions: the temporal linearization of the nonlinear differential equations 4.13 is based on fixed point linearization same as that used by Brox [21] and numerical iterations. Specifically, applying

Taylor expansion on image function gets following approximations:

$$I_t{}^{k+1} = I(X + W^{k+1}) - I(X) \approx I_t{}^k + \nabla I^k \cdot dW^{k+1} \tag{4.14}$$

$$\nabla I_t{}^{k+1} \approx \nabla I^k + \nabla(\nabla I^k) \cdot dW^{k+1} \tag{4.15}$$

$$W^{k+1} = W^k + dW^{k+1} \tag{4.16}$$

In equations 4.13 $\psi' = \psi'^k$, $\nabla I = \nabla I^k$. Other terms such as ∇I_t and ∇W use linearized equation at k+1 as equations 4.14$\sim$ 4.16. The nonlinear partial differential equations are transformed to linear equations with unknown dW^{k+1}. Specifically, substitute equations 4.14$\sim$ 4.16 into equations 4.13, to get following linearized partial differential equations on each pixel for unknowns: $dW^{K+1} = (du^{k+1}, dv^{k+1}, dw^{k+1})$.

$$\psi'(|I_t{}^k|^2 + \gamma|\nabla I_t{}^k|^2)((I_t{}^k + \nabla I^k \cdot dW^{k+1})I_x{}^k + \gamma(\nabla I_t{}^k + \nabla\nabla I^k dW^{k+1})\nabla I_x{}^k)$$
$$-\alpha \cdot div(\psi'(|\nabla u^k|^2 + |\nabla v^k|^2 + |\nabla w^k|^2)\nabla(u^k + du^{k+1})) = 0 \tag{4.17a}$$

$$\psi'(|I_t{}^k|^2 + \gamma|\nabla I_t{}^k|^2)((I_t{}^k + \nabla I^k \cdot dW^{k+1})I_y{}^k + \gamma(\nabla I_t{}^k + \nabla\nabla I^k dW^{k+1})\nabla I_y{}^k)$$
$$-\alpha \cdot div(\psi'(|\nabla u^k|^2 + |\nabla v^k|^2 + |\nabla w^k|^2)\nabla(v^k + dv^{k+1})) = 0 \tag{4.17b}$$

$$\psi'(|I_t{}^k|^2 + \gamma|\nabla I_t{}^k|^2)((I_t{}^k + \nabla I^k \cdot dW^{k+1})I_z{}^k + \gamma(\nabla I_t{}^k + \nabla\nabla I^k dW^{k+1})\nabla I_z{}^k)$$
$$-\alpha \cdot div(\psi'(|\nabla u^k|^2 + |\nabla v^k|^2 + |\nabla w^k|^2)\nabla(w^k + dw^{k+1})) = 0 \tag{4.17c}$$

At each iteration, the k terms are known and the equations are linear with respect to unknowns du^{k+1}, dv^{k+1} and dw^{k+1}.

The image function I=I(x,y,z) is not continuous, applying equation 4.17 to solve for incremental displacement field dW^{k+1} requires derivative of image function I with respect to x, y and z coordinates. The spatial derivatives of I are implemented by finite difference discretization on the image grid. Discretization of the partial differential equations transform the analytical problem to a numerical problem of solving a large sparse matrix of linear equations: Ax=b. Where A and b are the coefficients for the system matrix and are

functions of reference image I_0, deformed template image I, and current displacement field W. Based on this framework, following procedures have been used for the implementation.

As discussed in section 3.7.2, multi-resolution scheme is necessary to speed up and give solution leading to global minimum of the objective function. To implement the multi-resolution scheme, first an image pyramid was constructed with a resampling factor of 0.5 (Figure 4.2). Considering the heterogeneous properties of concrete material, averaged local pixels were used as the resampled image pixel at each pyramid level. The multi-resolution scheme was based on this pyramid but with a larger resampling factor of 0.95 use interpolation between nearest two levels in the pyramid. Ideally an image pyramid with a resampling factor of 0.95 should be built directly from full resolution images. However, the full resolution images are 3D volumetric images which have intensive demand on computer memory to store the whole scale pyramid or have intensive demand on computing time. The solution was started from the highest level in image pyramid. The highest level image has fewer resampled pixels, and are able to represent major large deformation of the whole specimen, so as to avoid the problem of trapping into local minimum.

At each pyramid level, all the information for generating the data part (first part of the equations) are related with image intensity or image gradient, which are available. For smoothing part, the divergence of flow vector part at grid is discretized by central difference as follows (as shown in Figure 4.3):

$$\begin{aligned} div({\psi'}_{i,j,k}) = {\psi'}_{i+1/2,j,k} - {\psi'}_{i-1/2,j,k} \\ + {\psi'}_{i,j+1/2,k} - {\psi'}_{i,j-1/2,k} \\ + {\psi'}_{i,j,k+1/2} - {\psi'}_{i,j,k-1/2} \end{aligned} \tag{4.18}$$

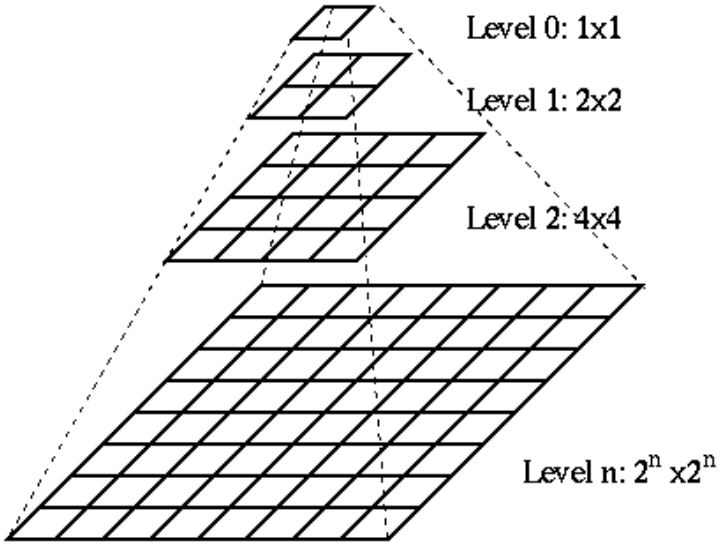

Figure 4.2: Diagram of Image Pyramid

and the gradient of u,v,w at half pixel location are expressed as:

$$\frac{\partial u}{\partial x_{(i,j+1/2,k)}} = \frac{1}{2}\sum_{j=j}^{j+1} u_{i+1,j,k} + u_{i-1,j,k} - 2u_{i,j,k} \tag{4.19a}$$

$$\frac{\partial u}{\partial z_{(i,j+1/2,k)}} = \frac{1}{2}\sum_{j=j}^{j+1} u_{i,j,k+1} + u_{i,j,k-1} - 2u_{i,j,k} \tag{4.19b}$$

$$\frac{\partial u}{\partial y_{(i,j+1/2,k)}} = u_{i,j+1,k} - u_{i,j,k} \tag{4.19c}$$

$$\frac{\partial u}{\partial y_{(i+1/2,j,k)}} = \frac{1}{2}\sum_{j=j}^{j+1} u_{i,j+1,k} + u_{i,j-1,k} - 2u_{i,j,k} \tag{4.19d}$$

$$\frac{\partial u}{\partial z_{(i+1/2,j,k)}} = \frac{1}{2}\sum_{j=j}^{j+1} u_{i,j,k+1} + u_{i,j,k-1} - 2u_{i,j,k} \tag{4.19e}$$

$$\frac{\partial u}{\partial x_{(i+1/2,j,k)}} = u_{i+1,j,k} - u_{i,j,k} \tag{4.19f}$$

$$\frac{\partial u}{\partial x_{(i,j,k+1/2)}} = \frac{1}{2}\sum_{j=j}^{j+1} u_{i+1,j,k} + u_{i-1,j,k} - 2u_{i,j,k} \tag{4.19g}$$

$$\frac{\partial u}{\partial y_{(i,j,k+1/2)}} = \frac{1}{2}\sum_{j=j}^{j+1} u_{i,j+1,k} + u_{i,j-1,k} - 2u_{i,j,k} \tag{4.19h}$$

$$\frac{\partial u}{\partial z_{(i,j,k+1/2)}} = u_{i,j,k+1} - u_{i,j,k} \tag{4.19i}$$

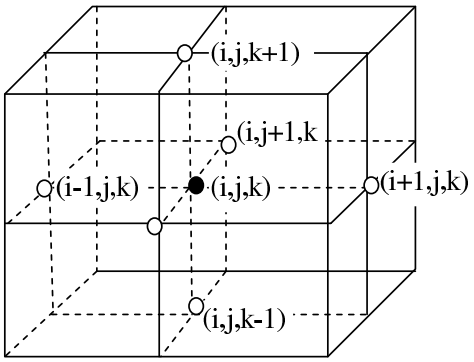

Figure 4.3: Diagram of Image Grid for Calculating Flow Gradient

The gradients of v and w are computed in a similar manner.

The pseudo code of the iteration process is:

1. Construct image pyramid with down sampling factor of 0.5;

2. Outer iteration 1 from coarse resolution level to fine level with down sampling factor of 0.95, the image at this level is from resampling of the image pyramid built in step 1;

3. Start outer iteration 2

   (a) Construct trial version of image from current displacement W, and compute $I_t, \nabla I_t, \nabla I, \nabla\nabla I$, update data term according to equations 4.14∼4.16;

   (b) start outer iteration 3

      i. Update smooth term from updated flow field according to equations 4.18, prepare linear system of equations A and b according to equation 4.17.

      ii. Solving the linear system of equations by SOR iteration method to compute flow increment under current image level to get dW^{k+1};

      iii. Check convergence on dW;

   (c) End outer iteration 3 with converged dW^{k+1}

(d) $W^{K+1} = W^k + dW^{k+1}$ and Check convergence on W;

4. End outer iteration 2 with converged W for current resolution

5. Project total flow to next resolution level;

6. End outer iteration 1

The boundary condition can be either W=0 or $\nabla W = 0$, test results didn't show great difference as the image boundaries are large areas of black background which mean W and $\nabla W = 0$ essentially same.

4.3 Test of the Algorithm

Prior to applying the algorithm to the bond test specimens, three simple data sets were generated to test the algorithm. Each data set comprised a pair of 3D images. Each image was defined by a 100x100x100 grid of 10^6 pixels. In each data set, one image represented the initial condition and the second image represented a deformed condition. These three data sets were used to test the rigid body motion, deformation and cracking conditions.

The first test specimen is a black box with a white plane inside the box. The white planes in the reference image specimen and deformed template image specimen have different positions. The distance for the two white plane in the z direction is $w = 6\overleftarrow{k}$, where $\overleftarrow{k}$ is the unit vector in the z direction. This pair of images is intended to test the ability of the algorithm to handle rigid body motion. Figure 4.4 shows the results. The upper row shows the estimated displacement field, the maximum displacement of w is 6.28, and u an v direction have displacement less than 0.8. The bottom row shows the original image and deformed image and the difference between the original image and reconstructed image from the displacement field. The color plot of the flow field follows the color encoding from Middlebury Website [159], as shown in the figures.

The second test specimen is a black box with a white ball inside the box. The ball in the deformed image has radius that is 3 pixels larger than in the reference image. This pair of images is intended to test the accuracy of the algorithm for handling elastic body deformation. Figure 4.5 shows the results images. The upper row of images show the estimated displacement field, the maximum displacement for u,v,w are all 3.33. The bottom row shows the original image and deformed image and the difference between the original image and reconstructed image.

In the third pair of images, the reference image data is a solid black cube. The deformed image is generated by setting a rotated white plane in the middle of the black cube (Figure 4.4). The white plane has thickness of 7, length and width of 50 pixels . The first row of images shows the 3D view of the motion field. The second row of images shows the cross-section view of the motion flow field. The third row of images shows comparison of the reconstructed image from the flow field and the deformed image. The displacement magnitude of (u,w) in the cracked plane is around 4.

Besides the visual observation of the flow field and the difference images between the original image and reconstructed image, quantitative evaluation of the test results include comparing of the major flow magnitude with the known displacement, and the percentage of pixels with image gray scale error exceeds a threshold. This is an approximate procedure as no ground truth displacement available. As the generated data set has only white and black intensities, the discrete displacement predefined can only be used as a reference for calculated results, but not ground truth. For the rigid motion test, the error in displacement estimation is $0.28/6 \approx 5\%$, and 99.8% of pixels have error less than 10%. For the ball deformation test, the error in displacement estimation is $0.3/3 \approx 10\%$ with 99.5% For the cracking test, 99.2% pixels have error less than 10%. The use of 10% error is due to the displacement field calculated has around 10% error. When the true displacement flow field is unknown, the percentage of pixels with an error threshold will provide information beyond visual observation of the correctness of the computing results.

From the comparisons of reference image and reconstructed image (Figures 4.4(e), 4.5(e) and 4.6(g)), the accuracy for calculated displacement needs to be improved at regions with cracking or texture changes. This is due to the over-smoothing of the displacement gradient and image intensity gradient in the original formulation of this algorithm as shown in Equation 4.2.

The above three simple data sets do not have same textures as bond specimen images. To further test the performance of the algorithm on gray scale bond specimen images. Another two tests from a small portion of the bond images were conducted. The first test is to test numerical accuracy of the algorithm on pixels levels. A cube with size of 20×20×20 pixels was taken from one set of bond specimen images. The cube was enriched with black background so as to generate reference image and deformed image with displacement v of 1 pixel, 5 pixels and 9 pixels separately (Figure 4.7). The calculated displacement field for this three pre-defined displacement were also shown in the same figure. For v=1, the calculated displacement v=1.08. For v=5, the calculated displacement v=5.20. For v=9, the calculated displacement v=9.36. These calculated displacement are maximum displacement within the gray scale cubes. To further evaluate the overall accuracy for each case, the relative error between reconstructed image and reference image were calculated. All three cases have 98% of pixels with relative intensity error of less than 5%. This algorithm can handle well a variety of displacement and deformation scales.

Another test is used to test the ability of the algorithm to capture cracking in textured gray scale bond specimen images. A small portion (50×50×20) of untracked reference image and cracked image were used for the test. For this test, three different outer iteration step (multi-resolution resampling factor of 0.9, 0.99 and 0.99) were used to test the performance of the algorithm on different iteration time step. The multi-resolution resampling factor represents the ratio of image size (or image resolution) between two adjacent time step. For example, on the last iteration, the image size is full resolution 50×50×20, on the second last iteration, the image size will be resampled to (50×50 × 20)×(0.9 or 0.99 or 0.999), and so

on, until to the first integration, which will have image size of only several pixels. Figure 4.8 shows the sensitivity of the results to the time step (or iteration numbers). The smaller the time step, or the larger the integrations, the better the algorithm on capturing the cracks. For iteration of 2000, which is corresponding to multi-resolution factor of 0.999, the crack width captured are 6.09 on a cross-section plane and 5.11 on a vertical section plane. The crack width is an approximate number calculated by taking the difference between maximum and minimum displacement in u direction. With iteration of 100 corresponding to multi-resolution factor of 0.9, the calculated crack width is 5.24 on the same cross-section plane and 4.89 on the same vertical section plane. By comparing the reconstructed image with the reference image, none of the three cases have calculated the cracking 100% accurate, as in reconstructed image the cracks can still be seen. Ideally the reconstructed image should be exactly same with the reference image. To evaluate the overall behavior, the gray intensity error between reference image and reconstructed image were also calculated. For iterations of 2000, 92.1% of pixels have error less than 10%. For iterations of 700 (multi-resolution factor of 0.99), 92.0% of pixels have error less than 10%. For iterations of 100, 91.8.0% of pixels have error less than 10%. These numbers show that the overall performance are similar for different time steps. However, small time step has enhanced the results on cracked region.

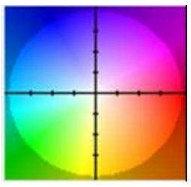

(a) Flow Color

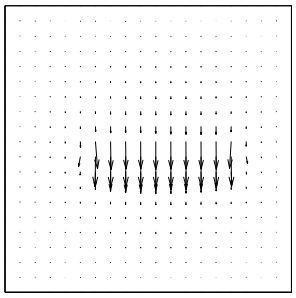

(b) (u,w) Vector

(c) (u,w) color hue

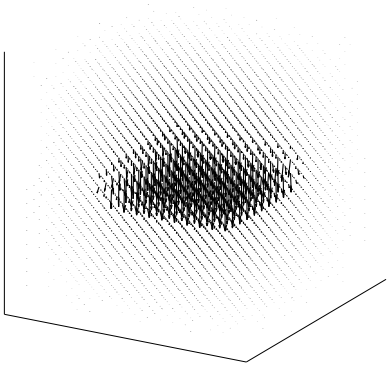

(d) (u,v,w) vector

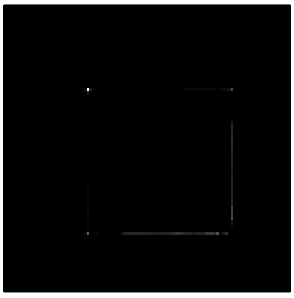

(e) Difference between Original Image and Recovered Image from (u,v,w)

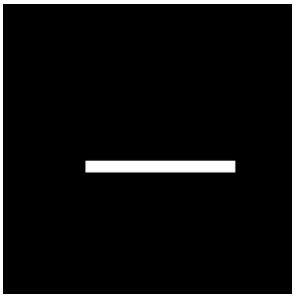

(f) Section View of Origianl Image

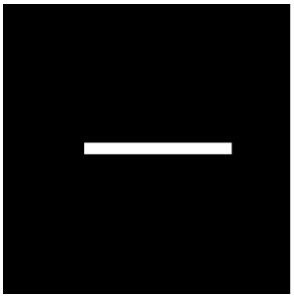

(g) Section View of Image after Rigid Motion

Figure 4.4: Displacement Field of Rigid Motion Test: the Yellow Color Indicates Downward Flow Direction

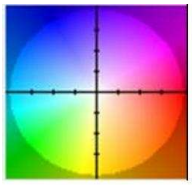

(a) Flow Color

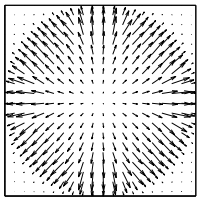

(b) (u,w) Vector

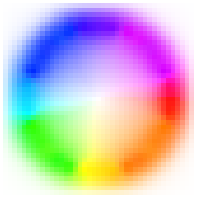

(c) (u,w) color hue

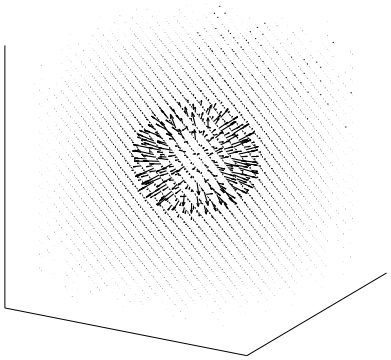

(d) (u,v,w) vector

(e) Difference between Original Image and Recovered Image from (u,v,w)

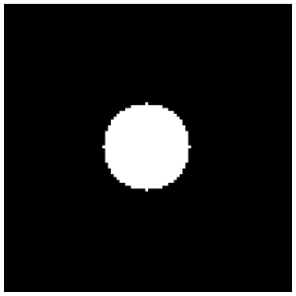

(f) Section View of the Original Ball

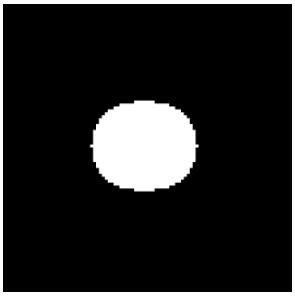

(g) Section View of the Deformed Ball

Figure 4.5: Displacement Field of Deformation Test

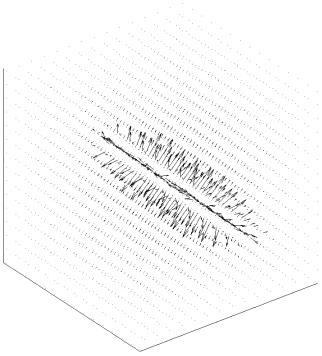

(a) Three Displacement Vector

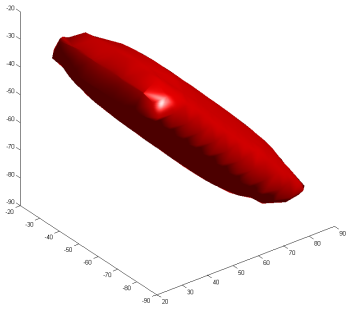

(b) Displacement Surface

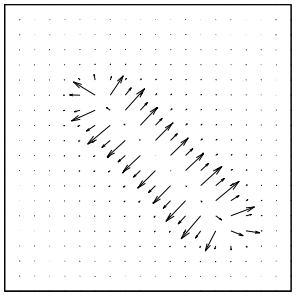

(c) (u,w) Vector

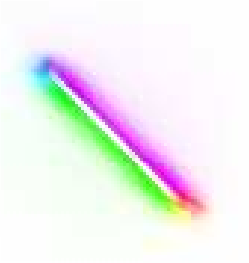

(d) (u,w) color hue

(e) Flow Color

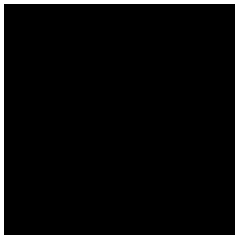

(f) Origianl Image

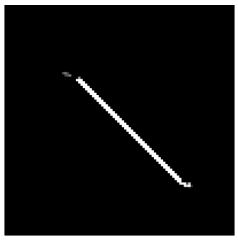

(g) Difference between Original Image and Recovered Image from (u,v,w)

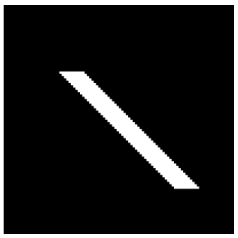

(h) Cracked Image

Figure 4.6: Displacement Field of Cracking Test

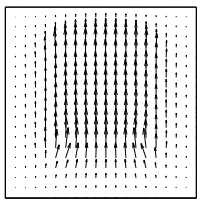

(a) Displacement Vector (v=1.08)

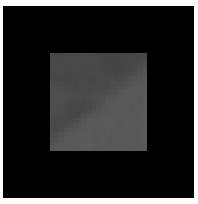

(b) Section View of Reference Image

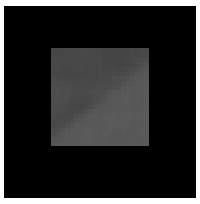

(c) Section View of Displaced Image (v=1)

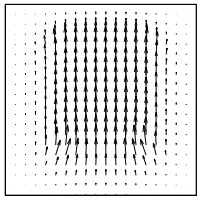

(d) Displacement Vector (v=5.20)

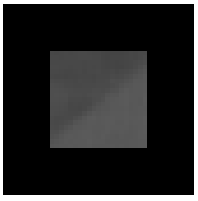

(e) Section View of Reference Image

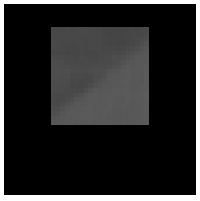

(f) Section View of Displaced Image (v=5)

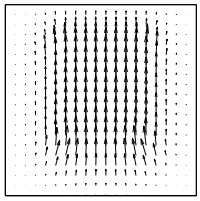

(g) Displacement Vector (v=9.36)

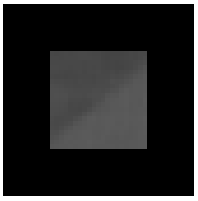

(h) Section View of Reference Image

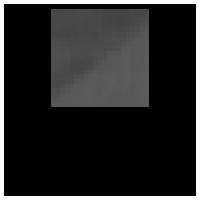

(i) Section View of Displaced Image (v=9)

Figure 4.7: Small Specimen Test for Displacement Scale

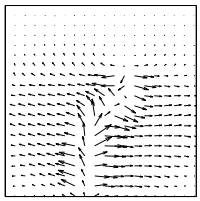

(a) Displacement Vector Cross Section

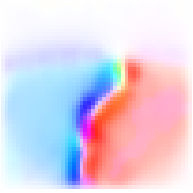

(b) Displacement Color Cross Section

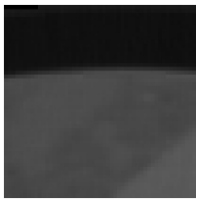

(c) Reference Image Cross Section

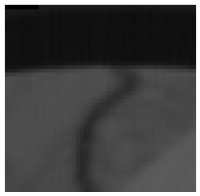

(d) Deformed Image Cross Section

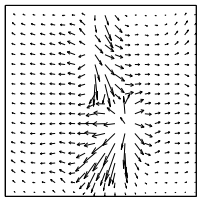

(e) Displacement Vector Vertical Section

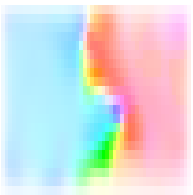

(f) Displacement Color Vertical Section

(g) Reference Image Vertical Section

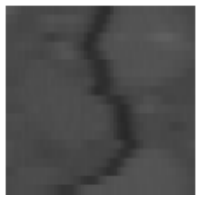

(h) Deformed Image Vertical Section

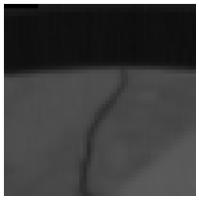

(i) Reconstructed Image Cross Section (Iterations=100, crack width=5.24)

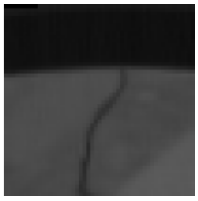

(j) Reconstructed Image Cross Section (Iterations=700, crack width=5.96)

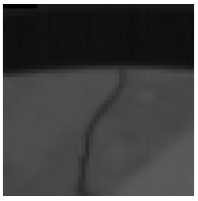

(k) Reconstructed Image Cross Section (Iterations=2000, crack width=6.09)

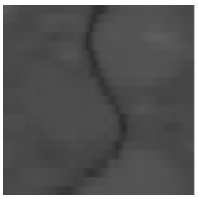

(l) Reconstructed Image Vertical Section (Iterations=100, crack width=4.89)

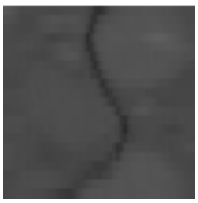

(m) Reconstructed Image Vertical Section (Iterations=700,, crack width=4.97)

(n) Reconstructed Image Vertical Section (Iterations=2000, crack width=5.11)

Figure 4.8: Small Specimen Test for Cracking

4.4 Development of Parallel Domain Decomposition Method in Implementing the Algorithm

Application of the proposed optical flow algorithm to analyze bond test specimens requires significant CPU time and memories. The high-resolution three-dimensional bond test images are computationally demanding on speed and especially memory resources due to the large data size. Each set of pull-out specimen image has size of $512 \times 512 \times 104$ pixels and each set of flexural bond test specimen image has size of $800 \times 800 \times 150$ pixels. In the case of flexural bond specimen, each iteration of the solution algorithm requires solution of the linear system Ax=b. The system matrix A has a sparse bandwidth of 9, with each node has 3 degree of freedom and 6 neighboring nodes (Equation 4.17). The sparse matrix A will contain $800 \times 800 \times 150 \times 9 \times 3 \times 8 = 20.7 \times 10^9$ bytes of data if using single domain computation. Additional properties of the problem also make desirable the implementation of the algorithm for solution in a parallel domain. First, a fundamental assumption in optical flow algorithm is that displacement field describing motion from one image to the next is a small displacement field. This means that one pixel in original image corresponds to a pixel in the deformed image within a local region. Regional implementation of the algorithm will not change the displacement greatly, as shown in Figure 4.9(a), which is from separate implementation of the algorithm. Stitching of the four region suggests a very similar flow field with results from single domain computation except in the boundary region. Figure 4.9(a) is the displacement field from four independent implementations of the algorithm on full volumetric image data. Each sub-image is one quarter in width and height of original image, but with full depth (Original image size: $800 \times 800 \times 150$, sub-image size $400 \times 400 \times 150$). Figure 4.9(b) is the displacement field of original image data on a coarse pyramid level (image size: approx: $270 \times 270 \times 50$). The two figures show very close displacement field. Second, system of linear equations is highly narrow banded with a pixel is only related with pixels on the six neighborhood pixels. It is more computationally efficient if using parallel algorithm as it is not reasonable to read a large amount of data into memory block and only do the computation using small amount of data [64].

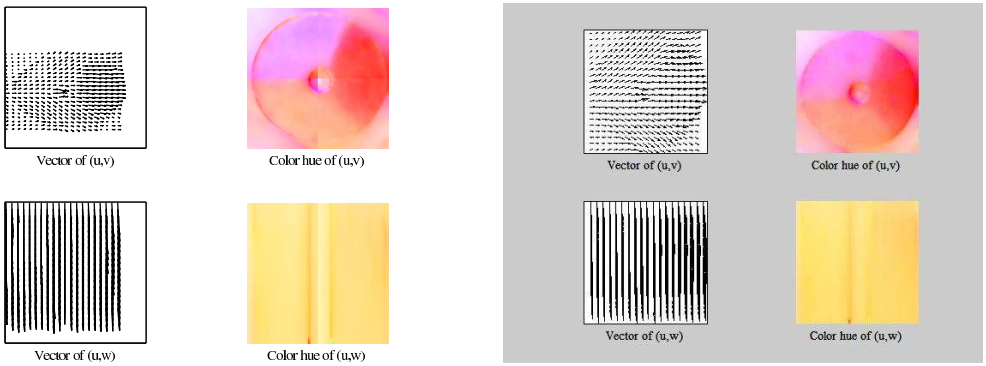

(a) Four Independent Implementations on Quarter Full Resolution Specimens

(b) One Implementation on Resmapled Low Resolution Full Specimen

Figure 4.9: Implementation of the Optical Flow Algorithm on Small Resampled Specimens

There are three possible ways to implement the solution algorithm with parallel domain decomposition:

1. Build the whole system of equations matrix, and solve the large system of equations using a parallel algorithm. This is extremely slow as the storage and access of the large sparse matrix A.

2. Implement the algorithm on sub-images during each iteration, and need communication of displacement field on boundary of sub-images. The system matrix needs to be adjusted according to the current displacements on the boundaries of the sub-image with each iteration step of updating the global displacement field. The frequent communications between domains lead to slow convergence.

3. Implement the algorithm independently on sub-images until convergence for each sub-images (faster), then implement the algorithm on interface nodes with the displacements sub-domain images as boundary conditions.

For this study, the procedure 3 was implemented as the problems associated with first two procedures. Equation 4.20 is the system of equations for sub-domain i, where

A^i_{II}, dW^i_I and b^i_I are from part of system equation Ax=b related with inner sub-domain i;

A^i_{TT}, dW^i_T and b^i_T are from part of system equation Ax=b related with boundary for sub-domain i;

A^i_{TI} and A^i_{IT} are interactions between inner domain I and the boundary T.

A_{TT} and b_T are from part of system equation Ax=b related with all inter-domain boundaries.

For each sub-domain i of the problem, given current displacement W_T at domain boundary, the displacement increment dW_I is from equations 4.20 and 4.21. After the displacement field is updated from all inner domains, the displacement increments dW_T for interface between all domains is then updated from equation 4.22.

$$\begin{pmatrix} A^i_{II} & A^i_{IT} \\ A^i_{TI} & A^i_{TT} \end{pmatrix} \begin{pmatrix} dW^i_I \\ dW^i_T \end{pmatrix} = \begin{pmatrix} b^i_I \\ b^i_T \end{pmatrix} \tag{4.20}$$

$$A^i_{II} dW^i_I = b^i_I - A^i_{IT} dW^i_T \tag{4.21}$$

$$A_{TT} dW_T = b_T - \sum_i A^i_{TI} dW^i_I \tag{4.22}$$

All solutions of sub-domains can be computed in parallel mode as no interaction between them. After that, the solution for interface between inner domains was calculated using single processor.

4.5 3D Motion Estimation of Uniform Tension Test Specimen

The optical flow algorithm introduced in Section 3.7.2 was applied to the flexural bond specimen (Figure 4.10) using sequential pairs of images (Under load level 0, 2400 lbs 6000 lbs and 8400 lbs) to 1): evaluate the utility of high-energy imaging and image processing for

investigation of the behavior of reinforced concrete components and 2): investigate bond-zone behavior.

Each 3D image used was 800×800×150 pixels. Each pixel represented a volume of 0.2×0.2×1 mm. Visual observation shows the crack initiator position under 0 load (Figure 4.10(a)), development of transverse cracking under 2400 lbs load (Figure 4.10(b)), initiation of secondary cracking near major transfers cracking under 6000 lbs load (Figure 4.10(c)), and the major transverse cracking and secondary cracking inclined to bar under 8400 lbs load (Figure 4.10(d)). The transverse and secondary cracking under load level 2400 and 6000 are very subtle.

For this specimen, the parameter α=30, and g=30 were used. α is the weight factor of flow field gradient and g is the weight factor of image intensity gradient in the objective function 4.2. This parameters were chosen by experiments in obtaining the best results. The sub-domain size used for the motion calculation was 200×200×150 pixels. As the limitation of memory resources, the four domains were calculated sequentially instead of in parallel. The peak memory requirement was around 15 G-bytes. It took about 72 hours for convergence ratio of 0.1. The implementation was coded in MATLAB and on Intel(R)Xeon(R) 2 processors 3.4 GHZ CPU with Windows 64-bit operating system. The implementation on MATLAB platform has limited the optimization of the codes on computing speed and memory allocation. In addition to the computing speed, the implementation has to deal with convergence problem. Future work is worthwhile on improving convergence with a more rigorous criteria.

4.5.1 Displacement Field

The calculated displacement field from load 0 to 2400 lbs is shown in Figure 4.11. Figure 4.11(a) and Figure 4.11(d) are vector and color plots of the displacement (u,v) for a cross-section of the specimen. Figure 4.11(b) and Figure 4.11(e) are vector and color plots of the displacement (u,w) for a vertical section of the specimen. Figure 4.11(c) is a vector

plot of full 3D displacement. Figure 4.11(f) is color plot of displacement (u,v) in full 3D view of the specimen. The displacement field shows rigid motion of the specimen images from load 0 to load 2400. The maximum displacement in cross-section plane is 2.3 pixels, and in longitudinal z direction is 1.8 pixels. By comparing the referece image at 0 load and reconstructed image from calculated displacement and deformed image at 2400 lbs load, 75% of image areas has pixel intensity error of less than 10%.

To test the motion displacement field, using the specimen images at load level 2400 and the displacement field can reconstruct the specimen images at load level 0, i.e. $I_{0-reconstructed}$(X) $= I_{2400}(X + W)$. Figure 4.11(g) shows a cross section view of the specimen at load 0. Figure 4.11(h) shows the reconstructed image at load 0. Figure 4.11(i) shows the specimen at load 2400. Figure 4.11(j) shows the difference between the original reference image and reconstructed image at load 0, the differences present the errors in estimating the displacement field.

Similarly, Figure 4.11(k)∼Figure 4.11(n) show the vertical view of original specimen and reconstructed specimen and the motions estimation errors. From load 0 to load 2400 lbs, the major displacement is rigid motion. The reason for the rigid motion could be the movement of specimen during test or from the imaging process. The major errors happen within bar region, which is obvious from visual observation that the bar is not all white. The error are due to the small circular noises in the bar.

The calculated displacement field from load 2400 lbs to 6000 lbs is shown in Figure 4.12. Figure 4.12(a) and Figure 4.12(d) are vector and color plots of the displacement (u,v) for a cross-section of the specimen. Figure 4.12(b) and Figure 4.12(e) are vector and color plots of the displacement (u,w) for a vertical section of the specimen. Figure 4.12(c) is a vector plot of full 3D displacement. Figure 4.12(f) is a color plot of displacement (u,v) in full 3D view of the specimen. The displacement field shows rigid motion of the specimen images from load 2400 to load 6000. The maximum displacement in cross-section plane is 3.6 pixels, and in longitudinal z direction is 32.4 pixels. By comparing the referece image at

0 load and reconstructed image from calculated displacement and deformed image at 2400 lbs load, 84% of image areas has pixel intensity error of less than 10%.

To test the motion displacement field, using the specimen images at load level 6000 and the displacement field can reconstruct the specimen images at load level 2400, i.e. $I_{2400-reconstructed}(X) = I_{6000}(X + W)$. Figure 4.12(g) shows a cross section view of the specimen at load 2400. Figure 4.12(h) shows the reconstructed image at load 2400. Figure 4.12(i) shows the specimen at load 6000. Figure 4.12(j) shows the difference between the original reference image and reconstructed image at load 2400, the differences present the errors in estimating the displacement field.

Similarly, Figure 4.12(k)∼Figure 4.12(n) show the vertical view of original specimen and reconstructed specimen and the motions estimation errors. From load 2400 to 6000 lbs, the major displacement shown is rigid motion. Besides the error image shown in Figure 4.12(j), visual checking of the aggregate pattern between reference images and reconstructed images show the accuracy of the results.

The calculated displacement field from load 6000 lbs to 8400 lbs is shown in Figure 4.13. Figure 4.13(a) and Figure 4.13(d) are vector and color plots of the displacement (u,v) for a cross-section of the specimen. Figure 4.13(b) and Figure 4.13(e) are vector and color plots of the displacement (u,w) for a vertical section of the specimen. Figure 4.13(c) is a vector plot of full 3D displacement. Figure 4.13(f) is a color plot of displacement (u,v) in full 3D view of the specimen. The calculated displacement field has captured not only rigid motion but also the cracking (splitting). The maximum displacement in cross-section plane is 2.3 pixels, and in longitudinal z direction is 15.6 pixels. By comparing the reference image at 0 load and reconstructed image from calculated displacement and deformed image at 2400 lbs load, 80% of image areas has pixel intensity error of less than 10%.

To test the motion displacement field, using the specimen images at load level 8400 and the displacement field can reconstruct the specimen images at load level 6000, i.e. $I_{6000-reconstructed}(X) = I_{8400}(X + W)$. Figure 4.13(g) shows a cross section view of the

specimen at load 6000. Figure 4.13(h) shows the reconstructed image at load 6000. Figure 4.13(i) shows the specimen at load 8400. Figure 4.13(j) shows the difference between the original reference image and reconstructed image at load 6000, the differences present the errors in estimating the displacement field.

Similarly, Figure 4.13(k)∼Figure 4.13(n) show the vertical view of original specimen and reconstructed specimen and the motions estimation errors. From load 6000 to 8400 lbs, the major displacement shown is splitting and bar slip. Comparing of reference images and reconstructed images shows the consistent aggregate patterns, but the cracking can not be fully recovered to no cracking state, as seen in Figure 4.13(h) and Figure 4.13(j). This is because the limitation of the algorithm, as seen in the test results in section 4.3.

4.5.2 Bar Slip and Radial Expansion

Using the displacement field presented in section 4.5.1, the slip of the reinforcing bar relative to the concrete and the radial expansion of the concrete around the bar were estimated. The bar slip is computed as the movement of the bar, in the direction of the bar axis, with respect to the concrete surface at a distance of 0.2 inch from the surface of the bar. Radial expansion is the radial motion of concrete away from the center of the specimen and is computed for three concrete cylinder surfaces that located at a radius of 0.2 inch, at approximately middle of the concrete cylinder surrounding the bar and at the surface of the specimen. Figure 4.14, 4.15 and 4.16 show bar slip captured at load incremental from 0 to 2400 lbs, 2400 to 6000 lbs and 6000 to 8400 lbs. Figure 4.14, 4.15 and 4.16 show radial expansion/contraction calculated at same incremental.

Figure 4.14 shows the bar slip at initial load stage represented by load incremental 1 (0 to 2400 lbs). The slippage is larger at locations that are close to main cracks, with slip of 0.14 mm. The slippage in the middle of the plot is approximately 0.07 mm, this part is between the two major cracks. The slippage at right end of plot has unexpected higher numbers. This is mainly due to the image is partial specimen instead of full specimen length. Not

like the cross-section direction, which has surrounding black background as the boundary, in longitudinal direction, the partial specimen images lack enough boundary conditions for regions near one end of the 3D image. This is a special condition as the bar has regular patterns, which will make the one end z direction displacement w goes to opposite direction to match the pattern of ribs. However this didn't happen for concrete as the aggregate patterns are different everywhere. Another reason for this unexpected large slippage is the noise level of the displacement is very high at the particular bond zone. With the small scale of numbers, the results are only for a rough reference.

Figure 4.15 shows the bar slip between load 2400 lbs and 6000 lbs. The slippage at locations close to main cracks have slips of 1.05 mm. The slippage between the major cracking is approximately 0.4 mm. Same as previous load level, the right end has higher slip which can be explained same as above.

Figure 4.16 shows the bar slip from load 6000 lbs to 8400 lbs. The slippage near left major crack is 1.6 mm; The slippage in the middle of the plot is approximately 1 mm and the right end has unexpected slippage.

Figure 4.17 shows the radial displacement of the concrete at load incremental from 0 to 2400 lbs. Bond-zone layer has radial expansion around 0.01 mm. The middle layer has smaller radial expansion, about 0.005 mm. The outer layer has radial contraction, with magnitude of -0.005 mm. For bond-zone and outer-layer, more expansion happens at right end of the specimen. For middle layers, the magnitude of expansion at left end is larger than that from right end. As the subtle deformation at this initial load stage, the results fluctuation can be explained as the local noise in the results.

Figure 4.18 shows the radial displacement of the specimen from load 2400 lbs to 6000 lbs. Bond-zone layer has slight radial contraction around 0.01 mm. The middle layer has radial expansion around 0.01 mm. The outer layer has radial expansion around about 0.02 mm. For bond layer, the contraction can be explained as local cracking and longitudinal strain of steel. For middle and outer layers, the magnitude of expansions at the left end is

larger than that at right end. This is due to the development of a major transverse cracking at left end.

Figure 4.19 shows the radial displacement from load 6000 lbs to 8400 lbs. Bond-zone layer has radial contraction around 0.1 mm. The middle layer has radial expansion from 0.05 to 0.1 mm. The outer layer has radial expansion from 0.07 to 0.15 mm. The bond layer has been further contracted from last load level and the outer layers have been further expanded from last level. The peaks in radial expansion are in the location of major transverse crack, which means local splitting happens.

The data for the bond-zone slip and radial deformation are fluctuate and can only be treated as rough references. This conclusion was also consistent with test results of the optical flow algorithm. In region with high gradient, the results are not accurate.

4.5.3 Maximum Principal Strain and Equivalent Total Strain

From the displacement field, it is possible to compute the strain field which offers further potential for investigation and improved understanding of the bond-zone response. For each computed displacement field (u,v,w), the strain is calculated by first order derivative of the the displacement field (small strain) as follows:

$$\varepsilon = \begin{pmatrix} \frac{\partial u}{\partial x} & 0.5(\frac{\partial u}{\partial y} + \frac{\partial v}{\partial x}) & 0.5(\frac{\partial u}{\partial z} + \frac{\partial w}{\partial x}) \\ & \frac{\partial v}{\partial y} & 0.5(\frac{\partial v}{\partial z} + \frac{\partial w}{\partial y}) \\ & & \frac{\partial w}{\partial z} \end{pmatrix} \tag{4.23}$$

This small strain formulation has potential errors with large displacement or rotation. Although the bond specimen has overall rigid motion, the small strain calculation is based on pixel level. Thus the use of small strain is a reasonable approximation of the strain field given the current accuracy of displacement data. The maximum principal strain was the maximum eigen values of the strain tensor. The maximum principal strain can be used to identify cracks if it exceeds the tensile cracking strain of concrete, which is the ratio of

tensile strength and Young's modulus of concrete. For concrete with tensile strength of 0.5 ksi and Young's modulus of 3000 ksi, the cracking strain is 0.0017.

Figures 4.21-4.23 show the maximum principle strain field for load increment one (0 to load 2400, two (2400 to 6000 lbs) and three (6000 to 8400 lbs). It can be seen that the maximum principle strain (indicating cracking) initiates at local bond near rib zone and location of cracking initiator (Figure 4.21), development of major transverse cracking (Figure 4.22) and splitting failure (Figure 4.23).

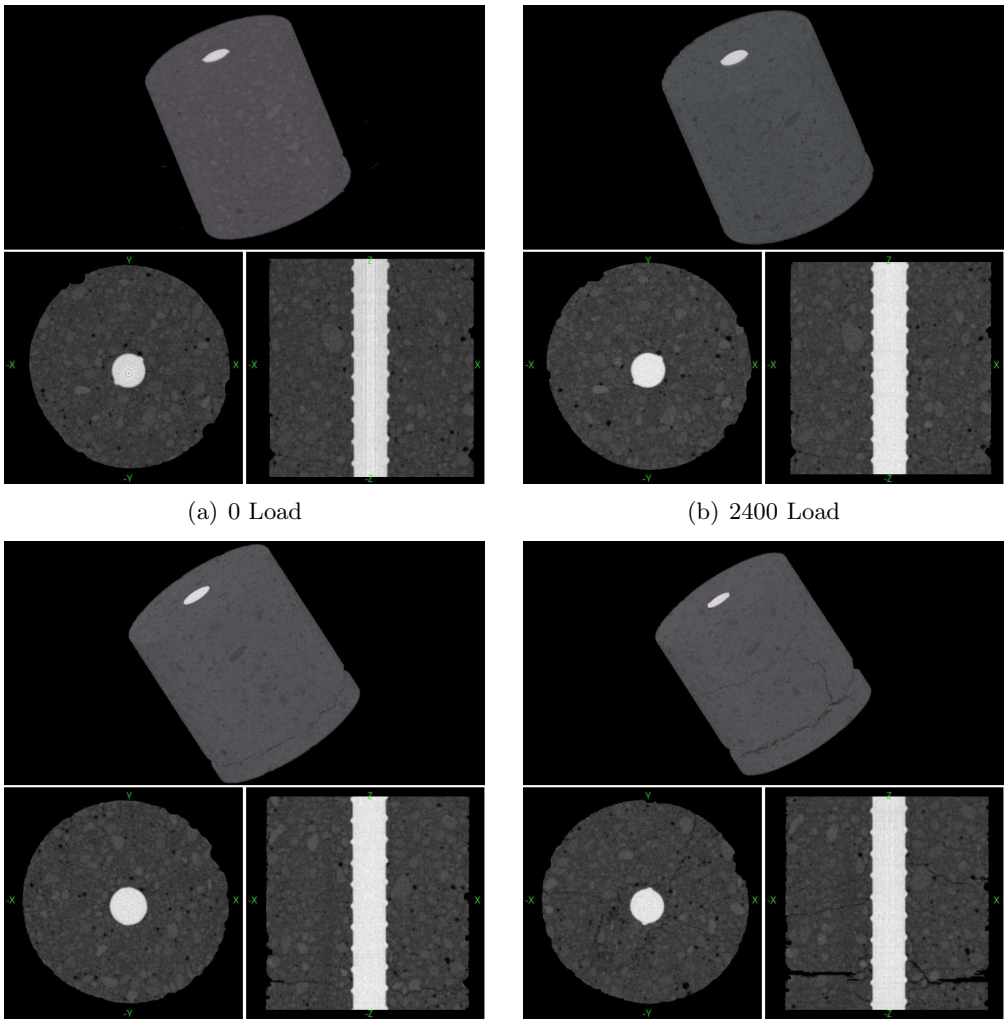

(a) 0 Load

(b) 2400 Load

(c) 6000 Load

(d) 8400 Load

Figure 4.10: Flexural Specimen at 8400 Load

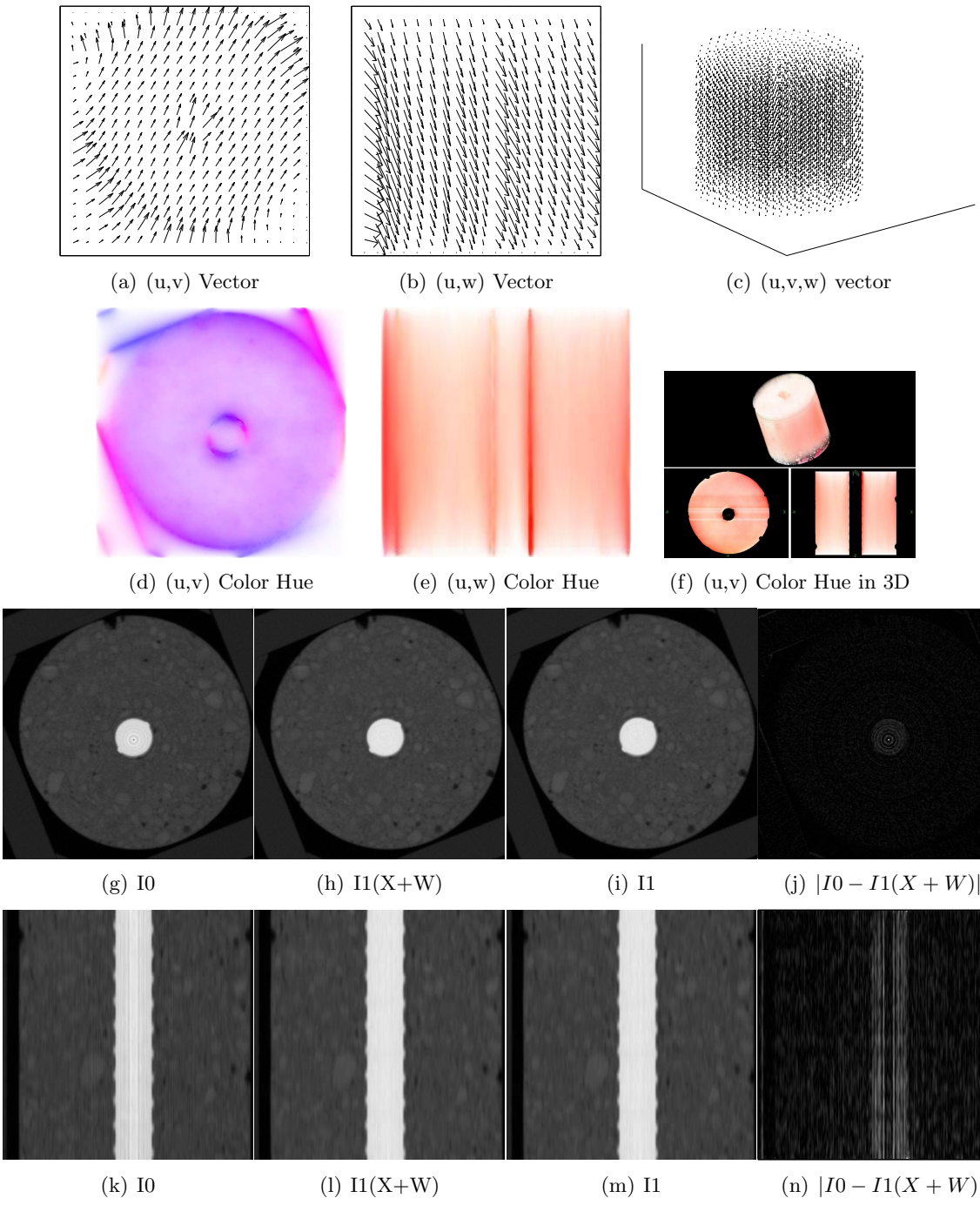

(a) (u,v) Vector (b) (u,w) Vector (c) (u,v,w) vector

(d) (u,v) Color Hue (e) (u,w) Color Hue (f) (u,v) Color Hue in 3D

(g) I0 (h) I1(X+W) (i) I1 (j) $|I0 - I1(X + W)|$

(k) I0 (l) I1(X+W) (m) I1 (n) $|I0 - I1(X + W)|$

Figure 4.11: Motion Estimation from Load Level 0→2400

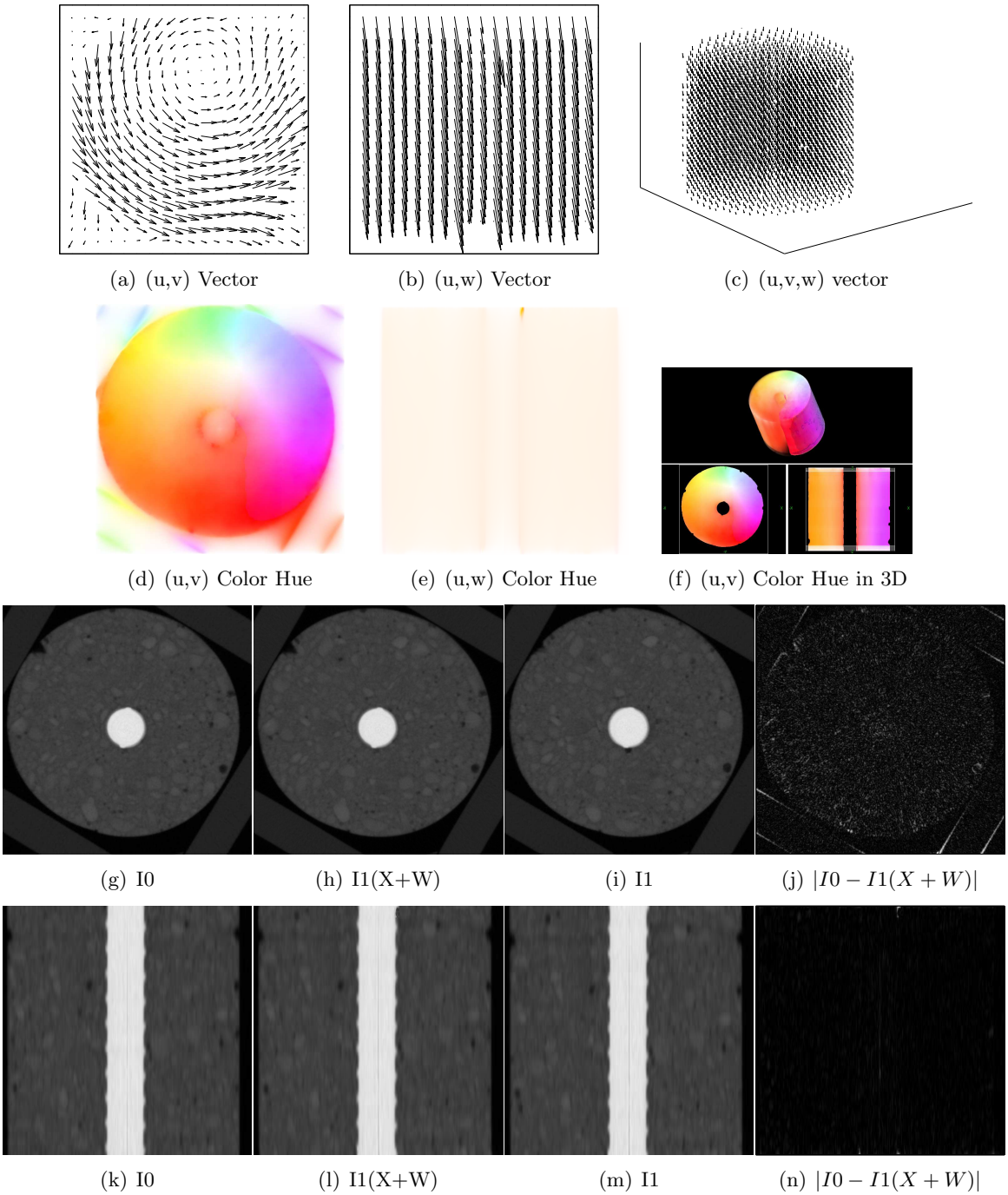

(a) (u,v) Vector (b) (u,w) Vector (c) (u,v,w) vector

(d) (u,v) Color Hue (e) (u,w) Color Hue (f) (u,v) Color Hue in 3D

(g) I0 (h) I1(X+W) (i) I1 (j) $|I0 - I1(X + W)|$

(k) I0 (l) I1(X+W) (m) I1 (n) $|I0 - I1(X + W)|$

Figure 4.12: Motion Estimation from Load Level 2400→6000

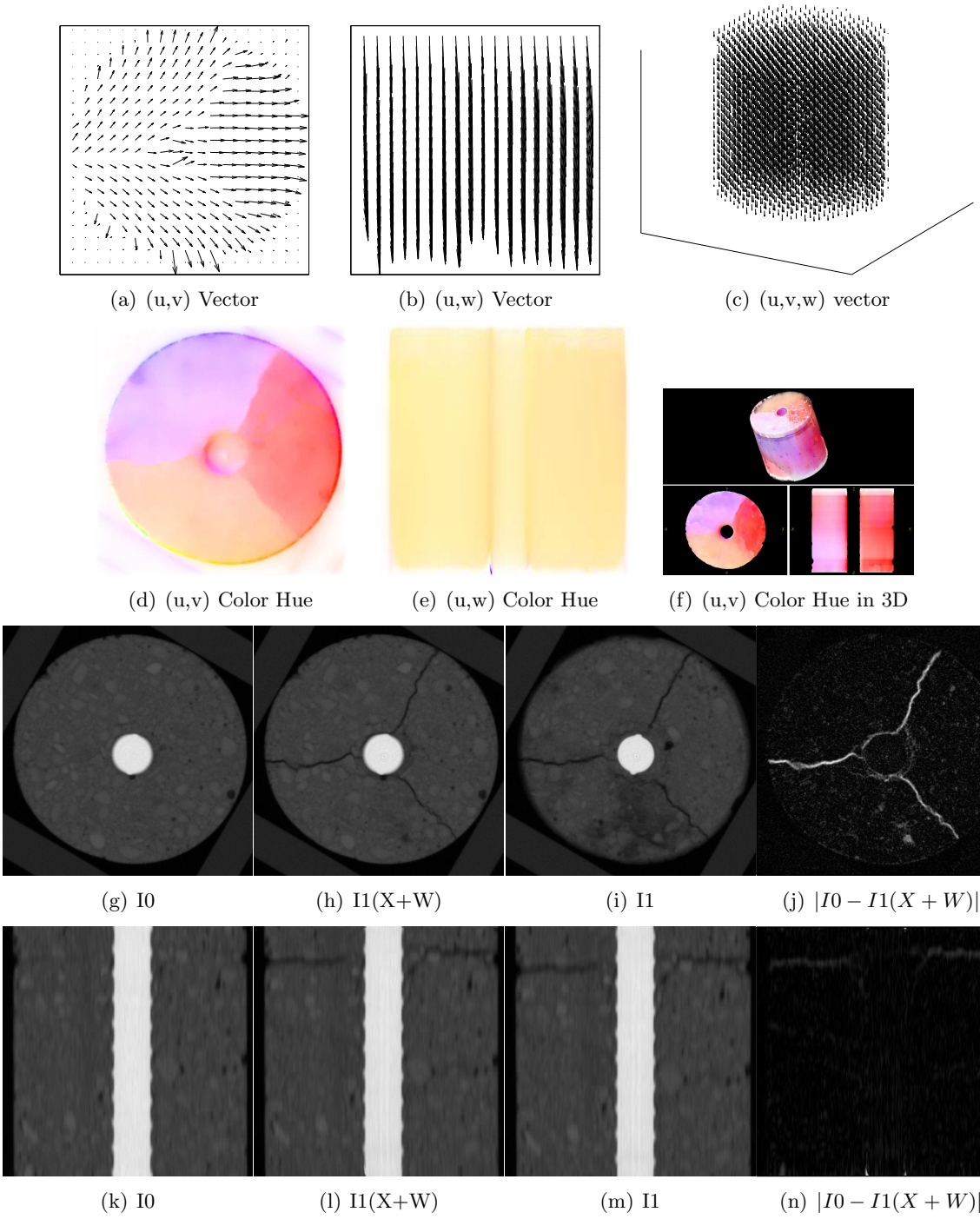

(a) (u,v) Vector (b) (u,w) Vector (c) (u,v,w) vector

(d) (u,v) Color Hue (e) (u,w) Color Hue (f) (u,v) Color Hue in 3D

(g) I0 (h) I1(X+W) (i) I1 (j) $|I0 - I1(X + W)|$

(k) I0 (l) I1(X+W) (m) I1 (n) $|I0 - I1(X + W)|$

Figure 4.13: Motion Estimation from Load Level 6000→8400

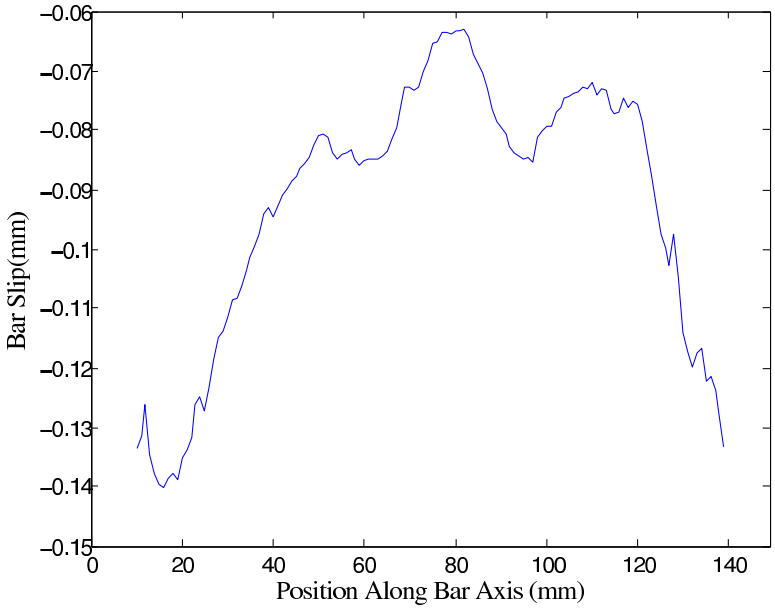

Figure 4.14: Bar Slip for Tension Test Load 0→2400

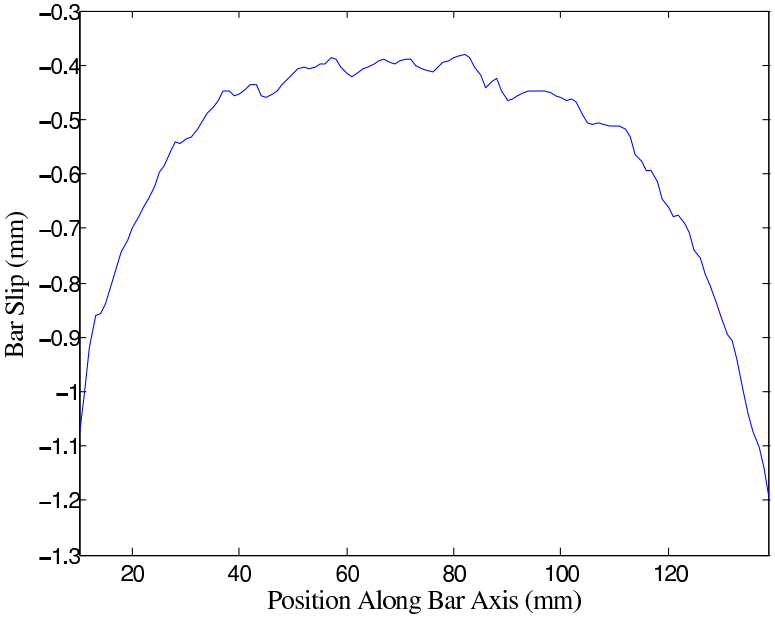

Figure 4.15: Bar Slip for Tension Test Load 2400→6000

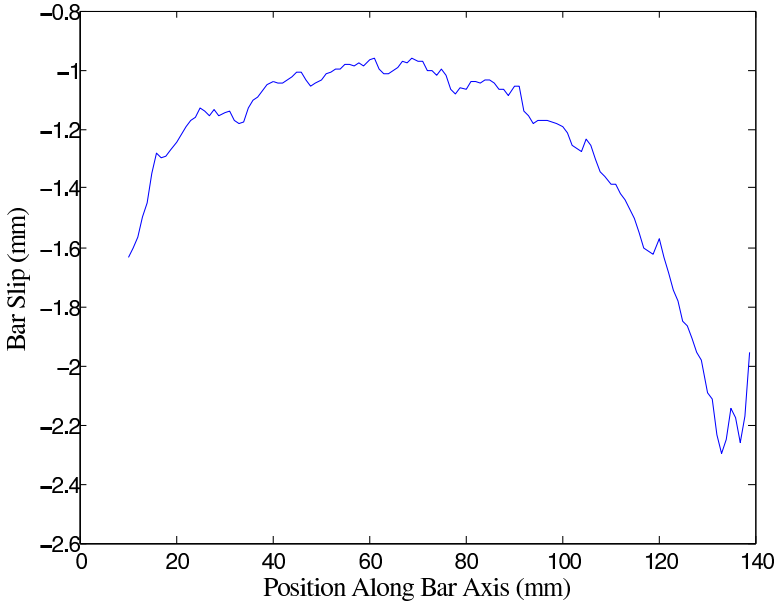

Figure 4.16: Bar Slip for Tension Test Load 6000→8400

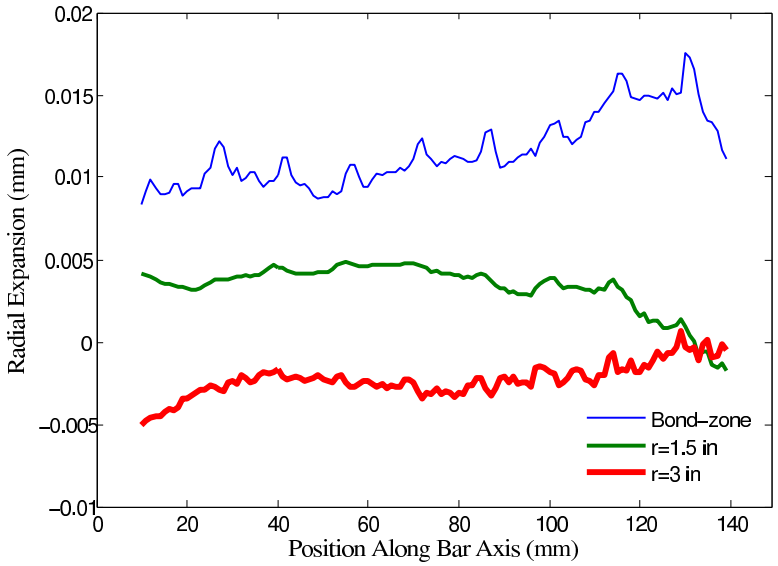

Figure 4.17: Radial Expansion for Tension Test Load 0→2400

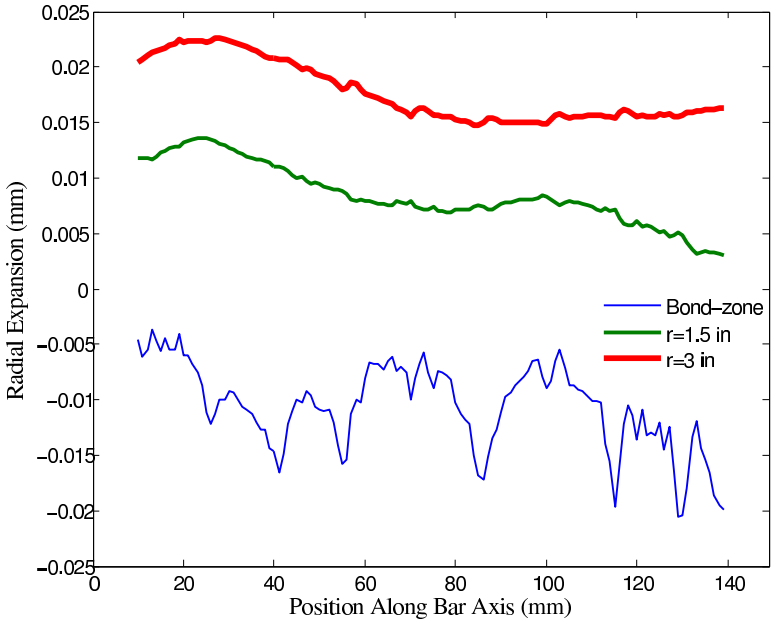

Figure 4.18: Radial Expansion for Tension Test Load 2400→6000

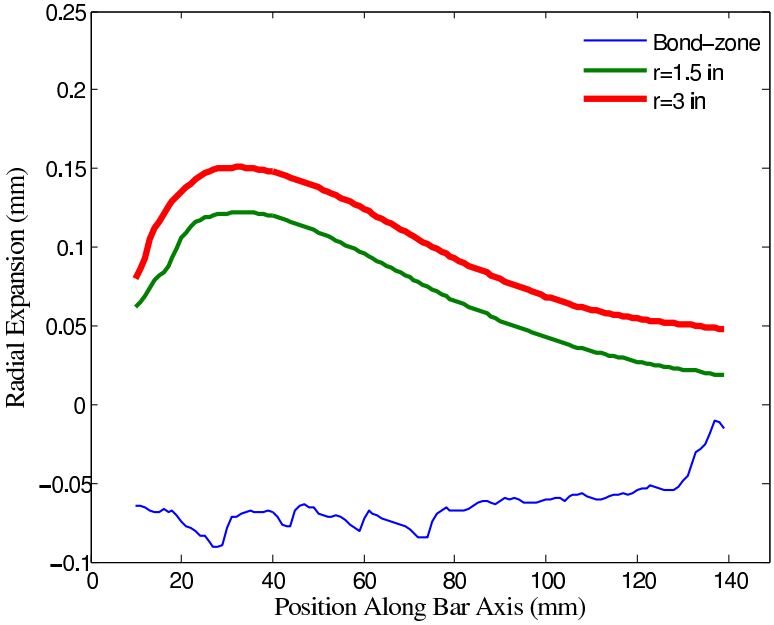

Figure 4.19: Radial Expansion for Tension Test Load 6000→8400

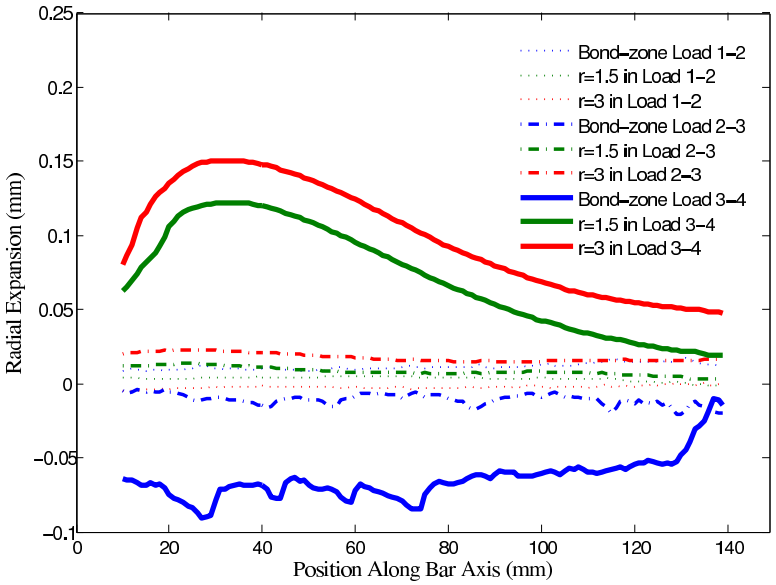

Figure 4.20: Radial Expansion for Tension Test

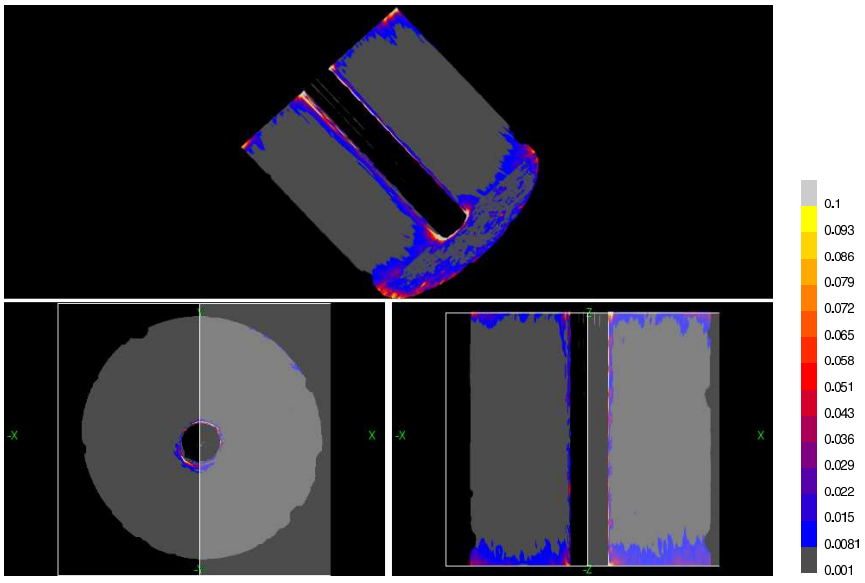

Figure 4.21: Maximum Principal Strain for Tension Test Load 0→2400

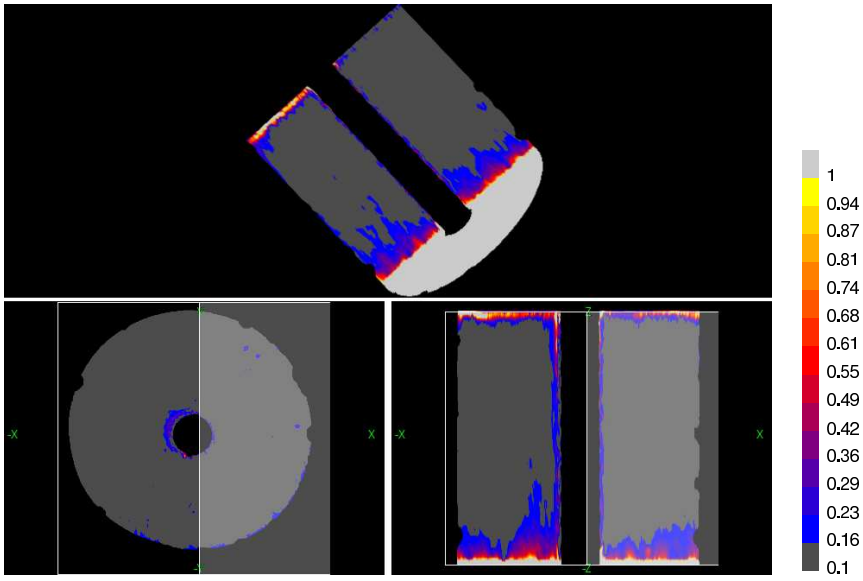

Figure 4.22: Maximum Principal Strain for Tension Test Load 2400→6000

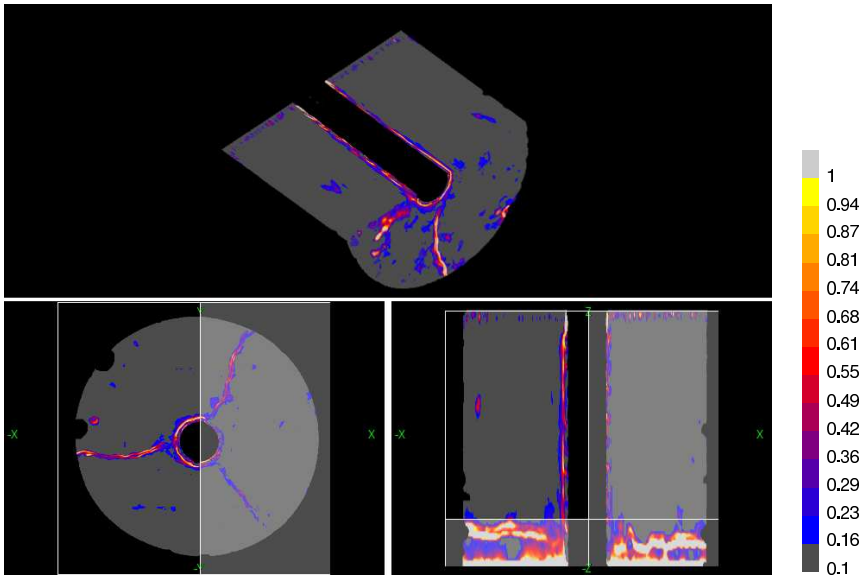

Figure 4.23: Maximum Principal Strain for Tension Test Load 6000→8400

4.6 3D Motion Estimation of Pull-out Test Specimen

4.6.1 Introduction

The optical flow algorithm introduced in Section 3.7.2 was also applied to the pull-out specimen (Figure 4.24) using sequential pairs of images (Under load level 1 (initial load), 2 (pre-peak load), 3 (post-peak load) and 4 (residual load) to evaluate the utility of high-energy imaging and image processing for investigation of the behavior of reinforced concrete components and investigate bond-zone behavior for pull-out test. There are no visual difference between load level 1 and 2. After load 3, the specimen has splitting cracking as can be seen in Figure 4.24(c) and 7.1(c).

Each 3D image has 512×512×104 pixels. Each pixel represented a volume of 0.35×0.35× 1mm. For this specimen, the parameter a=30 and g=100. This parameters were set by trials and experience showed that images with different texture and noise levels need different parameters to achieve best performance. The calculation was performed with single domain on the same machine with flexural specimen. The time spent for calculation of displacement between adjacent load levels was about 48 hours.

4.6.2 Displacement Field

The calculated displacement field from load level 1 to load level 2 is shown in Figure 4.25. Figure 4.25(a) and Figure 4.25(d) are vector and color plots of the displacement (u,v) for a cross-section of the specimen. Figure 4.25(b) and Figure 4.25(e) are vector and color plots of the displacement (u,w) for a vertical section of the specimen. Figure 4.25(c) is a vector plot of full 3D displacement. Figure 4.25(f) is color plot of displacement (u,v) in full 3D view of the specimen. The displacement field shows rigid motion of the specimen images from load 1 to load 2. the discontinuous displacement fields in local bond zone can be seen. Besides the local bond zone, there are no much variation in specimen from initial load to pre-peak load with current image resolution. The maximum displacement in cross-section plane is 1.4 pixels, and in longitudinal z direction is 1.8 pixels, 99.7% of image areas has

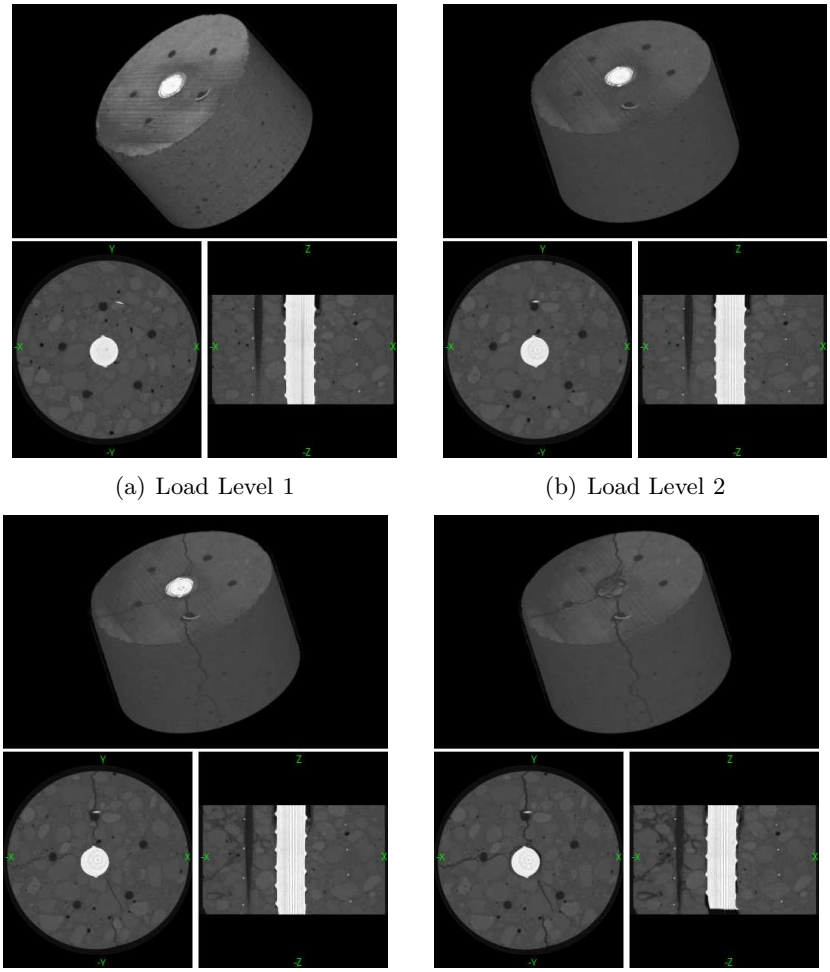

(a) Load Level 1

(b) Load Level 2

(c) Load Level 3

(d) Load Level 4

Figure 4.24: Volumetric Images of Pull-out Test Specimen

pixel intensity calculation error of less than 10%.

To test the motion displacement field, using the specimen images at load level 2 and the displacement field can reconstruct the specimen images at load level 1, i.e. $I_{1-reconstructed}$(X) = I_2(X+W). Figure 4.25(g) shows a cross section view of the specimen at load 1. Figure 4.25(h) shows the reconstructed image at load 1. Figure 4.25(i) shows the specimen at load 2. Figure 4.25(j) shows the difference between the original reference image and reconstructed image at load 1, the differences present the errors in estimating the displacement

field.

Similarly, Figure 4.25(k)∼Figure 4.25(n) show the vertical view of original specimen and reconstructed specimen and the motions estimation errors. Due to the image noises in central bar region, the major errors of results are concentrated at these regions. The displacement field shows the relative slip between bar and concrete, which is not seen from visual observation.

The calculated displacement field from load level 2 to load level 3 is shown in Figure 4.26. From load level 2 to load level 3, the specimen has experienced the peak load and splitting happened, as can be seen from the figure. Figure 4.26(a) and Figure 4.26(d) are vector and color plots of the displacement (u,v) for a cross-section of the specimen. Figure 4.26(b) and Figure 4.26(e) are vector and color plots of the displacement (u,w) for a vertical section of the specimen. Figure 4.26(c) is a vector plot of full 3D displacement. Figure 4.26(f) is color plot of displacement (u,v) in full 3D view of the specimen. The displacement results show the splitting behavior and the discontinuous displacement fields in local bond zone are also captured by the results. Figure 4.26(b) shows the slippage of bar out of concrete after the splitting. The maximum displacement in cross-section plane is 1.8 pixels, and in longitudinal z direction is 2.9 pixels, 98.4% of image areas has pixel intensity error of less than 10%.

To test the motion displacement field, using the specimen images at load level 3 and the displacement field can reconstruct the specimen images at load level 2, i.e. $I_{2-reconstructed}(X) = I_3(X + W)$. Figure 4.26(g) shows a cross section view of the specimen at load 2. Figure 4.26(h) shows the reconstructed image at load 2. Figure 4.26(i) shows the specimen at load 3. Figure 4.26(j) shows the difference between the original reference image and reconstructed image at load 2, the differences present the errors in estimating the displacement field. Figure 4.26(j) shows the errors concentrated at cracking regions.

Similarly, Figure 4.26(k)-Figure 4.26(n) show the vertical view of original specimen and reconstructed specimen and the motions estimation errors. The major errors happen at

regions with large image gradient change such as near lugs and cracks.

The calculated displacement field from load level 3 to load level 4 is shown in Figure 4.27. Figure 4.27(a) and Figure 4.27(d) are vector and color plots of the displacement (u,v) for a cross-section of the specimen. Figure 4.27(b) and Figure 4.27(e) are vector and color plots of the displacement (u,w) for a vertical section of the specimen. Figure 4.27(c) is a vector plot of full 3D displacement. Figure 4.27(f) is color plot of displacement (u,v) in full 3D view of the specimen. Load level 3$\sim$4 represents the residual bond strength stage in the pull-out test. At this load stage, the specimen experienced residual radial splitting and bar longitudinal slippage as can be seen from the figure 4.27(a) and Figure 4.27(b). The maximum displacement in cross-section plane is 3.2 pixels, and in longitudinal z direction is 17.3 pixels, 98.7% of image areas has pixel intensity error of less than 10%.

To test the motion displacement field, using the specimen images at load level 4 and the displacement field can reconstruct the specimen images at load level 3, i.e. $I_{3-reconstructed}(X) = I_4(X + W)$. Figure 4.27(g) shows a cross section view of the specimen at load 3. Figure 4.27(h) shows the reconstructed image at load 3. Figure 4.27(i) shows the specimen cross-section image at load 4. Figure 4.27(j) shows the difference between the original reference image and reconstructed image at load 3, the differences present the errors in estimating the displacement field. Figure 4.27(j) shows the errors concentrated at bond-zone.

Similarly, Figure 4.27(k)-Figure 4.27(n) show the vertical view of original specimen and reconstructed specimen and the motions estimation errors. The large bar slippage at this load stage is very well represented by the displacement results, as seem from the similarity between Figure 4.27(k) and Figure 4.27(m)

Figure 4.27(e) shows snap back of steel deformation. From the color encoding, yellow represents downward displacement, which is the direction of load at the end of bar, purple represents upward displacement, which means snap back of bar after the peak load. This is not consistent with test results. Further examination of the images found that bar has large slippage from concrete. This leads to 5 ribs in image 4.27(m) under load level 4,

while originally there are 6 ribs in image 4.27(k). This disappearance of one rib leads to the calculation error in bar displacement. This error is inevitable if only partial specimen image is available as the uncertainty of boundary conditions. Fortunately, this error can be corrected by adding rib spacing to the z direction displacement w for the bar. And furthermore, the deformation and damage of concrete is the main interest here.

4.6.3 Bar Slip and Radial Expansion

Using the displacement field presented in section 4.6.2, the slip of the reinforcing bar relative to the concrete and the radial expansion of the concrete around the bar were estimated. The bar slip is computed as the movement of the bar, in the direction of the bar axis, with respect to the concrete surface at a distance of 0.2 inch from the surface of the bar. Radial expansion is the radial motion of concrete away from the center of the specimen and is computed for three concrete cylinder surfaces that located at a radius of 0.2 inch, at approximately middle of the concrete cylinder surrounding the bar and at the surface of the specimen.

Figure 4.28 shows the bar slip from initial load to pre-peak load. The slippage is larger at load end with magnitude of 0.06 mm. At free end close to zero with slight opposite direction slip. The fluctuation in slip plot reflects the influence of rib to the slip.

Figure 4.29 shows the bar slip from pre-peak load to immediate post-peak load. The slippage at free end is 0.8 mm. The slippage at load end is 1 mm. The slippage in the middle bonded part is from 0.5 to 0.7 mm. This is not reasonable if the assumption of linear distribution of slip is correct.

Figure 4.30 shows bar slip from immediate post-peak load to residual load. The slippage at free end is 4 mm. However, the slippage at load end is -4 mm at opposite slip direction. This is not consistent with physical phenomenon. Due to the partial imaged specimen and fixed boundary condition, the slippage at residual load stage is offset by half of rib spacing, as shown from Figure 4.27(k) to Figure 4.27(m). If this offset of 7.5 mm is used to correct

the result, the slippage for both end is about 4 mm, which is the residual slippage after the splitting

Figure 4.31 shows the radial displacement from initial load to pre-peak load. Bond layer has radial expansion about 0.002 mm. Outer layer has radial expansion from 0.006 mm to 0.008 mm. The middle layer has radial contraction to expansion from -0.002 mm to 0.002 mm. Considering the magnitude of the number, the data for middle layer is not reliable.

Figure 4.32 shows the radial displacement of specimen from pre-peak load to immediate post-peak load. Bond-zone layer has slight radial expansion from 0.1 to 0.15 mm. The middle layer and outer layer have almost same radial expansion from 0.27 mm at free end to 0.2 mm at the load end. At this load stage, longitudinal splitting happened. The major radial expansion for middle layer and outer layer is due to this splitting.

Figure 4.33 shows the radial displacement from immediate post-peak load to residual load. Bond-zone layer has fluctuate radial expansion from 0.01 to 0.16 mm. The middle layer and outer layer have radial expansion from 0.7 mm at free end to 0.06 mm at load end. The free end has more splitting expansion than that at load end. This is consistent with lab test pictures, which show the longitudinal splitting are wider at free end.

Figure 4.34 is plot of radial displacement under three load levels. The splitting process, represented by load level 2 and 3, exhibits maximum radial expansion. At residual stage, the radial expansion is reduced but with significant slippage.

4.6.4 Maximum Principal Strain

The maximum principal strain field for the pull-out test specimen is shown in figure 7.4(a)∼figure 4.37, calculated in the same way as Section 4.5.3. Figure 7.4(a) shows the local cracking in rib zone before splitting happens. In Figure 7.5(a), the maximum strain happens at splitting locations and the spiral wire has maximum hoop strain comparing with initial load stage and residual load stage. This is consistent with results from Malvar [107].

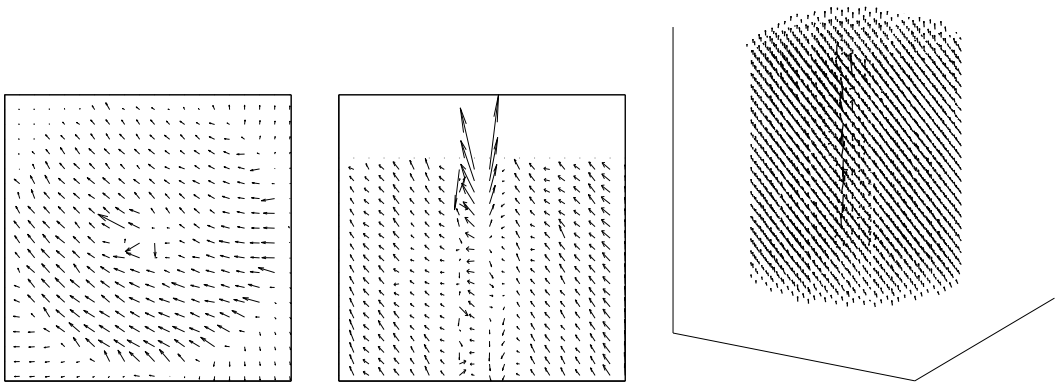

(a) (u,v) Vector (b) (u,w) Vector (c) (u,v,w) vector

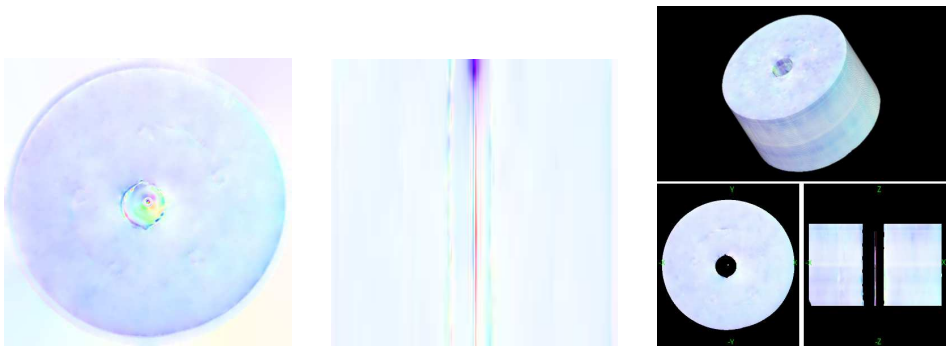

(d) (u,v) Color Hue (e) (u,w) Color Hue (f) (u,v) Color Hue in 3D

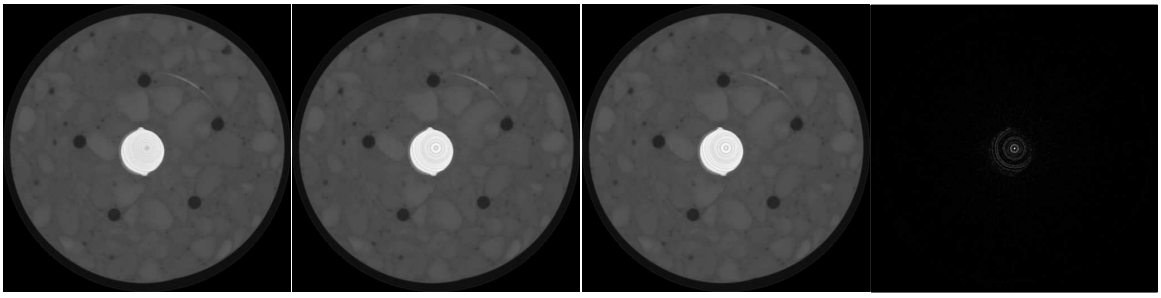

(g) I0 (h) I1(X+W) (i) I1 (j) $|I0 - I1(X + W)|$

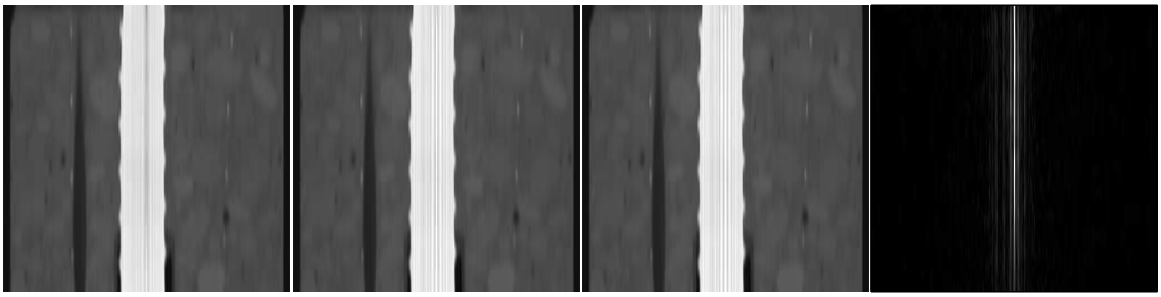

(k) I0 (l) I1(X+W) (m) I1 (n) $|I0 - I1(X + W)|$

Figure 4.25: Motion Estimation from Load Level 1→2

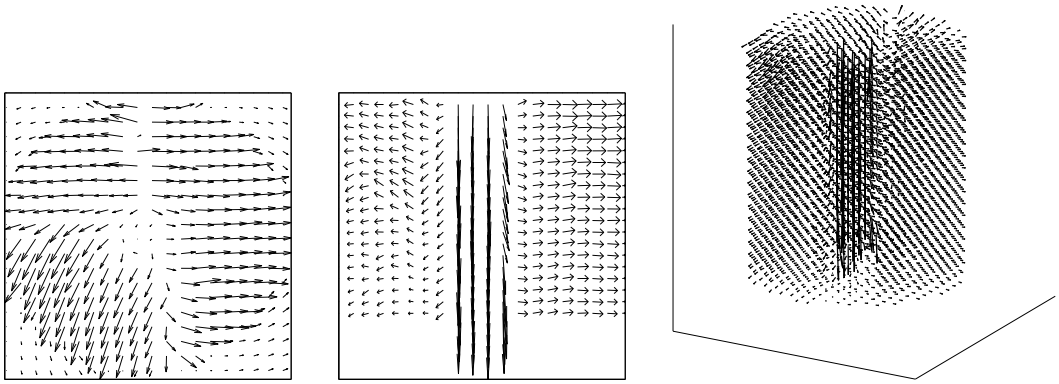

(a) (u,v) Vector (b) (u,w) Vector (c) (u,v,w) vector

(d) (u,v) Color Hue (e) (u,w) Color Hue (f) (u,v) Color Hue in 3D

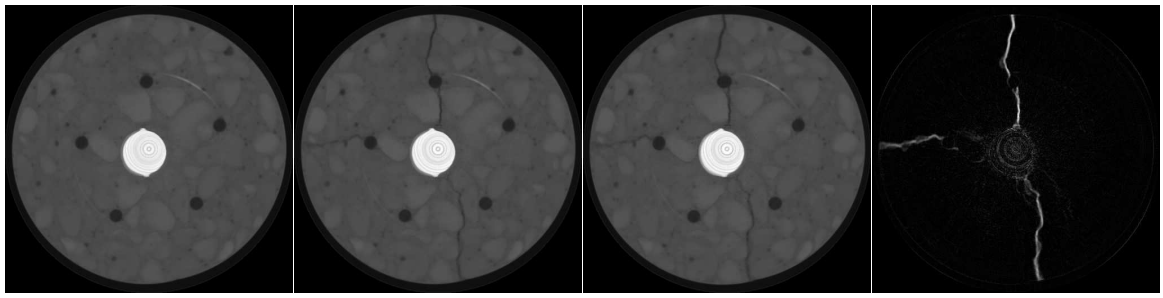

(g) I0 (h) I1(X+W) (i) I1 (j) $|I0 - I1(X + W)|$

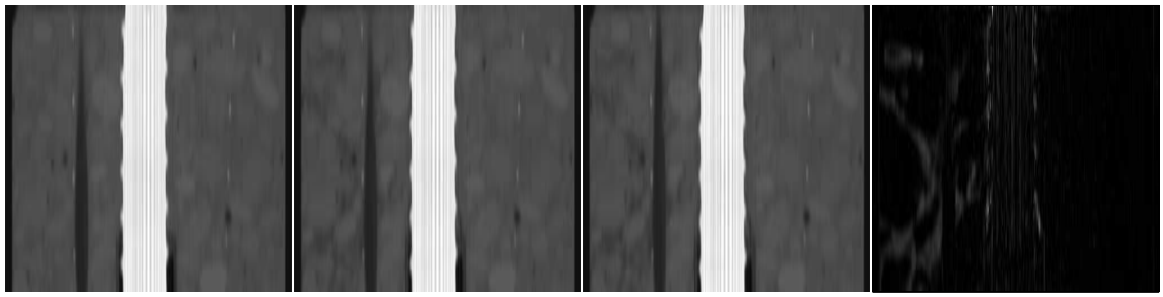

(k) I0 (l) I1(X+W) (m) I1 (n) $|I0 - I1(X + W)|$

Figure 4.26: Motion Estimation from Load Level 2→3

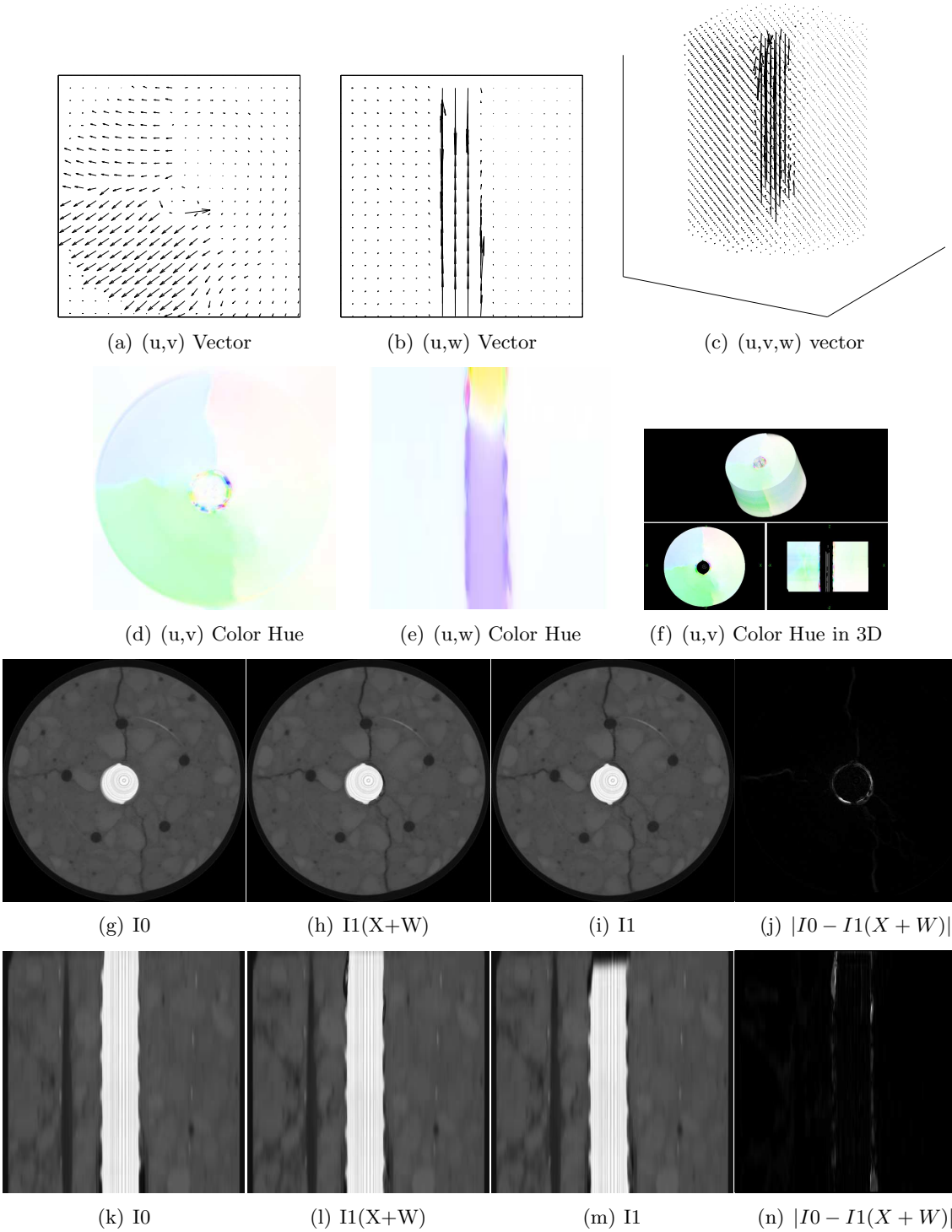

(a) (u,v) Vector (b) (u,w) Vector (c) (u,v,w) vector

(d) (u,v) Color Hue (e) (u,w) Color Hue (f) (u,v) Color Hue in 3D

(g) I0 (h) I1(X+W) (i) I1 (j) $|I0 - I1(X + W)|$

(k) I0 (l) I1(X+W) (m) I1 (n) $|I0 - I1(X + W)|$

Figure 4.27: Motion Estimation from Load Level 3→4

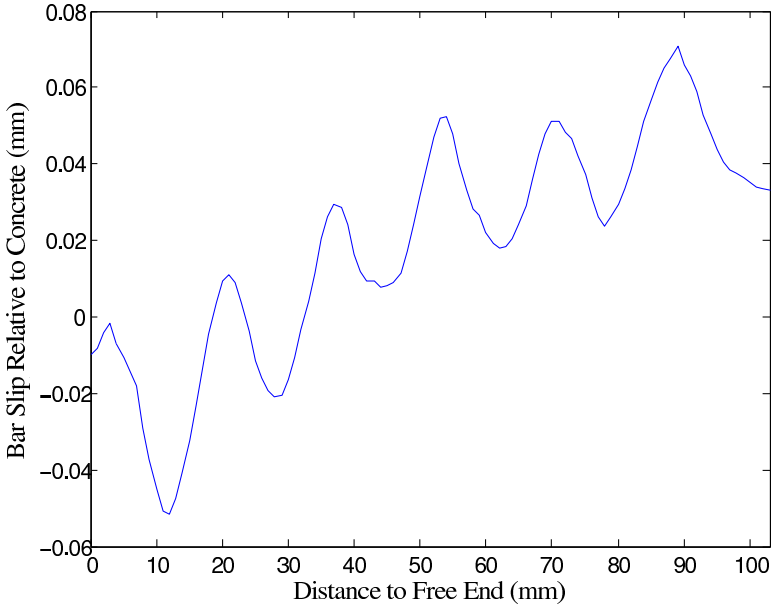

Figure 4.28: Bar Slip for Pull-out Test Load 1→2

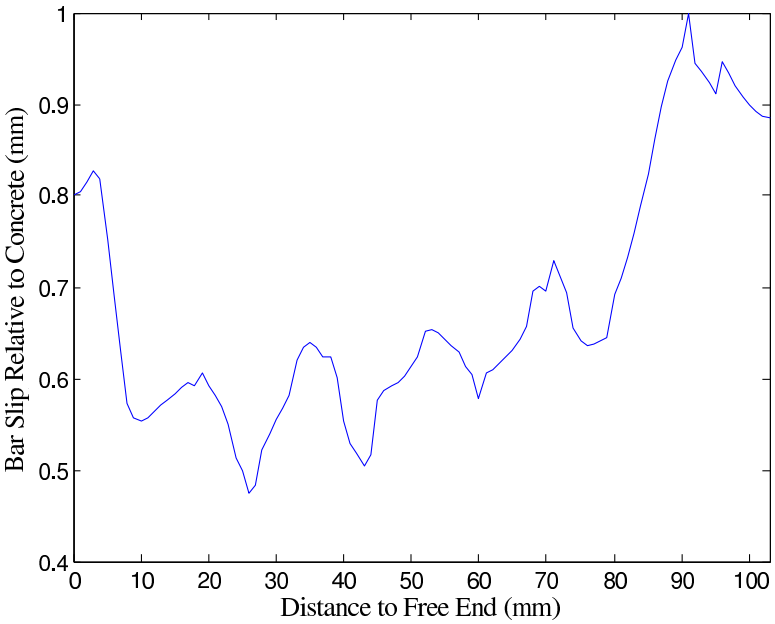

Figure 4.29: Bar Slip for Pull-out Test Load 2→3

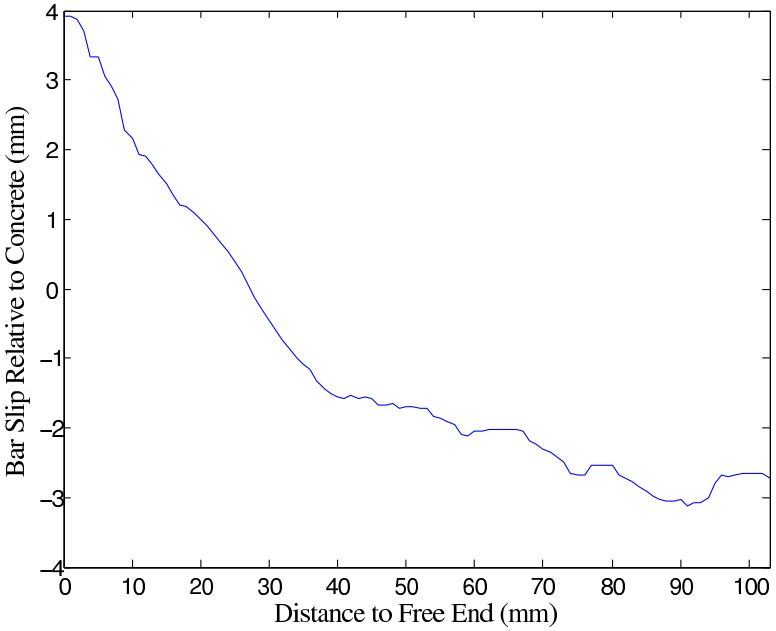

Figure 4.30: Bar Slip for Pull-out Test Load 3→4

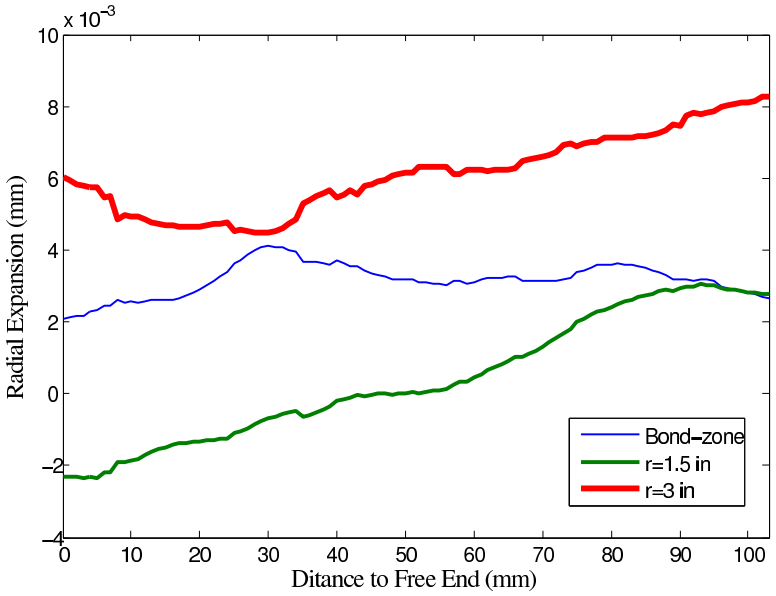

Figure 4.31: Radial Expansion for Pull-out Test Load 1→2

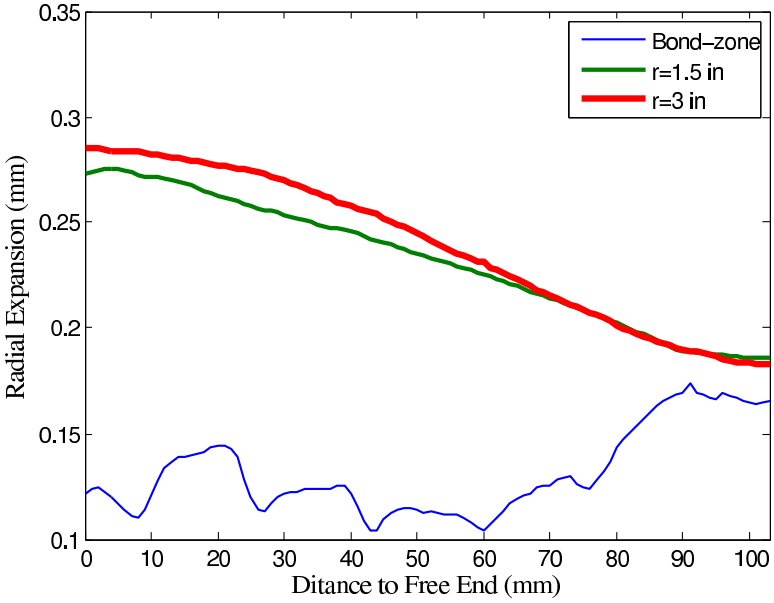

Figure 4.32: Radial Expansion for Pull-out Test Load 2→3

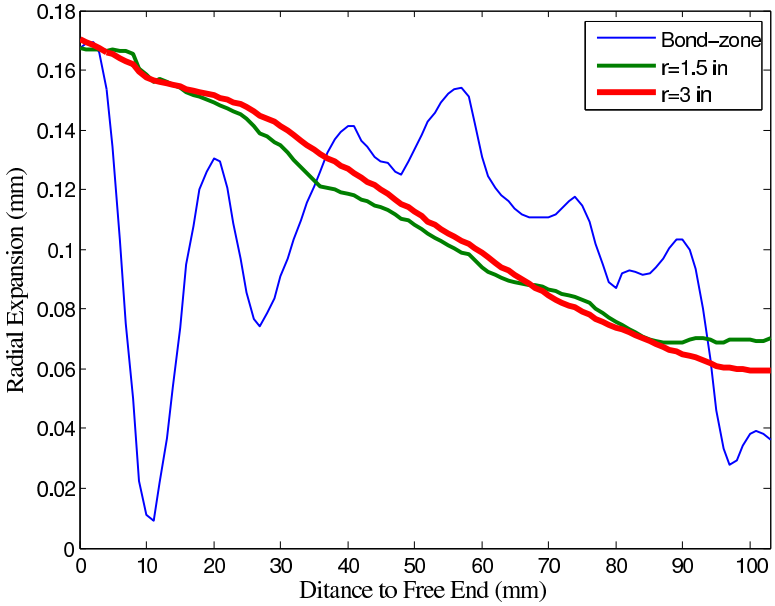

Figure 4.33: Radial Expansion for Pull-out Test Load 3→4

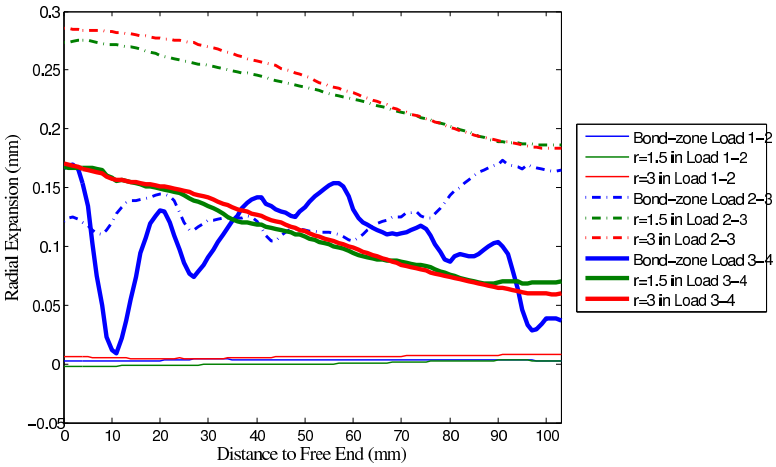

Figure 4.34: Radial Expansion for Pull-out Test

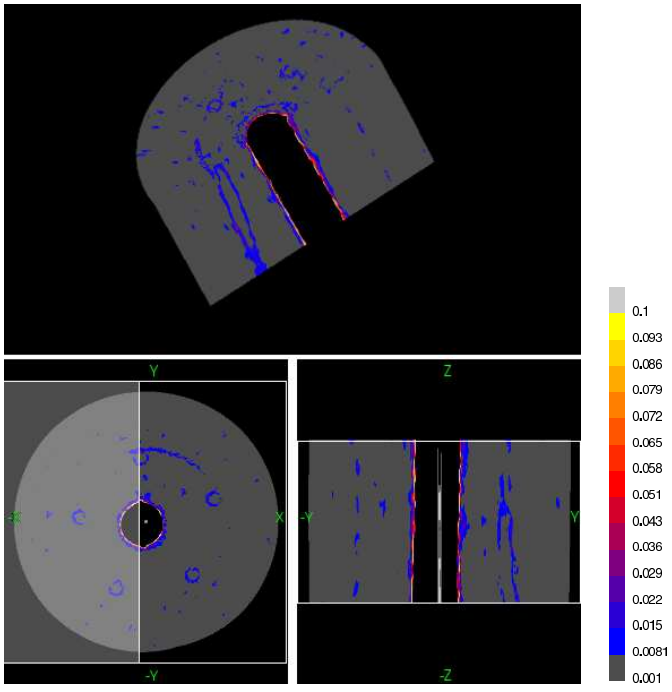

Figure 4.35: Maximum Principal Strain Load Level 1→2

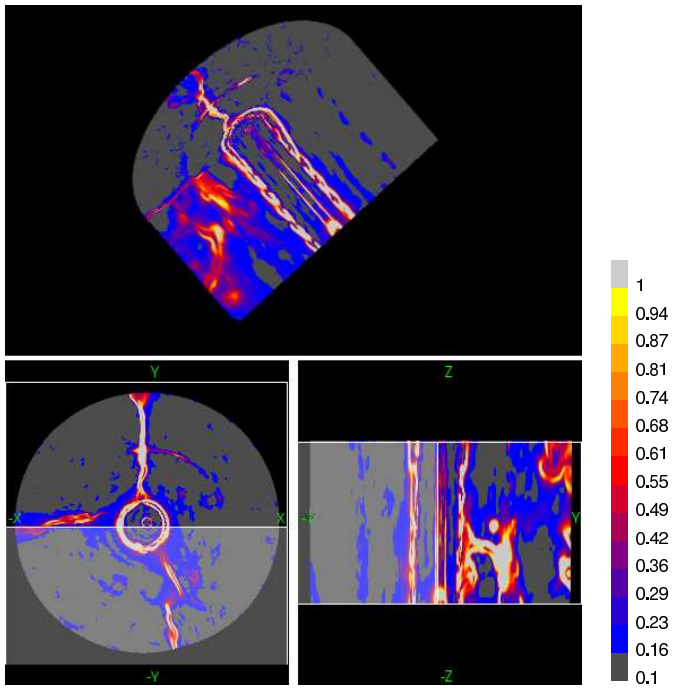

Figure 4.36: Maximum Principal Strain Load Level 2→3

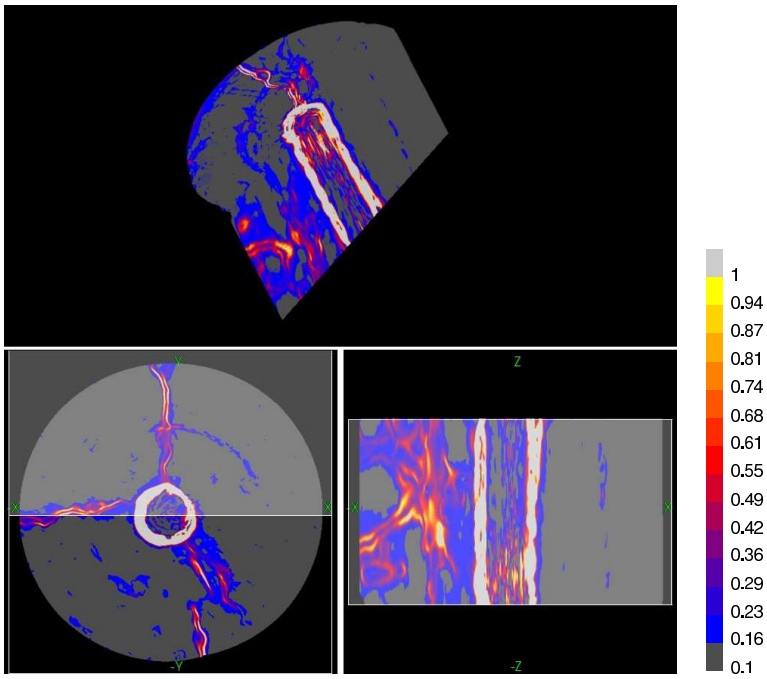

Figure 4.37: Maximum Principal Strain Load Level 3→4

4.7 Summary

An optical flow algorithm for spatially three-dimensional volumetric images was applied on concrete cylinder bond test to investigate the damage pattern of the test specimen under different load levels. The algorithm uses an energy function accounting for the square sum of the image gray scale intensity and the first order gradient of the intensity, as well as gradient of the flow field as the objective function. Reducing effect of image noises and reserving the cracking discontinuity are achieved by a rising concave function, which leads to smaller weight for larger numbers. Tests of the algorithm show that the calculated displacement field has overall good performance with accuracy of less than 10% of error, and more than 90% of reconstructed pixels have intensity error less than 10%. The calculated displacement field represent very well the cracking region except that the cracking is smeared in the local cracked region instead of discrete cracks, due to the continuous formulation of the displacement field in the total energy function. To apply the optical flow method to a large size of bond image series, a domain decomposition procedure was also developed. Applying the spatially three-dimensional optical flow algorithm on the 3D bond image data, the implemented algorithm did a fairly good job on capturing the deformation characteristics of test images and bond specimens. The motion estimation algorithm was applied to investigate two types of bond test specimens using X-ray image data.

For flexural bond test, the three-dimensional displacement field between adjacent load levels was estimated using the motion optical flow algorithm. The calculated displacement field and maximum principal strain show the capture of major transverse cracking and longitudinal splitting. However, the displacement discontinuity at cracking region is smeared out in local region when comparing the reference image with reconstructed image.

The radial deformation and slip were calculated from the displacement data. Bond-zone exhibits radial contraction due to elongation of the bar. The outer layers concrete exhibit slight radial expansion due to the rib induced longitudinal splitting.

For pull-out test, the splitting cracks were also captured by the estimated motion.

More splitting happens at free end than that at load end for this specimen. The bar slip was captured after correcting the calculated displacement according to rib spacing. Both bond-zone slip and radial expansion on three different layers of concrete were presented.

The results show a good overall performance and capture of large displacement field. However, the calculated displacement for both flexural specimen and pull-out specimen didn't show the cone shape secondary cracking expected. As the algorithm takes the number of pixels as unit, the cracks will be represented by more pixels if the image resolution is high enough, which will improve the results in representing cracks.

On the other hand, given current resolution of the images, several potential improvements are worthwhile in future work to improvement the displacement discontinuity near cracks. Current algorithm has the deficiency of over-smoothing the flow field, which may contribute to the facts that secondary cracking is not well represented. This problem can be improved by either modifying the smooth term regulators adaptively such that the flow field near cracks has smaller weight than other regions, or by discrete representation of the displacement field.

To improve the accuracy and efficiency of solution procedure, more work can be put to refine the domain decomposition implementation and the solution procedure in solving the nonlinear partial differential equations.

Chapter 5

Finite Element Modeling of Bond Behavior

5.1 Introduction

In analysis of concrete structures, it is necessary to include bond-zone response to accurately predict structural performance. From experimental observation, there is a general understanding of bond response and bond damage patterns, and a number of modeling procedures have been proposed for simulating this response. This chapter focuses on modeling the bond zone using 2D and 3D continuum models, and investigate the importance of different material models, geometric models and solution procedures. Analysis results are evaluated on the accuracy with which bond strength, load-displacement response, and damage patterns such as cracking and crushing of concrete are simulated.

The reference model is a direct contact model, in which concrete and steel are two separate contact bodies. Under loading, the bond is represented by the contact behavior between concrete and rebar lugs. Software MSC.marc is used for the analysis. Section 5.2 introduces the geometry of the reference contact model. Section 5.3 is a detailed discussion of the material models employed in the analysis. Details of the concrete material model, including simulation of tension, compression under uniaxial and multi-axial loadings are discussed. Softening phenomenon and related problems such as geometry dependency, strain formulations are also addressed. Section 5.4 discusses the solution procedures employed. Material and geometrical nonlinearity make convergence a big challenge for the modeling. Different numerical methods intended to improve convergence are discussed. Section 5.5 presents the results of preliminary analysis of the contact model considering different concrete material assumptions. Specifically, the geometric contact model is evaluated using linear-elastic model, tension softening only model, compression plasticity only model, and

finally using the fully nonlinear model considering both tension softening and compression hardening and softening. Section 5.6 is a full evaluation of the contact model, which includes investigation of the sensitivity of predicted response to mesh refinement, material properties, solution procedures and other parameters.

Modeling contact needs high resolution fine mesh to detect the contact surface, in combination with the nonlinear material model, thus makes the model computationally expensive. As reviewed by chapter 2, the behavior of bond depends on the concrete material model used, even using interface model. The concrete material model used here addressing both tension cracking and compression yielding. Using this model, different geometric models employ different interface connections between concrete and steel, including displacement compatibility between concrete and steel enforced at nodes with or without explicit modeling of bar ribs are also evaluated. Section 5.7 presents results of models that employ these different approaches for simulating the concrete-steel interface.

5.2 Rib-Scale Bond Zone Model

5.2.1 Model Geometry

The physical specimen is a concrete cylinder with a bar in the center. Figure 5.1 is a pull-out test cylinder. The bar is pulled from the concrete cylinder with reaction force acting on the concrete. Figure 5.2 is a uniform tension test cylinder. The specimen is pulled at two extruded bar ends until concrete is cracked to break into stable segments transversely.

Figure 5.3 is a finite element model at rib scale. The rib is arc shape, with height of 0.1 inch, spacing at 0.5 inch. Each rib ring is normal to the bar axis. The reference model has three ribs. The lead length (from first rib center to reaction section of concrete) is 1 inch. The total model length is 2.25 inch.

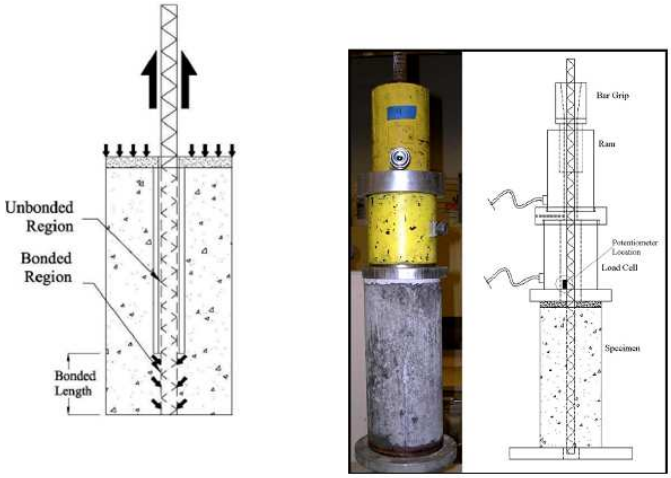

Figure 5.1: Pull-out Test Specimen

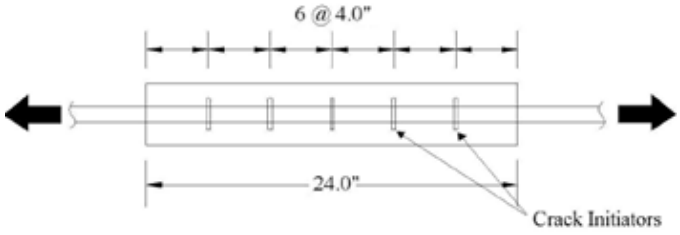

Figure 5.2: Tension-test Specimen

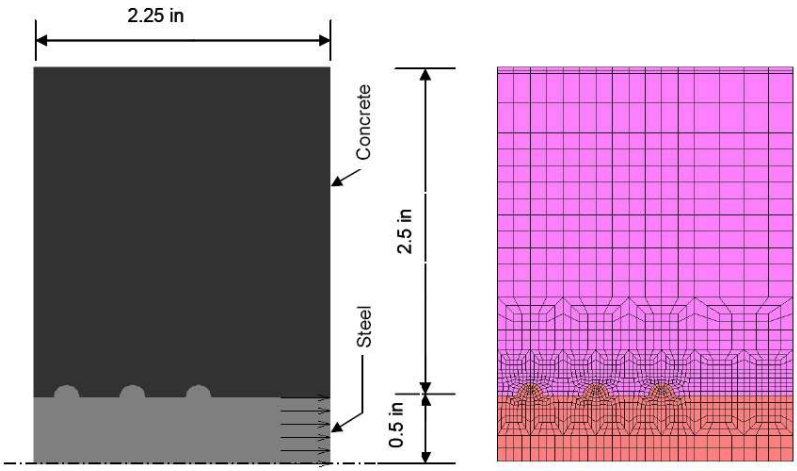

Figure 5.3: Finite Element Model at Rib Scale

5.2.2 Contact Model

The reference finite element contact model reflects the most direct interaction behavior between concrete and steel at rib scale. MSC.marc [37] software has a robust subroutine to conduct contact analysis. Marc software uses direct constraint to implement the contact algorithm. All nodes on the contact surface of one body will be checked against the contact surface of another body, if the relative displacement in direction perpendicular to the potential contact surface is larger than tolerance, then the contact condition is satisfied. The displacement of the contact node is then restricted to the surface of another body. The displacement compatibility is in normal direction, while gliding is allowed in tangential direction. In this study, steel and concrete are treated as two separate contact bodies. The contact surface represents the interface between concrete and steel.

5.3 Concrete Constitutive Model

5.3.1 Introduction

Two phenomena exist for concrete materials. In uniaxial tension test, the concrete will crack when the tensional stress reaches the tensional strength of concrete. After cracking initiates, the tensional capacity of concrete does not disappear immediately, but decreases gradually as the cracking develops further. In uniaxial compression test, stress-strain relationship show linear elastic, plastic hardening until peak strength and plastic softening stage after peak strength. To mathematically describe the tension and compression behavior of concrete, the material constitutive model used here is linear Mohr-Coulomb model with associate flow rule, with multi-fixed cracking model on principle tensional strain. Within Mohr-Coulomb plastic frame work, the principle tensional stresses need to satisfy the stress-strain law as in tension part of Figure 5.4. At each integration point, a maximum of three orthogonal cracks are allowed. And once the crack is initiated, the direction is fixed. The material model for steel is perfect plastic model with the yield stress of 60 ksi.

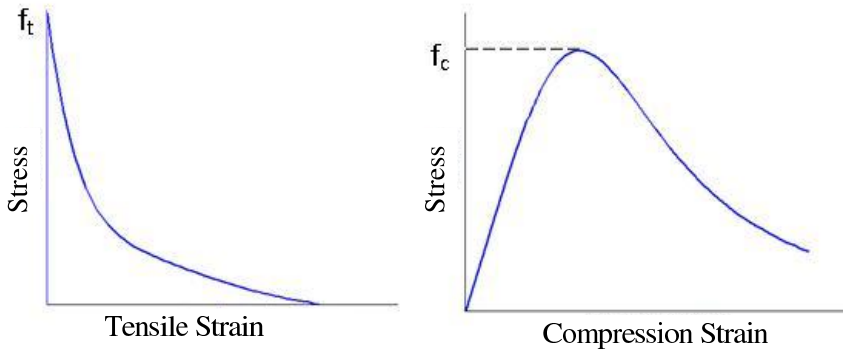

Figure 5.4: Tension and compression behavior of concrete

5.3.2 Compression Plasticity of Concrete

The yield surface for linear Mohr-Coulomb model is:

$$f(\sigma) = \alpha I_1 + \sqrt{J_2} - \frac{\overline{\sigma}}{\sqrt{3}} \tag{5.1}$$

$$\sigma_i \leq \sigma_{ft} \tag{5.2}$$

where,$I_1 = \sigma_{ii}$, $\sqrt{J_2} = \sqrt{\frac{1}{2}S_{ij}S_{ij}}$,$S_{ij} = \sigma_{ij} - \frac{I_1}{3}$, σ_i is principle stress, σ_{ft} is critical cracking stress, is the same with tensional strength of concrete f_t here.

Two scalar parameters, α and $\overline{\sigma}$, need to be obtained from experimental data, such as uniaxial and biaxial compression strength. The yield surface assume α is a constant, and equivalent stress is a function of current material strength. Assume the concrete biaxial strength is 1.2 times the uniaxial strength [83], the uniaxial compression stress tensor is:

$$\sigma = \begin{pmatrix} 0 & 0 & 0 \\ 0 & 0 & 0 \\ 0 & 0 & -f_c \end{pmatrix}$$

So $I_1 = -f_c, \sqrt{J_2} = \frac{f_c}{\sqrt{3}}$.

The biaxial compression stress tensor is:

$$\sigma = \begin{pmatrix} 0 & 0 & 0 \\ 0 & -1.2f_c & 0 \\ 0 & 0 & -1.2f_c \end{pmatrix}$$

So $I_1 = -2.4f_c, \sqrt{J_2} = 0.69f_c$.

Substitute the two pairs of parameters into the failure function, solve for α and $\overline{\sigma}$ to get: $\alpha = 0.08$, and $\overline{\sigma} = (1 - \sqrt{3})f_c = 0.69f_c$

The uniaxial compression behavior is according to Popovics [128] as shown in Figure 5.5. Assume this data is from standard cylinder test. The characteristic length for this compression model is assumed 12 inch. This will be used in modeling softening of material, as introduced later in section 5.3.3 and section 5.3.4. The yielding stress is assumed 30% of peak compression strength. The uniaxial compression stress-strain relationship is expressed as [128]:

$$f = f_c(\frac{\varepsilon}{\varepsilon_0})\frac{n}{n - 1 + (\frac{\varepsilon}{\varepsilon_0})^n} \tag{5.3}$$

With $n = 0.4 \times 10^{-3} f_0 + 1.0$, $\varepsilon_0 = K \times 10^{-4} \sqrt[4]{f_0}$, f_c is compression strength of concrete, K is a parameters between 2.2$\sim$2.9.

Plasticity theory uses a hardening parameter (plastic modulus) H to describe the change of yield stress as a function of equivalent strain. The equivalent strain and strain increment is defined as :

$$\varepsilon_p = \sqrt{\frac{2}{3}\varepsilon_{ij}\varepsilon_{ij}} \tag{5.4a}$$

$$d\varepsilon_p = \sqrt{\frac{2}{3}d\varepsilon_{ij}d\varepsilon_{ij}} \tag{5.4b}$$

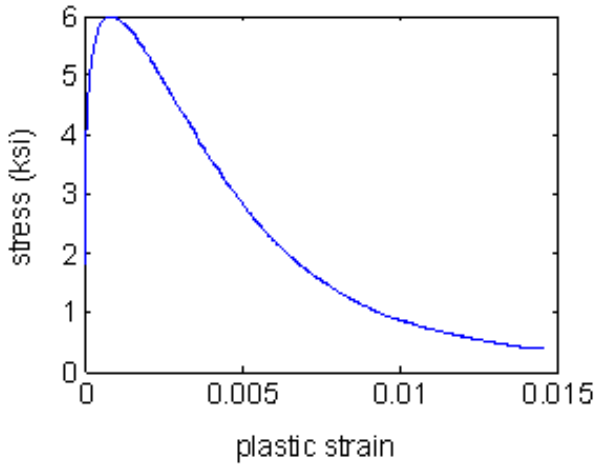

Figure 5.5: Uniaxial Compression Stress-strain Curve [128]

Assuming associate flow rule, the plastic strain is expressed as:

$$d\varepsilon_{ij}{}^{p} = d\lambda \frac{\partial f}{\partial \sigma_{ij}} \tag{5.5}$$

For linear Mohr-coulomb model:

$$\frac{\partial f}{\partial \sigma_{ij}} = \alpha \delta_{ij} + \frac{1}{2\sqrt{J_2}} S_{ij} \tag{5.6}$$

For the case of uniaxial compression:

$$S = \begin{pmatrix} \frac{f_c}{3} & 0 & 0 \\ 0 & \frac{f_c}{3} & 0 \\ 0 & 0 & \frac{-2f_c}{3} \end{pmatrix}$$

and

$$\frac{\partial f}{\partial \sigma} = \begin{pmatrix} \alpha + \frac{1}{2\sqrt{3}} & 0 & 0 \\ 0 & \alpha + \frac{1}{2\sqrt{3}} & 0 \\ 0 & 0 & \alpha - \frac{1}{\sqrt{3}} \end{pmatrix}$$

Substitute S and $\frac{\partial f}{\partial \sigma}$ into the plastic flow function to get:

$d\varepsilon_p = d\lambda\sqrt{2\alpha^2 + \frac{1}{3}}$ and $d{\varepsilon_{33}}^p = d\lambda(\alpha - \frac{1}{\sqrt{3}})$

From above two equations to get the relationship between equivalent plastic strain and uniaxial compression plastic strain as:

$$d\varepsilon_p = \frac{\sqrt{2\alpha^2 + \frac{1}{3}}}{\alpha - \frac{1}{\sqrt{3}}} d{\varepsilon_{33}}^p \tag{5.7}$$

with $\alpha = 0.08$, $d\varepsilon_p = -1.183 d{\varepsilon_{33}}^p$.

With uniaxial tension, uniaxial compression stress-strain relationship and biaxial compression strength as known input data, the relationship between equivalent plastic strain and uniaxial plastic strain is established as above, so as to the relationship between equivalent stress and equivalent strain. The equivalent stress-strain relationship will be used for calculation of plastic strain in the general multi-directional stress state.

5.3.3 Tension Cracking of Concrete

The concrete cracking properties used here are tensional strength f_t and fracture energy G_t. Concrete structures have relative small specimen size comparing with aggregate. Fracture of concrete shows tension softening behavior due to the interlock of aggregates along the cracking surface [75]. Figure 5.6 shows the nonlinear softening behavior and the linear softening models adopted in the FE analysis [1].

Softening modulus is a parameter for linear model of tensional softening, it is the slope in the stress-cracking strain curve. Cracking energy is the area under the curve of tensile stress-crack opening, the relationship between softening modulus and cracking energy density G_F

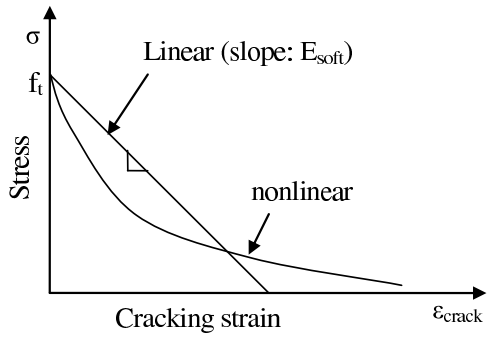

Figure 5.6: Concrete tension softening models

is:

$$G_F = \int \sigma \cdot dCOD = \int_0^{\varepsilon_{crack}} \sigma \cdot L_c \cdot d\varepsilon_{crack} \tag{5.8}$$

Where, COD is the cracking opening distance, it is the production of cracking strain ε_{crack} and the characteristic length L_c, which is assumed as a constant. Physically the cracking energy is the area under uniaxial stress-cracking opening curve, or the area of uniaxial stress-cracking strain curve multiplied by the characteristic length L_c. For linear softening model, the slope of stress-cracking strain curve E_{soft} is a constant, and the ultimate cracking strain $\varepsilon_{crackult}$ is f_t/E_{soft}, which ends with:

$$E_{soft} = \frac{1}{2} {f_t}^2 \cdot L_c/G_t \tag{5.9}$$

With f_t and G_t fixed as material properties, the softening modulus is dependent on L_c, which is related with element type and mesh size used.

5.3.4 Mesh Dependency of the Material Model

It has been recognized that material damage is a local behavior. The cracking energy density g, which is the area of stress-cracking strain curve under tension (denoted by g_t)

or stress-post peak plastic strain curve under compression (denoted by g_c), is dependent on a characteristic length of the material. The product of cracking energy density and the characteristic length is G_t or G_c, named cracking energy, which is recognized as material properties. The inclusion of characteristic length will lead to mesh dependency if same stress-strain curve is used for different mesh size. To overcome this problem, given G_t and G_c for concrete, the stress-cracking strain relationship is adjusted by assuming the characteristic length is the average element mesh size in bond zone. Same method is applied to adjust the uniaxial compression stress-plastic strain curve. However, the adjustment is only for post peak part, as localization only happens at post peak phase.

The softening modulus is the slope of stress-cracking strain curve. For same specimen, and same deformation, localization of cracking damage to one element will introduce mesh dependency, as in Figure 5.8. The strain for one element is half of the strain in one of the two element mesh (Figure 5.7). To simulate the same tensional cracking behavior, the softening modulus of two element mesh must be half of that in one element mesh, to obtain same stress. Several methods were proposed to define the characteric length Lc for different element type. they are related with Jocobian matrix or integration weight or element area [45, 116, 133]. For four nodes quadrilateral element, the strain field within the element is related with the relative displacement of the four nodes, it is assumed that Lc equals to mesh size. For Eight nods quadrilateral element, the strain field within each element is related with eight nodes, in other words, it is mostly decided by the adjacent two nodes closing to the integration point. So for eight nodes quadrilateral elements, Lc equals approximately to half of the mesh size. Figure 5.9 shows the consistent load-displacement responses after the tension softening modulus is adjusted with mesh size.

The post peak softening part of compression stress-strain curve implied the damage behavior of the material. The weak (damaged) part of the material will control the strength to meet the force equilibrium government equation. Previous work has stated the size dependency of the softening behavior. Furthermore, without adjusting for the size (mesh)

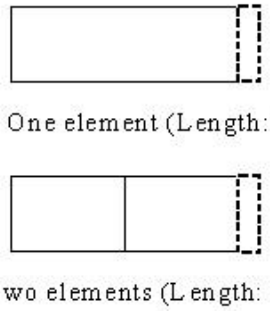

Figure 5.7: Relationship between Displacement and Strain after Softening

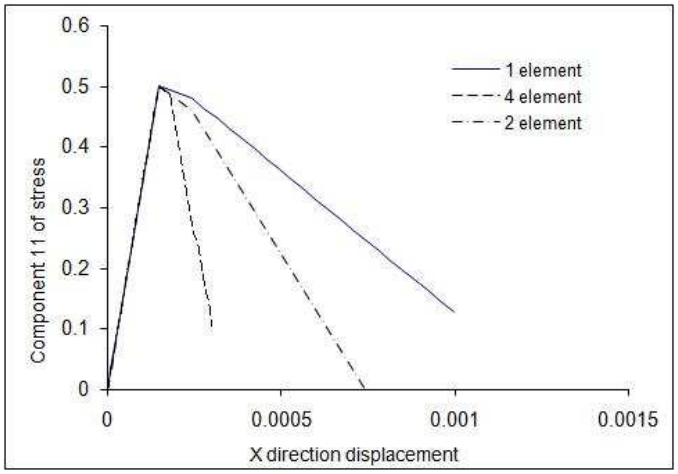

Figure 5.8: Mesh Dependency of Tension Cracking

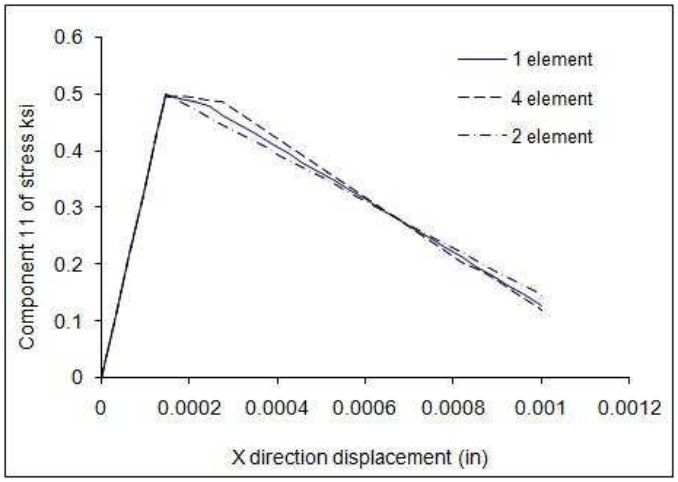

Figure 5.9: Mesh Independence after Adjusting Stress-strain Relationship

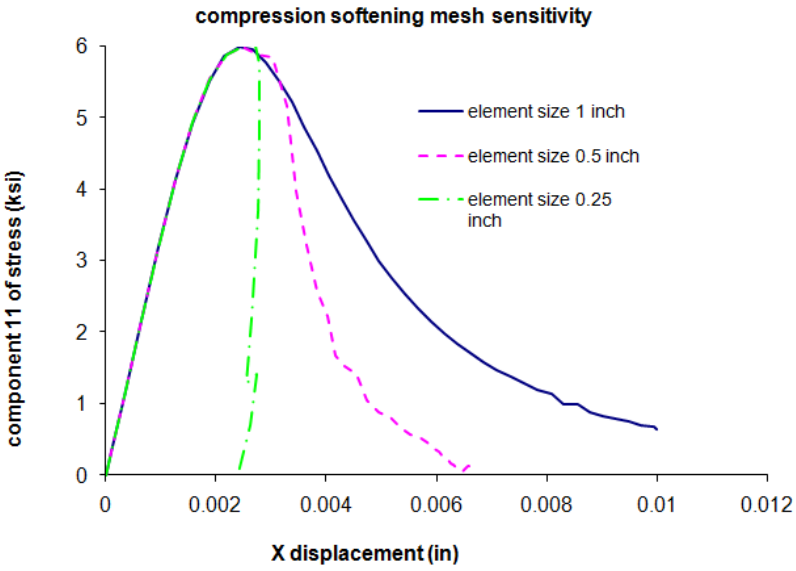

Figure 5.10: Compression Softening Mesh Sensitivity

dependency, the finer mesh used, the brittle will the structure becomes, since damage of one small element will lead to the failure of the whole structure. That is not coincident with the physical behavior of the structure. Therefore, in modeling the compression softening behavior of concrete, similar procedure as tension softening is adopted. The uniaxial stress-strain curve is adjusted according to mesh size by following equation:

$$\varepsilon_{adjusted} = (\varepsilon_t - \varepsilon_0)\frac{L_c}{meshsize} + \varepsilon_0 \tag{5.10}$$

$\varepsilon_{adjusted}$ is the adjusted total strain according to element mesh size. ε_t is the model total strain. ε_0 is model strain at peak compression stress. Lc is the characteristic length of 12 in. Figure 5.10 shows that mesh sensitivity of uniaxial compression behavior. Figure 5.11 shows the consistent responses after adjusting the compression softening modulus with mesh size. Figure 5.12 is bi-axial compression responses after considering the mesh sensitivity.

Shear retention factor is the ratio of reduced shear stiffness vs. the original untracked

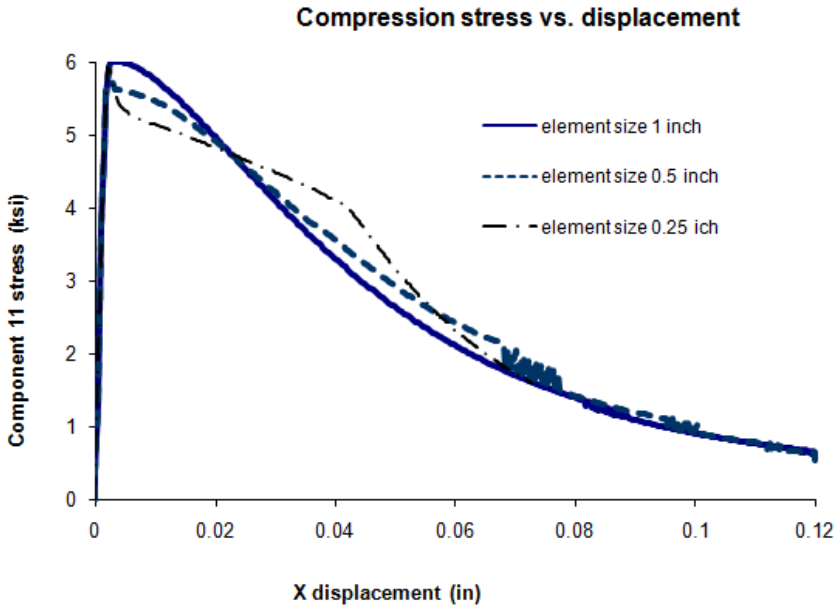

Figure 5.11: Mesh Independence after Adjusting Stress-strain Relationship

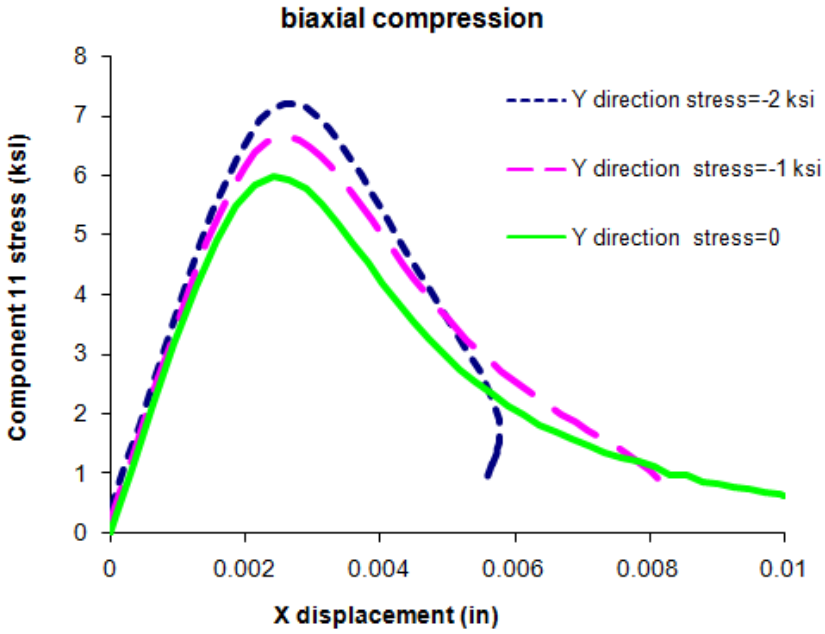

Figure 5.12: Biaxial Compression for Unit Element

shear stiffness along the cracked plane. In this application, shear retention factor is assumed as a constant small number.

5.3.5 Finite Element Implementation of Plasticity and Cracking

Formulation of nonlinear constitutive model including compression plasticity and tension cracking. The incremental stress strain relationship is:

$$\dot{\sigma} = C\dot{\varepsilon_e} = C(\dot{\varepsilon} - \dot{\varepsilon_c} - \dot{\varepsilon_p}) \tag{5.11}$$

where C is elastic properties. The cracking strain increment is a function a current cracking strain, current stress and current stress increment:

$$\dot{\varepsilon_c} = f_t(\varepsilon_c, \sigma, \dot{\sigma}) \tag{5.12}$$

The plastic strain increment is proportional to the stress space tangential of the yield surface as:

$$\dot{\varepsilon_p} = \dot{\gamma}\frac{\partial\overline{\sigma}}{\partial\sigma} \tag{5.13}$$

Where $\overline{\sigma}$ is yielding criteria function, and γ is a scalar to quantify the magnitude of the plastic strain increment. The yielding of material is decided by the yielding function of current stress state as:

$$f(\sigma) = \overline{\sigma} \tag{5.14}$$

And the yielding criteria as a function of the scalar γ is assumed as known condition and can be derived from uniaxial and biaxial test data, as the compression plasticity in section 5.3.2.

γ is also named as equivalent plastic strain and $\overline{\sigma}$ named as equivalent stress.

$$\overline{\sigma} = f(\gamma) \tag{5.15}$$

From:

$$d\overline{\sigma} = \frac{\partial \overline{\sigma}}{\partial \sigma}\dot{\sigma} = \frac{\partial \overline{\sigma}}{\partial \gamma}\partial\dot{\gamma} \tag{5.16}$$

$$\tag{5.17}$$

Following equations can be derived:

$$\frac{\partial f(\sigma)}{\partial \sigma} C(\dot{\varepsilon} - \dot{\varepsilon_c} - \dot{\gamma}\frac{\partial f(\sigma)}{\partial \sigma}) = \frac{\partial \overline{\sigma}}{\partial \gamma}\dot{\gamma} \tag{5.18}$$

$$\dot{\varepsilon_p} = \frac{\frac{\partial f(\sigma)}{\partial \sigma} C(\dot{\varepsilon} - \dot{\varepsilon_c})\frac{\partial f(\sigma)}{\partial \sigma}}{\frac{\partial f(\sigma)}{\partial \sigma} C \frac{\partial f(\sigma)}{\partial \sigma} + \frac{\partial \overline{\sigma}}{\partial \gamma}} \tag{5.19}$$

Equation 5.19 is the incremental stress-strain relationship for concrete model including tensional softening and compression plastic hardening and softening. For given stress strain state and incremental strain, iteration procedure is needed to calculate the incremental cracking strain and plastic strain to satisfy both cracking softening function and yielding function.

5.3.6 Strain Formulation

The complexity of compression softening lies in not only the mesh size dependency, but also the sensitivity of the solution procedure to the adjustment of material properties. Cracking damage energy is assumed as a material property which is the area under the stress-displacement curve. To obtain same stress-displacement curve from different mesh sizes, the equivalent stress-strain curve is adjusted with mesh size as introduced in section 5.3.4.

Before peak stress behavior is mesh independent, the adjustment is not needed. The post peak part is adjusted as same engineering stress, different strain induced by same displacement requirement. Because the large strain from small mesh size will induce the stress measurement problem, the engineering stress is assumed same at each displacement point. This assumption basically guaranteed that the same load-displacement curve for uniaxial test data is followed.

Due to the small element size used, strain formulation is another consideration in adjusting the material properties with mesh size. When small mesh size is used, the strain is no longer small strain to achieve same cracking or post peak yielding displacement. To simulate the post peak damage behavior using current model, physical phenomenon is that the strain for the localized small element is large strain. However, by appropriately adjusting the stress-strain curve, this problem can also be avoided. Assuming the uniaxial compression model in Figure 5.5 is engineering stress vs. engineering strain (small strain formulation), the true stress vs. logarithmic strain (true strain) relationship can be derived.

Engineering strain:

$$\varepsilon_E = \frac{L_n - L_0}{L_0} \tag{5.20}$$

Logarithmic strain:

$$\varepsilon_l = ln(\frac{L_n}{L_0}) \tag{5.21}$$

Cauchy strain:

$$\varepsilon_g = \frac{L_n^2 - L_0^2}{2L_0^2} \tag{5.22}$$

relationship between true cross section area and original cross section area:

At length l, transverse strain increment:

$$\frac{dl}{l}\nu = -\frac{db}{b} \tag{5.23}$$

where, l is current length, b is current width, ν is Poisson ratio. integrate from original length to current length l_n,

$$\int_L^{l_n} \frac{dl}{l}\nu = \int_B^{b_n} -\frac{db}{b} \tag{5.24}$$

$$ln(\frac{l_n}{L}\nu) = -ln(\frac{b_n}{B}) \tag{5.25}$$

$$\frac{B}{b_n} = (\frac{l_n}{L})^{\nu} \tag{5.26}$$

so:

$$\frac{A}{A_0} = \frac{b_n^2}{B^2} = (\frac{L}{l_n})^{2\nu} = (1+\varepsilon_E)^{-2\nu} \tag{5.27}$$

Engineering stress:

$$\sigma_E = \frac{P}{A_0} \tag{5.28}$$

Cauchy stress (true stress):

$$\sigma = \frac{P}{A} = \frac{P}{A_0(1+\varepsilon_E)^{-2\nu}} = \sigma_E(1+\varepsilon_E)^{2\nu} \tag{5.29}$$

Second Piola-Kirchhoff stress: S, relationship with Cauchy stress:

$$S = JF^{-1}\sigma F^{-T} \tag{5.30}$$

For elastic behavior, using Hooks law, under uniaxial loading: $\vec{u} = \begin{Bmatrix} u_x \\ u_y \\ u_z \end{Bmatrix}$ and $\varepsilon_x = \varepsilon_E = \frac{\partial u_x}{\partial x}$

F is deformation gradient, $F = \frac{\partial \vec{x}}{\partial \vec{X}}$, J is determinant of F, so,

$$F = \begin{bmatrix} 1+\varepsilon_E & 0 & 0 \\ 0 & 1-\nu\varepsilon_E & \\ 0 & 0 & 1-\nu\varepsilon_E \end{bmatrix} \tag{5.31}$$

$$\sigma = \begin{bmatrix} \sigma_E(1+\varepsilon_E)^{2\nu} & 0 & 0 \\ 0 & 0 & 0 \\ 0 & 0 & 0 \end{bmatrix} \tag{5.32}$$

$$S = \begin{bmatrix} \sigma_E(1-\nu\varepsilon_E)^2(1+\varepsilon_E)^{2\nu-1} & 0 & 0 \\ 0 & 0 & 0 \\ 0 & 0 & 0 \end{bmatrix} \tag{5.33}$$

Thus the relationship between different stress definition and different strain definitions are established. For large strain with total Lagrangian formulation, the elastic modulus represents the initial second Piola-Kirchhoff stress and Green-Lagrange strain, the stress strain relationship. For small strain formulation, young's modulus is the initial slope of engineering stress strain curve. When using material properties consistent with strain formulation, the results are same, as shown in Figure 5.13.

5.3.7 Limitation of the Material Model

The concrete material model used has described the bond behavior with great accuracy. However, certain limitations exist for the finite element simulation, especially the concrete material model. First, currently the tensional softening is modeled with linear softening,

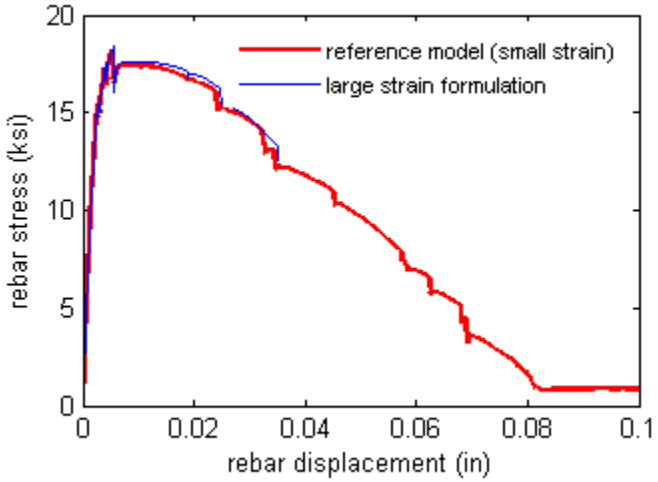

Figure 5.13: Solution using large strain formulation and small strain formulation

which is different from the real nonlinear softening behavior. This limitation is not difficult to overcome by applying the nonlinear softening function.

Another major limitation is the conflict between localization of damage and fine mesh finite element formulation. When using very small element size, compression softening is very hard to happen because it is not possible to achieve certain post peak displacement when element size is very small. On tension side, the cracking follows certain narrow element line, which is not consistent with the smeared crack concept. The physical behavior is not displayed correctly. As concrete has zigzag crack instead of a narrow discrete crack.

Finally, other limitation lies on the mesh size dependency. Although material model is adjusted by element size, the method of computing the characteristic length for each element is hard to be objective. Currently the characteristic length is assumed as element size. There are also other methods on how to compute the characteristic length as stated in section 5.3.4. Possible solutions for above limitations are application of nonlocal model, or higher order gradient method.

5.4 Solution Procedures

From material aspect, the reference rib-scale model is a highly nonlinear model describing the cracking and post peak residual bond strength. The solution procedure for this model is critical to get converged post peak softening response. Material softening is a localized phenomenon. Mathematically, there is no unique solution for the softening stage if the softening is not pre-defined by initiating at a specific location. Multiple path of failure exist [43, 44, 79, 95]. In traditional Newton-Raphson solution of the nonlinear equations, examination of full stiffness matrix shows that the stiffness matrix is not longer positive definite, which means stress strain increment may have different signs. Several factors have contributed to deal with this problem:

First, in models with multiple elements, results show that the numerical rounding error will always lead to one point reaches the softening damage first. This numerical rounding error exactly represent the random material properties that failure will happen at a random location.

Second, localization of damage happens at only one element, contribution from other adjacent elements will improve the positive definite property of the stiffness matrix [95].

Third, by using displacement control instead of load control, the rank of stiffness matrix is reduced, such that the rank reduced stiffness matrix will be positive definite. Experiments with load control and arc-length method show that arc-length method has limited improvement on convergence and show unexpected unloading.

Finally, at residual load stage, the number of softening element increases, which leads to the non-positive stiffness matrix eventually. This is further overcome by adding damping properties to the system matrix to improve the convergence.

5.5 Results of Preliminary Models-Model Validation

The proposed contact model is both geometrically and materially nonlinear. Geometric nonlinearity lies in the contact detection between concrete and reinforcing bar ribs. To

validate the bond model using contact analysis, a series of preliminary models are tested. The models are all two-dimensional with different concrete properties. The four different models are:

linear elastic model

tension elastic and compression plastic model

tension softening and compression elastic model

tension softening and compression plastic model

Figure 5.14 shows the load-displacement response for above four models. With linear elastic model strongest, and model considering both tension cracking and compression plasticity weakest, the proposed model give reasonable representation of different material properties.

In analyzing the stress state in elastic analysis, initiation of cracking or yielding in bond zone can be captured, as in Figure 5.15, which shows stress state for linear elastic analysis of the contact model. The potential cracking direction is perpendicular to maximum principle stress or parallel with minimum principle stress. Figure 5.15 shows the potential initial secondary cracking in direction of 45 degree to bar axis, at up front of rib.

In the model with tension cracking only, the radial displacement is very large due to the longitudinal splitting, as shown in Figure 5.16. In contrast, model with compression yielding only shows pull-through behavior due to yielding of concrete in front of ribs, no significant radial displacement observed, as in Figure 5.17. The concrete at the bar surface has large shear deformation. Finally, Figure 5.18 shows the bond response with model considering both tension cracking and compression yielding, which is the combination of radial splitting and concrete yielding in front of ribs. The preliminary models present a clue for bond mechanism, such as the sources where the splitting comes from and where the pull-through comes from.

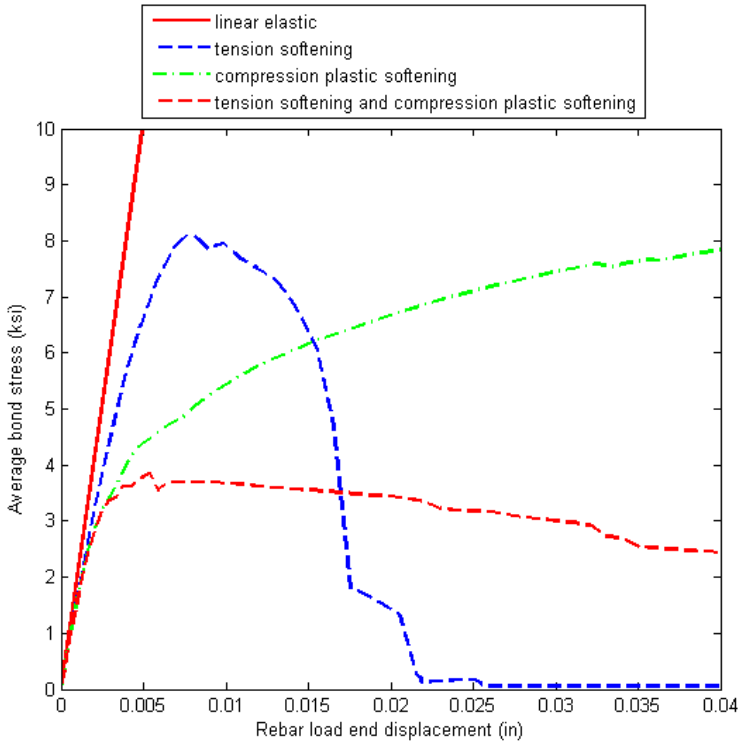

Figure 5.14: Bond Stress vs Bar End Displacement for Different Material Models

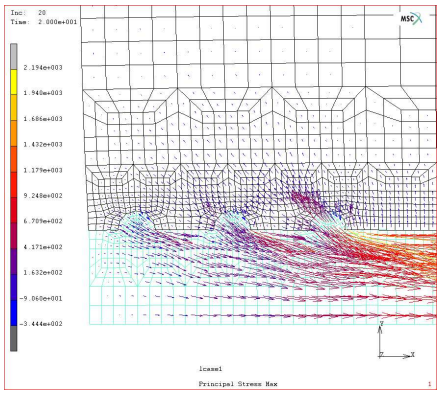

(a) Maximum Principal Stress

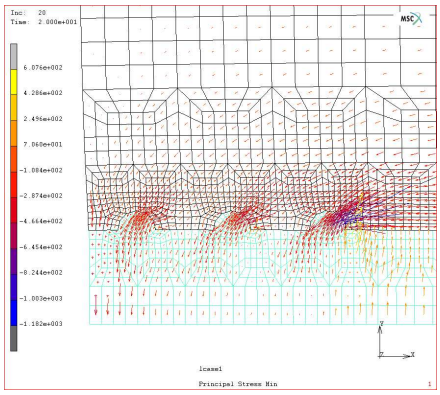

(b) Minimum Principal Stress

Figure 5.15: Linear Elastic Model Principal Stress

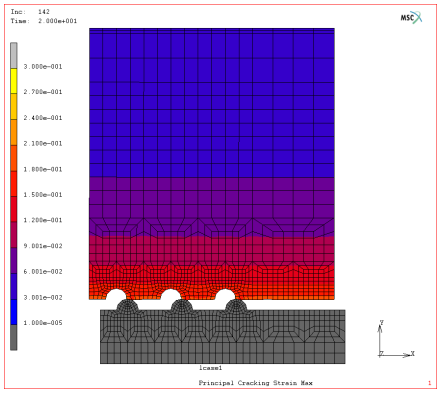

Figure 5.16: Maximum Cracking Strain from Model with Tension Softening

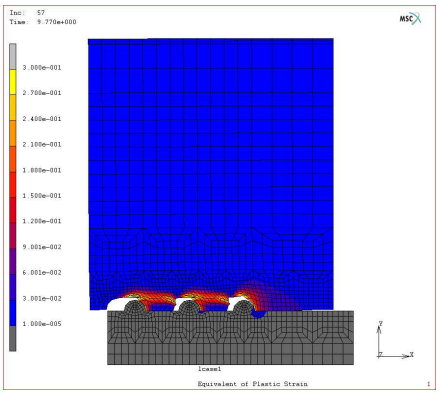

Figure 5.17: Equivalent Plastic Strain from Model with Compression Hardening and Softening Only

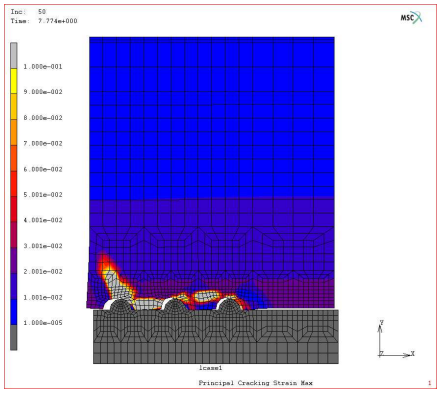

(a) Maximum Cracking Strain

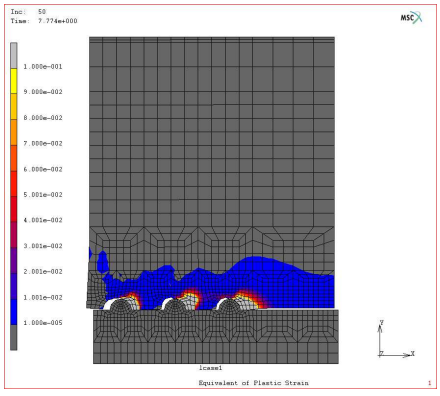

(b) Equivalent Plastic Strain

Figure 5.18: Cracking and Plastic strain for Tension and Compression Softening Models

5.6 Contact Model Validation-Parametric Study

In this section, a series of sensitivity analysis are conducted to prove the robustness of the solution and the basic factors affecting the bond behavior. The parameters considered affecting the nonlinear results are mesh sensitivity and numerical criteria sensitivity. The parameters possibly affecting bond behaviors are concrete material properties, numerical procedures, geometric mesh sizes and confinement pressure.

Figure 5.19 shows mesh sensitivity of the finite element model. Under three different mesh sizes, results show same initial response, comparable bond peak strength. However, the post peak responses are dramatically different. This is due to the 2D axisymmetric model used. In axisymmetric model with isotropic material properties, splitting cracking is smeared over the perimeter in hoop direction. Thus the element size in hoop direction is far larger than that from in-plane direction along the bar axis. Possible solutions are use of orthotropic material models to separate the cracking properties in in-plane direction and hoop direction, or use of full 3D models. As concrete material is often modeled isotropically and 2D model will exhibit same other properties with full 3D models except the additional hoop confinement, isotropic material properties are used with 2D axisymmetric models in following parametric study. Figure 5.20 shows the sensitivity of the load-displacement response to softening modulus. This was computed using reference model with medium mesh size with softening modulus differed by 10 times. The post peak behaviors are very different from each other. The larger the softening modulus, which means the smaller the cracking energy, the more brittle of the bond response. Figure 5.21 shows the analyzed load-displacement responses without adjusting softening modulus according to mesh sizes. Results are different at peak and beginning part of post peak response, which shows the mesh sensitivity if no adjustment of softening modulus is applied. However, consistent results are found at the residual part of the responses. This confirms that internal radial cracking happens before the longitudinal splitting since internal bond-zone mesh sizes are different, which leads to the different performance near peak response zone. The final failure

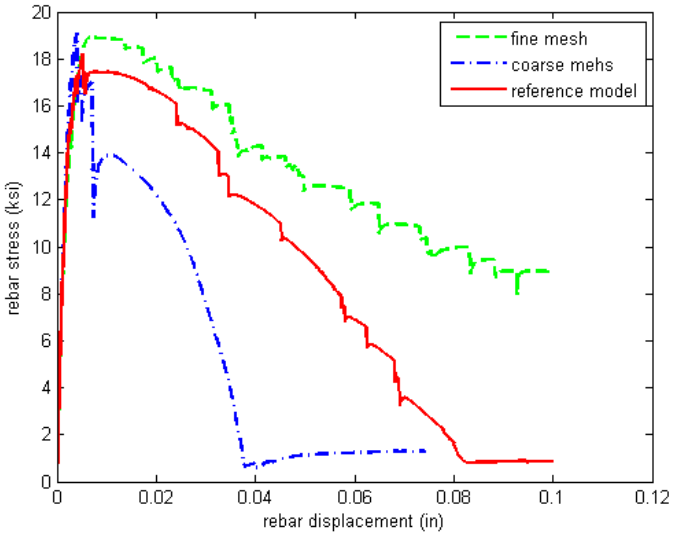

Figure 5.19: Bond Stress vs. Bar End Displacement for Different Mesh Sizes

of this pull-out analysis is due to longitudinal splitting, which is in hoop direction and is independent of the mesh size, leading to the consistent residual responses.

Modeling of softening may rely on the numerical procedures in getting the correct solutions. During softening, when part of elements go to softening stage, other elements will be unloaded to obtain the system balance of forces. To evaluate the sensitivity of the model to numerical solution procedures, different load steps and convergence criteria are used to check the robustness of the model. The sensitivity of results to load step and convergence criteria are tested as shown in Figure 5.22 and Figure 5.23. The figures show consistent load-displacement response under different load steps and convergence criteria.

Test results show that confinement has important influence on bond behavior. Several critical confinement conditions are applied to the contact model. The first confinement is passive steel hoop confinement. The second confinement condition is constraint of radial displacement on the outside the specimen, no radial displacement to constrain the dilation of the cylinder. The third confinement condition is active pressure of 5 ksi. The active pressure is large enough to contract the cylinder. Figure 5.24 shows the influence of confinement on

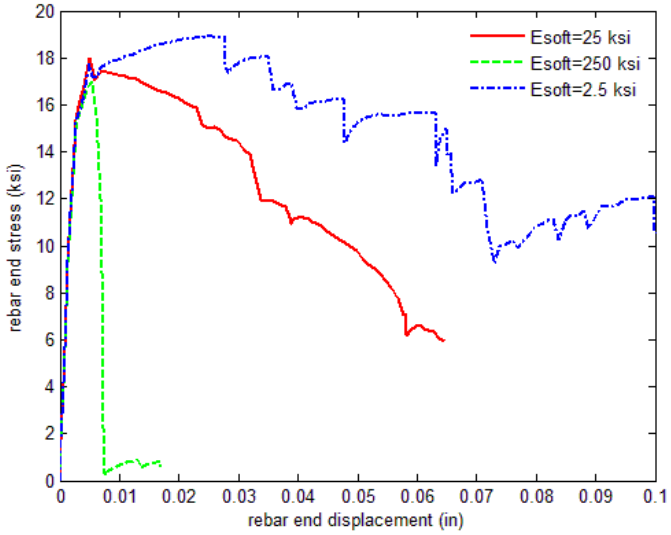

Figure 5.20: Bond Stress vs. Bar End Displacement with Same Medium Mesh Size but Different Softening Modulus

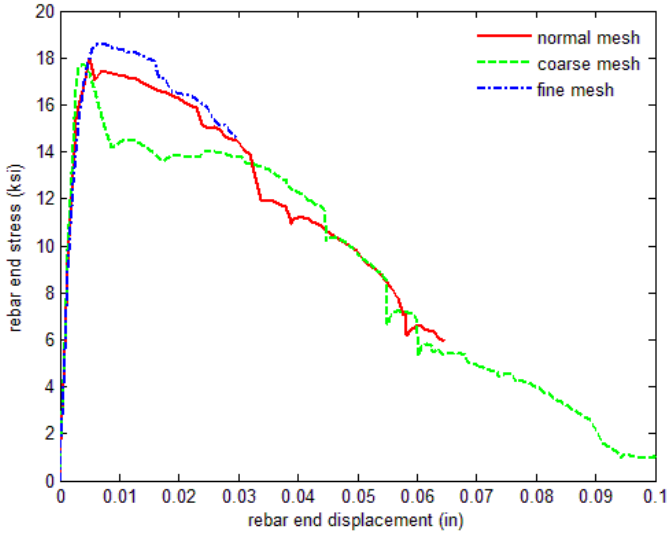

Figure 5.21: Bond Stress vs. Bar End Displacement with Different Mesh Sizes but Same Softening Modulus

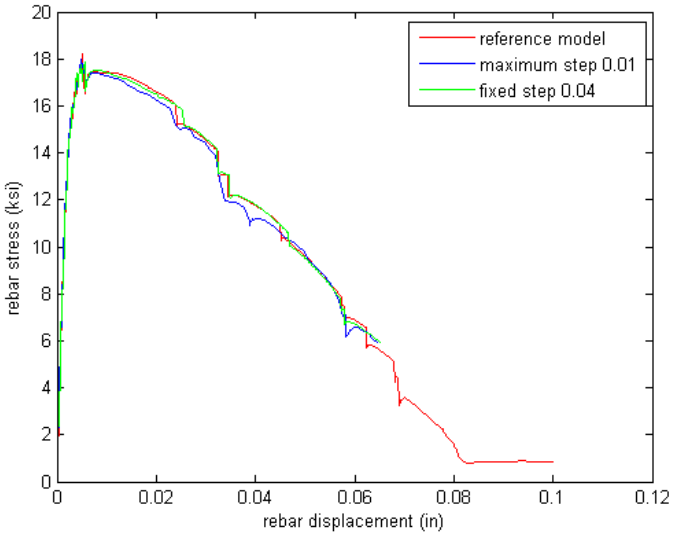

Figure 5.22: Bond Stress vs. Bar End Displacement under Different Load Steps

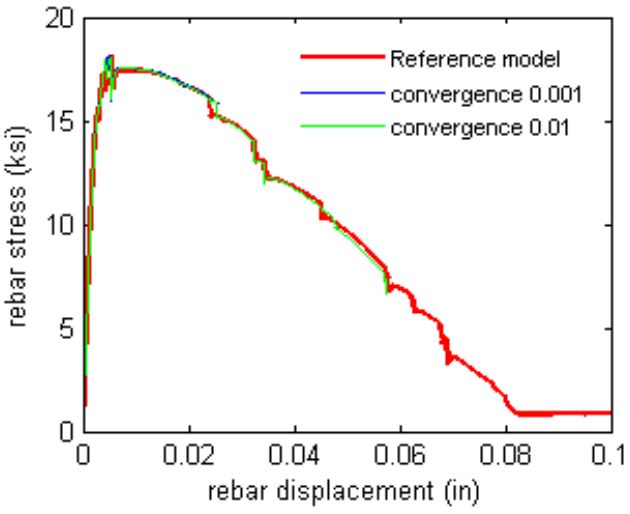

Figure 5.23: Bond Stress vs. Bar End Displacement under Different Convergence Criteria

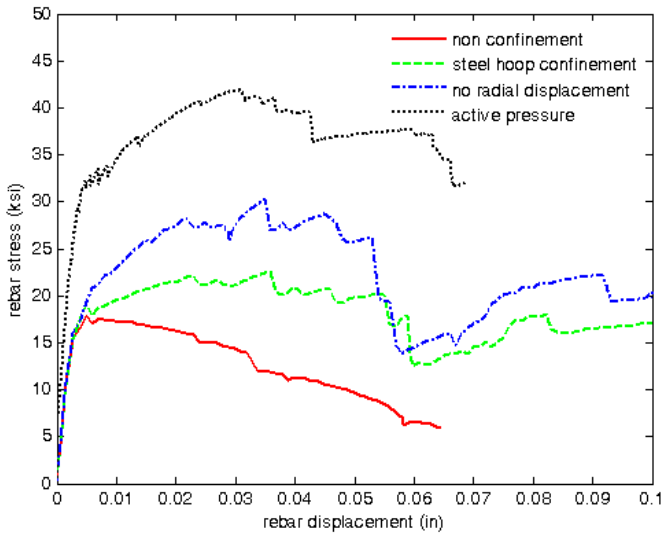

Figure 5.24: Bond Stress vs. Bar End Displacement under Different Confinement Levels

bond response. The higher the confinement, the larger the bond peak strength and post peak residual strength. Except condition of active pressure, passive confinement and lower active confinement do not have significant influence on initial bond stiffness. High active confinement pressure that leads to contraction of concrete cylinder increases the initial bond stiffness. On influence of concrete strength to bond, experimental results show bond strength is proportional to square root of concrete compressive strength [50, 73]. Analysis with different compression strength and tension strength show consistent results, both tension and compression strength of concrete have positive impact to bond strength. The larger the compressive strength, the large the peak bond stress, as in Figure 5.25 and Figure 5.26, the peak bond stress is proportional to square root of concrete compressive strength and tensional strength.

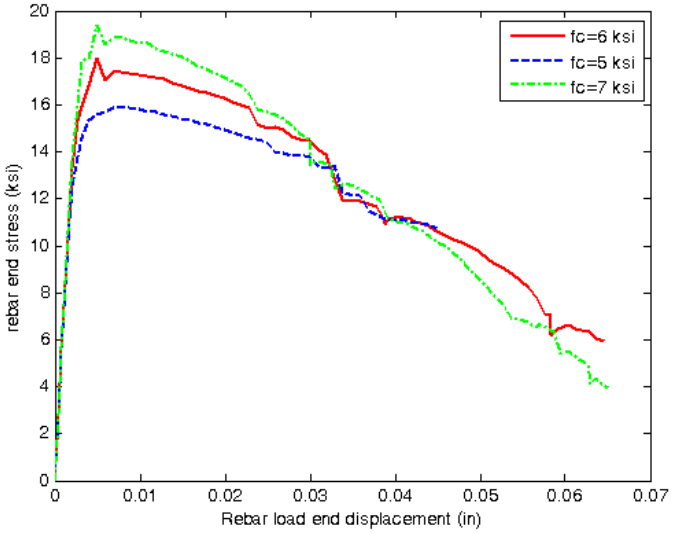

Figure 5.25: Bond Stress vs. Bar End Displacement for Different Compression Strength of Concrete

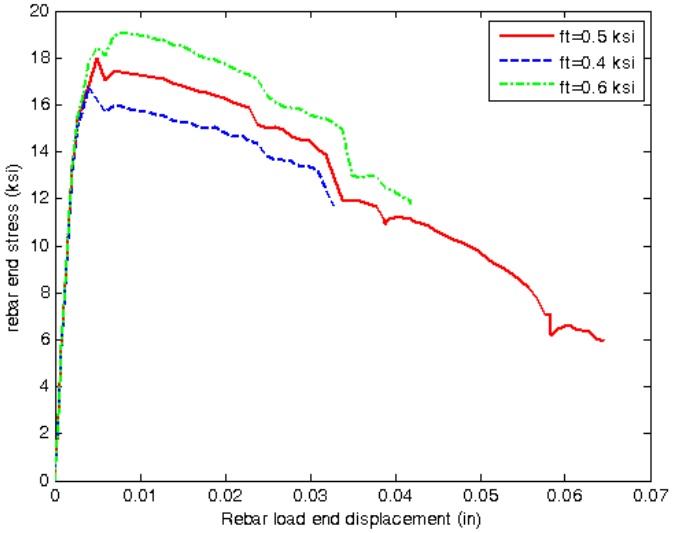

Figure 5.26: Bond Stress vs. Bar End Displacement for Different Tension Strength of Concrete

5.7 Comprehensive Study of Different Bond Interface Models

5.7.1 Introduction

To evaluate the impact of different modeling procedures, a series of models including different interface representations are studied. The different models are categorized as rib-scale models and bar-scale models. For each category, different interface modeling procedures are used. All models include 2D axisymmetric implementation and full 3D implementation. Although 2D axisymmetric model has defects of smearing the longitudinal cracks, it has very good behavior under pre-peak load, which is the load stage that secondary cracks exist. Thus the main goal of including 2D models is to evaluate internal cracking for different bond interface modeling procedures.

For rib-scale model, the rib geometry is the same as the reference contact model, three interface conditions between concrete and ribs are assumed (Figure 5.27) including full displacement compatibility between concrete and steel nodes except lead length; partial displacement compatibility, with only nodes shared by rib and concrete having displacement compatibility; compression side displacement compatibility, with only nodes that in compression side of the rib having displacement compatibility with concrete.

Modeling ribs is computationally demanding as the level of mesh refinement to represent ribs. Modeling bond in rib-scale may not be practical when modeling reinforced concrete structures. In reinforced concrete (RC) structural models, reinforcing bar is often modeled with truss element or solid continuum steel element, with or without interface element between concrete and steel. A number of publications have presented models with bond interface elements, while others concluded that it is not necessary to use interface elements [134]. Here the models without bond interface elements and rib geometries are investigated. The bond failure is represented by the bond zone concrete material failure. The different no rib bar-scale models are summarized in Figure 5.28. Table 5.1 summarizes all models and unique properties for each model.

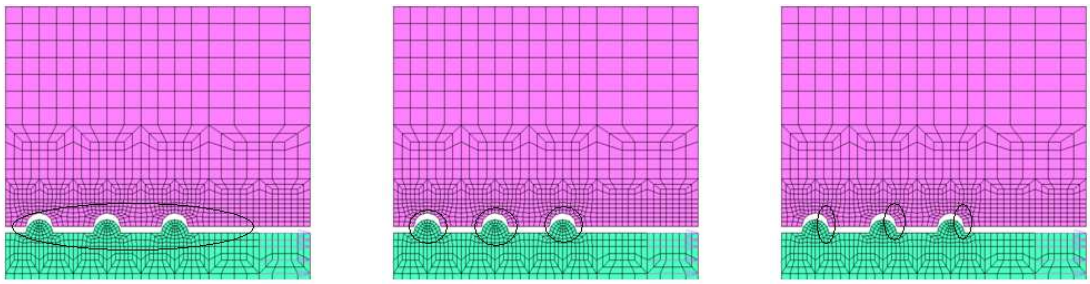

(a) Full Displacement Compatibility

(b) Rib Displacement Compatibility

(c) Compression Side Rib Displacement Compatibility

Figure 5.27: Displacement Compatibility Cases for Non-contact Rib Scale Model

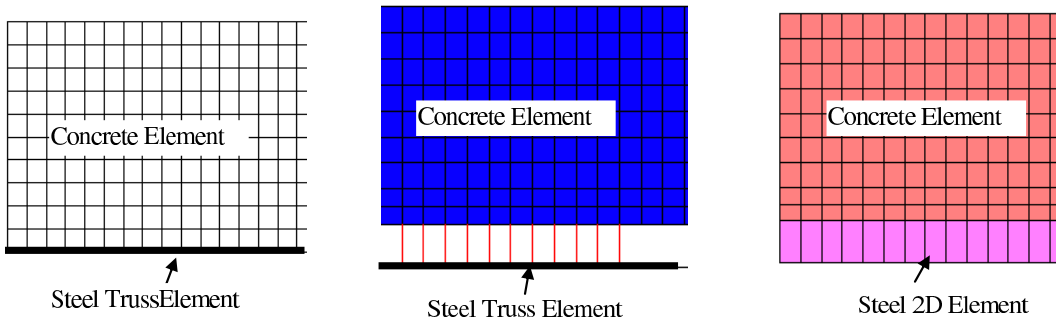

Figure 5.28: (a): Attached Truss Model (b): Detached Truss Model (c): Solid Steel Model Formulation of No-rib Bar-scale Models

5.7.2 Two-dimensional Axisymmetric Modeling

Two-dimensional axisymmetric modeling is computationally efficient and show reasonable behavior in describing the local cracking and crushing near bond-zone as presented in previous sections. The comparisons among different FE bond models with 2D analysis results were made on global response as well as local bond zone cracking and crushing.

Figure 5.29 shows the analyzed average bond strength vs. displacement response for the four rib-scale models. The average bond stress is computed as bar end load divided by bonding area, which is calculated as product of bar perimeter and bar embedded length. Direct contact model predicts smallest bond strength (peak average bond stress) value of

Table 5.1: Finite Element Models for Analyzing Bond-zone

Model category	Model Name	Properties
Model with rib (rib scale modeling)	Contact model	Direct contact between concrete and rib
	Discomp1	Bar and concrete share nodes, full displacement compatibility
	Discomp2	Only rib and concrete share nodes
	Discomp3	only compression side of rib share nodes with concrete
Model without rib (bar scale modeling)	Attached truss	Truss elements share nodes with concrete elements
	Detached truss	Truss elements separate from concrete, with nodal displacement restrain
	Solid steel	3D rebar element share nodes with concrete elements

3 ksi, friction contact model predicts bond strength of 3.5 ksi, model Discomp3 predicts bond strength of 3.7 ksi, model Discomp3 predicts bond strength of 4 ksi, and model Discomp3 (displacement compatibility model) predicts highest bond strength of 4.3 ksi. It is understood that with tension softening presented, the residual tension capacity has contributed to the increasing of bond strength as more displacement compatibility is applied. This can also be seen from the closeness of results between direct contact model and compression side rib displacement compatibility model. From Figure 5.29, the higher the bond strength, the more rapidly the post-peak bond strength drops. The area under the bond stress-displacement curve is tending to be constant, which reflect that the dissipated damage energy is constant.

From previous research on rib-scale models, bond zone damage is reflected by bond zone concrete cracking or yielding and ignoring the friction slip, since bond zone damage happens as concrete damage. Is it reasonable to model the bond mechanical interaction by bar-scale models with displacement compatibility? As shown in Table 5.1, three bar-scale models were evaluated using a full length bond specimen. Figure 5.30 shows the analyzed load displacement response for the three bar-scale models. All the load displacement responses

show typical characteristics of bond response: initial linear stage, nonlinear before peak stage and post peak descending stage. However, all three bar-scale models show smaller bond strength than the reference contact model. Detached truss model and 2D solid steel model show almost same load-displacement response with peak bond strength of 2.4 ksi; Attached truss model has much smaller bond strength with peak bond strength of 1.2 ksi. The contact model predicts peak bond strength of 2.7 ksi. The difference between direct contact model and Attached truss are more than 100%.

As shown in the following sections, all models show splitting behavior, which are consistent with test results. However, the performance of secondary cracking is different between rib-scale models and bar-scale models. Rib-scale models show the secondary cracking inclined to bar axis. In bar-scale models, without explicit representation of ribs, the secondary cracking is smeared in the shear deformed concrete elements. The bar-scale models didn't show cracking associated with bar ribs. The presentation of these bond damages for all models are as follows and they are corresponding to three critical load stages: initial loading, just before peak bond strength and post peak descending stage.

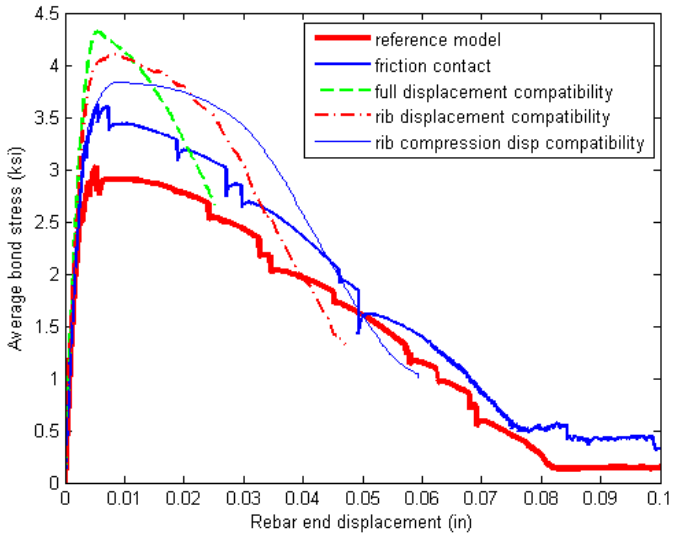

Figure 5.29: Bond Stress vs. Bar Displacement for 2D Models with Ribs

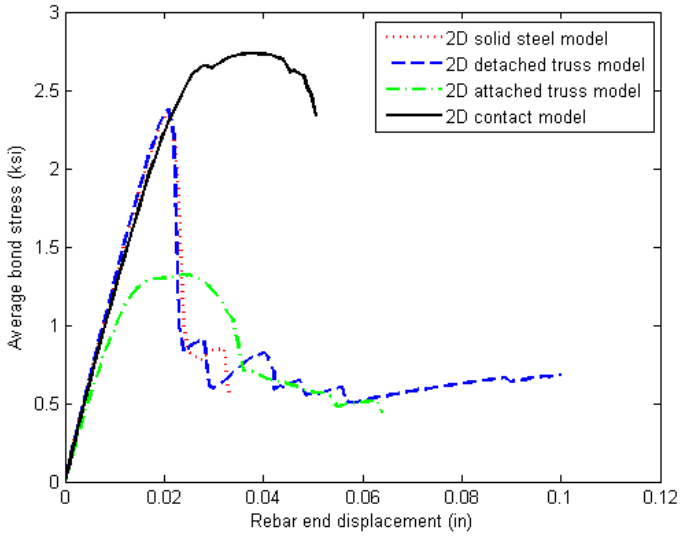

Figure 5.30: Bond Stress vs. Bar Displacement for 2D Models without Ribs

5.7.2.1 Contact Model

In contact model, the displacement compatibility between concrete and steel was not used. The interaction between concrete and steel is through the interaction of ribs with surrounding concrete. If friction is ignored, the full contact model simulate directly the bearing pressure between ribs and concrete when they are in contact. Figure 5.32∼Figure 5.34 present the strain propagations in local bond-zone.

The in-plane secondary cracking initiates and propagates from load end to the free end with angle of about 45 degree to the bar axis. This can be seen from the plots of maximum and minimum principal stress as in Figure 5.32(f) and Figure 5.32(g). The compression zone of concrete in front of ribs yielded and the yielding also propagated from load end to free end. This is same with previous analysis results and laboratory observations [73]. Before reaching peak bond strength, the propagation of longitudinal cracking was also observed. At post peak stage, longitudinal cracking propagate all through the specimen and compression

yielding propagates through more areas near bond zone. However, secondary cracks stay in local zones without further propagation to outer surface of the concrete cylinder but have changed directions as further development of bond-zone damage. The direction of principal cracking strain is changed to almost vertical to the bar axis, which means the longitudinal cracking plane separating concrete from the bar surface.

5.7.2.2 Dispcomp 1 (Full Displacement Compatibility between Concrete and Steel)

Figure 5.35∼Figure 5.37 presents analysis results for model Dispcomp1, with rib-scale model but full displacement compatibility between bar and concrete in bonded region.

At initial stage, the internal secondary cracking was observed from Figure 5.35(a) and 5.35(b). This initial cracking is in-plane as can be seen the x and y in-plane components from Figure 5.35(c)∼5.35(e). Figure 5.35(f) and 5.35(g) show the maximum and minimum principal stress which clearly shows the cracking direction is about 45 degree along the horizontal x axis. From the magnitude of cracking strain, the maximum cracking strain is larger at ribs closer to load end. The internal cracking propagates from ribs near load end to ribs closer to free end in this pull-out test. At compression side, the compression yielding around the rib zone has not been activated due to the full displacement compatibility. The only yielding location is where the embedded bond length begins (see Figure 5.35(h)).

After initial stage of loading, the global load-displacement response goes from linear stage to nonlinear stage. This is contributed from further secondary cracking and most important, the longitudinal cracking propagating from inside to outside of the specimen, as can be seen from Figure 5.36. The longitudinal cracking is induced by the hoop strain as shown in Figure 5.35(e).

After the peak strength, at the descending part of load-displacement response, longitudinal splitting continue to propagate, the secondary cracking has changed direction from 45 degree to horizontal, as shown in Figure 5.37(a) the vertical cracking strain. At final stage, the concrete is separated away from the bar and longitudinal cracking happened. Due to

the displacement compatibility, the separation of concrete and bar (loss of bond) is due to local secondary cracking and splitting of concrete.

5.7.2.3 Dispcomp 2 (Rib Displacement Compatibility between Concrete and Steel)

Figure 5.38∼Figure 5.40 presents analysis results for model Dispcomp2, with rib-scale model but only displacement compatibility between ribs and concrete.

This model applies displacement compatibility only on ribs and shared node concrete, no sharing nodes between rib zone. At initial loading, the cracking only happens at ribs, and the cracking is due to separation of rib with concrete at tension side. This is different from our understanding that the internal cracking is due to lug wedge shear effect. At compression side, compression yielding of concrete happens at the first rib. The cracking and yielding both propagate from load end to free end of the specimen.

As load increases, the bond response also goes from linear to nonlinear, and the behavior goes closer to model Dispcomp1, full displacement compatibility. The post peak strength shows similar behavior with full displacement compatibility. Due to the separation of nodes at location between ribs, separation between concrete and steel is desirable behavior, but penetration of the two bodies in radial direction is not the physical bond behavior.

5.7.2.4 Dispcomp 3 (Compression Side Rib Displacement Compatibility)

Figure 5.41∼Figure 5.43 presents analysis results for model Dispcomp3, with rib-scale model but only displacement compatibility between compression side of ribs and adjacent concrete.

This model applies displacement compatibility only on compression sides of ribs. It assumes that concrete and steel are separate except where the ribs compress against the concrete. This model ignores chemical adhesion and friction on other parts of bond zone. At initial loading, the in-plane cracking is initiated in the upper front of ribs, which are different from models Discomp1 and Discomp2. Progression of longitudinal cracking is similar to previous models. Longitudinal cracking is initiated from concrete steel interface

toward the outer surface. At before peak bond strength stage, the response is nonlinear with that the longitudinal cracking is extensive but not extending through the whole specimen. At post peak stage, the whole specimen is split. The model still shows the shear-through behavior near bond zone, as shown in Figure 5.43, but not as localized as previous two models.

5.7.2.5 Attached Truss Model

Figure 5.44∼Figure 5.47 presents analyzed results for model Attached truss, with truss element representing the bar, without modeling of rib geometry.

Attached truss model has shared nodes between truss elements and adjacent 2D concrete elements. Figure 5.44 shows the initial cracking for this model. Half of the truss near load end is separate from concrete to represent the de-bonding lead part. The initial cracking is from the first attached element near load end. The cracking direction is around 45 degree to the bar axis. Figure 5.44(f) and 5.44(f) show the maximum and minimum principal stresses. Although ribs are not specifically modeled, the hoop stress can still be developed by the concrete element in bar-scale model.

Figure 5.45 shows the cracking progress from load end to free end of specimen. In-plane response is the shear behavior of concrete elements adjacent to bar elements. The longitudinal cracking due to hoop stress can also be observed initiated from bond-zone toward outer surface of the cylinder. Figure 5.47 shows the longitudinal splitting at post peak state. Besides cracking, compression yielding can also be observed for all elements. The direction of cracking is changed to almost parallel with the bar. This means the separation of concrete and bar after local bond damage.

The explanation for lower bond strength for the attached truss model is that the truss element is line element that has physically zero perimeter for the bond. So the bond strength is artificially reduced unless a larger mesh is used, then the shear block of concrete can contribute part of the bond perimeter, which make the bond strength increased with

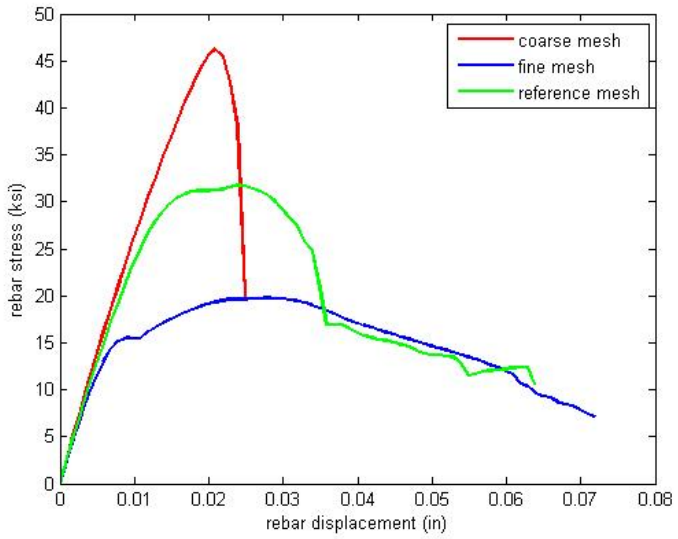

Figure 5.31: Mesh Sensitivity for Attached Truss Model

the increased mesh size, as shown in the Figure 5.31.

5.7.2.6 Detached Truss Model

Figure 5.48∼Figure 5.50 presents analysis results for model Detached truss, with truss element representing bar, without modeling of rib geometry. Unlike the Attached truss model, in Detached truss model, the truss element was not embedded in concrete elements, the connection between concrete and steel was simulated by rigid link element that enforces the displacement compatibility between the separate concrete and bar nodes. The physical perimeter of bond zone is modeled which avoided the mesh sensitivity problem as stated for Attached truss model. The nodal displacement compatibility along the bar axis are defined between steel truss and adjacent concrete. The bond behavior is reflected in the concrete close to the bar, the local cracking and crushing are smeared in the elements adjacent to the bar. Same as Attached truss model, the cracking direction in the bond layer varies from initial 45 degree to parallel to the bar axis. The Detached truss model also successfully

captured the splitting. However, the Detached truss model shows the splitting propagates from load end, instead of free end as shown in Attached truss model.

5.7.2.7 Continuum Solid Steel Model

Figure 5.51∼Figure 5.53 presents analysis results for model Solid steel, the bar is modeled with four nodes continuum element to fully represent the scale of bar. Displacement compatibility between bar and concrete is assumed. The Continuum steel model use 2D axisymmetric elements for both concrete and bar. In this model, the local bond-zone concrete cracking and crushing are also smeared in the elements adjacent to the bar. And the cracking direction in the bond layer varies from initial 45 degree to parallel to the bar axis under further load. The splitting happens at free end, this is same with Attached truss model, but different from Detached truss model. Of all the three bar-scale models, the Solid steel model has the closest global load displacement response and splitting behavior to the contact model.

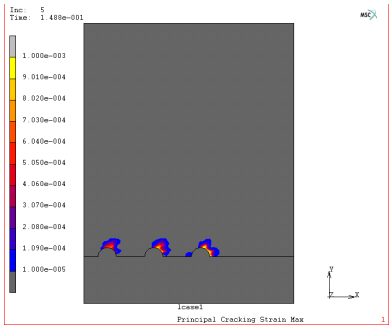

(a) Maximum Cracking Strain

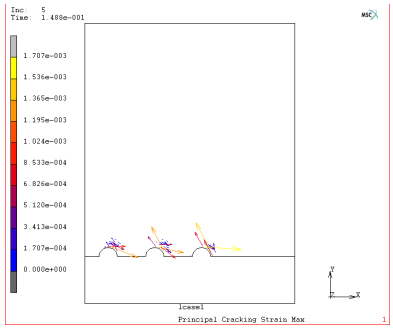

(b) Maximum Cracking Strain

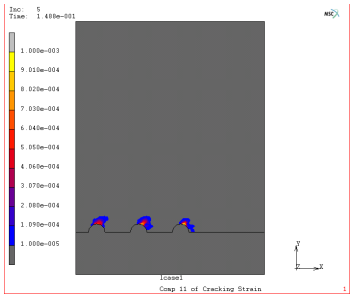

(c) xx Cracking Strain

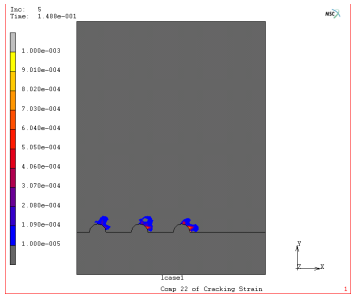

(d) yy Cracking Strain

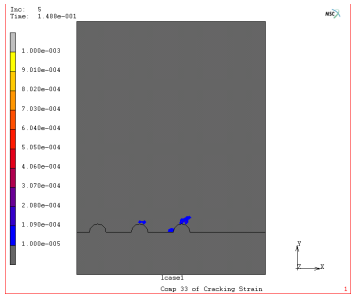

(e) zz Cracking Strain

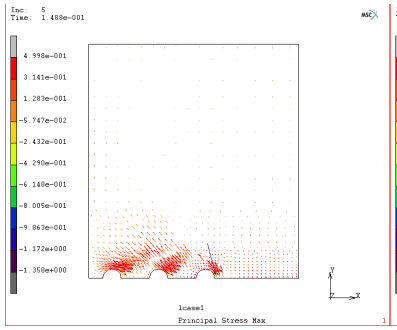

(f) Maximum Principle Stress

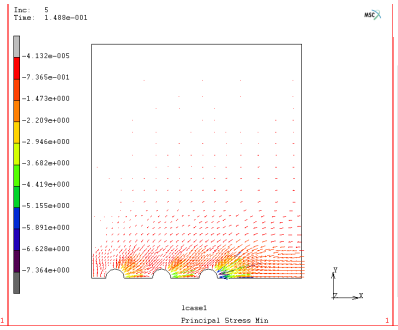

(g) Minimum Principle Stress

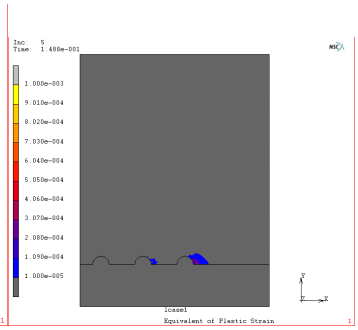

(h) Equivalent Plastic Strain

Figure 5.32: 2D Contact Model Stress Strain at Initial Load

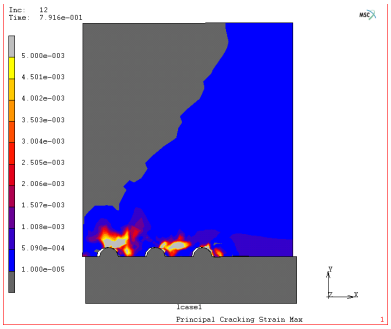

(a) Maximum Cracking Strain

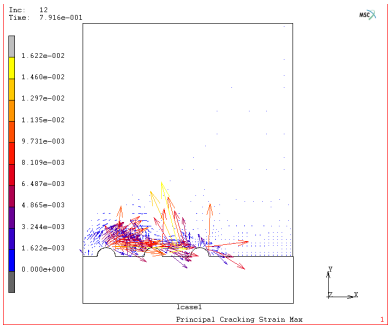

(b) Maximum Cracking Strain

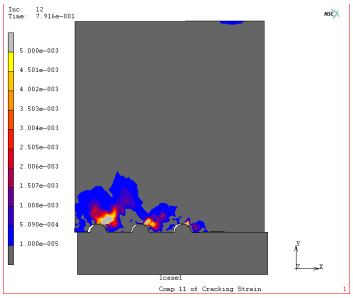

(c) xx Cracking Strain

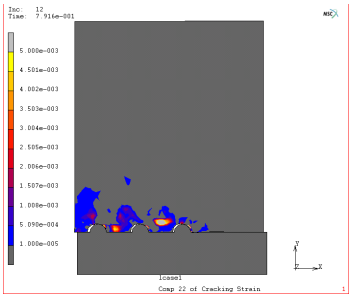

(d) yy Cracking Strain

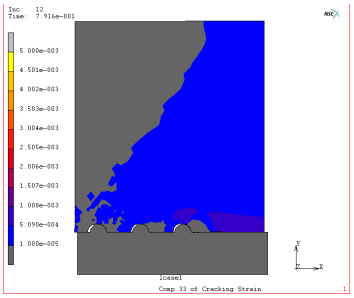

(e) zz Cracking Strain

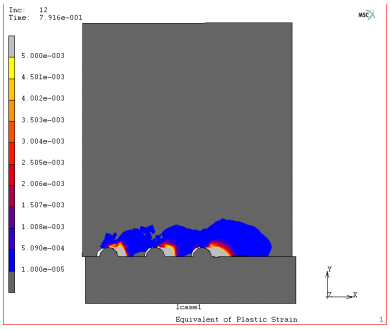

(f) Equivalent Plastic Strain

Figure 5.33: 2D Contact Model at Before Peak Load

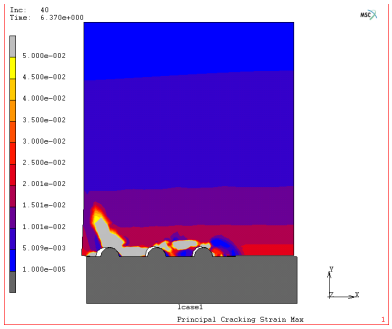

(a) Maximum Cracking Strain

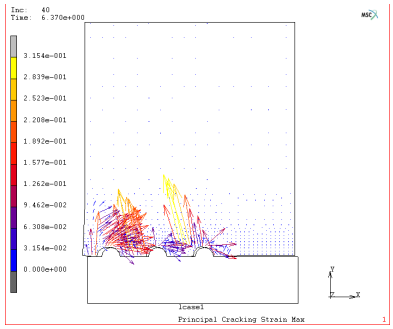

(b) Maximum Cracking Strain

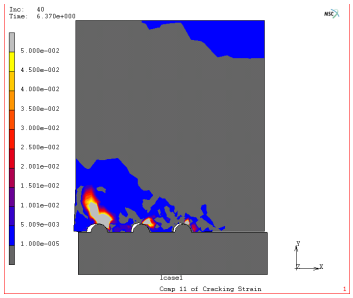

(c) xx Cracking Strain

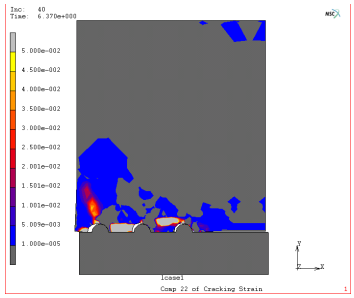

(d) yy Cracking Strain

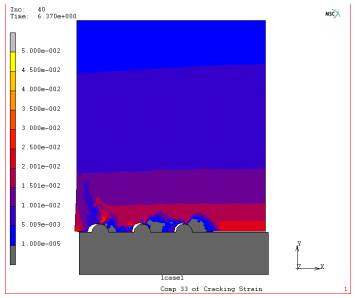

(e) zz Cracking Strain

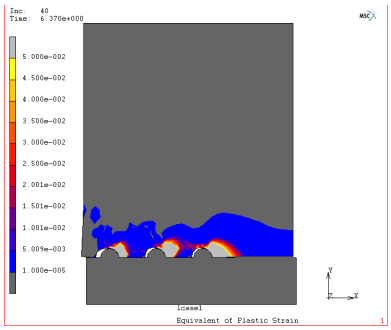

(f) Equivalent Plastic Strain

Figure 5.34: 2D Contact Model at Post Peak Load

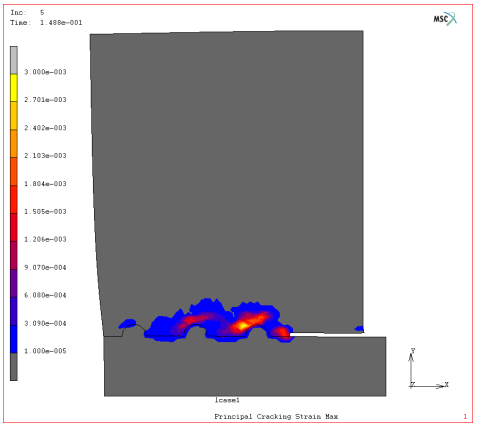

(a) Maximum Cracking Strain

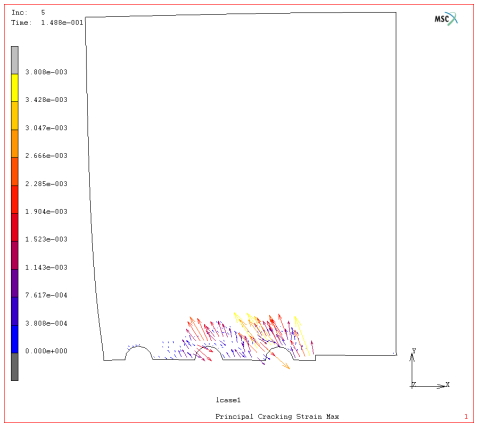

(b) Maximum Cracking Strain

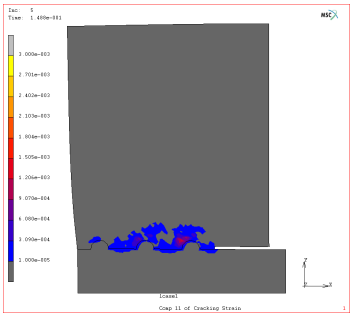

(c) xx Cracking Strain

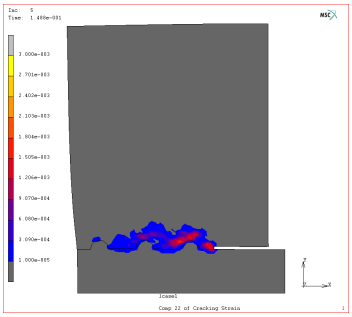

(d) yy Cracking Strain

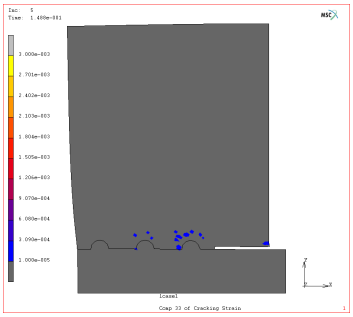

(e) zz Cracking Strain

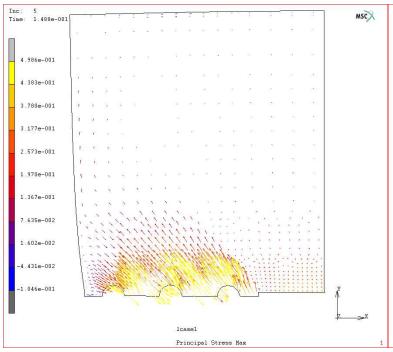

(f) Maximum Principal Stress

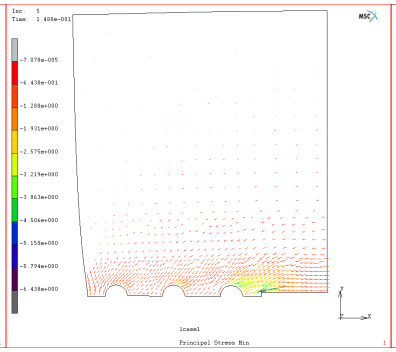

(g) Minimum Principal Stress

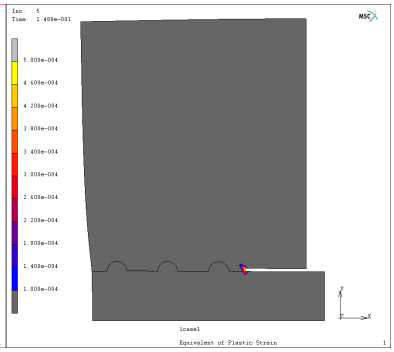

(h) Equivalent Plastic Strain

Figure 5.35: Model Discomp1 Stress Strain at Initial Load Stage

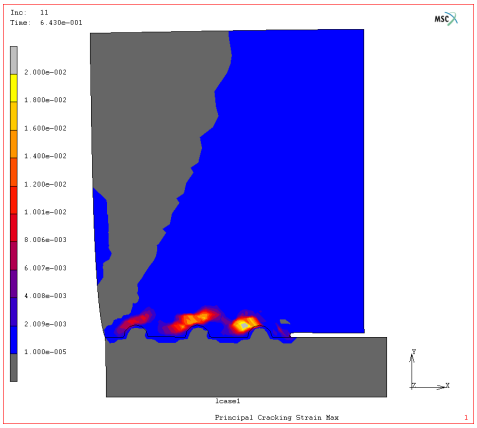

(a) Maximum Cracking Strain

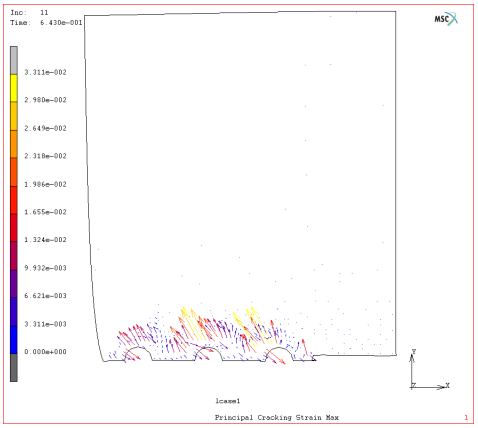

(b) Maximum Cracking Strain

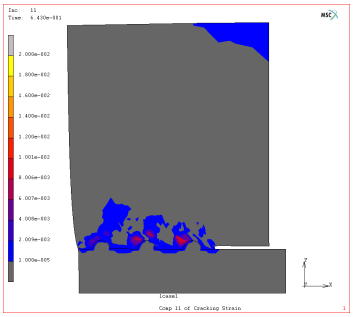

(c) xx Cracking Strain

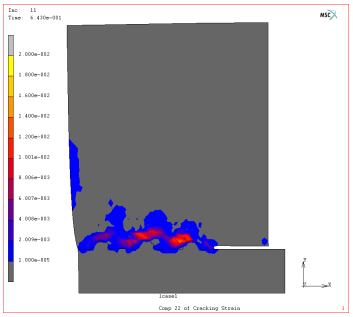

(d) yy Cracking Strain

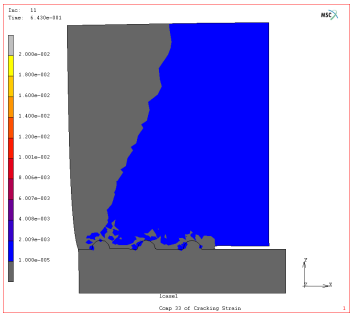

(e) zz Cracking Strain

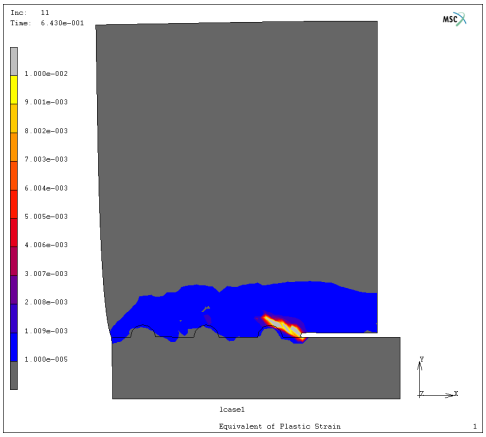

(f) Equivalent Plastic Strain

Figure 5.36: Model Discomp1 Stress Strain at Before Peak Load

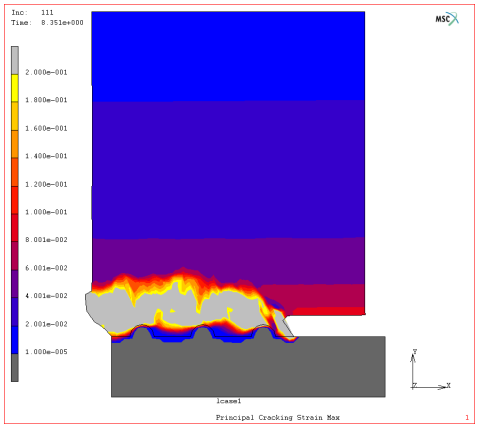

(a) Maximum Cracking Strain

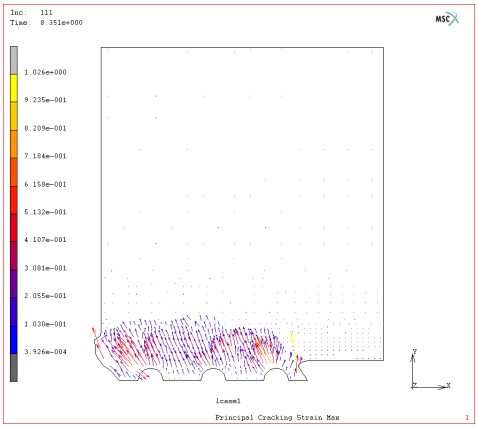

(b) Maximum Cracking Strain

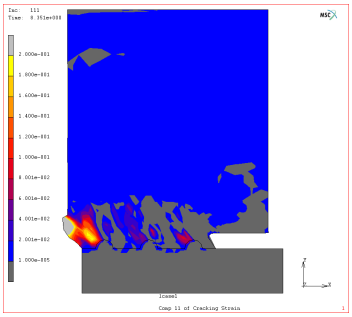

(c) xx Cracking Strain

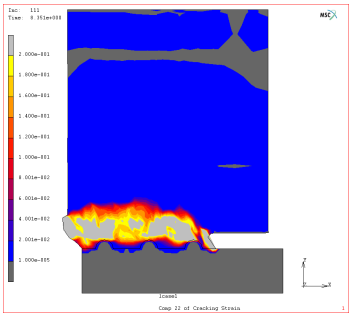

(d) yy Cracking Strain

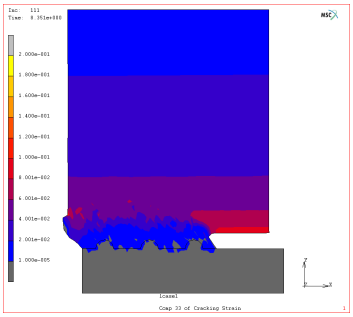

(e) zz Cracking Strain

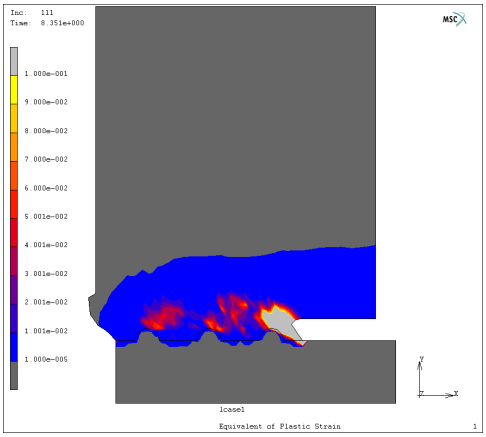

(f) Equivalent Plastic Strain

Figure 5.37: 2D Model Discomp1 Stress Strain at Post Peak Load

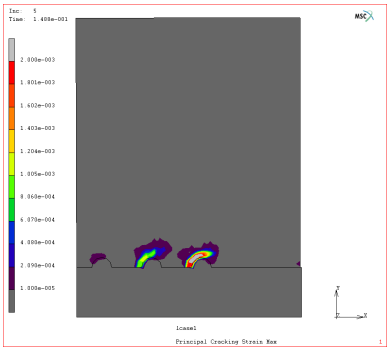

(a) Maximum Cracking Strain

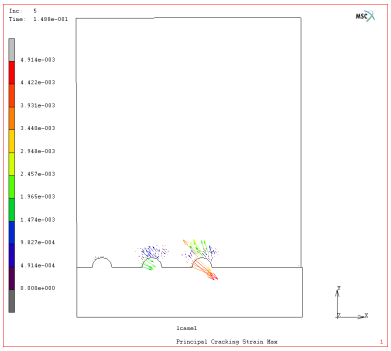

(b) Maximum Cracking Strain

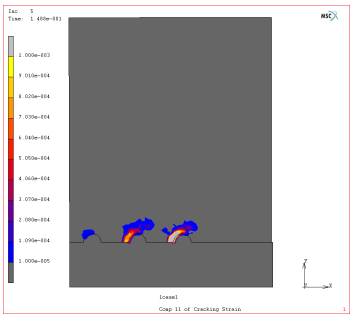

(c) xx Cracking Strain

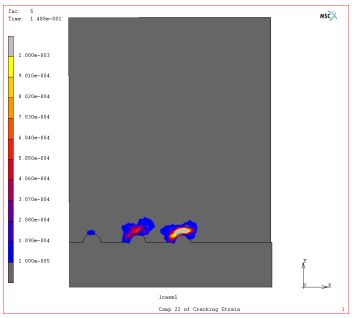

(d) yy Cracking Strain

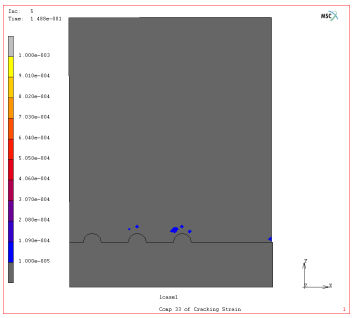

(e) zz Cracking Strain

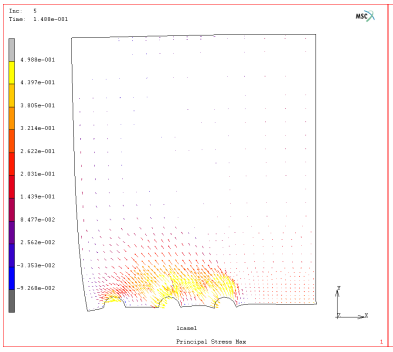

(f) Maximum Principal Stress

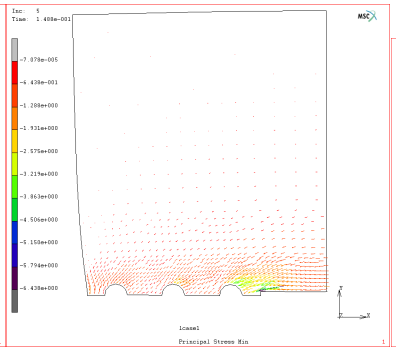

(g) Minimum Principal Stress

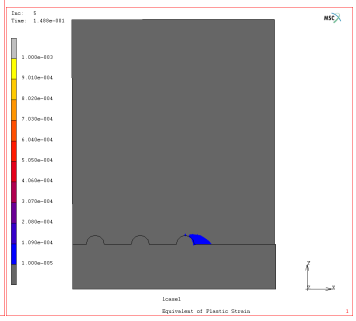

(h) Equivalent Plastic Strain

Figure 5.38: Model Discomp2 Stress Strain at Initial Load

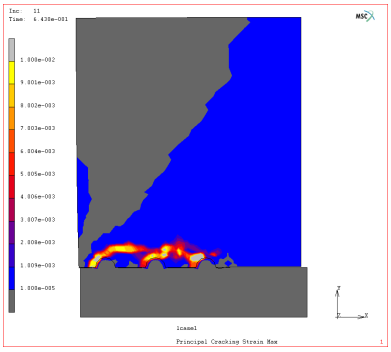

(a) Maximum Cracking Strain

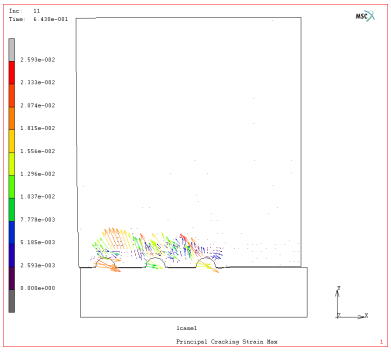

(b) Maximum Cracking Strain

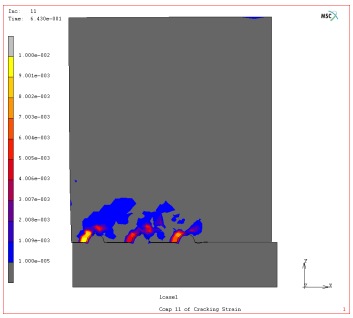

(c) xx Cracking Strain

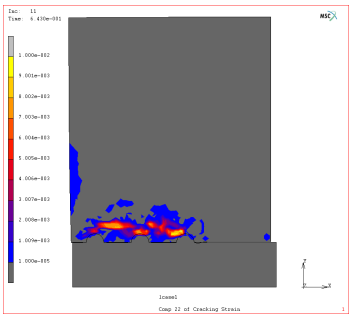

(d) yy Cracking Strain

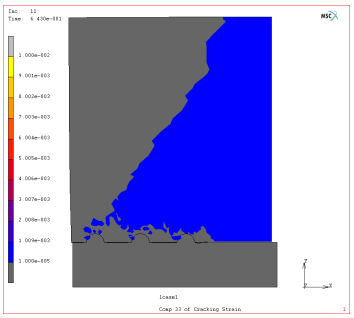

(e) zz Cracking Strain

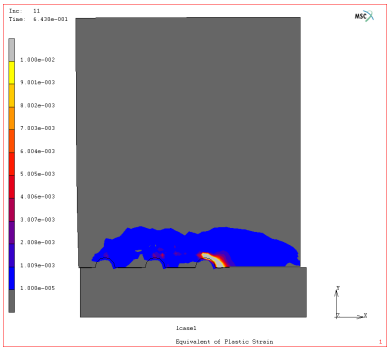

(f) Equivalent Plastic Strain

Figure 5.39: Model Discomp2 Strain at Before Peak Load

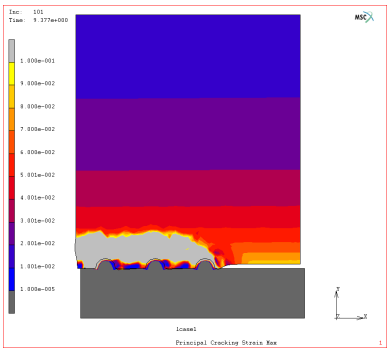

(a) Maximum Cracking Strain

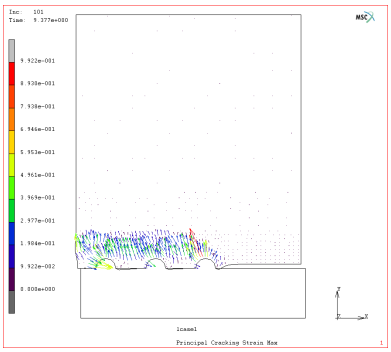

(b) Maximum Cracking Strain

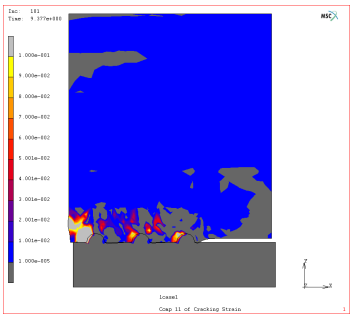

(c) xx Cracking Strain

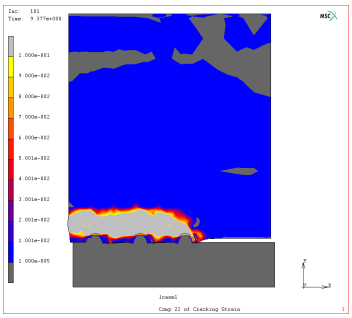

(d) yy Cracking Strain

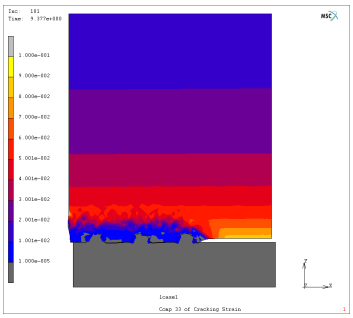

(e) zz Cracking Strain

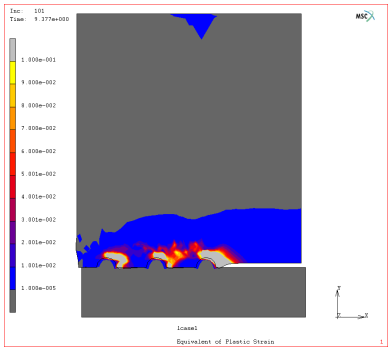

(f) Equivalent Plastic Strain

Figure 5.40: 2D Model Discomp2 Strain at Post Peak Load

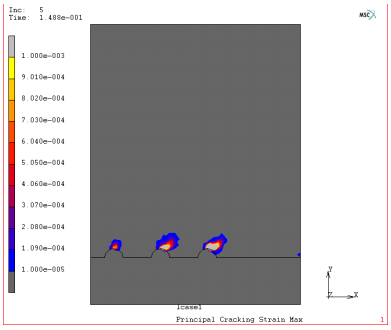

(a) Maximum Cracking Strain

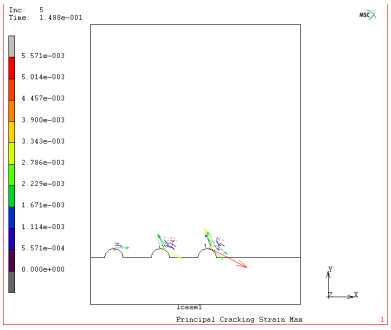

(b) Maximum Cracking Strain

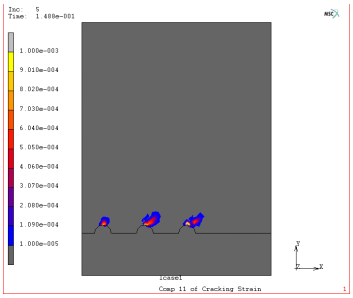

(c) xx Cracking Strain

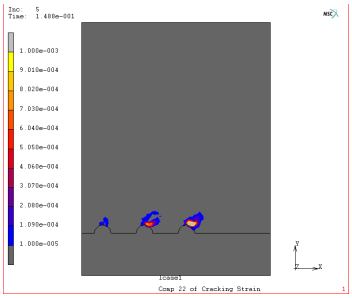

(d) yy Cracking Strain

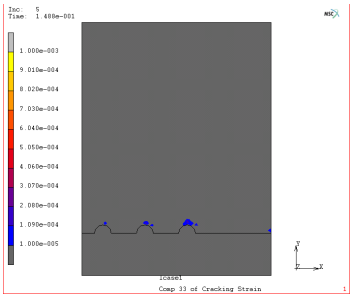

(e) zz Cracking Strain

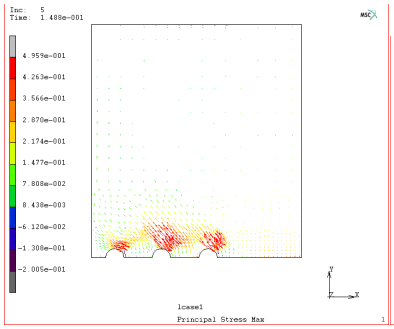

(f) Maximum Principal Stress

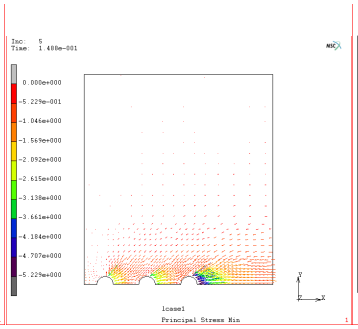

(g) Minimum Principal Stress

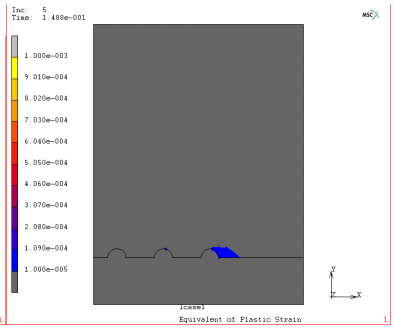

(h) Equivalent Plastic Strain

Figure 5.41: Model Discomp3 Stress Strain at Initial Load

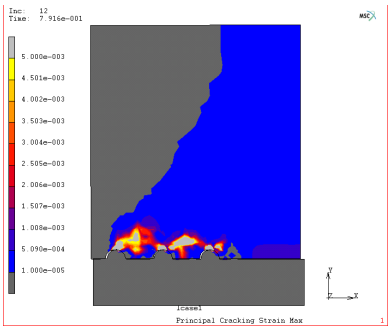

(a) Maximum Cracking Strain

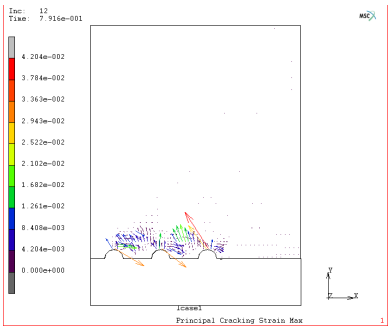

(b) Maximum Cracking Strain

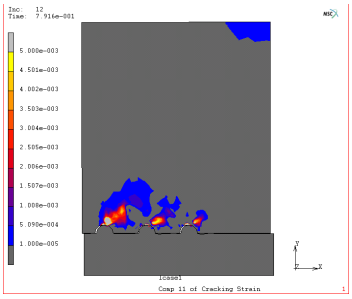

(c) xx Cracking Strain

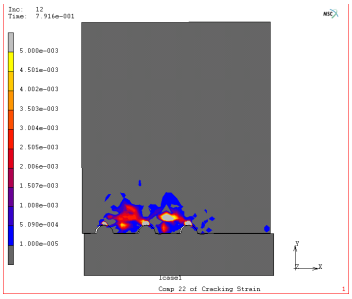

(d) yy Cracking Strain

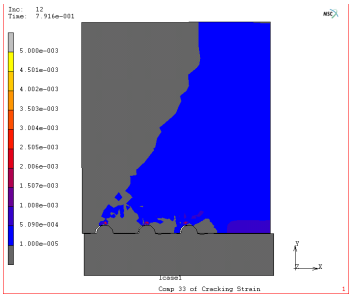

(e) zz Cracking Strain

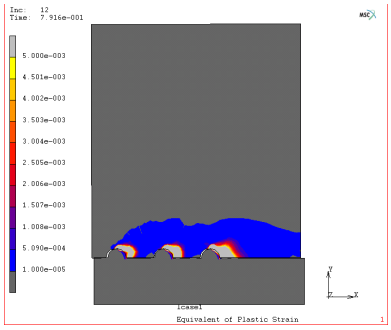

(f) Equivalent Plastic Strain

Figure 5.42: Model Discomp3 Strain at Before Peak Load

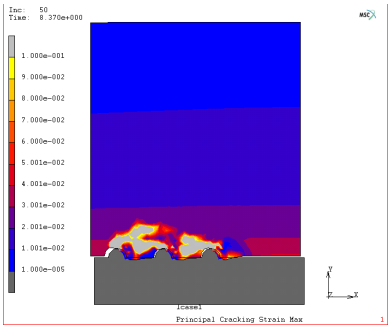

(a) Maximum Cracking Strain

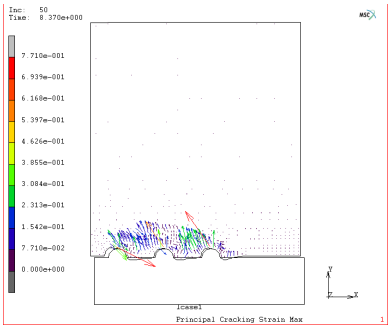

(b) Maximum Cracking Strain

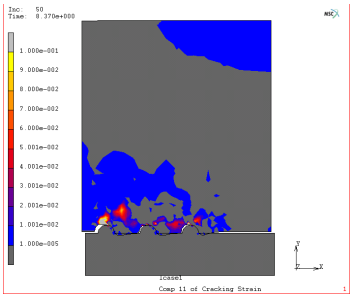

(c) xx Cracking Strain

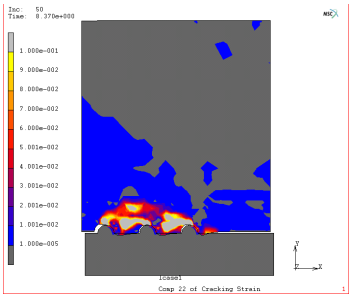

(d) yy Cracking Strain

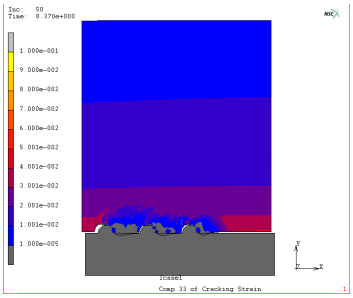

(e) zz Cracking Strain

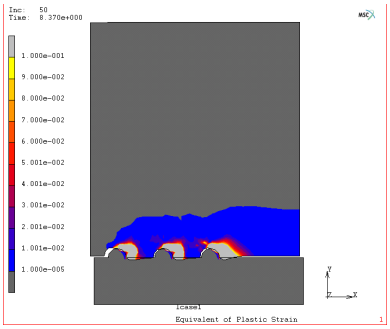

(f) Equivalent Plastic Strain

Figure 5.43: 2D Model Discomp3 Strain at Post Peak Load

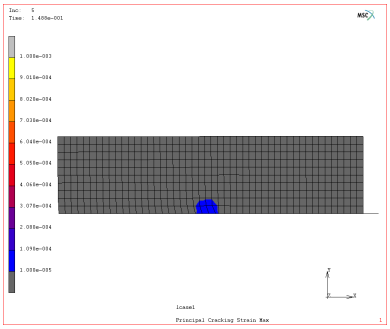

(a) Maximum Cracking Strain

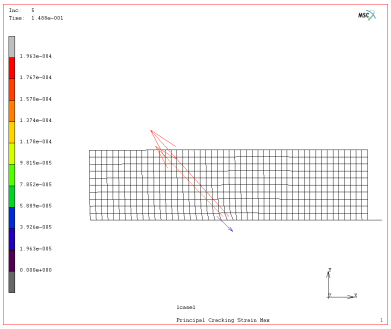

(b) Maximum Cracking Strain

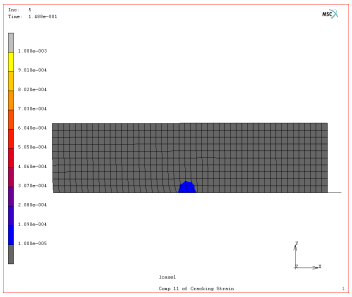

(c) xx Cracking Strain

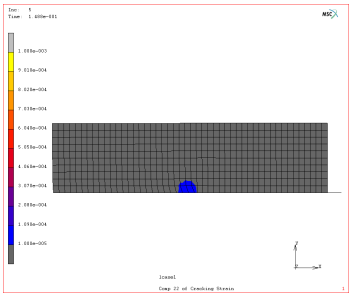

(d) yy Cracking Strain

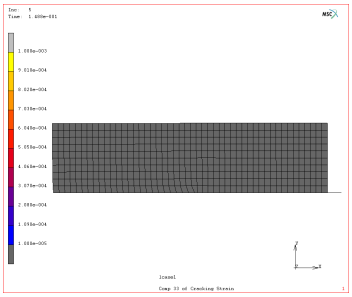

(e) zz Cracking Strain

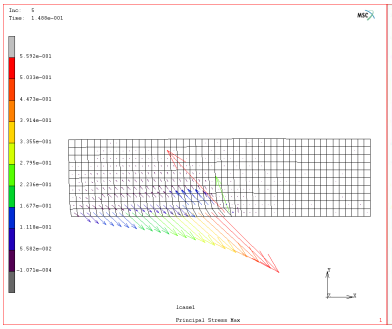

(f) Maximum Principal Stress

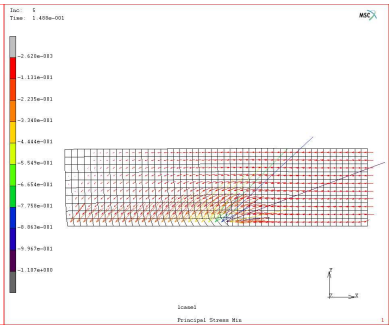

(g) Minimum Principal Stress

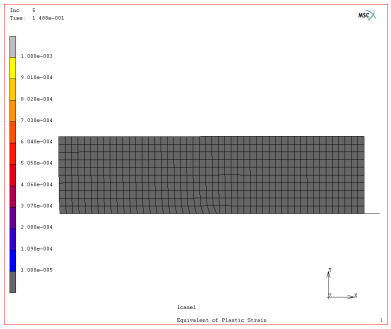

(h) Equivalent Plastic Strain

Figure 5.44: Attached Truss Model Stress Strain at Initial Loading

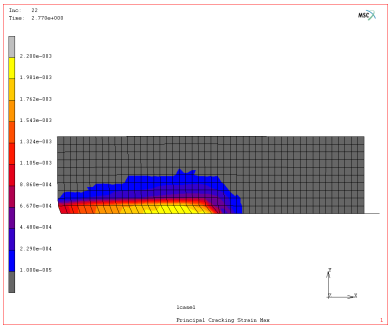

(a) Maximum Cracking Strain

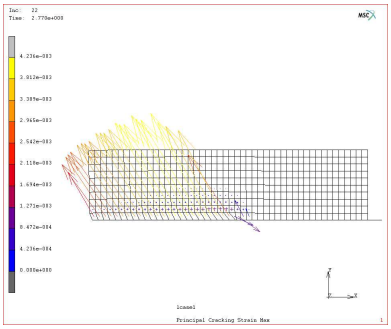

(b) Maximum Cracking Strain

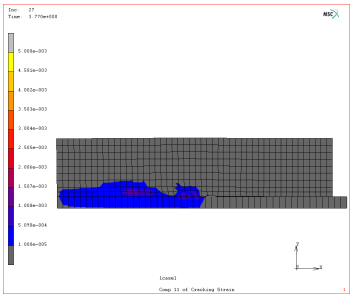

(c) xx Cracking Strain

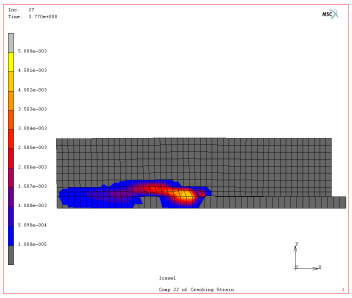

(d) yy Cracking Strain

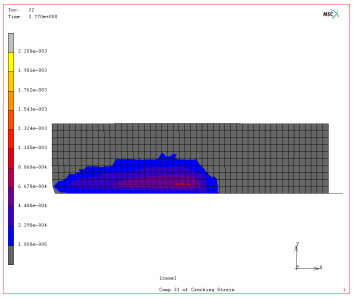

(e) zz Cracking Strain

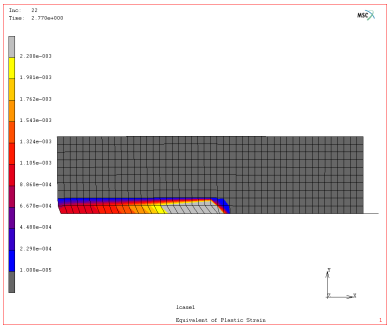

(f) Equivalent Plastic Strain

Figure 5.45: Attached Truss Model Strain at Before Peak Load

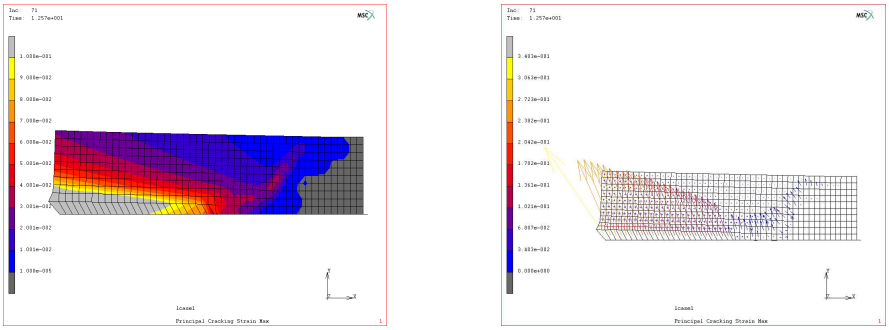

Figure 5.46: Maximum Principal Cracking Strain at Post Peak Stage

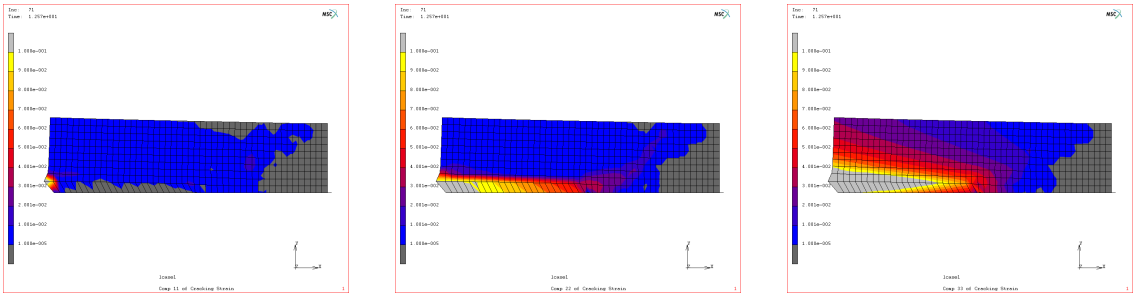

(a) xx Cracking Strain

(b) yy Cracking Strain

(c) zz Cracking Strain

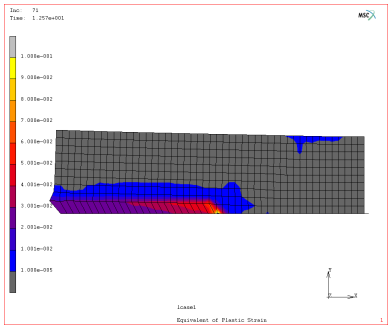

(d) Equivalent Plastic Strain

Figure 5.47: 2D Attached Truss Model Strain at Post Peak Load

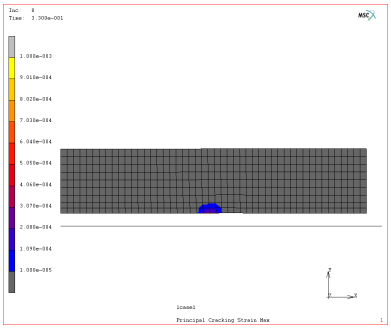

(a) Maximum Cracking Strain

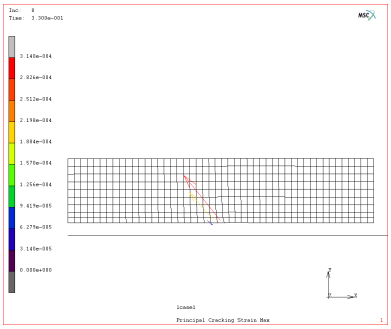

(b) Maximum Cracking Strain

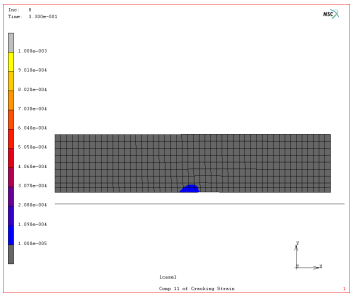

(c) xx Cracking Strain

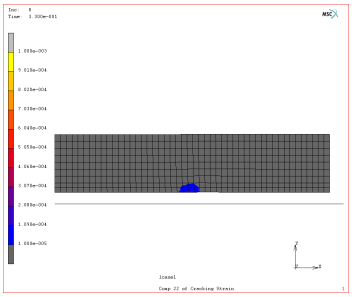

(d) yy Cracking Strain

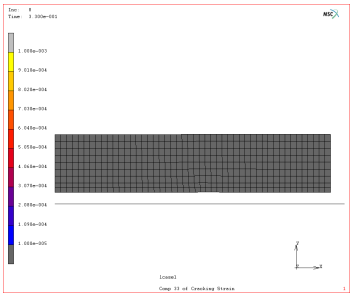

(e) zz Cracking Strain

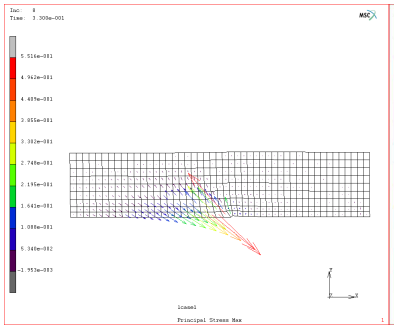

(f) Maximum Principal Stress

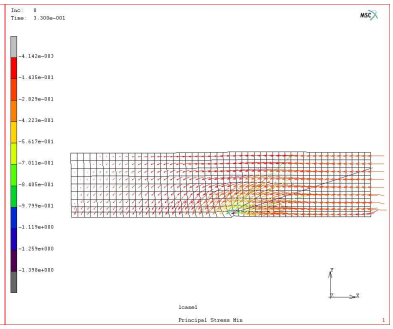

(g) Minimum Principal Stress

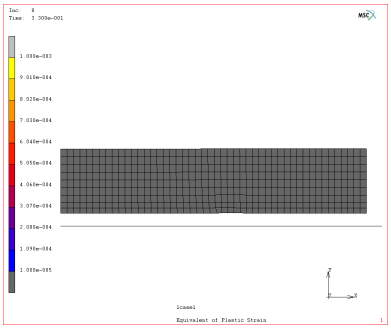

(h) Equivalent Plastic Strain

Figure 5.48: Detached Truss Model Stress Strain at Initial Load

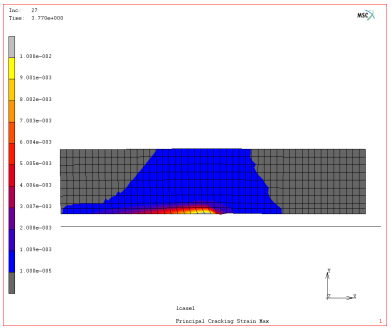

(a) Maximum Cracking Strain

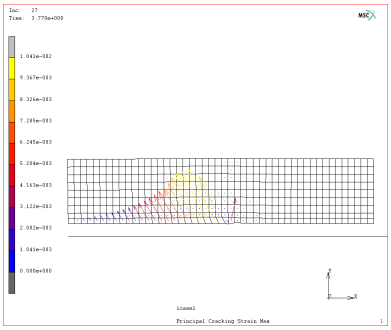

(b) Maximum Cracking Strain

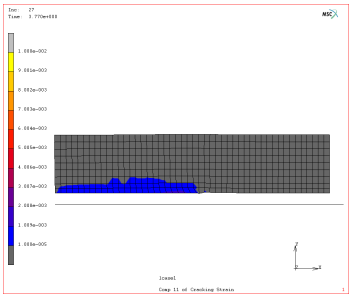

(c) xx Cracking Strain

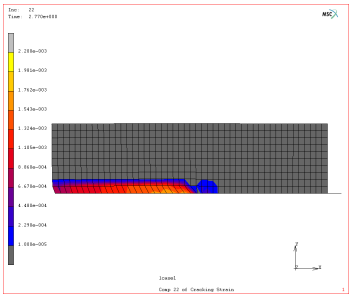

(d) yy Cracking Strain

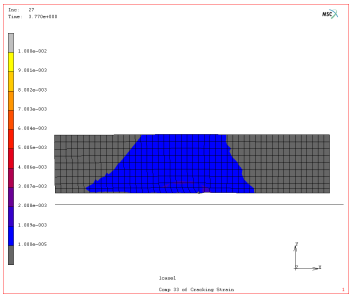

(e) zz Cracking Strain

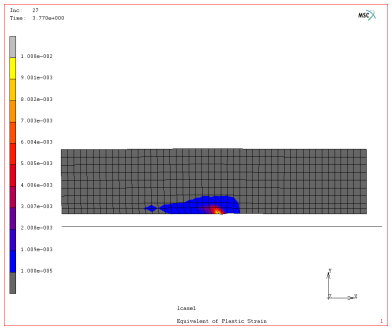

(f) Equivalent Plastic Strain

Figure 5.49: Detached Truss Model Strain at Before Peak Load

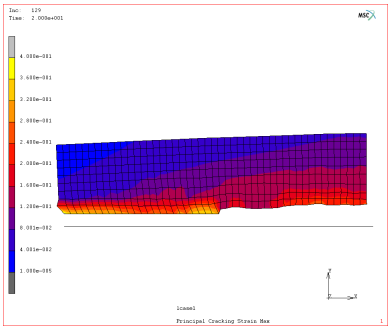

(a) Maximum Cracking Strain

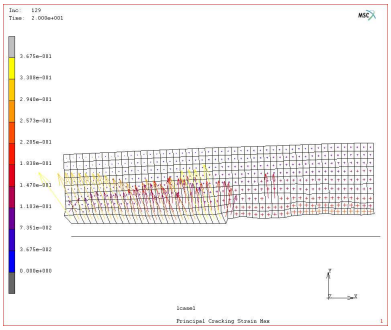

(b) Maximum Cracking Strain

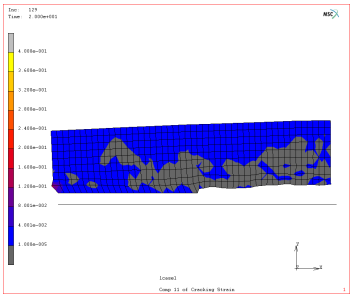

(c) xx Cracking Strain

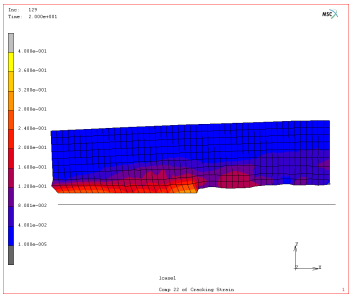

(d) yy Cracking Strain

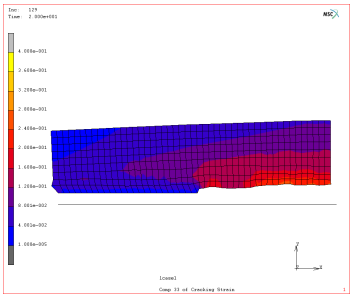

(e) zz Cracking Strain

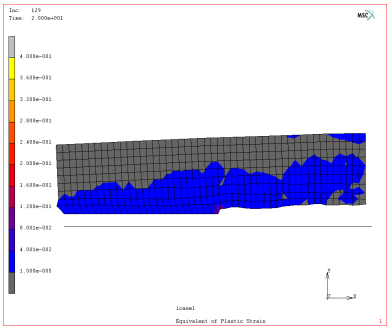

(f) Equivalent Plastic Strain

Figure 5.50: 2D Detached Truss Model Strain at Post Peak Load

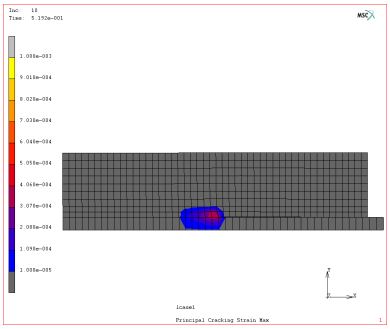

(a) Maximum Cracking Strain

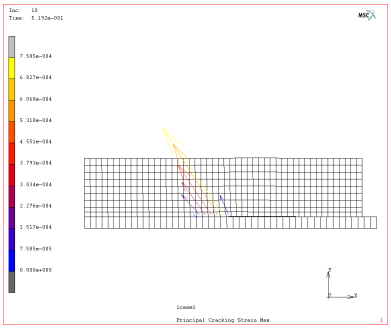

(b) Maximum Cracking Strain

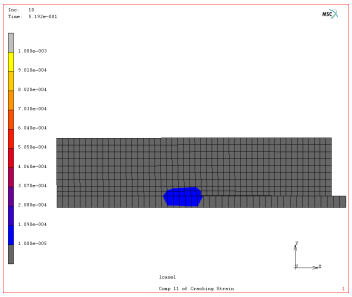

(c) xx Cracking Strain

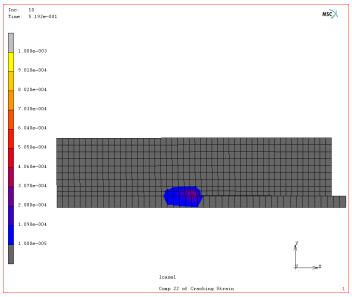

(d) yy Cracking Strain

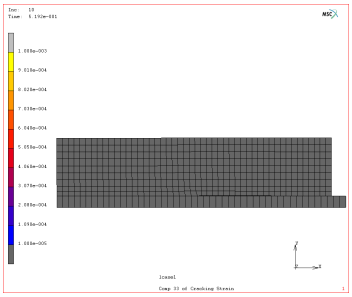

(e) zz Cracking Strain

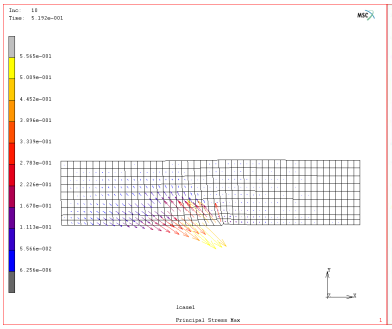

(f) Maximum Principal Stress

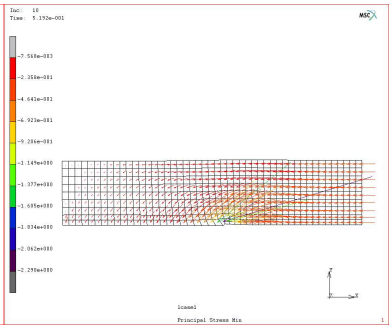

(g) Minimum Principal Stress

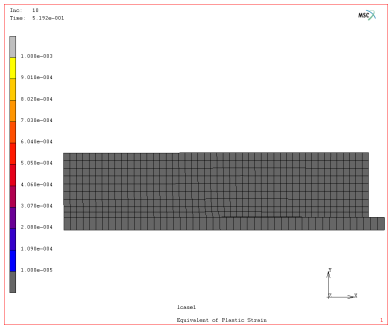

(h) Equivalent Plastic Strain

Figure 5.51: Solid Steel Model Stress Strain at Initial Load

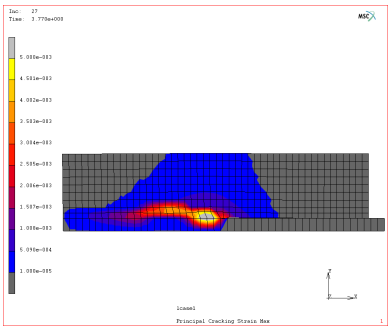

(a) Maximum Cracking Strain

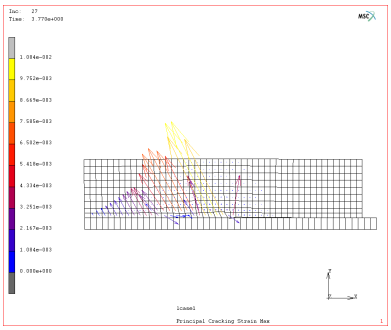

(b) Maximum Cracking Strain

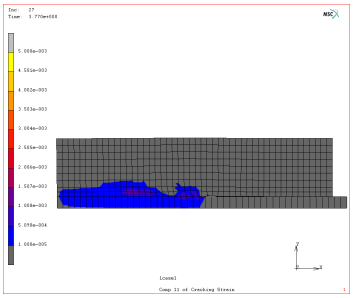

(c) xx Cracking Strain

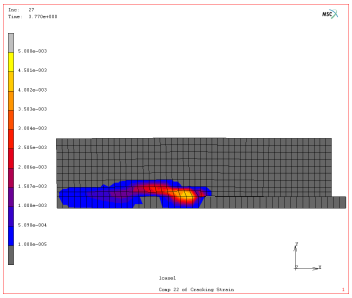

(d) yy Cracking Strain

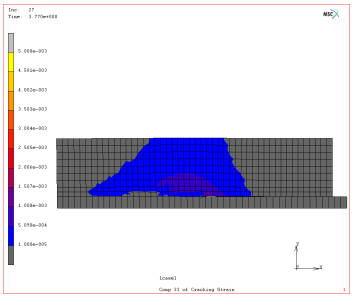

(e) zz Cracking Strain

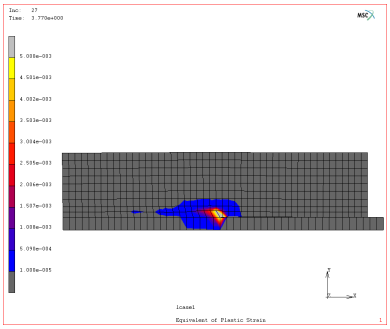

(f) Equivalent Plastic Strain

Figure 5.52: Solid Steel Model Stress Strain at Before Peak Load

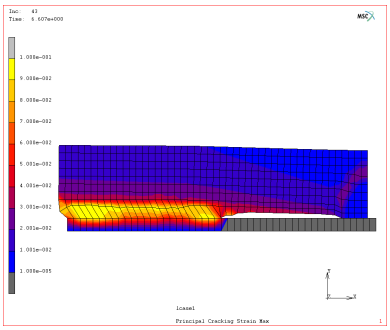

(a) Maximum Cracking Strain

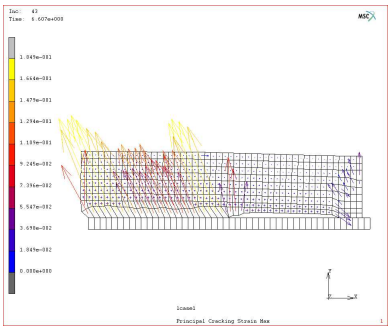

(b) Maximum Cracking Strain

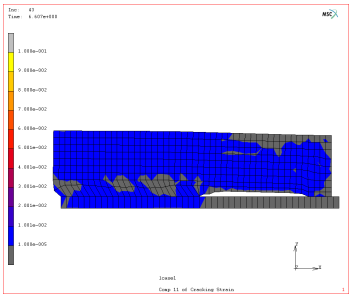

(c) xx Cracking Strain

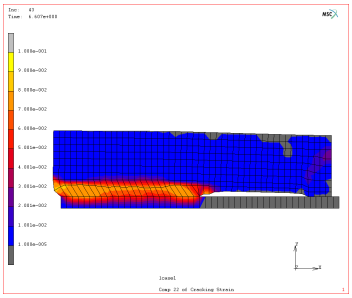

(d) yy Cracking Strain

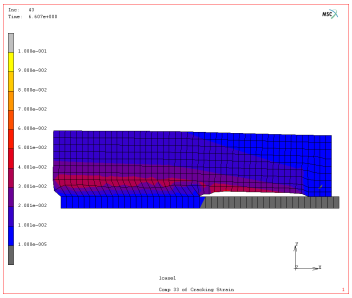

(e) zz Cracking Strain

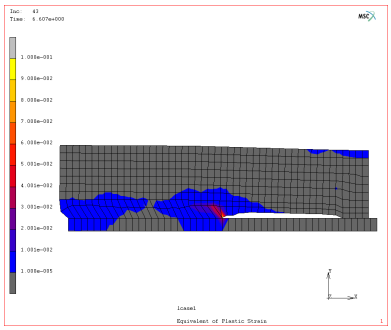

(f) Equivalent Plastic Strain

Figure 5.53: 2D Solid Steel Model Stress Strain at Post Peak Load

5.7.3 Three-dimensional Modeling

In two-dimensional modeling, secondary cracking was very well represented. However, by standard axisymmetric models, the longitudinal cracking is smeared over the perimeter of the concrete cylinder. The localization of longitudinal cracking cannot be achieved by two-dimensional axisymmetric model. A full three-dimensional model is necessary to simulate the bond behavior especially for unconfined specimens which are controlled by the splitting. Corresponding to two-dimensional models in section 5.7.2, three-dimensional models were implemented to capture the longitudinal cracking localization and global load-displacement responses.

Figure 5.54 shows the global load displacement response for 3D rib-scale models. All models show brittle response induced by longitudinal cracking. Same as two-dimensional models, models with displacement compatibility show stiffer and higher bond strength than direct contact model. Figure 5.55 shows the global load-displacement responses for bar-scale models. Same as 2D models, the Attached truss model has very lower results which is due to the reduced interface concrete zone to resist the bar end load.

Figure 5.56 presents analysis results for full 3D Contact model. The local bond-zone damages are similar to 2D model. However, 3D model has good performance on describing longitudinal splitting. Figure 5.56(a)∼Figure 5.56(e) show the initial secondary cracking, and longitudinal cracking along the specimen during before peak and post peak bond strength stage. The localization of longitudinal cracking is the major improvement over two dimensional modeling. Figure 5.57 presents rib-scale analysis results for model Dispcomp1 with full displacement compatibility model. Local in-plane cracking is similar with 2D model: the cracking starts from separation of rib and concrete in the back of ribs and finally develops into a shear plane along bar axis. The equivalent plastic strain starts from the bonding region near load end and develops towards free end. The location of maximum equivalent plastic strain is in the up-front of ribs, which represents not only compression behavior but shear behavior that is different from contact model. In hoop direction, the first

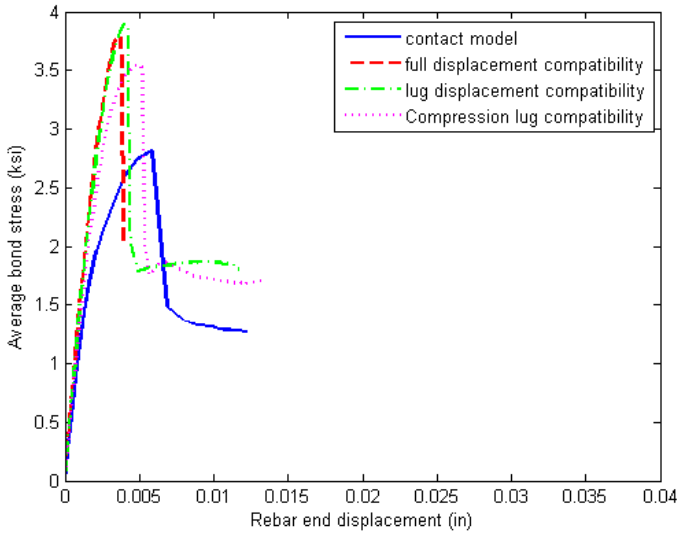

Figure 5.54: Bond Stress vs. Bar Displacement for Different Interface Conditions

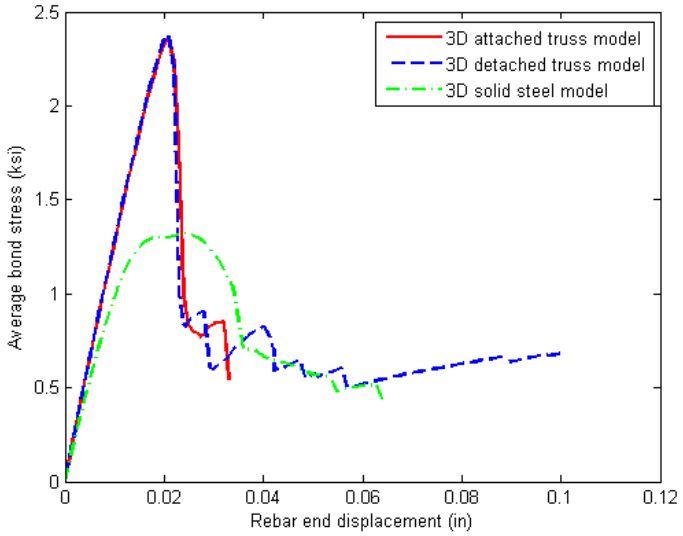

Figure 5.55: Bond Stress vs. Bar Displacement for Different Modeling Procedures in 3D

major localized splitting can be observed. Figure 5.58 presents analysis results for model Dispcomp2 with displacement compatibility at location of ribs. The local in-plane cracking and yielding are similar to model Dispcomp1, a shear plane on the outer surface of bar ribs is formed as the progression of load. In hoop direction, one major splitting and two minor splitting are developed toward the outsider of the cylinder. Figure 5.59 presents analysis results for full 3D model Dispcomp3 with compression side displacement compatibility between ribs and concrete. The local in-plane cracking is very close to cracking patterns in contact model. The cracking starts from up-front of ribs and yielding starts from front of ribs. The cracking and yielding region are localized near ribs. But the shear plane about the bar outer surface can also be observed. In hoop direction, one major splitting and three minor splitting are developed toward the outsider of the cylinder.

Figure 5.60 presents analysis results for full 3D Attached Truss model. Figure 5.61 presents analysis results for full 3D Detached truss model model, and Figure 5.62 presents analysis results for full 3D Continuum Steel model.

5.7.4 Summary

Using the **rib-scale** geometric configuration and material models proposed in the reference model 5.2, three different interface conditions were considered in addition to the contact analysis in the reference model. The three interface cases are full displacement compatibility between concrete and steel on the interface, rib displacement compatibility on the interface and displacement compatibility for only compression side of the ribs. 2D axisymmetric analysis and full 3D analysis were finished for all these three interface conditions as well as the reference contact model. Figure 5.63 shows the global bond stress versus bar end displacement for all rib-scale models.

Three dimensional analysis results show brittle longitudinal splitting. The bond strength is within 10% lower than that from same model 2D axisymmetric analysis. In two-dimensional models, the longitudinal splitting is smeared in the perimeter of the cylinder instead of lo-

calizing into one or several major cracks. This is equivalent to increase the fracture energy in hoop direction, because the material softening properties are corresponding to the small in-plane element size instead of the unit length in hoop direction and concrete was assumed as isotropic material. For the influence of different interface conditions, full displacement compatibility model Discomp1 has peak bond strength of 10% higher than model Discomp1, and model Discomp1 has peak bond strength of almost 30% higher than the contact model.

Due to different interface conditions, The four rib-scale models have different local cracking patterns. Model Discomp1 and Discomp2 have initial separation cracking that starts at back of the ribs. As load increases, accompanying the yielding of concrete in front of ribs, a shear plane for concrete on top of ribs were formed which represents the bond-zone slip and radial separation of bond and concrete. For Model Discomp2 and the direct contact model, the initial cracking was from up-front of the ribs with direction of approximately 45 degree to the bar axis. As load increases, the cracking direction changes and close to parallel with bar axis. The formation of shear plane is not so obvious as the previous two models.

Three-dimensional **bar-scale** models without modeling of ribs also show longitudinal splitting. Figure 5.64 shows the global load-displacement responses for all models without ribs. The 3D models are much more brittle than the 2D models and the bond strength by all 3D models are much smaller than 2D models, with Attached truss model 100% difference, Detached truss model 40% difference and Solid steel model 30% difference. Same as stated in section 5.6, the two-D models have imposed more confinement to bond zone due to the smeared longitudinal splitting. All bar-scale models show smaller bond strength than full contact model, with Detached truss model and Solid steel model 15% less than that from contact model and Attached truss model 50% less than the strength from full contact model.

The local cracking and yielding of concrete near ribs have similar patterns for all three bar-scale models. The cracking and yielding were initiated from the bonding location close to the load end and propagated to the free end. The initial cracking was 45 degree to the bar axis and varies to approximately parallel to the bar axis as load goes on. The cracking

and yielding were localized into one single layer of concrete element adjacent to the bar.

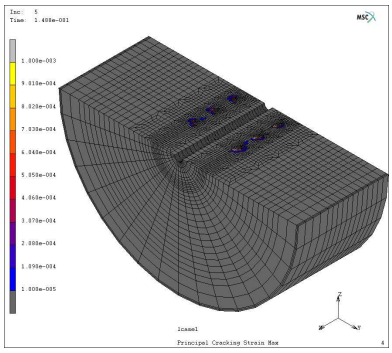

(a) Initial Maximum Cracking Strain

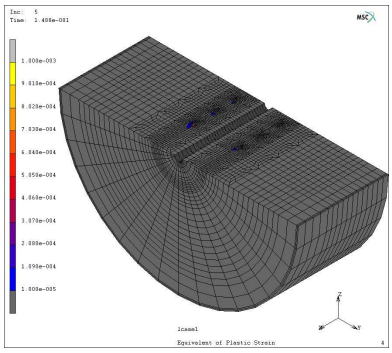

(b) initial equivalent plastic strain

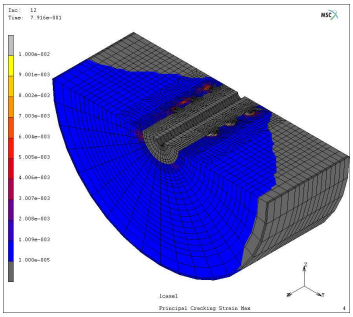

(c) Maximum Cracking Strain Before Peak Load

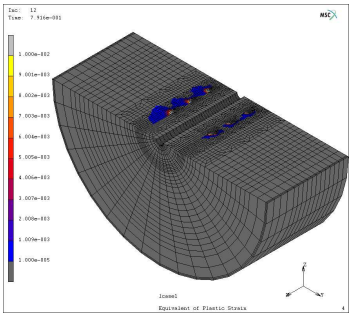

(d) equivalent plastic strain Before Peak Load

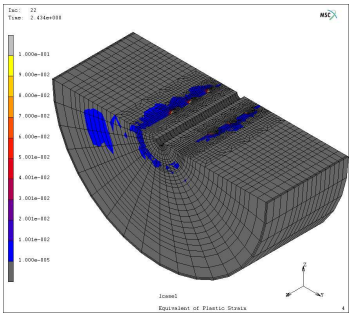

(e) Equivalent Plastic Strain Post Peak Load

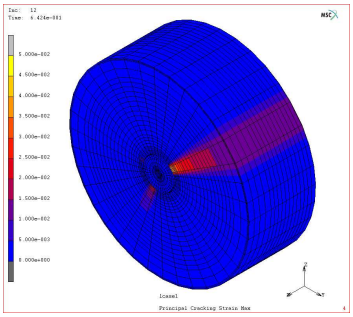

(f) Maximum Cracking Strain Post Peak Load

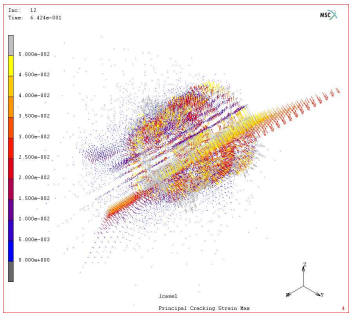

(g) Maximum Cracking Strain Post Peak Load

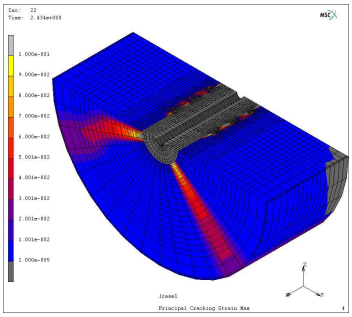

(h) Maximum Cracking Strain Post Peak Load

Figure 5.56: 3D Contact Model Strain

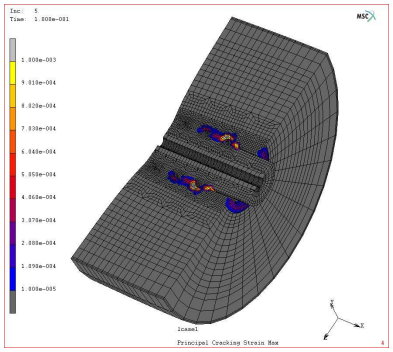

(a) Initial Maximum Cracking Strain

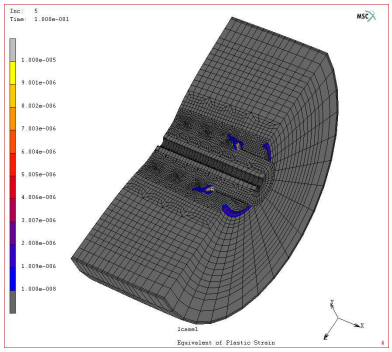

(b) initial equivalent plastic strain

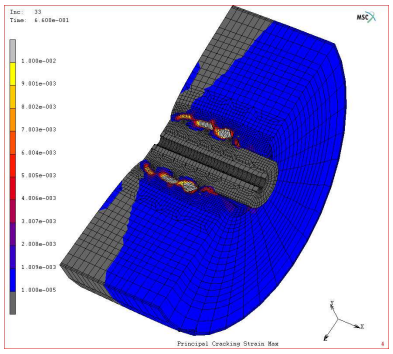

(c) Maximum Cracking Strain Before Peak Load

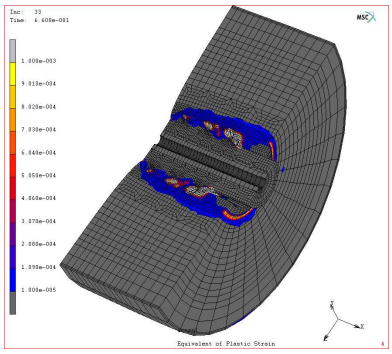

(d) equivalent plastic strain Before Peak Load

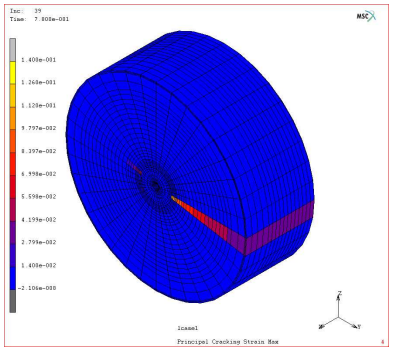

(e) Maximum Cracking Strain Post Peak Load

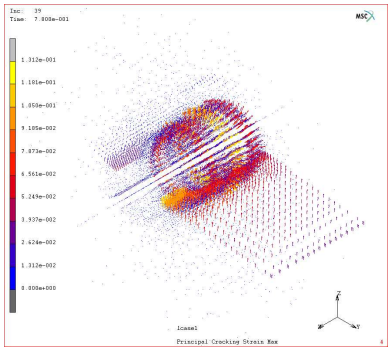

(f) Maximum Cracking Strain Post Peak Load

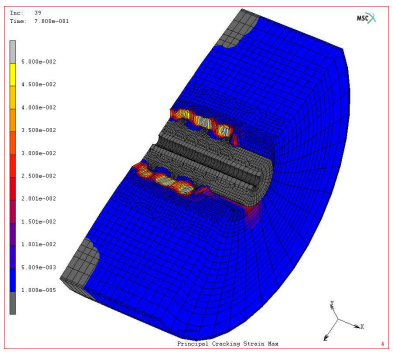

(g) Maximum Cracking Strain Post Peak Load

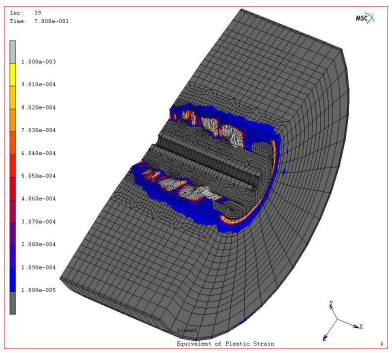

(h) Equivalent Plastic Strain Post Peak Load

Figure 5.57: 3D Dispcomp1 Model Strain

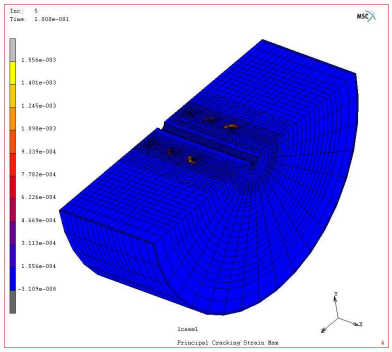

(a) Initial Maximum Cracking Strain

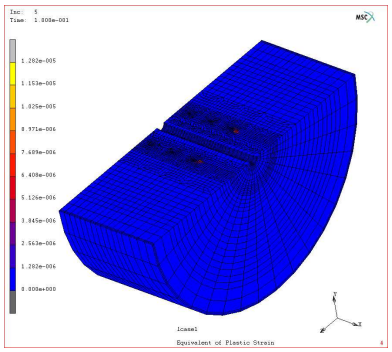

(b) initial equivalent plastic strain

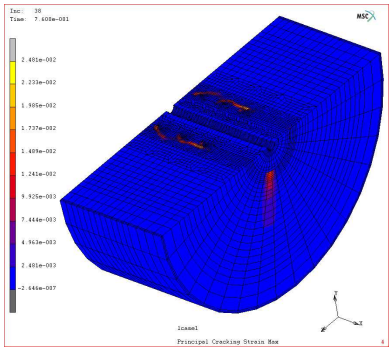

(c) Maximum Cracking Strain Before Peak Load

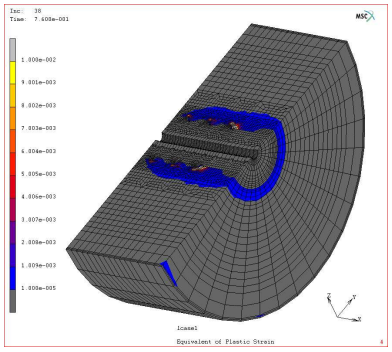

(d) equivalent plastic strain Before Peak Load

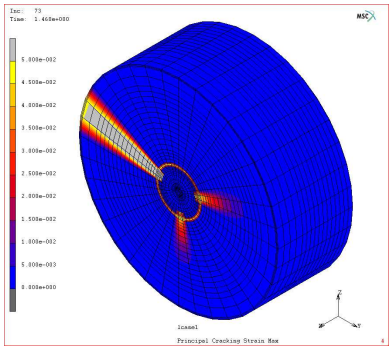

(e) Maximum Cracking Strain Post Peak Load

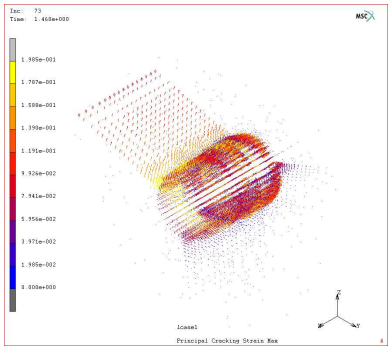

(f) Maximum Cracking Strain Post Peak Load

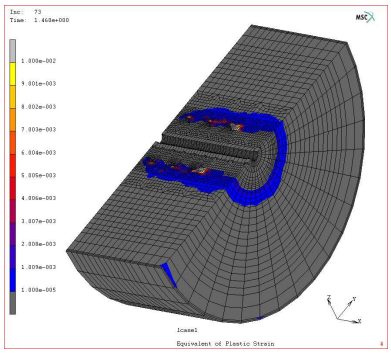

(g) Equivalent Plastic Strain Post Peak Load

Figure 5.58: 3D Discomp2 Model Strain

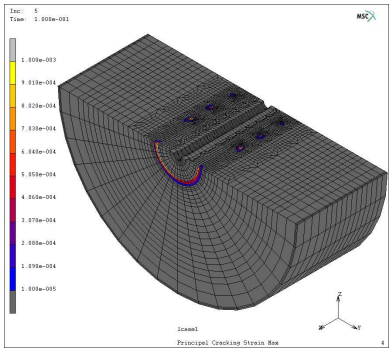

(a) Initial Maximum Cracking Strain

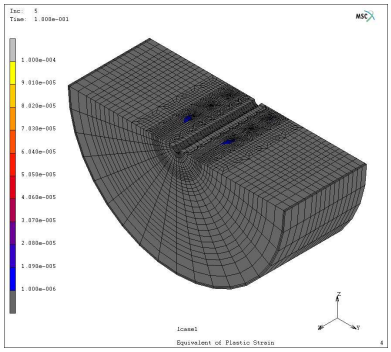

(b) initial equivalent plastic strain

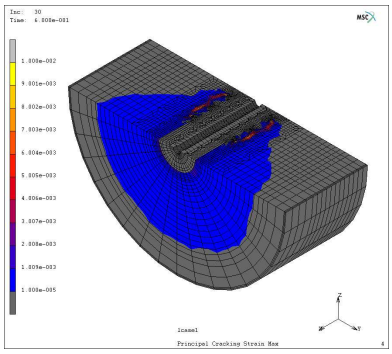

(c) Maximum Cracking Strain Before Peak Load

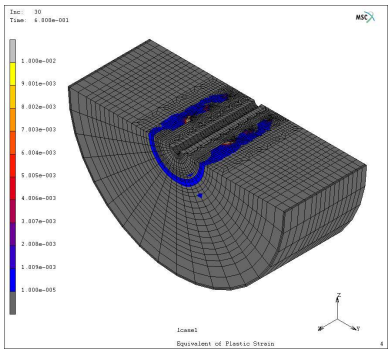

(d) equivalent plastic strain Before Peak Load

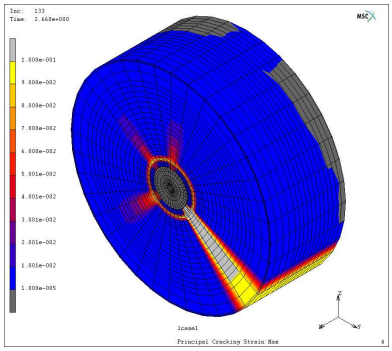

(e) Maximum Cracking Strain Post Peak Load

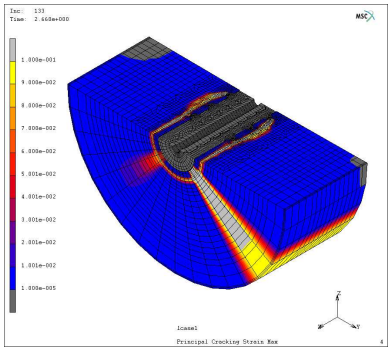

(f) Maximum Cracking Strain Post Peak Load

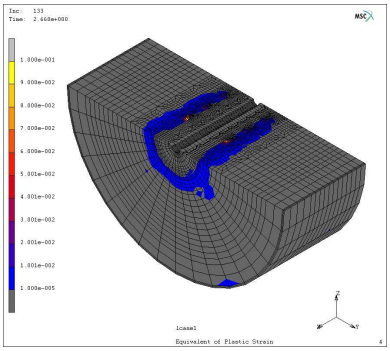

(g) Equivalent Plastic Strain Post Peak Load

Figure 5.59: 3D Discomp3 Model Strain

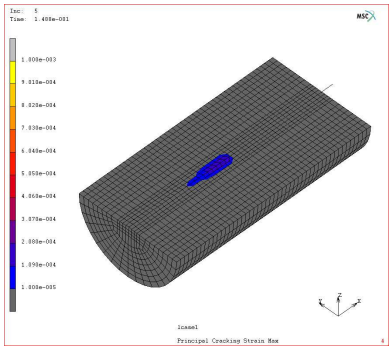

(a) Initial Maximum Cracking Strain

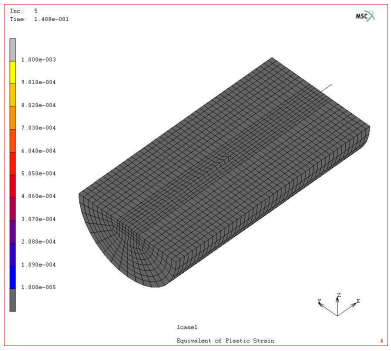

(b) initial equivalent plastic strain

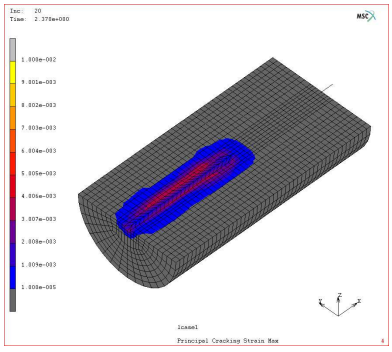

(c) Maximum Cracking Strain Before Peak Load

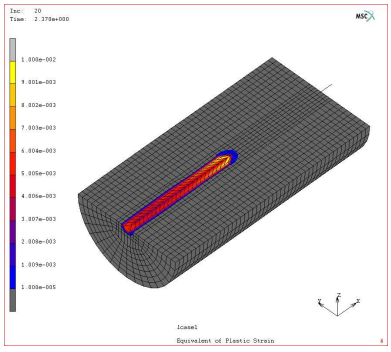

(d) equivalent plastic strain Before Peak Load

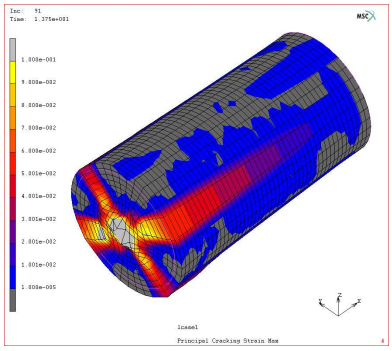

(e) Maximum Cracking Strain Post Peak Load

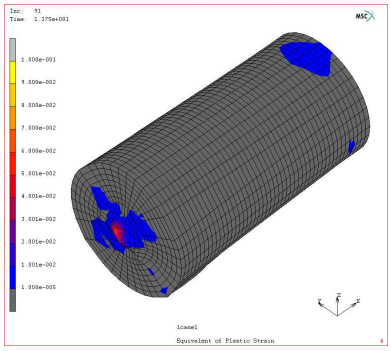

(f) Equivalent Plastic Strain Post Peak Load

Figure 5.60: 3D Attached Truss Model Strain

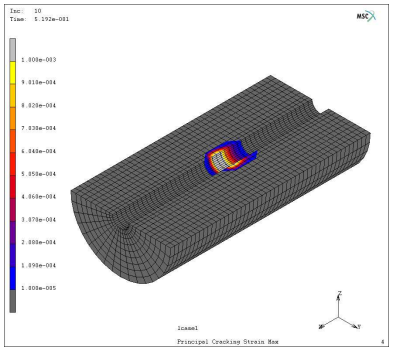

(a) Initial Maximum Cracking Strain

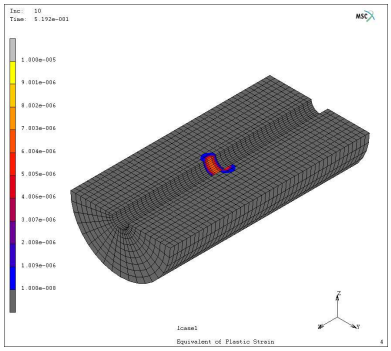

(b) initial equivalent plastic strain

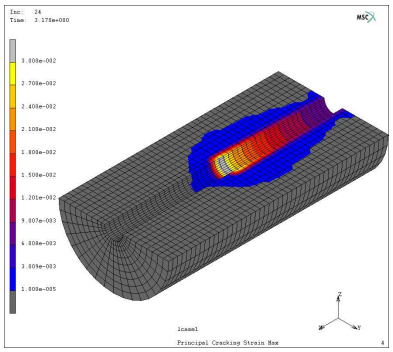

(c) Maximum Cracking Strain Before Peak Load

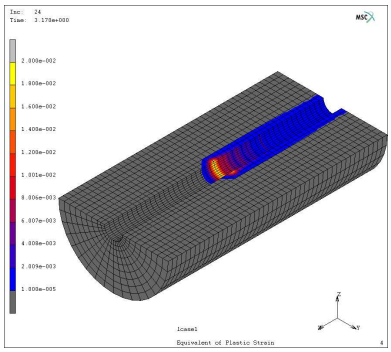

(d) equivalent plastic strain Before Peak Load

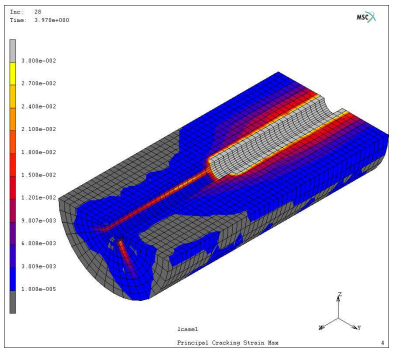

(e) Maximum Cracking Strain Post Peak Load

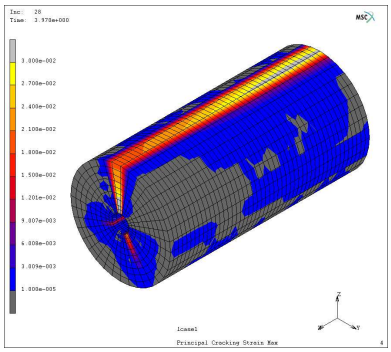

(f) Maximum Cracking Strain Post Peak Load

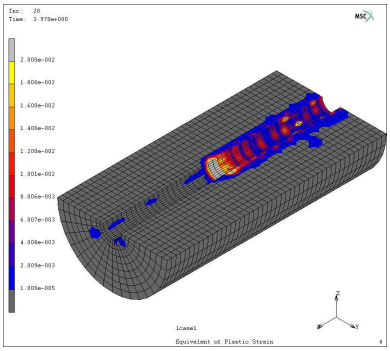

(g) Equivalent Plastic Strain Post Peak Load

Figure 5.61: 3D Detached Truss Model Strain

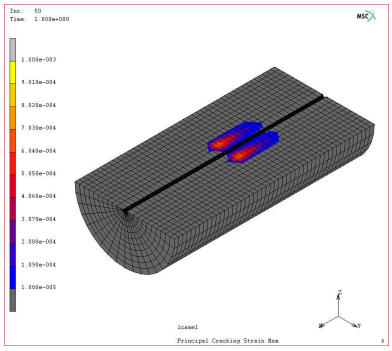

(a) Initial Maximum Cracking Strain

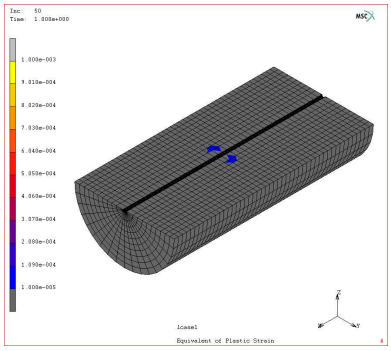

(b) initial equivalent plastic strain

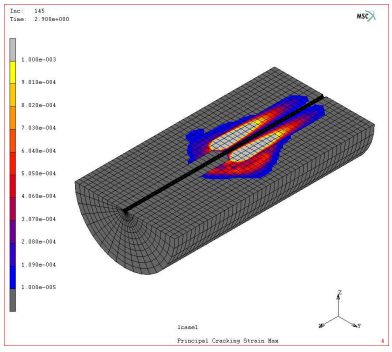

(c) Maximum Cracking Strain Before Peak Load

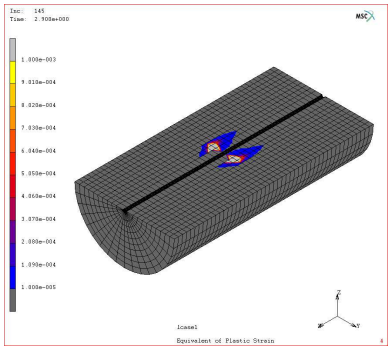

(d) equivalent plastic strain Before Peak Load

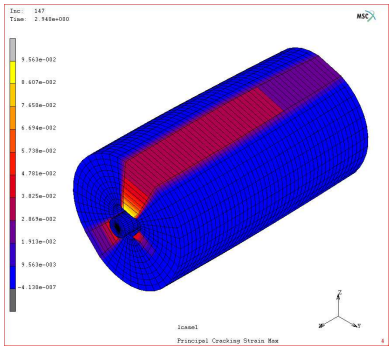

(e) Maximum Cracking Strain Post Peak Load

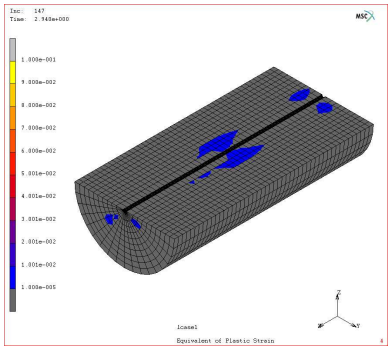

(f) Equivalent Plastic Strain Post Peak Load

Figure 5.62: 3D Solid Steel Model Strain

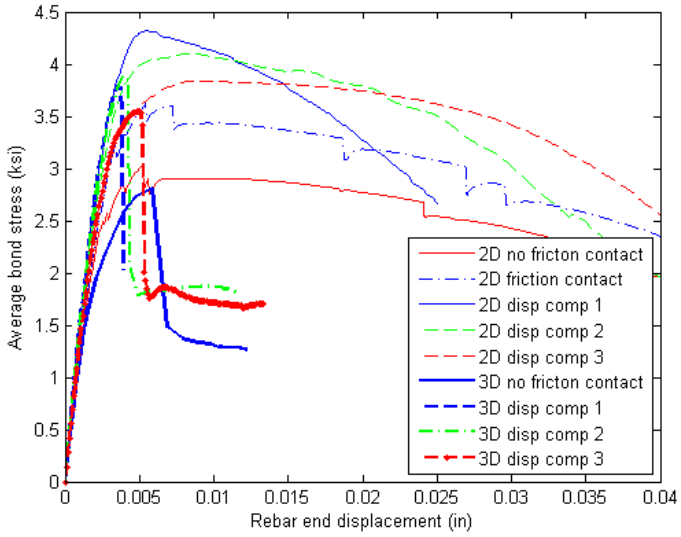

Figure 5.63: Bond Stress vs. Bar Displacement for All 3D Models with Ribs

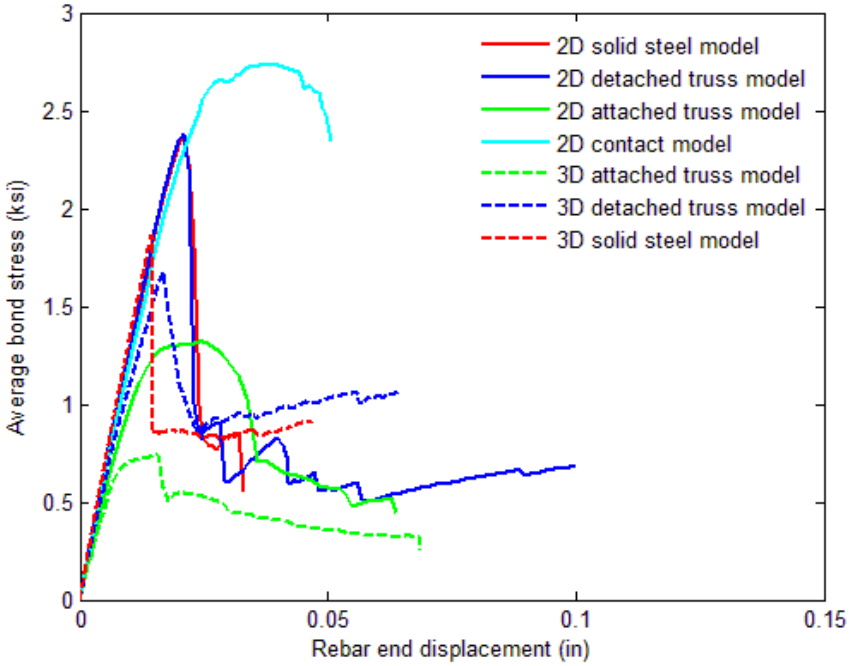

Figure 5.64: Bond Stress vs. Bar Displacement for 3D Models without Ribs

Chapter 6

Modeling Bond Tests

6.1 Introduction

Using results of FE analysis of idealized bond-zone and bond-zone test specimens, preferred methods for modeling bond-zone are identified in Chapter 5. These methods are used to model some of the bond specimens tested by Martin[108] with the objective of :

1). Investigating the impact of bond-zone design parameters on FE simulated response.

2). Generating data for comparison with experimental (both from traditional instrument and from X-ray CT images) data.

The results of simulating bond test specimens are presented as follows: Section 6.2 describes the models employed to conduct the analysis as well as the test specimen information. Section 6.3 presents detailed FE analysis results of pull-out test. Section 6.4 presents results of uniform tension test. Section 6.5 presents summary and conclusions.

6.2 Modeling UW Test Specimens

6.2.1 FE models assumptions

Contact model and full compatibility model are used to simulate the four test specimens. As found in Section 5.7, full compatibility model considering diameter of steel bar has comparable performance to predict the load displacement response. In real test simulation, the full compatibility model is bar-scale solid steel model presented in Section 5.7. In this model, the bar is modeled with continuum elements and full displacement compatibility between bar and concrete nodes.

6.2.2 Scope of FE Modeling

Martin [108] presented a comprehensive results of bond test with different specimen geometries and confinements. The test specimens are all concrete cylinder with one bar located

at center of the cylinder. Test category A to E are pull-out tests, test group G is uniform tension test. Four tests from different categories are simulated with the contact model and the bar-scale solid steel. Table 6.1 and Table 6.2 are the geometry and material properties of the specimens simulated. Some material properties are assumed as in parenthesis when not available. Table 6.3 is the load-displacement test result data.

As the test results are reflected on the load-displacement curves, these curves are used to compare the analysis results with test results. Quantitative comparisons were put on peak strength and peak displacement. In addition, the first major failure event was also compared. Table 6.4 presented simulated results with parameters corresponding to test data from Table 6.3. Detailed bond behavior for each simulation is discussed in the later part of this chapter.

Table 6.1: UW Test Specimens Geometry Data

Specimen	Cylinder dimension D*H(in)	Rebar size	Bonding length (in)	Confinement type
SA-0612-06-03-AL-A	D=6, H=12	No. 6 (d=0.75 in)	3	Aluminum jacket
SB-0612-08-06-NO-C	D=6, H=12	No. 8 (d=1 in)	6	No
SE-0612-08-03-W59-A	D=6, H=12	No. 8 (d=1 in)	2	0.059 in wire
SG-0424-06-24-NO-A	D=4, H=24	No. 6 (d=0.75 in)	24	No

Table 6.2: UW Test Specimens Material Properties

specimen	fc (ksi)	ft (ksi)	E (ksi)	Gf (lb/in)
SA-0612-06-03-AL-A	N/A(6)	N/A (0.5)	N/A(4400)	0.6 (average)
SB-0612-08-06-NO-C	6.143	0.568	N/A(4400)	0.6 (average)
SE-0612-08-03-W59-A	6.787	0.592	4910.6	0.6 (average)
SG-0424-06-24-NO-A	7.929	0.626	5282.8	0.6 (average)

Table 6.3: Load-displacement Test Data

Specimen	Peak load (kips)	Bar displacement at peak load (in)	Failure mechanism	Test name
SA-0612-06-03-AL-A	26.4	0.081	Pull-through	Pull-out
SB-0612-08-06-NO-A	51.1	0.04	splitting	Pull-out
SE-0612-08-03-W59-A	36.2	0.041	splitting	Pull-out
SG-0424-06-24-NO-A	N/A	N/A	N/A	Uniform tension

Table 6.4: Load-displacement Analysis Data

Specimen	Model	Peak load (kips)	Bar displacement at peak load (in)	Failure mechanism	Test name
SA-0612-06-03-AL-A	2D contact	28	0.05	Pull-through	Pull-out
	2D compatibility	37	0.4		
SB-0612-08-06-NO-A SB-0612-08-06-NO-B SB-0612-08-06-NO-C	2D contact	50	0.035	splitting	Pull-out
	2D compatibility	44	0.025		
	3D contact	45	0.025		
	3D compatibility	35	0.020		
SE-0612-08-03-W59-A SE-0612-08-03-W59-B	2D contact	35	0.045	splitting	Pull-out
	2D compatibility	45	0.040		
	3D contact	35	0.045		
	3D compatibility	42	0.035		
SG-0424-06-24-NO-A	3D contact	N/A	N/A	N/A	Uniform tension

6.3 Modeling Pull-out Test

6.3.1 Specimen SA

Specimen SA is heavily confined specimen with two inch thick of aluminum jacket confining the concrete cylinder during testing. The experimental data show ductile pull-through failure, with the gradually descending part of load displacement response instead of brittle splitting response. Under high confinement, the bar was pulled through from the specimen instead of splitting of the specimen cylinder. The cracking is mainly secondary cracking in local bond-zone. The failure behavior of this specimen is largely dependent on the compression side. Under this consideration, only two-dimensional results are presented as

the difficulty in obtaining converged post-peak response. Considering no big difference exist between 2D model and 3D model for this high level confinement, the use of 2D results for the comparison is reasonable. Figure 6.1 shows the comparison of simulated responses and lab test results. The contact model has peak bond strength comparable with test results, but with initial stiffness almost two times higher than the initial stiffness from test results. The 2D bar-scale model has peak strength approximately 40% higher than test results. The initial stiffness from the bar-scale model is same with the rib-scale contact model. The higher stiffness from analysis is possibly due to the actual material properties or test measurement errors. Figure 6.2 and 6.3 show the crack and yielding propagation at initial load, pre-peak load and post-peak load from 2D rib-scale contact model. The initial cracking is approximately 45 degree to the bar axis under high confinement. As load increases, the cracking direction approaches to parallel with bar axis which means separation of concrete from bar and rib surface. At residual load stage, local cracking direction changes to perpendicular to the bar axis which shows shear-off behavior of concrete between ribs. This stage also shows significant slippage between bar and concrete. Figure 6.5 and 6.6 show the crack propagation from 2D bar-scale model. The cracking initiation is same with rib-scale contact model, with 45 degree to bar axis beginning from bond near load end. As load increases, the cracking direction near load end changes to less than 45 degree, and new developed cracks with direction 45 degree to bar axis was propagated toward the free end. At residual load stage, all cracks on the interface elements have direction approximately parallel with bar axis which means the radial separation between concrete and the bar. In all models, the minimum plastic strain has constant direction of 45 degree to the bar axis toward the free end of the specimen throughout the load stage. Figure 6.4 shows the post-peak crack and yielding propagation from 3D contact model. The splitting is not extended to the outer surface of the specimen due to high confinement.

6.3.2 Specimen SB

Specimen SB is unconfined specimen and the test results show brittle splitting failure, as shown in the load-displacement response curve 6.7. For this unconfined specimen, cracking propagation for the 2D contact model is shown in Figure 6.8 and bar-scale model can be found in section 5.7.2.7. The in-plane cracking near bond-zone has similar propagation patterns with specimen SA. The initial cracking was around 45 degree to the bar axis and propagate from the loaded end to the free end. As loading goes on, the cracking direction changes from 45 degree to parallel to the bar axis for the bond-zone layer of concrete on outer surface of the bar. However, the shear-off of concrete near ribs happens at different load stage for confined model and unconfined model. For unconfined model specimen SB, the shear-off of concrete between ribs happens at residual post-peak load stage. For confined specimen SA, this shear-off behaviors happens earlier at pre-peak load stage. This is because the different failure mechanism for these two specimens. Specimen SB has splitting failure mode but specimen SA has pull-through failure mode. The radial separation between concrete and steel happens earlier for the unconfined specimen. The different failure mechanism for confined and unconfined specimen show the different dominance of bond strength. Bond strength for unconfined specimen SB is dominant by splitting but bond strength for confined specimen SA is dominant by shear-off of concrete between ribs. Figure 6.9 shows the propagation of principal cracking strain and equivalent plastic strain for 3D contact model. Figure 6.9(c) shows the longitudinal splitting from 3D model. 3D model shows the local cracking cone around ribs and the hoop direction strain propagation and localization.

6.3.3 Specimen SE

Specimen SE is moderately confined with 0.059 inch diameter steel wire. The respond is between specimen SE and specimen SA. The major failure event is splitting behavior, but the splitting is controlled due to the confinement. This can be seen from the tested load-displacement response in Figure 6.10 with the gradually descending post-peak branch.

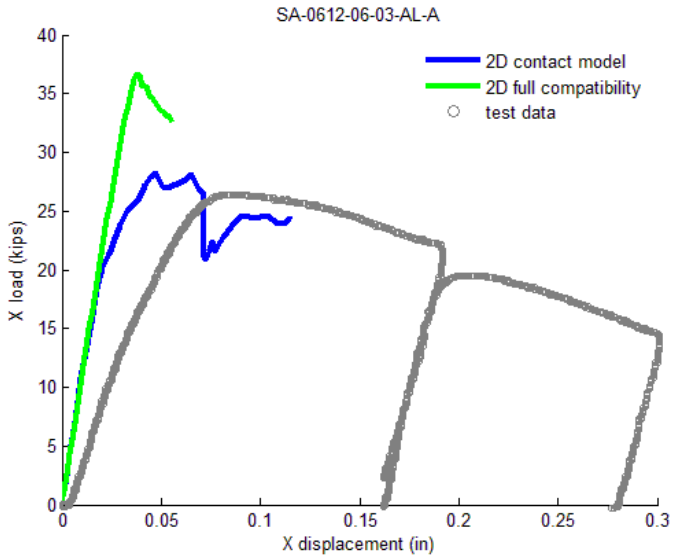

Figure 6.1: Load displacement response for specimen SA

Figure 6.11 and 6.13 show the simulated principal cracking strain and equivalent plastic strain at before peak load and post peak load stage from 2D contact model. The in-plane cracking propagation is very similar to specimen SA. However, specimen SE shows splitting propagating through out the specimen surface, which is different from high confinement specimen SA. Figure 6.14 and 6.15 show the simulated principal cracking strain and equivalent plastic strain at before peak load and post peak load stage from 2D bar-scale model. The behavior is very similar to specimen SA except the longitudinal splitting. Figure 7.1(d) shows the principal cracking strain from 3D contact model with three localized splitting cracks.

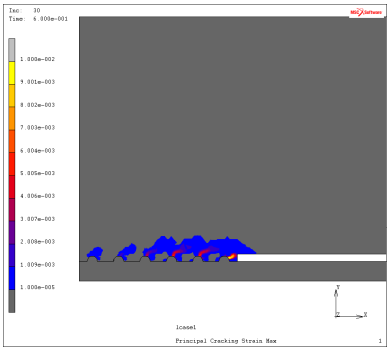

(a) Maximum Cracking Strain at Initial Stage

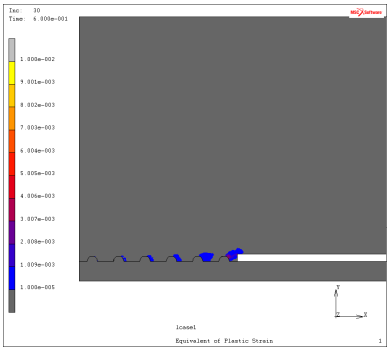

(b) Equivalent Plastic Strain at Initial Stage

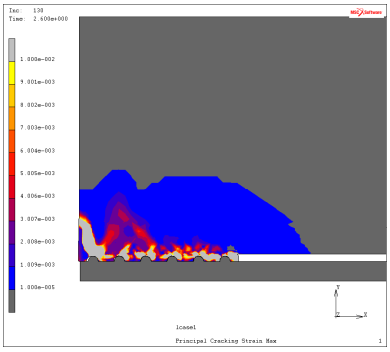

(c) Maximum Cracking Strain at Pre-Peak Load

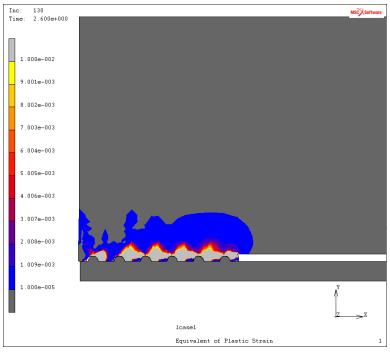

(d) Equivalent Plastic Strain at Pre-Peak Load

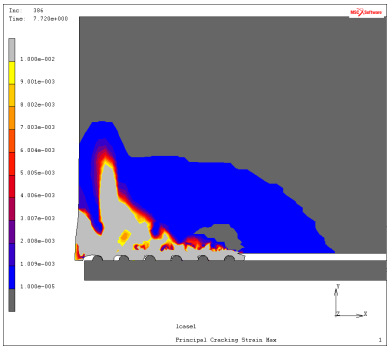

(e) Maximum Cracking Strain at Post-Peak Load

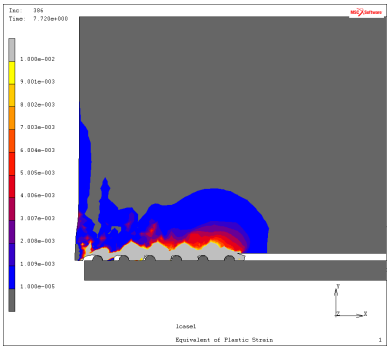

(f) Equivalent Plastic Strain at Post-Peak Load

Figure 6.2: Specimen SA Two-dimensional Contact Model

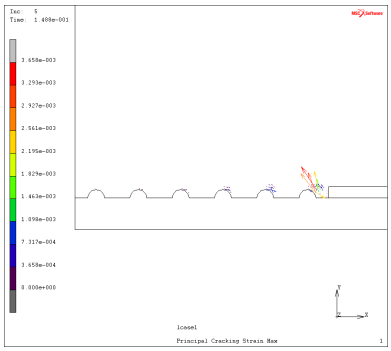

(a) Maximum Cracking Strain at Initial Stage

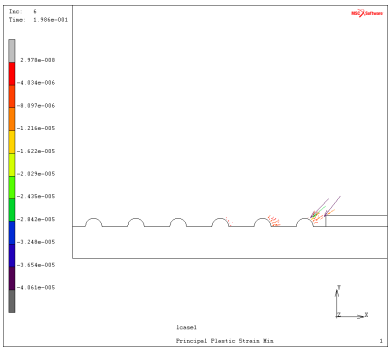

(b) Minimum Plastic Strain at Initial Stage

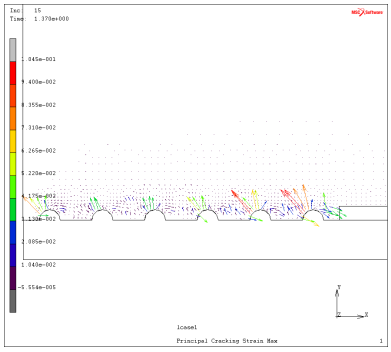

(c) Maximum Cracking Strain at Pre-Peak Load

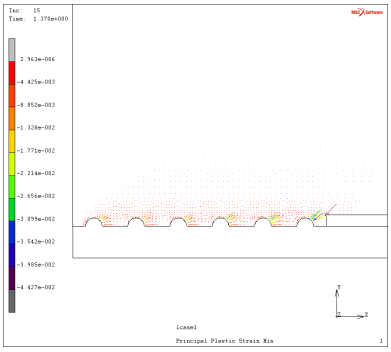

(d) Minimum Plastic Strain at Pre-Peak Load

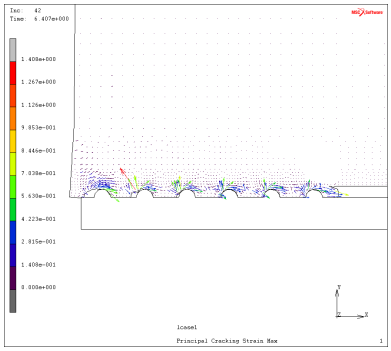

(e) Maximum Cracking Strain at Post-Peak Load

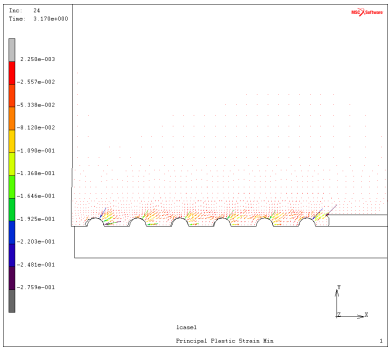

(f) Minimum Plastic Strain at Post-Peak Load

Figure 6.3: Specimen SA Two-dimensional Contact Model Vector Plot

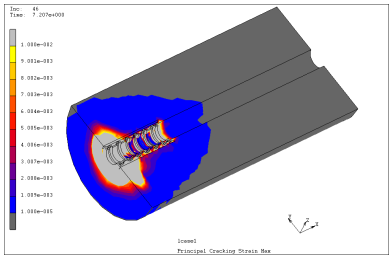

(a) Maximum Cracking Strain at Post-Peak Load

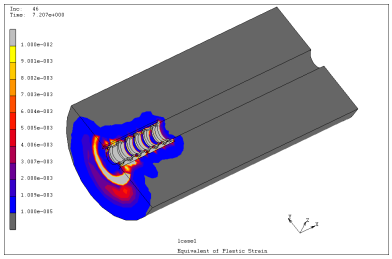

(b) Equivalent Plastic Strain at Post-Peak Load

Figure 6.4: Specimen SA Three Dimensional Contact Model

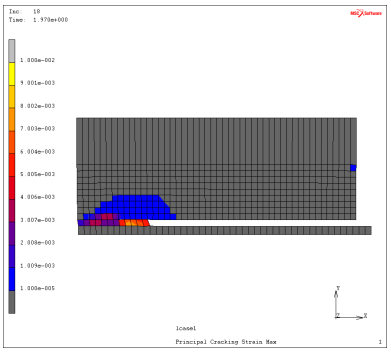

(a) Maximum Cracking Strain at Pre-Peak Load

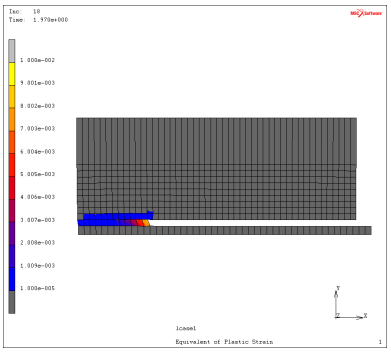

(b) Equivalent Plastic Strain at Pre-Peak Load

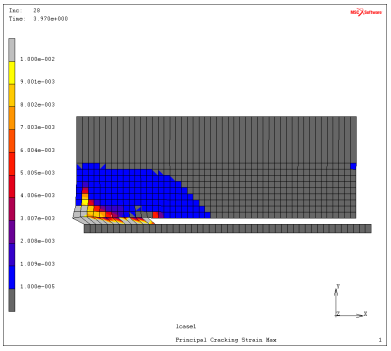

(c) Maximum Cracking Strain at Post-Peak Load

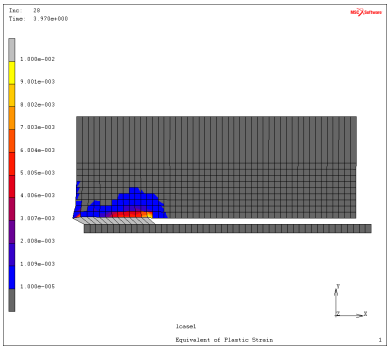

(d) Equivalent Plastic Strain at Post-Peak Load

Figure 6.5: Specimen SA Two-dimensional Continuum Steel Model

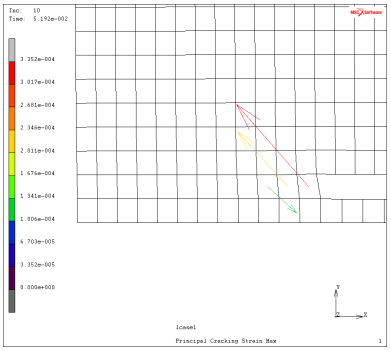

(a) Maximum Cracking Strain at Initial Load

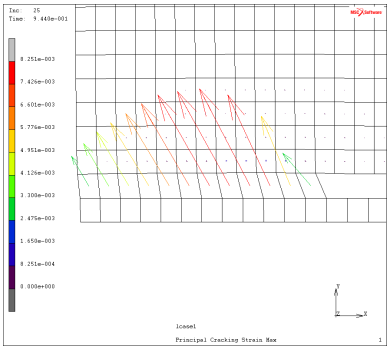

(b) Maximum Cracking Strain at Pre-Peak Load

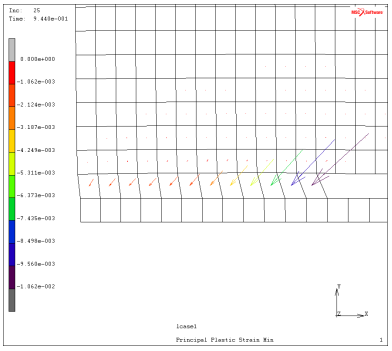

(c) Minimum Plastic Strain at Pre-Peak Load

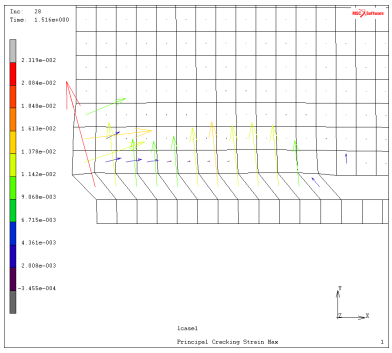

(d) Maximum Cracking Strain at Post-Peak Load

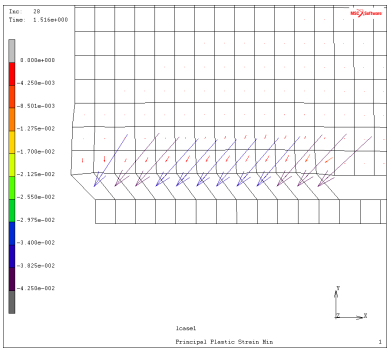

(e) Minimum Plastic Strain at Post-Peak Load

Figure 6.6: Specimen SA Two-dimensional Continuum Steel Model Strain Vector Plot

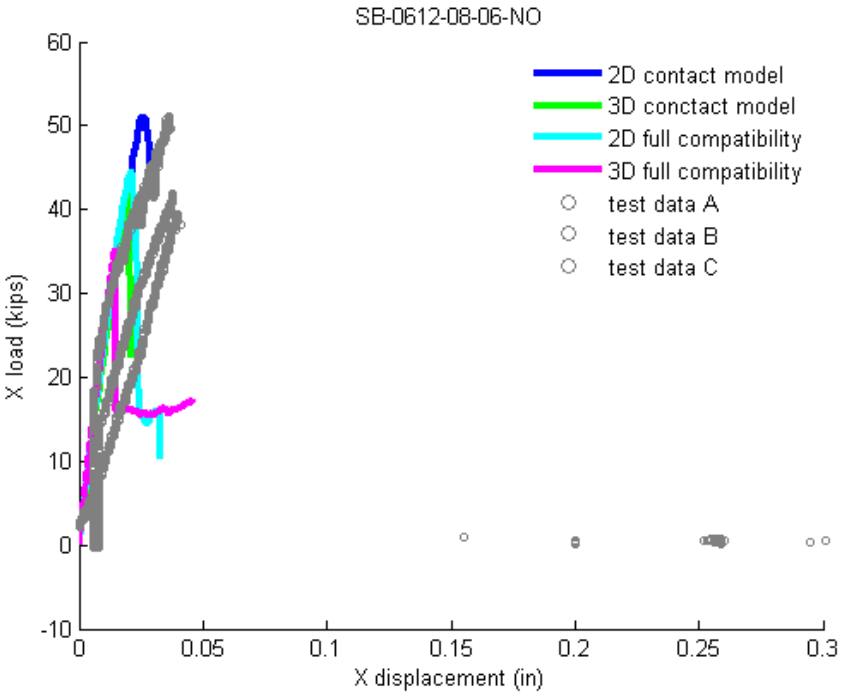

Figure 6.7: Load Displacement Response for Specimen SB

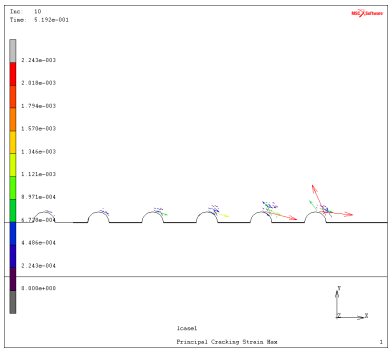

(a) Maximum Cracking Strain at Initial Load

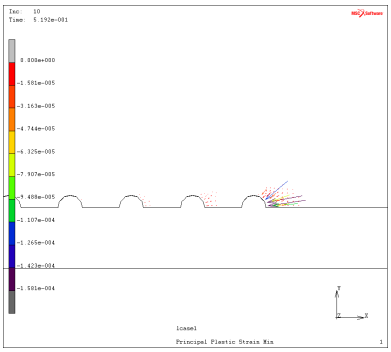

(b) Minimum Plastic Strain at Initial Load

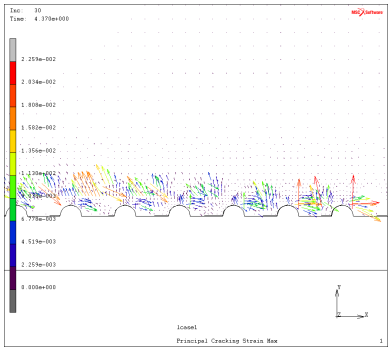

(c) Maximum Cracking Strain at Pre-Peak Load

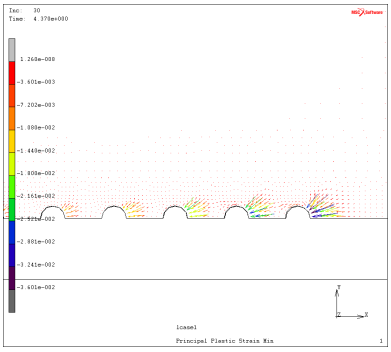

(d) Minimum Plastic Strain at Pre-Peak Load

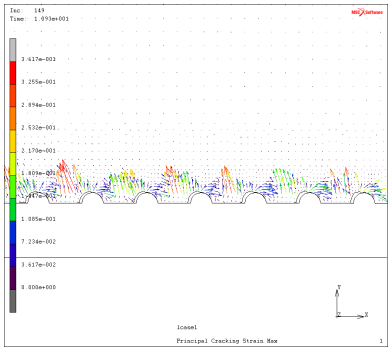

(e) Maximum Cracking Strain at Post-Peak Load

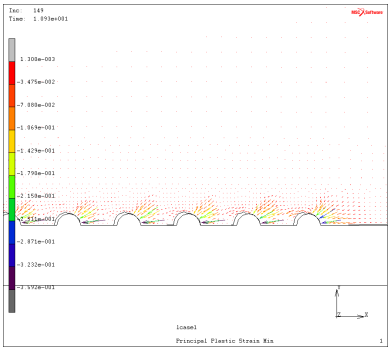

(f) Minimum Plastic Strain at Post-Peak Load

Figure 6.8: Specimen SB Two-dimensional Contact Model Strain Vector Plot

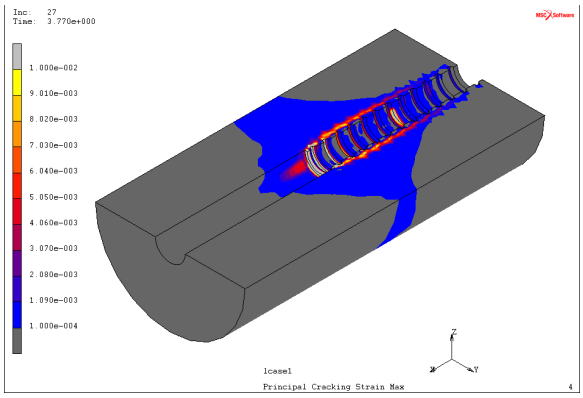

(a) Maximum Principal Cracking Strain at Pre-Peak Load

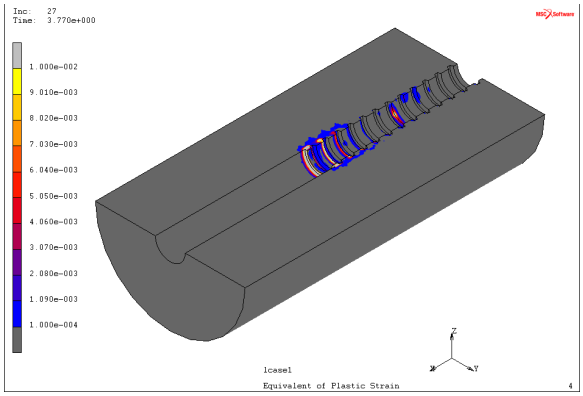

(b) Equivalent Plastic Strain at Pre-Peak Load

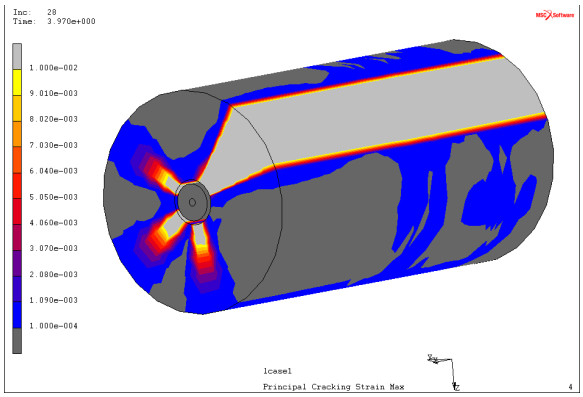

(c) Maximum Principal Cracking Strain at Post-Peak Load

Figure 6.9: Specimen SB 3D Contact Model

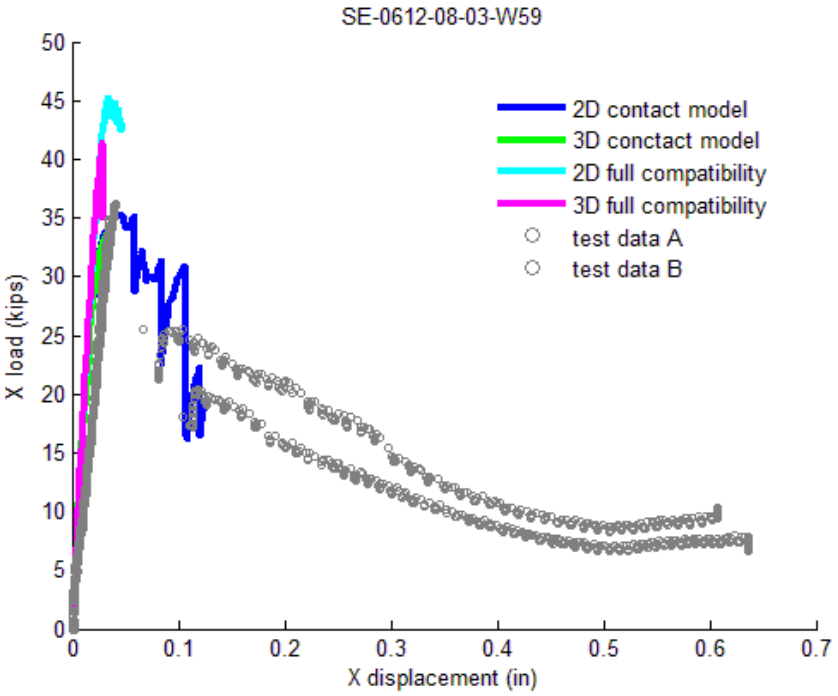

Figure 6.10: Load Displacement Response for Specimen SE

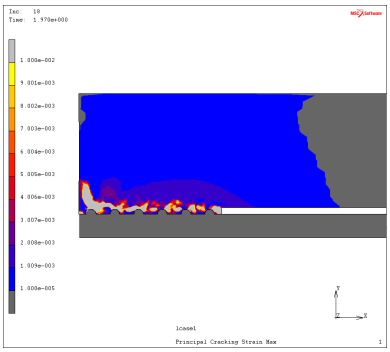

(a) Maximum Cracking Strain at Pre-Peak Load

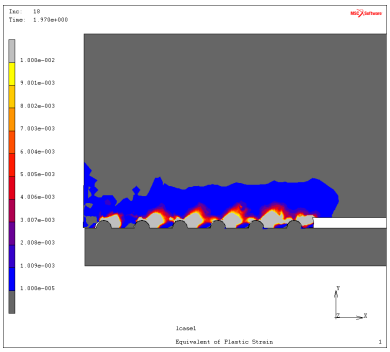

(b) Equivalent Plastic Strain at Pre-Peak Load

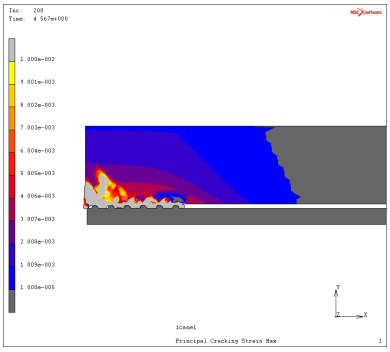

(c) Maximum Cracking Strain at Post-Peak Load

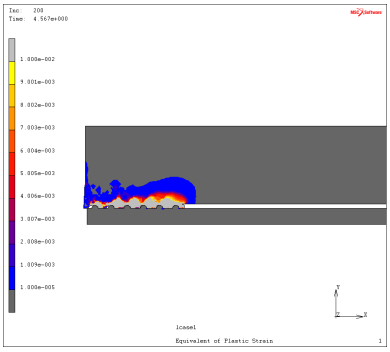

(d) Equivalent Plastic Strain at Post-Peak Load

Figure 6.11: Specimen SE 2D Contact Model

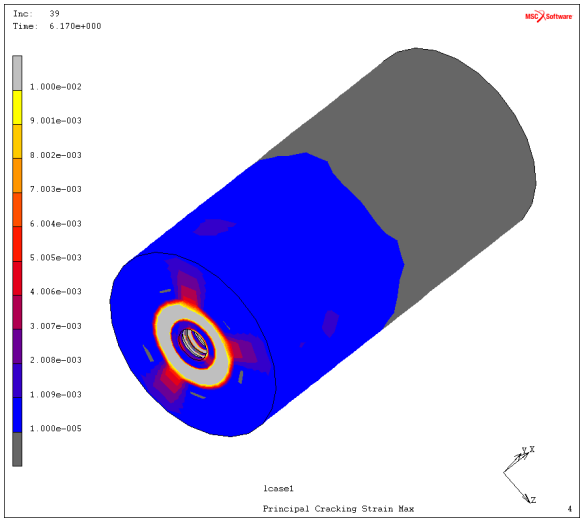

Figure 6.12: Specimen SE 3D Contact Model Splitting Failure

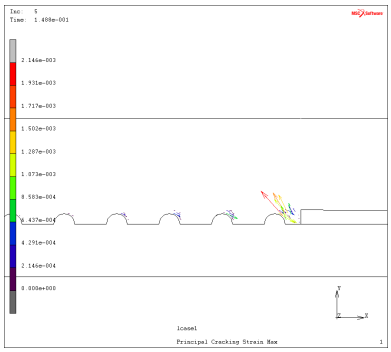

(a) Maximum Cracking Strain at Initial Load

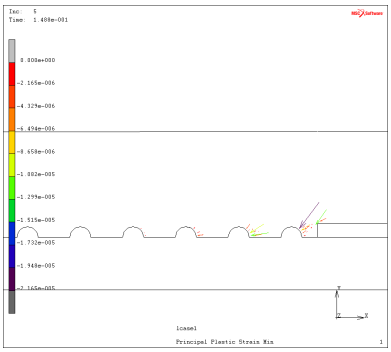

(b) Minimum Plastic Strain at Initial Load

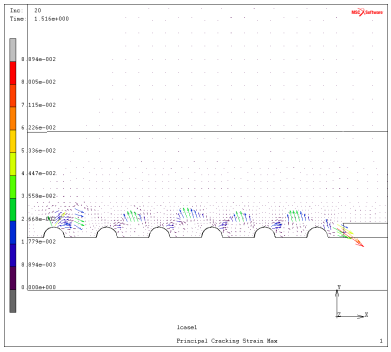

(c) Maximum Cracking Strain at Pre-Peak Load

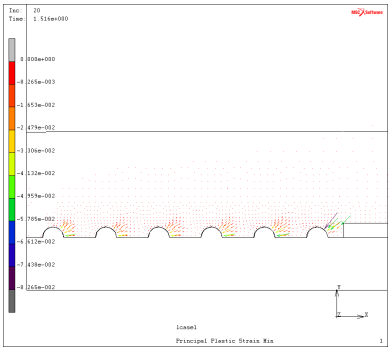

(d) Minimum Plastic Strain at Pre-Peak Load

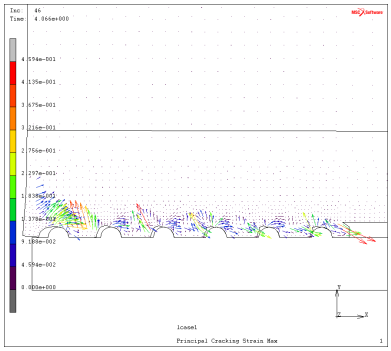

(e) Maximum Cracking Strain at Post-Peak Load

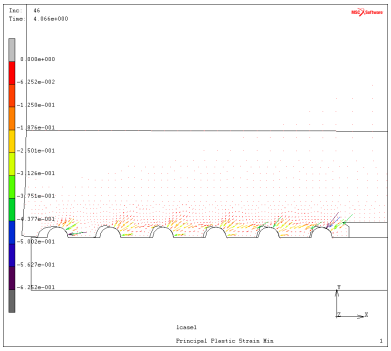

(f) Minimum Plastic Strain at Post-Peak Load

Figure 6.13: Specimen SE Two-dimensional Contact Model Strain Vector Plot

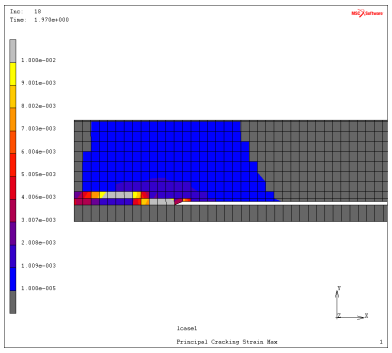

(a) Maximum Cracking Strain at Pre-Peak Load

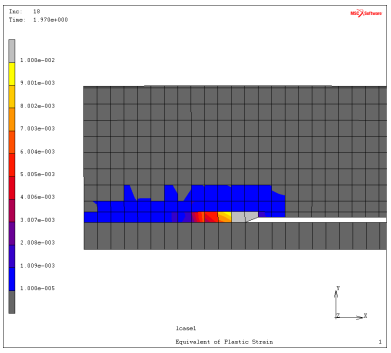

(b) Equivalent Plastic Strain at Pre-Peak Load

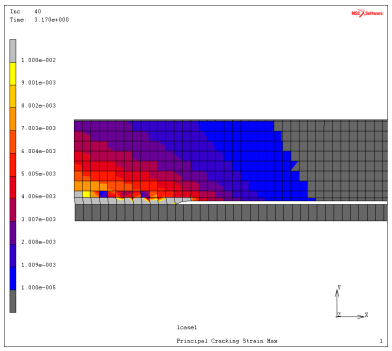

(c) Maximum Cracking Strain at Pre-Peak Load

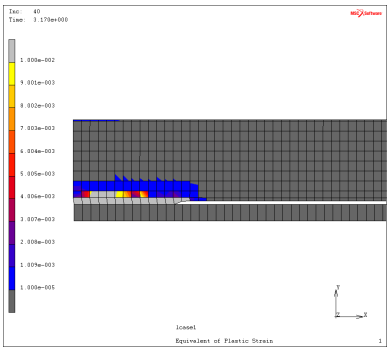

(d) Equivalent Plastic Strain at Post-Peak Load

Figure 6.14: Specimen SE 2D Continuum Steel Model

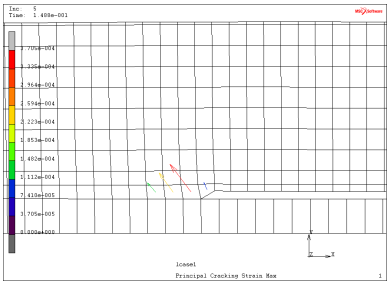

(a) Maximum Cracking Strain at Initial Load

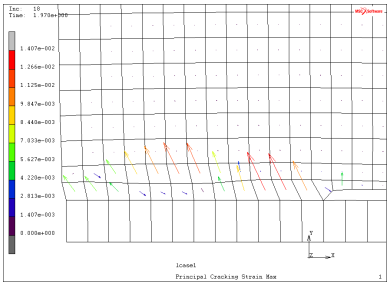

(b) Maximum Cracking Strain at Pre-Peak Load

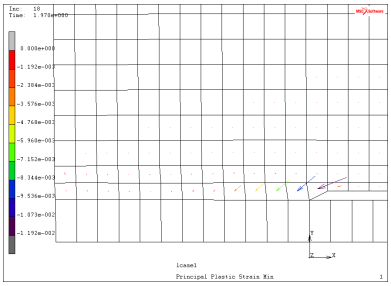

(c) Minimum Plastic Strain at Pre-Peak Load

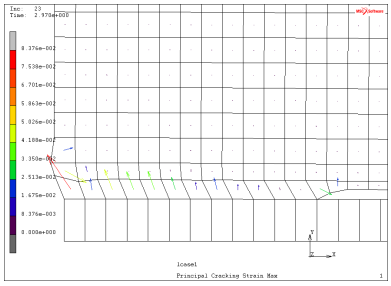

(d) Maximum Cracking Strain at Post-Peak Load

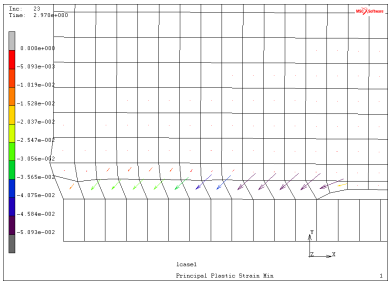

(e) Minimum Plastic Strain at Post-Peak Load

Figure 6.15: Specimen SE Two-dimensional Continuum Steel Model Strain Vector Plot

6.4 Modeling Uniform Tension Test

In uniform tension test, transverse cracking initiator is set spacing at every 4 inch. Test results show all transverse cracking happen simultaneously, simulation results show transverse cracking happen progressively, as shown in Figure 6.16 of load-displacement responses and Figure 7.2(c). Two cracks happen first, one is located at middle, another is located at quarter point along the specimen axis. The second stage of cracking happens at another quarter point of specimen. The third stage cracking happens at near end of specimen, adjacent to the first quarter point cracking. Lastly there is fourth stage of cracking between the first two cracks. The loads at development of each stage of cracks are corresponding to the stiffness change in the load-displacement response. Crack one corresponds to load step 8, crack two corresponds to load step 13 and crack three corresponds to load step 23 in Figure 6.16. The transverse cracking has approximately equal spacing except last cracking. The total number of transverse cracks is the same with test results.

The simulation results show initial internal secondary cracking and local longitudinal splitting at location near each transverse cracking induced free surface, as shown in Figure 6.17(a) and Figure 6.17(c). The in-plane secondary cracking happens before the development of transverse cracking, and longitudinal splitting follows the development of transverse cracking.

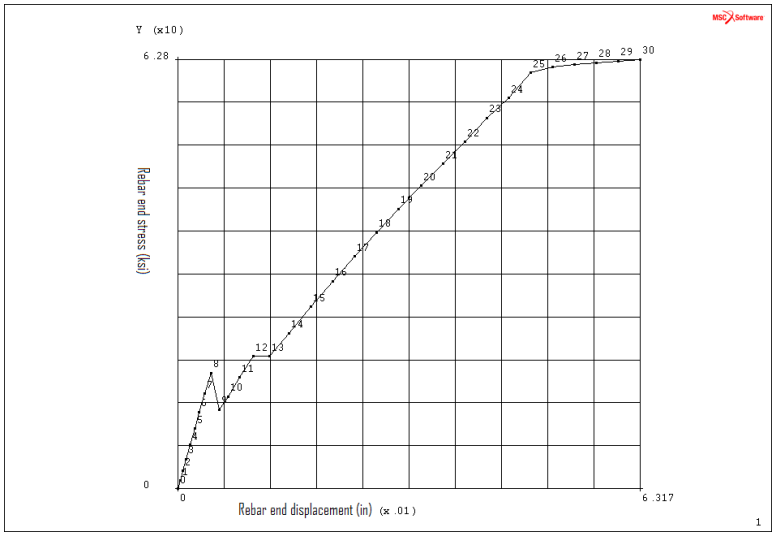

Figure 6.16: Uniform Tension Test Rebar End Stress vs. Rebar End Displacement

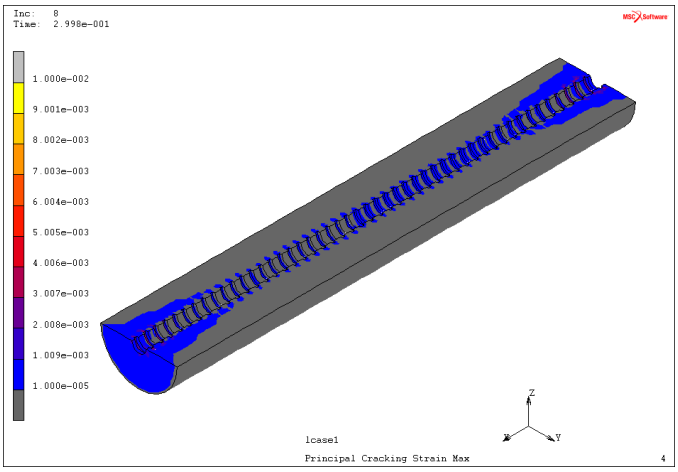

(a) Internal Cracking Before Initiation of Transverse Cracking

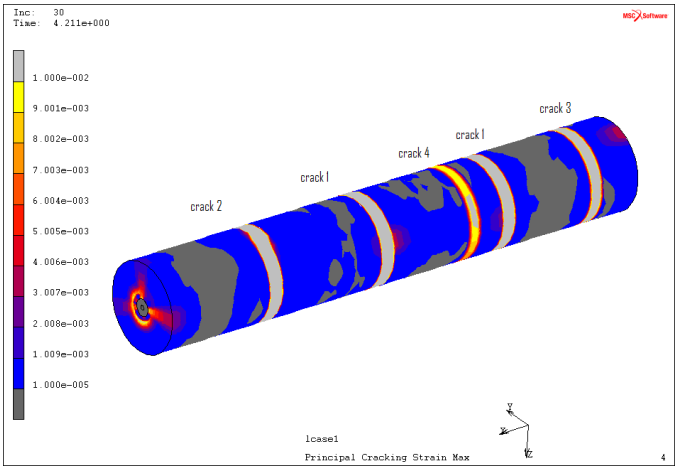

(b) Final Principal Cracking Strain

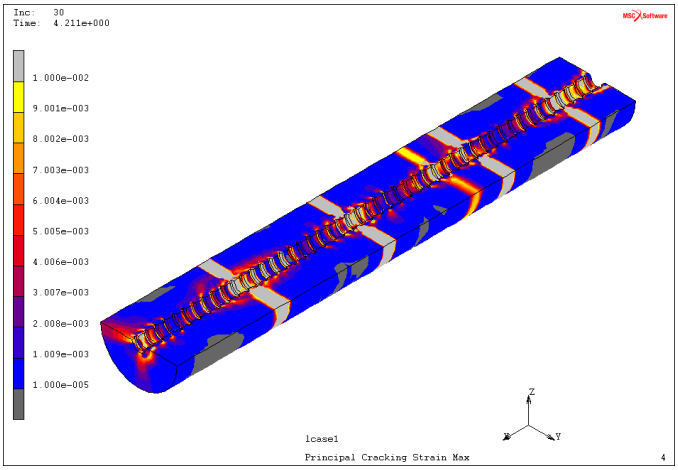

(c) Final Principal Cracking Strain Section View

Figure 6.17: Cracking Propagation and Pattern for Uniform Tension Specimen SG

6.5 Summary

This chapter presented results of analyzing bond test specimens using the selected FE models presented in Chapter 5. Three pull-out specimens representing high confinement, moderate confinement and no-confinement and one unconfined uniform tension specimen were analyzed. The global load-displacement responses were compared with lab observed results.

For **pull-out** tests, all analysis results show initial stiffness larger than that from test data, especially specimen SA. The bond strength from rib-scale contact model was very close to the test data for all three specimens. For confining specimens SA and SE, the bar-scale solid steel models results 10-30% higher bond strength than the test data. For the unconfined specimen SB, the bar-scale solid steel models results 10-20% lower bond strength than the test data. In addition, the bar-scale models have a poor representation of cracking localization due to full nodal displacement compatibility between concrete and the steel bar. All analyses have captured the failure behavior of the three specimens.

All analyses show the in-plane cracking initiated at start of bonding region near load end, with direction of 45 degree to the bar axis. This initial in-plane cracking happens at all three specimens with different confinement levels. However, the progression of the local in-plane cracking and global splitting are dependent on the confinement levels. For specimen with no or lower confinement, the bond strength is dominant by the longitudinal splitting. For specimen with high confinement, the bond strength is dominant by shearing of concrete between ribs.

For uniform **tension** test, both rib-scale contact model and bar-scale model have shown major transverse cracking and longitudinal splitting. In addition, the contact model shows regular secondary cracks inclined to bar axis. The locations of the major transverse cracks and spacings between cracks are very close the the lab test results, although lab test showed simultaneous development of the transverse cracks, but FE analyses showed progressive development of the major transverse cracks.

Chapter 7

Summaries of Bond Behavior from Image Analyses and FE Analyses

7.1 Introduction

The results of the image analyses presented in Chapter 4 and FE analyses presented in Chapters 5 and 6 provide additional information about bond-zone response. Basic image processing algorithms provide visualization of specimen damage under progressive loading while motion estimation provides the estimated 3D displacement field for the specimen. Finite element analyses provide the simulated concrete damage field, including cracking and crushing under the progressive loading, as well as the simulated displacement, strain, and stress fields. In this chapter, results from previous research, image analyses and FE analyses are compared and combined to develop conclusions about bond response mechanisms and damage progression corresponding to global response.

A pull-out test specimen, SE, and a uniform tension test specimen, SG, tested by researchers at the University of Washington [108] and discussed in chapter 4 and 6, were used as the comparison samples. Bond test specimen SE is a moderately, spirally confined specimen that represents an anchorage bond-zone in a RC structural component. Bond test specimen SG is an unconfined specimen that represents a flexural response zone in a RC structural component. Detailed results from X-ray CT image analyses and FE analyses for specimens SE and SG are presented in Chapters 4 and 6. Figures 7.1 and 7.2 show pictures of the laboratory tests, X-ray images and FE results of the two specimens. It should be noted that the specimens tested and subjected to X-ray CT imaging and the specimens shown in the laboratory pictures have same design and were subjected to the same loading conditions. However, they are not the same specimens.

In this chapter, Section 7.2 summarizes global bond behavior observed by past re-

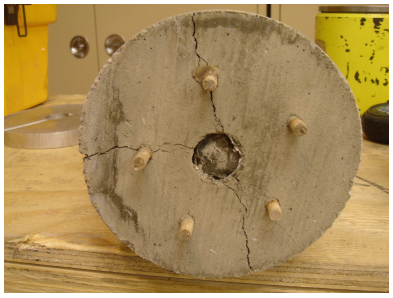

(a) Laboratory Picture Following Test

(b) Laboratory Picture Following Test

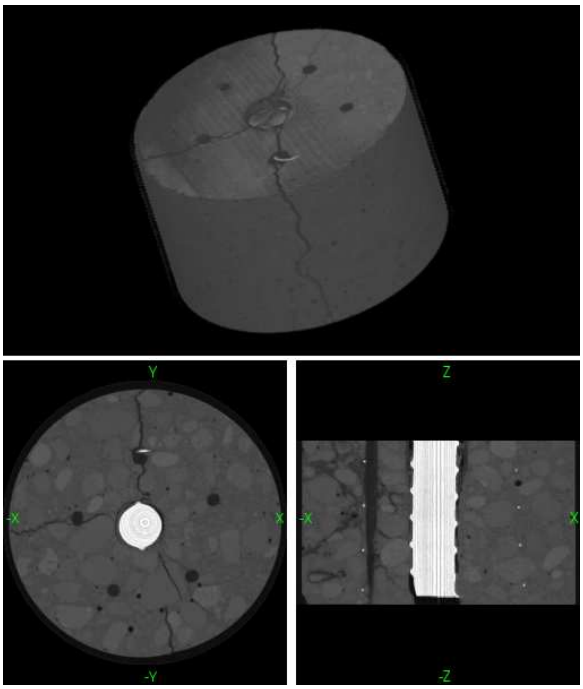

(c) X-ray CT Images at Post-peak Load

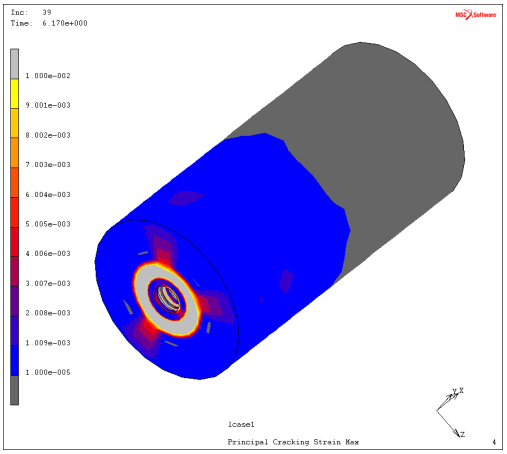

(d) Principal Cracking Strain from FE Analysis at Post-peak Load

Figure 7.1: Behavior of Pull-out Test

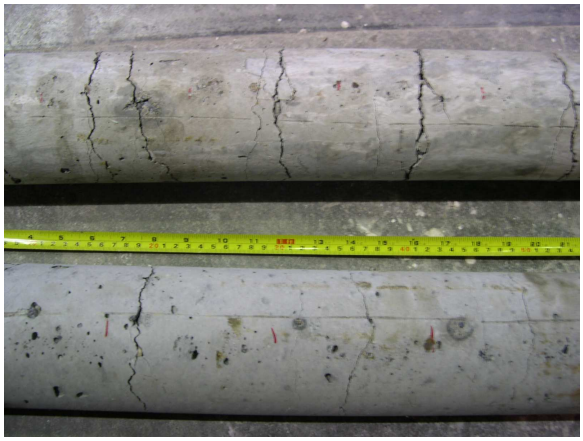

(a) Laboratory Picture Following Test

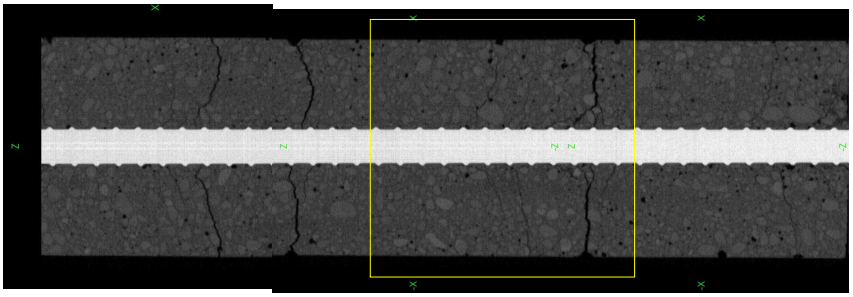

(b) X-ray CT Image Following Test

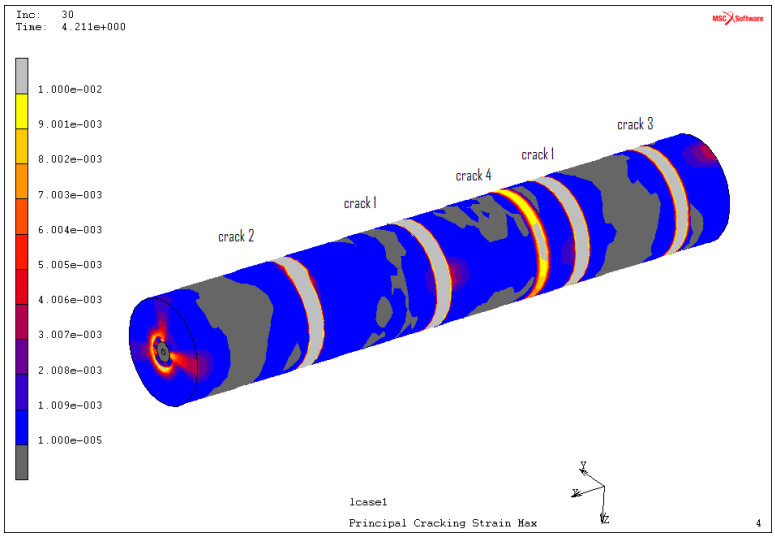

(c) Principle Cracking Strain at the End of FE Analysis. The order in which primary cracks developed is identified

Figure 7.2: Behavior of Uniform Tension Test

searchers and determined from image and FE analyses as part of this study. Section 7.3 focuses on damage progression in the local bond-zone. Section 7.4 compares deformation of the bond test specimens from image and FE analyses, as well as test data from previous research. Section 7.5 presents an analytical model based on the newly developed understanding of bond-zone behavior.

7.2 Global Observations of Bond Response

Previous research, image analyses, and FE analyses results provide information about "global response", which for the current study is considered to include load-displacement response, global damage patterns and the failure mode of the test specimens. These are summarized first for the pull-out specimen and then for the uniform tension specimen.

7.2.1 Pull-out Test

For the pull-out test, the test results from previous research [50, 73, 107, 108] provide a wealth of data addressing load-displacement, global damage patterns and failure models. In these tests, steel is typically elastic, as was the case for the test data used in this study. Load-displacement response is defined in terms of average bond stress over a relatively short embedment length versus slip of the unloaded end of the bar. Previous research shows that the bond stress versus bar slip response history is characterized by an initial, essentially linear stage that extends to approximately 80% of the maximum strength, a nonlinear stage that continues to peak strength in which significant stiffness is lost, a post-peak stage in which there is rapid strength loss, and a final residual-strength phase in which a low level of bond stress (<10% of bond strength) is maintained at large slip levels. A number of parameters influence the load-displacement response, these are discussed in Chapter 2. Confinement is the most critical parameter that controls the global response. Specimens without confinement typically exhibit brittle response with rapid loss of bond strength and minimum residual bond strength; specimens with confinement typically exhibit more ductile behavior with higher bond strength, gradual loss of bond strength; and some residual bond

strength. This behavior was observed in laboratory tests at UW and FE analyses presented in Chapter 6. For specimen SE, the FE analyses show very close pre-peak behavior with the lab test results, the pre-peak bond stiffness from analyses is slightly larger than test results. The peak bond stress and bar slip at the peak stress from laboratory tests and FE analyses are shown in Table 7.1. The difference in peak bond stress between the contact models and test results are less than 5%, and the difference in peak bond stress between bar-scale models and test results are approximately 20%. Due to the high level of nonlinearity developed in the concrete material models and geometric contact models, the FE analyses did not converge to a solution in the residual load stage of the tests. However, the global and local interior damage patterns at the residual load level is available from X-ray CT images of the specimen.

Table 7.1: Test and FE Analysis Results for Pull-out Specimen SE

	Test Results	2D Contact Model	3D Contact Model	2D Continuum Steel Model	3D Continuum Steel Model
Peak Bond Stress (ksi)	3.84	3.71	3.71	4.77	4.46
Bar-slip at Peak Bond Stress (in)	0.041	0.045	0.045	0.040	0.035

The pull-out test specimens have been observed as to fail due to longitudinal splitting of concrete, pull-out of the anchorage bar and bar yielding, with the failure mode determined primarily by the confinement provided by cover concrete and trasverse steel [50, 108]. Splitting failure, resulting in low strength and brittle response, is typically associated with low level of confinement. Pull-out and bar yielding resulting in high strength and ductile response, are typically associate with high level of confinement or long bonded length [108]. Figure 7.1 shows the failure mode of the pull-out specimen SE from laboratory test camera pictures, X-ray CT imaging pictures and FE analysis results. For this slightly confined specimen, the concrete cylinder was split into three pieces from the free end. The slip of the bar at the free end can be seen from all three types of images. Global response from

image analysis, FE analysis, laboratory test and previous research findings is consistent.

7.2.2 Uniform Tension Test

For the uniform tension test, response is dominated by transverse cracking perpendicular to the bar axis. Figure 7.2 shows cracking of the uniform tension test specimen from laboratory test pictures, X-ray CT images and FE analysis results. All show multiple major transverse cracks. It should be noted that the crack initiators for the specimen in the laboratory picture were spaced at 4 inches and the crack initiators for the specimen in the X-ray CT image were spaced at 6 inches. Crack initiators were not included in the FE analysis model. The actual spacing of the stabilized major transverse cracking was approximately 4 inches in the laboratory specimen pictured (Figure 7.2), 6 inches in the X-ray CT imaged specimen, and 5 inches in the FE model. In the FE analysis, the major transverse cracks developed progressively as load increases; the location of cracks is due to the random numerical rounding errors of computer. However, in the laboratory, simultaneous development of these transverse cracking was observed. It is possible that the load control in laboratory failed to capture the progressive cracking.

7.3 Bond-zone Damage Progression

The X-ray CT images and FE analyses using rib-scale models test specimens provide information about damage patterns and damage progression in the local bond-zone. These data are much less easily collected using traditional test methods and instrumentation, thus few data from previous tests exist. For the pull-out test specimens, the bond-zone damage included conical secondary cracking of concrete near the bar ribs, splitting cracks parallel to the bar axis (in a 2D section cut through to specimen parallel to the bar axis, these cracks are seen in the plane of the cut and inclined with respect to the axis of the bar), and crushing of concrete in front of the ribs. Here, this damage is assumed to be presented by the maximum principal strain, which quantifies the extent of cracking, and the minimum principal strain, which quantifies the extent of plastic deformation due to concrete crushing.

For flexural tension tests, bond-zone damage included inclined secondary cracking as well as primary transverse cracking perpendicular to the bar axis. Since, for the uniform tension test, response was determined primarily by cracking; only maximum principal strain data were used to quantify damage.

7.3.1 Pull-out Test

As previously noted, the global load-displacement response of pull-out test specimens is characterized by an initial, almost linear stage, a nonlinear pre-peak stage, post-peak stress deterioration stage and a residual stage with low bond stress and large bar slip. This global response is determined by local bond-zone damage including concrete cracking and crushing. Thus, improved understanding of the local damage patterns can contribute to improved understanding of bond-zone response. Previous experimental research [18, 73] investigated internal cracking by cutting specimens open after testing and observing internal cracks near the bar surface. Previous numerical analyses [73, 120] using discrete and smeared crack models also captured the local bond-zone cracking, noting inclined secondary cracks with respect to the bar axis at angles between 50 and 70 degrees. In this study, propagation of both concrete cracking and crushing through the load history were summarized from image and FE analyses.

For Rib-scale FE analyses, damage progression may be monitored continuously throughout the load history. For imaged specimens, images are available at critical load stages. These critical load stages are subsequently referred to as load levels 1 (860 lbs), 2 (21,790 lbs), 3 (16,800 lbs) and 4 (7,800 lbs), corresponding to initial load, pre-peak load, post-peak load, and residual load points on the load-displacement response curve (Figure 7.3). The displacement field calculated from the image data is the displacement between load levels 1 and 2, 2 and 3, and 3 and 4. These are referred to as the displacement at the pre-peak load level, post-peak level and residual load level. Of particular interest here is the investigation of local bond-zone damage at the pre-peak and post-peak load levels. The strain field at

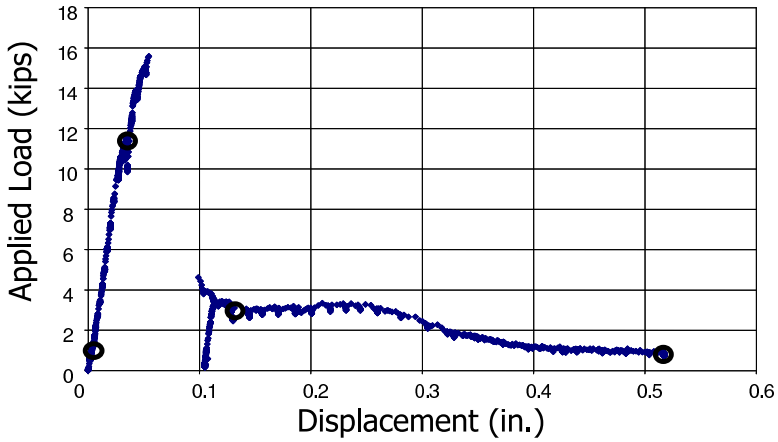

Figure 7.3: Pull Out Test Load-displacement Response [96, 108]

the pre-peak load level exposes the development of concrete cracking and crushing in the vicinity of concrete-steel interface. The post-peak load level exposes the increase in the local strains as well as the development of splitting cracks that result in failure. The residual load level is associated with significant slip of the bar from concrete, it occurs once significant bond-zone cracks and zones of crushing have developed. Thus, the damage presented here is for the pre- and post-peak load levels only. Figure 7.4 shows the maximum principal strain from image analyses and FE analyses at the pre-peak load level. The initiation of cracking is concentrated in the bond-zone near the bar ribs. Although both analyses show local cracking near the ribs, differences exist in the cracking patterns. Image analyses show smeared cracking at the concrete-steel interface, without distinct cracks in front of each rib, as is observed in the FE analysis. In addition, FE analyses show that bond damage propagates from the loaded end to the free end of the bar, with the bond region closest to the loaded end of the bar having the largest magnitude of principal cracking and compression strains. This is not observed in the image analysis results. These differences could be due to 1) the actual load levels used in the imaging test and FE analyses are not exactly same; 2) the FE analyses assume homogeneous material properties for concrete despite the fact that concrete is heterogeneous. 3) the short embedment length leads to the observed

actual damage progression along the bar axis at the four large load steps not as distinct as results from theoretical analysis with small incremental load steps. Computing cracking width from the maximum cracking strain as reference numbers, the crack width at first rib is approximately 0.01 mm from FE analyses and image analyses.

Figure 7.5 shows the maximum principal strain from image and FE analyses at the post-peak load level. Both image and FE analyses show similar results: longitudinal splitting of the specimen initiating at the free end of the specimen. The pattern of splitting cracks is not exactly the same in image and FE results, this is attributed to the random physical material properties in the lab specimen and numerical rounding errors that result in crack initiation in the analyses. The large strains near the bond-zone represent separation and significant slip between the concrete and steel bar. The secondary crack width at local bond-zone is approximately 0.1 mm from FE analyses and image analyses. Figure 7.6 shows the width of secondary concrete cracks at the ribs as a function of bar slip as determined from FE analysis. The first rib carries most of the bond stress and has a crack width of 0.06 mm at the post-peak load level. The last rib has a crack width larger than 0.1 mm after peak load due to the cone-shaped crack at the free end of the specimen as shown in Figure 6.13. The orientation of the cracks with respect to the bar axis change from approximately 45 degrees to approximately parallel to the bar axis; this implies the shear of concrete in front of ribs.

Figures 7.7 and 7.8 show the minimum principal strain at pre- and post-peak load levels. The minimum principal strain is used to quantify the extent of concrete crushing in front of the ribs. Image analysis results show the crushing strain near ribs with smaller magnitude at pre-peak load and larger magnitude at post-peak load. FE analyses not only show the development of crushing but also show that the crushing region at pre-peak load is locally concentrated in front of the ribs, the crushing region at post-peak load is extended between ribs exhibiting shear behavior of concrete. This is consistent with experimental observation after the specimen is split [50, 108].

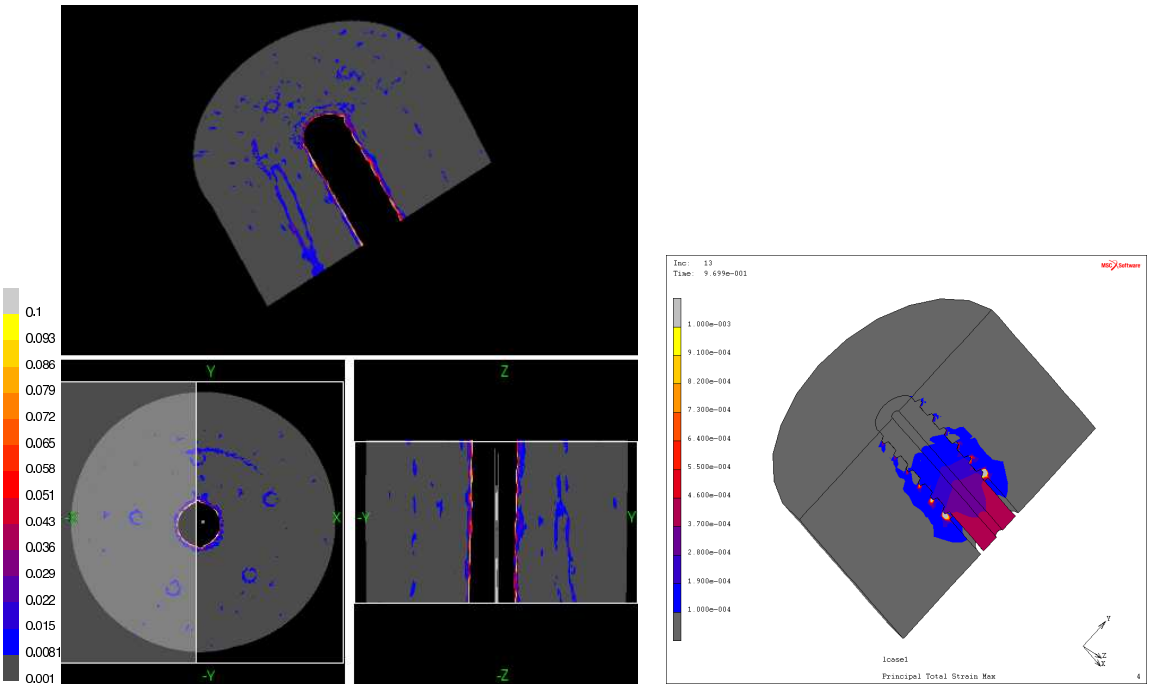

(a) Image Analysis (b) FE Analysis

Figure 7.4: Pull-out Test: Maximum Principal Strain at Pre-peak Load

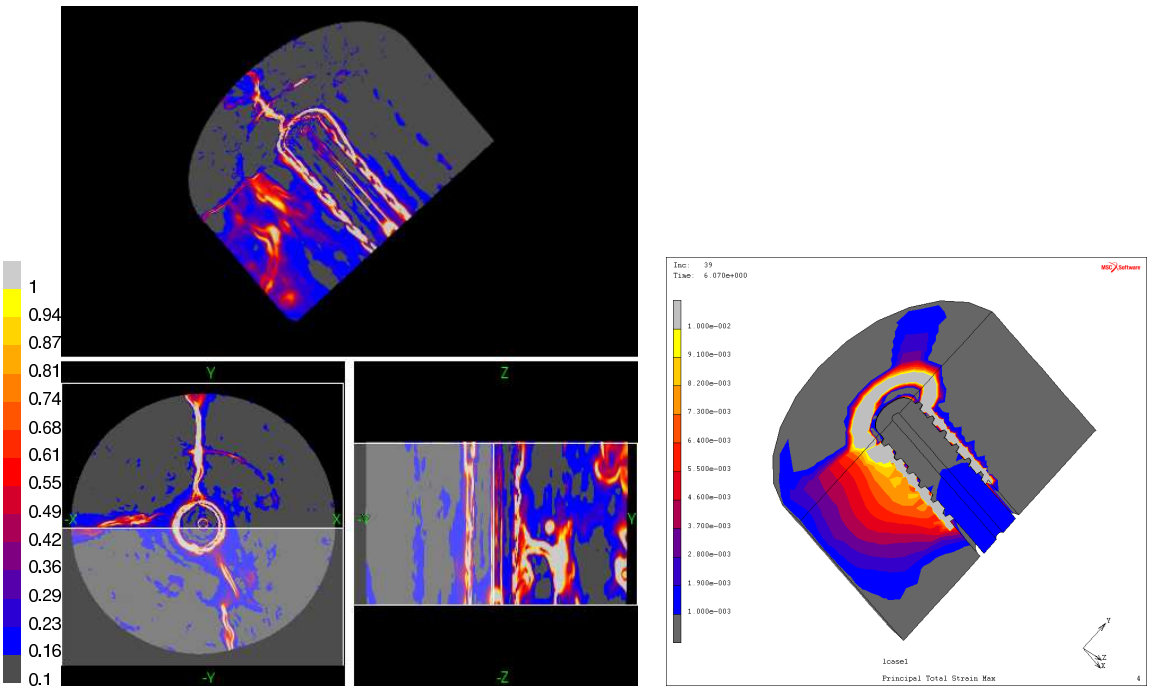

(a) Image Analysis (b) FE Analysis

Figure 7.5: Pull-out Test: Maximum Principal Strain at Post-peak Load

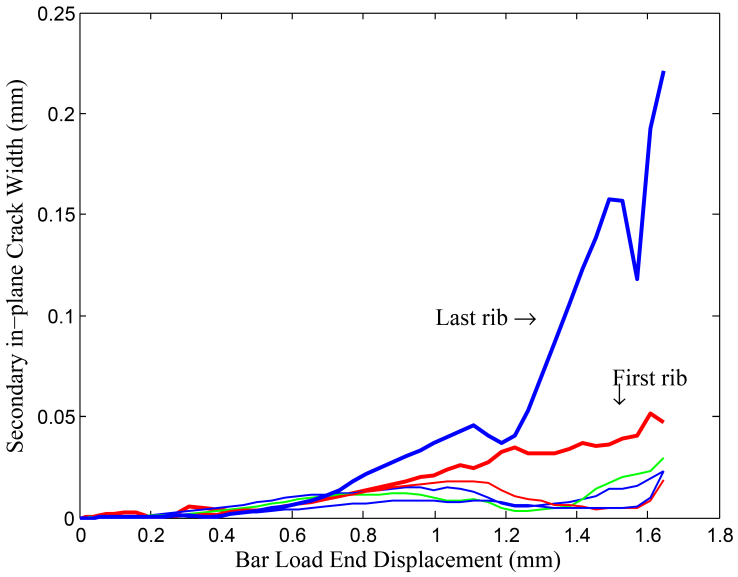

Figure 7.6: Secondary Crack Width from FE Modeling of Pull-out Test

7.3.2 Uniform Tension Test

Concrete cracking is the primary damage mechanism for tension test specimens. Figure 7.9 shows the initiation of local cracking near ribs from image and FE analyses. At the initial load level, cracks are concentrated near the concrete-steel interface propagating from ends to middle of the specimen. This is the same with local cracking patterns in pull-out test. The local crack width near ribs for the initial load stage is around 0.003 mm from FE analysis and 0.03 mm from image analysis.

Figure 7.10 shows the progression of local cracking near ribs as well as the major transverse cracking from image and FE analyses. Both image and FE analyses captured the development of bond-zone cracking and development of splitting near major transverse cracking. The secondary conical cracking near the transverse cracked surface are also captured by the enlargement of cracking zone in that region. FE analyses show a more regular pattern of the secondary cracking development than data from image analyses. This may be attributed to homogeneous material properties assumed in the FE analysis. The major

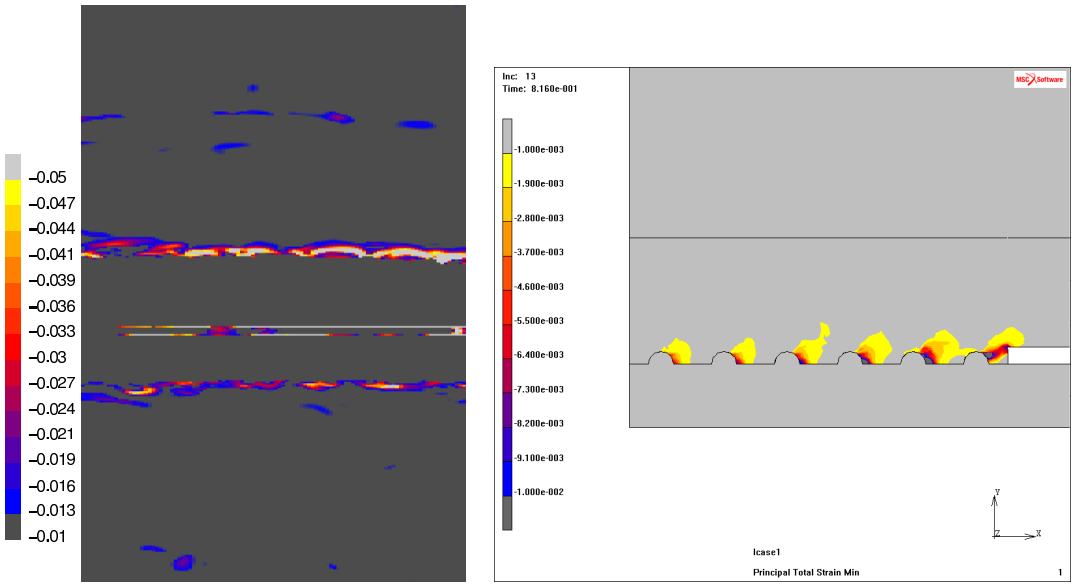

(a) Image Analysis: Whole section with Light Color Bond-zone

(b) FE Analysis: Axisymmetric Section

Figure 7.7: Pull-out Test: Minimum Principal Strain at Pre-peak Load

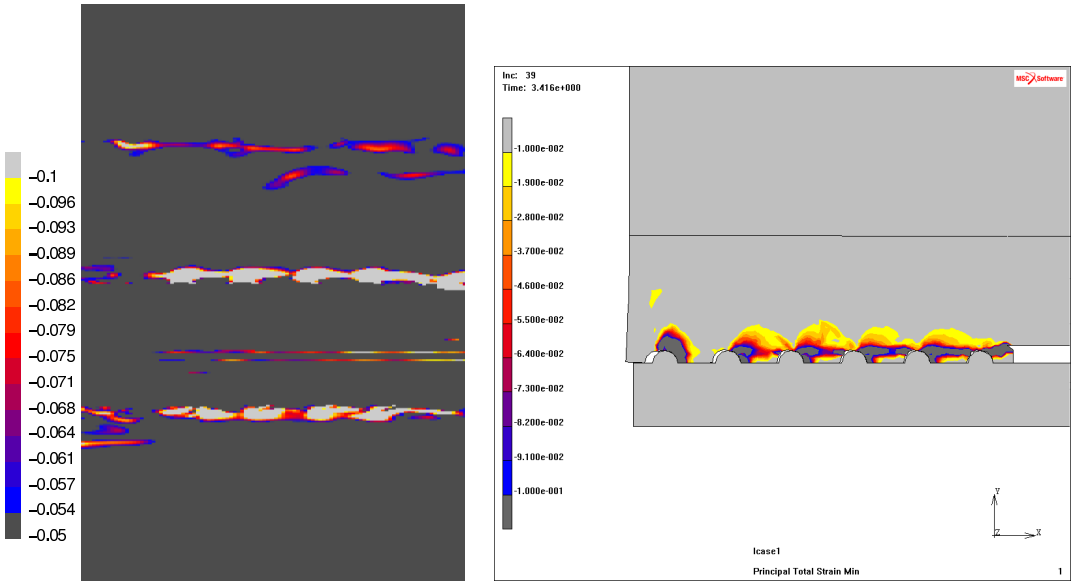

(a) Image Analysis: Whole section with Light Color Bond-zone

(b) FE Analysis: Axisymmetric Section

Figure 7.8: Pull-out Test: Minimum Principal Strain at Post-peak Load

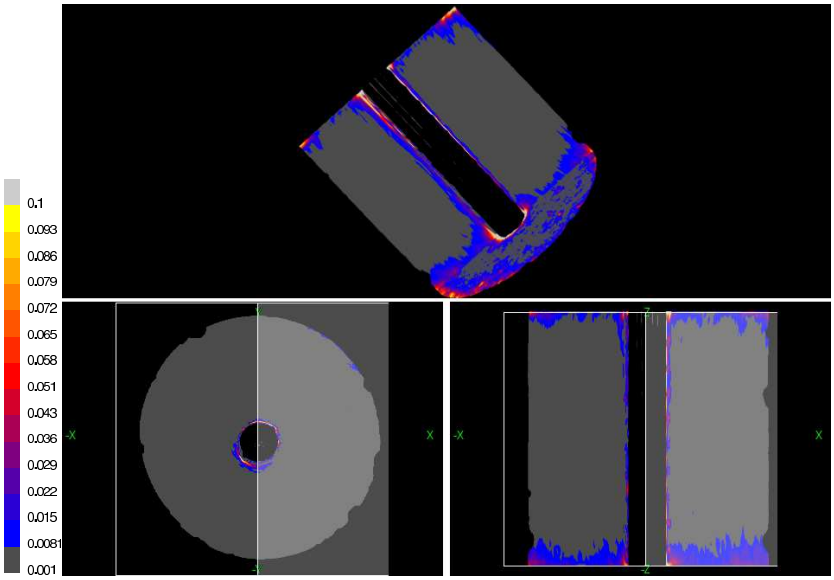

(a) Image Analysis

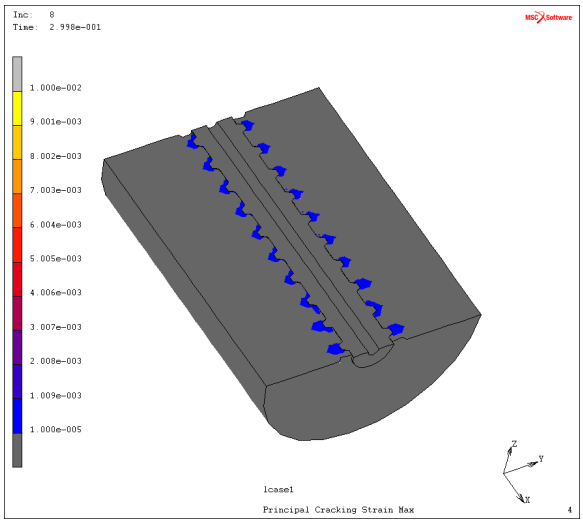

(b) FE Analysis

Figure 7.9: Tension Test: Maximum Principal Strain at Initial Load

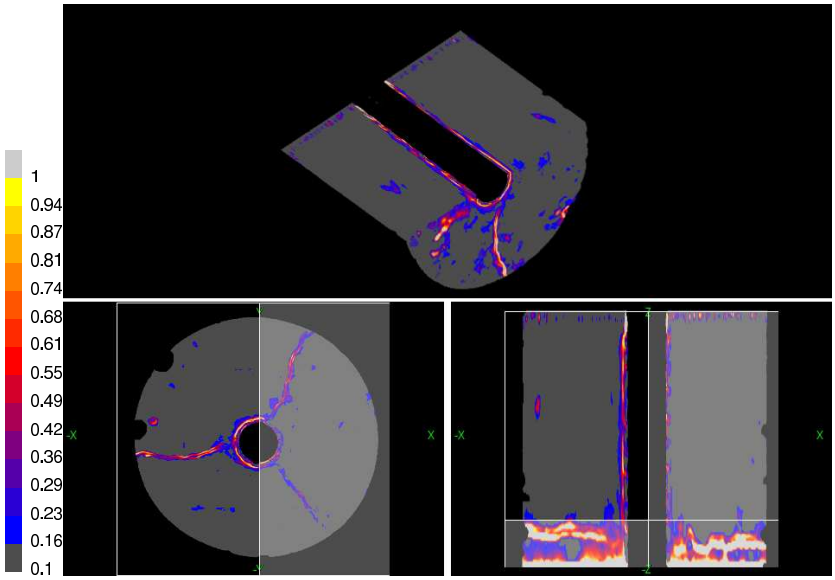

(a) Image Analysis

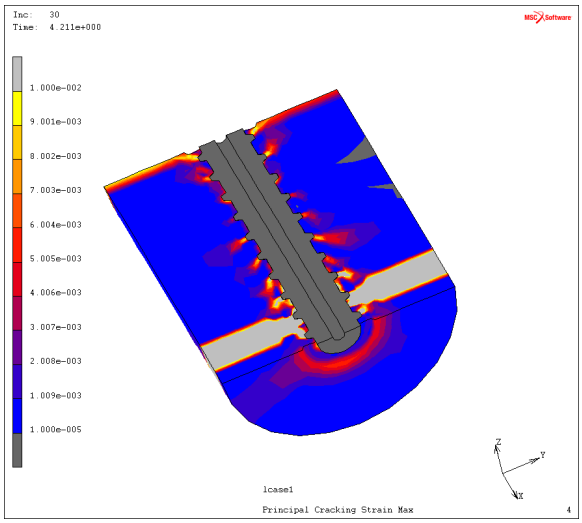

(b) FE Analysis

Figure 7.10: Tension Test: Maximum Principal Strain at Further Load

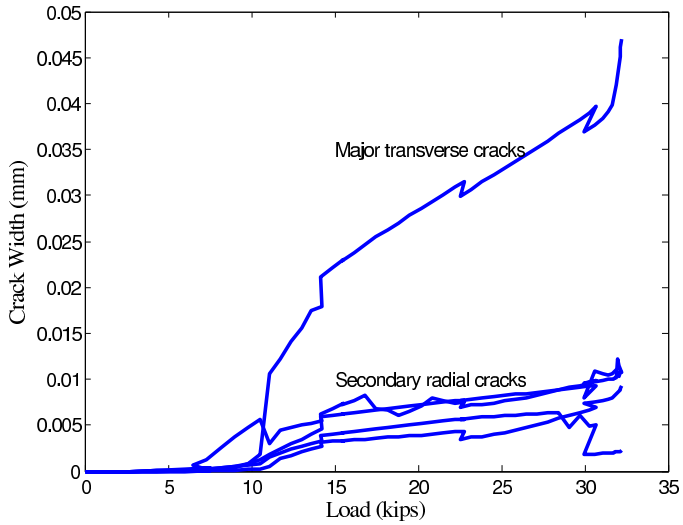

Figure 7.11: Bond-zone Crack Width from FE modeling of Flexural Tension Test

transverse crack width at outer layer of concrete is about 0.5 mm for both FE and image analyses. Figure 7.11 shows how the maximum crack width at the ribs near a major transverse crack changes as load increases in FE analysis. Concrete near the bar surface has a transverse crack width about 0.05 mm and multiple secondary cracks width less than 0.01 mm. This happens after 6 major cracks were developed and bar yielded.

The cracking patterns from FE analyses are more consistent with observations from previous research using traditional methods by Goto [65], where primary transverse cracks, inclined local cracks near ribs with average angle of 60 degree to bar axis, and splitting cracks were observed. FE analyses show initial regular inclined cracks with angle about 45 degree to the bar axis. Image analyses did not show the regular crack patterns as in FE analyses. The reasons are same as explained in pull-out test: the actual heterogeous concrete material properties and the limitation of the motion estimation algorithm in detecting fine cracks less than 1 pixel wide.

7.4 Bond-zone Deformation Field

Loss of bond strength and bond failure in a system are typically due to the development and widening of splitting cracks. Hence, understanding radial bond response and the linkage between radial response and bond stress parallel to the bar is critical to improved bond modeling. Currently, limited experimental data are available characterizing radial bond response [39, 107]. The data from image analyses and FE modeling results providing three-dimensional response of the bond-zone are particularly valuable. To evaluate radial response, radial expansion along the bar anchorage length is presented. As radial response induced splitting failure is typical for pull-out test, the data presented here is for pull-out specimen SE. Previous research results by Malvar [107] are also used to compare with results form the image and FE analyses.

Figure 7.12 shows radial deformation computed from image and FE analyses at the pre-peak load level, along the bar anchorage length for three different radial locations. Figure 7.13 presents similar data at post-peak load level. The FE analyses results are from the 2D axisymmetric models as the difficulties in obtaining converged post-peak response from full 3D FE analysis. In addition, from Chapter 6, for the confined pull-out specimen, 2D and 3D FE analysis have very close global response so that it is reasonably accurate to use 2D FE results to plot the radial deformation. The radial deformation is presented at radial locations of near-bond zone (0.2 inch to bar surface), middle layer of concrete cylinder (at radius of 1.5 inch) and outer layer of concrete cylinder (at radius of 3 inch).

For the load incremental from load level 1 to 2 (initial to pre-peak load), the radial deformation from image analyses has a magnitude of less than 0.01 mm, and the results show radial contraction at the middle layer of concrete and expansion at the outer layer and near concrete-steel interface. FE analyses show radial contraction for all layers at the free end and radial expansion for all layers at load end. At this load level, bond stress has not reached peak bond stress, and bond stress is larger at the loaded end than at the free end of the bar. FE analyses show reasonable results of larger radial expansion at load

end. The peak radial expansion near the loaded end of the anchorage zone is 0.028 mm at bond-zone, 0.018 mm at middle concrete layer and 0.015 mm at outer concrete layer. The larger expansion near bar surface shows that radial expansion is initiated at the local bond-zone.

For the load increment from load level 2 to 3 (pre-peak to post-peak load), image and FE analyses show similar radial expansion patterns. Image analyses results show radial expansion of the middle and outer layers of concrete varying from 0.27 mm at the free end to 0.19 mm at the loaded end of the anchorage zone. FE analyses show radial expansion of the middle and outer layers varying from 0.4 mm at the free end to 0.17 mm at the loaded end of the anchorage zone. These results are consistent to experimental data presented by Malvar [107] that show radial expansion of 0.2 mm at the loaded end for a pre-cracked pull-out specimen subject to a confining pressure of 1500 psi. The test specimen and confining pressure are not exactly same but comparable to specimen SE. Considering the possible differences of load at which the measurement was taken, the numbers are reasonably close. Radial deformation at outer layer is larger at free end than that from the loaded end, which is consistent from all three results: experimental camera picture, image analyses and FE analyses. This is due to the longer unboned lead length comparing with the anchorage length. The splitting was initiated from the specimen surface closest to the anchorage zone. The uncracked concrete at the loaded end of the specimen restrain the specimen from splitting. However, the radial deformation for bond layer shows great variation for both image analyses and FE analyses. Image analyses results show radial expansion of 0.1-0.15 mm from the free end to the loaded end of the anchorage zone. This could be due to the fact that some concrete are stick on bar surface after separation of concrete and the bar. This was observed in laboratory test specimens [50, 108]. FE analyses show the radial expansion of 0.4 mm and drops to 0.2 mm at free end, and goes up to the magnitude same as outer layers with 0.2 mm near load end. This is due to the extensive local in-plane cracking accompanying the splitting at the free end, as shown in Figure 6.11. The

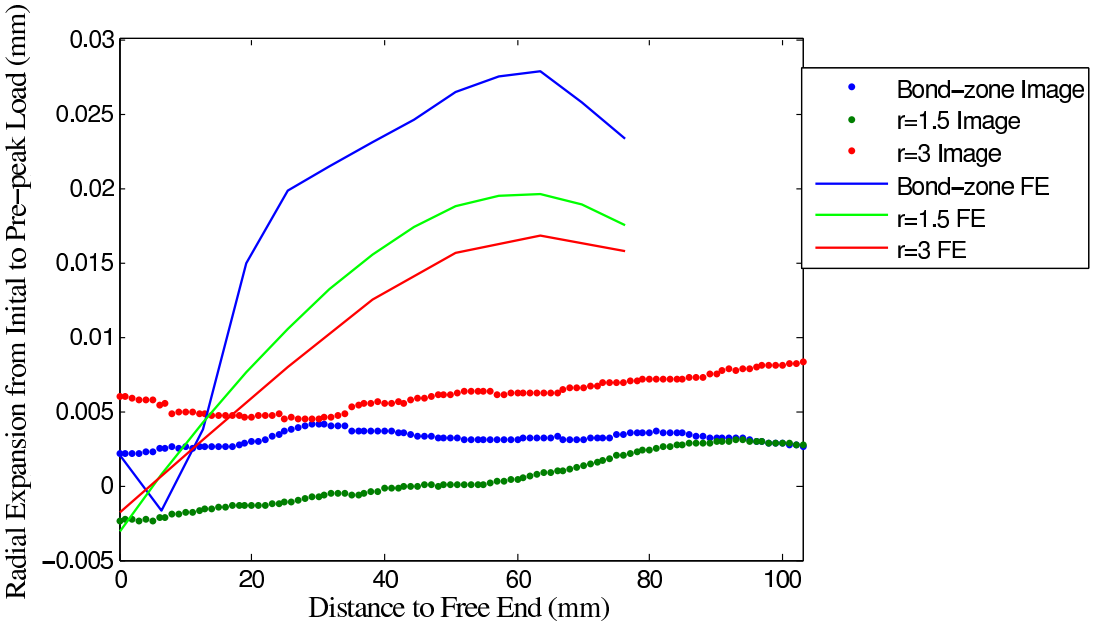

Figure 7.12: Radial Expansion from Initial to Pre-peak Load

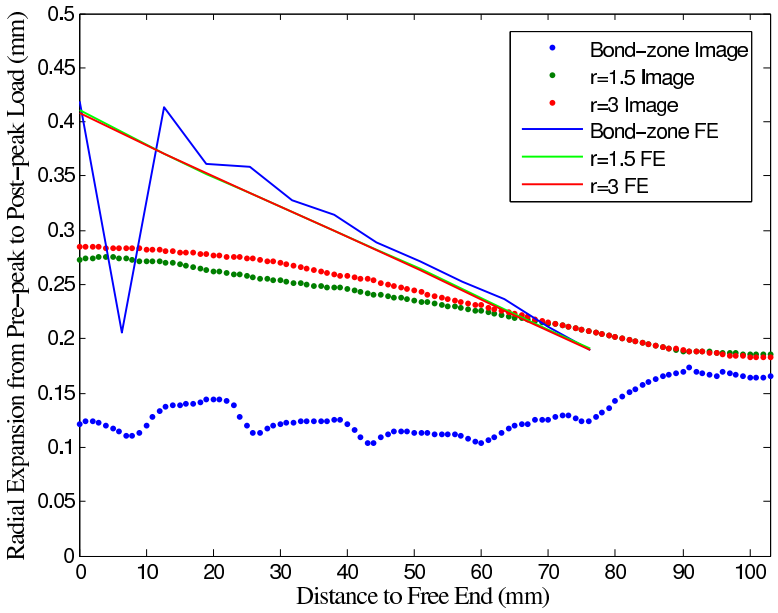

Figure 7.13: Radial Expansion from Pre-peak to Post-peak Load

difference of radial expansion at bond-zone between FE analyses and image analyses are reasonable considering the actual heterogeneous properties of concrete material and the idealized homogeneous assumption in FE analyses.

7.5 Simplified Model Describing Bond Behavior

The results of previous research as well as results from the image and FE analyses conducted as part of this study provide a basis for development of a simplified, multi-dimensional bond model for use in design and bar-scale or member-scale modeling of RC structures. Previous research has used the analogy of thick-wall cylinder subjected to internal pressure, in combination with constitutive models for cracked concrete, to derive maximum bond strength for unconfined pull-out type bond specimens with moderate concrete cover [114, 147, 156, 155]. The model developed here uses the same analogy, and includes consideration of concrete cracking, concrete compressive response, and the impact of confinement as well simplifying assumptions about the local bond-zone stress state developed from FE analysis. The simplified bond established the relationship between bond stress and bond-zone radial stress, calculation of the radial stress at the bar surface as a function of radial displacmenet, and relationship between radial displacement and bar slip.

7.5.1 Bond-zone Stress Field: Relationship between Radial Stress and Bond Stress

Figure 7.14 shows a series of diagrams that summarize the relationship between the local bond-zone stress field and global bond strength. Figure 7.14(a) and (b) show the idealized stress state in the local bond-zone under initial loading assuming no active confining pressure. It is assumed that the concrete surrounding the bar is subject to internal shear stress transferring from the bar ribs. This assumption follows from the results of FE analyses (Figure 5.15, 5.32(f), 5.32(g)), which show an initial stress state that is essentially pure shear, and has been used in previous research by Tepfers [147]. Local bond-zone concrete in a pure shear stress state (assuming no active confinement pressure) develops maximum

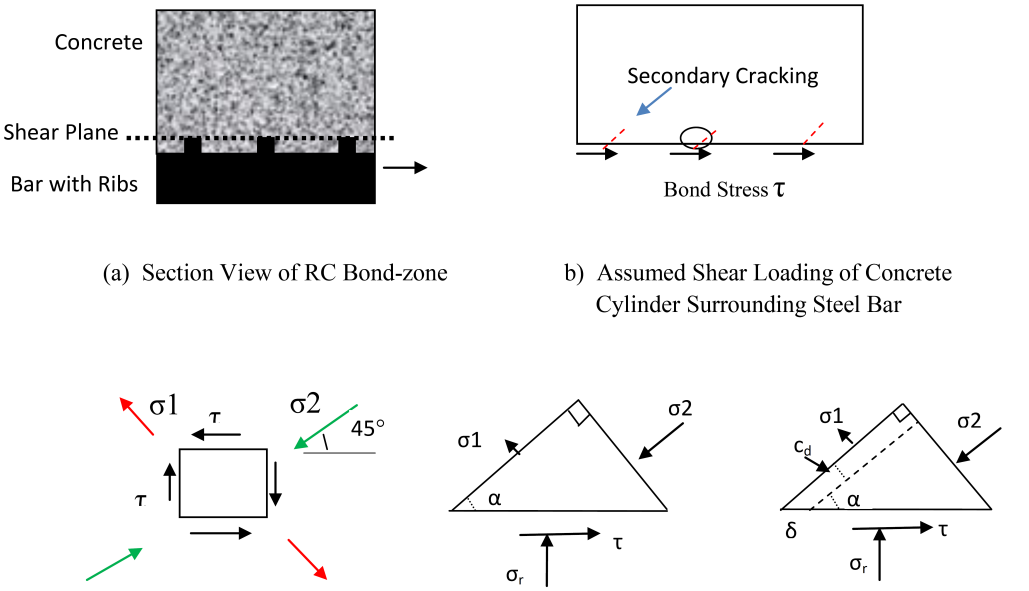

(a) Section View of RC Bond-zone

b) Assumed Shear Loading of Concrete Cylinder Surrounding Steel Bar

(c) Concrete Stress State in Initial Load Phase before Cracking

(d) Concrete Stress State after Crack

(e) Bar Slip δ and Crack Width Cd

Figure 7.14: Bond Mechanism Diagram

principal stress oriented at 135 degrees to bar axis (Figure 7.14(c)). Secondary cracking, initiating at the top-front region of the ribs, is induced by this maximum principal stress (Figure 7.14(b)). When the principal tensile stress reaches the tensile strength of concrete, secondary cracking initiates and the principal tensile stress reduces magnitude following the tension softening rule. The equilibrium of the concrete stress block shown in Figure 7.14(d), assuming no loss in bond stress, τ, requires the radial stress, σ_r which is the internal pressure leading to splitting behavior in the bond-zone. Figure 7.14(e) shows the stress block after secondary crack occurs, where c_d is the crack opening distance in the direction of maximum principal stress, σ_1, and δ is the bar slip.

Considering the stress state in Figure 7.14(d), the equilibrium equations in the direction

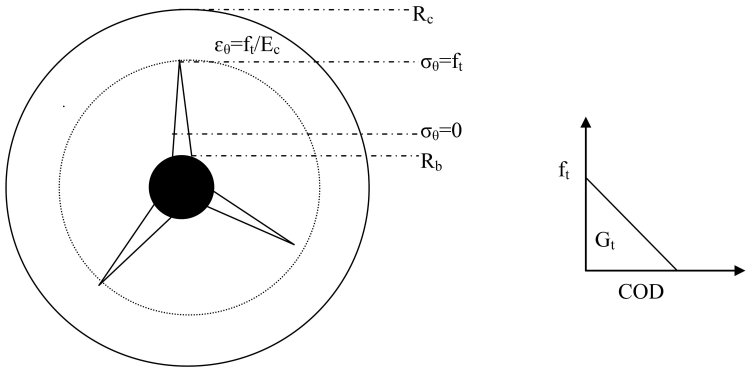

Figure 7.15: Idealized Bond Splitting and Concrete Linear Softening

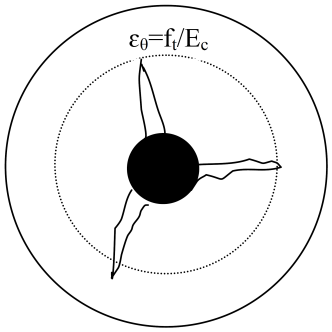

Figure 7.16: Radial Splitting of Bond-zone

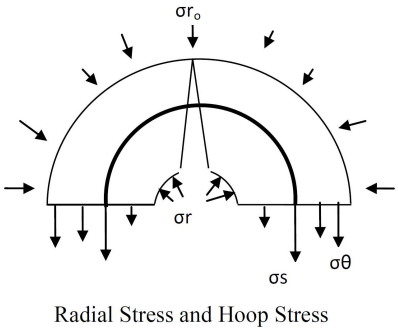

Figure 7.17: Stresses for Concrete Cracked Region

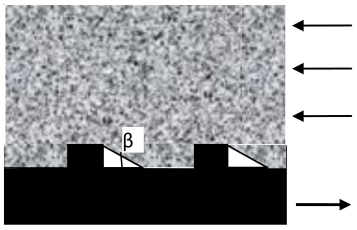

Figure 7.18: Relationship between Radial Displacement and Bar-slip

of the bar axis and the radial direction are

$$\sigma_1 sin(\alpha)cos(\alpha) + \sigma_2 cos(\alpha)sin(\alpha) = \tau \tag{7.1}$$

$$-\sigma_1 cos(\alpha)cos(\alpha) + \sigma_2 sin(\alpha)sin(\alpha) = \sigma_{rb} \tag{7.2}$$

$$\tag{7.3}$$

where $\sigma_1 = f(c_d) = f(\delta sin(\alpha))$, f is a function describing concrete tension softening, τ is the bond stress, σ_{rb} is the radial stress at the bar surface, α is the angle between the secondary crack and the bar axis, and δ is the bar slip. Rearranging Equations 7.1-7.2 leads to following relationship between bond stress, normal stress, and bond slip.

$$\tau = \frac{1}{tan(\alpha)}\sigma_{rb} + \frac{1}{tan(\alpha)}f(\delta sin\alpha) \tag{7.4}$$

Again it should be noted that Equation 7.4 defines bond stress without active confinement pressure in the bond-zone. If tension softening of concrete is not considered, $f(\delta sin(\alpha)) = \sigma_1 = 0$, then the relationship between bond stress and normal stress is $\tau = \sigma_{rb}/tan(\alpha)$, which has been used in previous analytical models [114, 147, 156]. Equation 7.4 implies that the mechanical bond strength is dependent on the radial stress, that develops at the concrete-steel interface due to the unequal magnitude of principal tension and compression stresses. This radial stress induces radial expansion of the concrete surrounding the bar and, ultimately, activate the confining transverse reinforcement, if present. This explains the dependence of bond strength on confining reinforcement. Under low or moderate confinement, the radial stress will induce large radial expansion, and splitting of the concrete; under higher levels of confinement, the radial stress is large but the radial expansion is small, the concrete splitting is controlled and the response of the local bond-zone is determined by compressive response of concrete. The following section introduces the derivation of the radial stress using the concrete constitutive model and enforcing compatibility between radial-direction and hoop-direction displacements .

7.5.2 Radial Stress at the Bar Surface

Radial stress induces multiple splitting cracks as shown in Figure 7.16. The radial stress can be derived from the radial displacement by treating the cracked inner region and uncracked outer region differently. For the uncracked outer region of the specimen, the displacement and stress field are determined by Timoshenko's [151] elastic solution for a thick-walled cylinder with internal pressure. Assuming an outer surface with zero radial stress (no active pressure), the relationship between radial and hoop stress for the uncracked elastic region is

$$\sigma_r = \sigma_\theta \frac{R_c^2 - r^2}{R_c^2 + r^2} \tag{7.5}$$

where σ_r is radial stress at radius r, σ_θ is hoop stress at radius, r, and R_c is the outer radius of concrete cylinder. The radial stress, σ_r, just before splitting can be determined by setting $\sigma_\theta = f_{ct}$. After splitting, the hoop strain is large but the hoop stress is significantly reduced.

For the inner cracked region, the radial displacement, u_r, is assumed to be constant and equal to the radial displacement at the bar surface. This assumption has also been used by previous researchers [147, 156] and is supported by the results of image and FE analyses in section 4.6.3 and 5.7. If it is further assumed that the Poisson effect may be ignored for cracked concrete and that elastic deformation in the radial direction due to radial pressure may be ignored, enforcing compatibility between radial and hoop deformations results in

$$u_r = \epsilon_\theta r = constant \tag{7.6}$$

where ϵ_θ is the hoop stain at radius r. Equation 7.6 implies that the hoop strain, ϵ_θ, must diminish as r increases. With the hoop strain, the hoop stress for the inner cracked region can be derived using a tension softening constitutive model for concrete.

The cracked inner ring is subject to radial pressure at the bar surface and at the splitting crack tips (Figure 7.15). The outer pressure of the cracked ring is calculated from Equation 7.5 by setting $\sigma_\theta = f_{ct}$. The radial stress, σ_r, at the bar surface is calculated by enforcing equilibrium on half of the cracked inner ring (Figure 7.17), considering the hoop stress in the cracked region, the outer pressure, and the confining reinforcement in the cracked region. The radial stress at the bar surface is expressed as

$$\sigma_{rb} = \frac{1}{R_b}\left(\int_{R_b}^{r_0} \sigma_\theta dr + \epsilon_s E_s A_s + f_{ct}\frac{R_c^2 - r_0^2}{R_c^2 + r_0^2} r_0\right) \tag{7.7}$$

where σ_{rb} is the radial stress at the bar surface, σ_θ is the hoop stress at radius r, R_b is the radius of bar, and R_c is the radius of the concrete cylinder or concrete cover, ϵ_s is the hoop strain at confining bars, E_s and A_s are modulus of elasticity and area of confining hoop bars per unit length, f_{ct} is the concrete tensile strength, and r_0 is the radius at which the hoop stress is f_{ct} and can be calculated as $r_0 = u_r E_c / f_{ct}$. The following section explain how to calculate the hoop stress σ_θ as a function of radius to enable calculation of σ_{rb}.

7.5.3 Hoop Stress as a Function of Radius

The hoop stress, σ_θ, in the crack region is a function of crack width at the radius, r. The crack with at radius r is interpolated between the maximum crack width at the bar surface and zero crack width at the crack tips. The crack width at the bar surface is a function of radial displacement (Equation 7.9) and concrete tension properties. With the assumptions of constant radial displacement in the cracked region, and the Poisson ratio resulting in negligible hoop strain due to radial stress at the bar surface [147, 156], following equations relating hoop stress and radial displacement are derived by enforcing displacement

compatibility:

$$\sigma_\theta = f(W_b) \tag{7.8}$$

$$2\pi u_r = 2\pi \frac{\sigma_\theta}{E} R_b + nW_b \tag{7.9}$$

where u_r is the radial displacement at the bar surface, W_b is the splitting crack width at the bar surface, σ_θ is the concrete hoop stress at the bar surface, E is elastic modulus of concrete, and n is the number of splitting cracks along hoop direction. Previous research [114], laboratory tests and FE analyses in this study have shown that the number of splitting cracks varies from two to four, and is typically three. In the following calculations, n is assumed to be three. Assuming concrete fracture energy, G_t, is a constant material property, the relationship between stress and crack opening can be used to determine the hoop stress for a given average crack width. If a linear softening relationship is assumed for concrete in tension (Figure 5.6), given a crack width w_b, the hoop stress is expressed as:

$$\sigma_{\theta b} = (1 - \frac{w_b f_{ct}}{2G_t}) f_{ct} \tag{7.10}$$

where f_{ct} is tensile strength of concrete, G_t is the fracture energy of concrete.

From Equations 7.9 and 7.10, the hoop stress, $\sigma_{\theta b}$, and crack width, W_b, at the bar surface can be calculated as

$$\sigma_{\theta b} = \frac{nG_t/f_{ct} - \pi u_r}{nG_t/f_{ct}^2 - \pi R_b/E_c} \tag{7.11}$$

$$W_b = (1 - \frac{w_b f_{ct}}{2G_t}) f_{ct} \tag{7.12}$$

The crack width, W_r at radius r is linearly interpolated between crack width at the bar surface and zero at the crack tip as

$$W_r = W_b \frac{u_r E_c - f_{ct} r}{u_r E_c - f_{ct} R_b} \tag{7.13}$$

After the crack with at radius r is available. The hoop stress, σ_θ at radius r, can be calculated using Equation 7.10 as

$$\sigma_\theta = f_{ct}(1 - \frac{f_{ct}W_b}{2G_t}\frac{u_r E_c - f_{ct}r}{u_r E_c - f_{ct}R_b}) \tag{7.14}$$

7.5.4 Relationship Between Radial Stress and Radial Displacement at the Bar Surface

Substituting σ_θ at radius r into Equation 7.7, the analytical equation of bond radial stress versus radial displacement is established:

$$\sigma_{rb} = \frac{1}{R_b}(\int_{R_b}^{r_0} f_{ct}(1 - \frac{f_{ct}W_b}{2G_t}\frac{u_r E_c - f_{ct}r}{u_r E_c - f_{ct}R_b})dr + \epsilon_s E_s A_s + f_{ct}\frac{R_c^2 - r_0^2}{R_c^2 + r_0^2}r_0) \tag{7.15}$$

Figure 7.19 shows the radial stress versus radial displacement (expansion) at the bar surface for unconfined concrete with different thickness of concrete cover. To compare with previous research results, assuming α is 45 degree and ignoring the second term in equation 7.4, the radial stress equals bond shear stress. Figure 7.20 shows the peak bond stress under different thickness of concrete cover (c/d is ratio of concrete cover to bar diameter) as well as similar results determined by Tepfers [147]. In this figure, the bond stress defined from elastic cracking is when the splitting cracks just initiates at the bar surface; the bond stress defined from plastic cracking is when the splitting crack tips just reach the outer surface of the concrete cover and Tepfers did not consider the tension softening; the stress defined by the partial cracking is when the splitting crack tips are within the concrete cover and tension softening between splitting cracks is not considered.

7.5.5 Effect of Confinement

The bond response for a confined bond-zone is very different from that of an unconfined bond-zone. For an unconfined bond-zone, bond strength loss is due to concrete splitting.

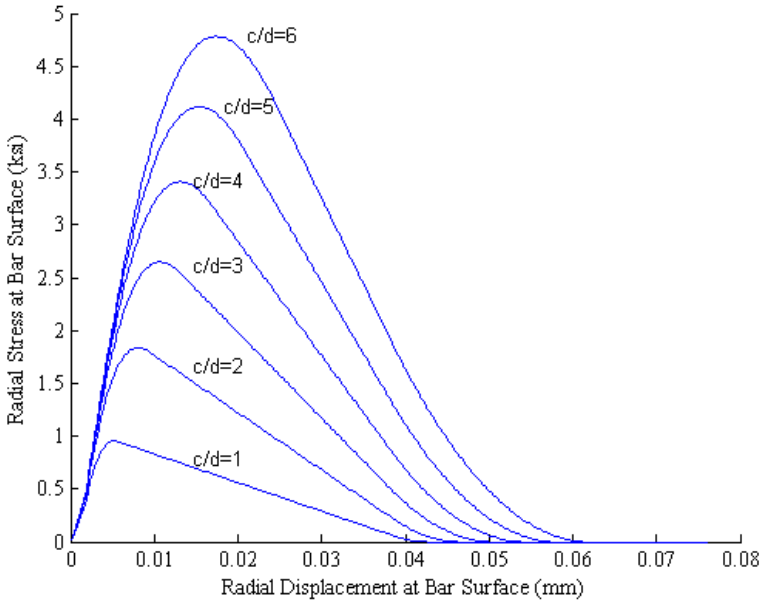

Figure 7.19: Bond Radial Stress versus Radial Displacement under Different Concrete Covers

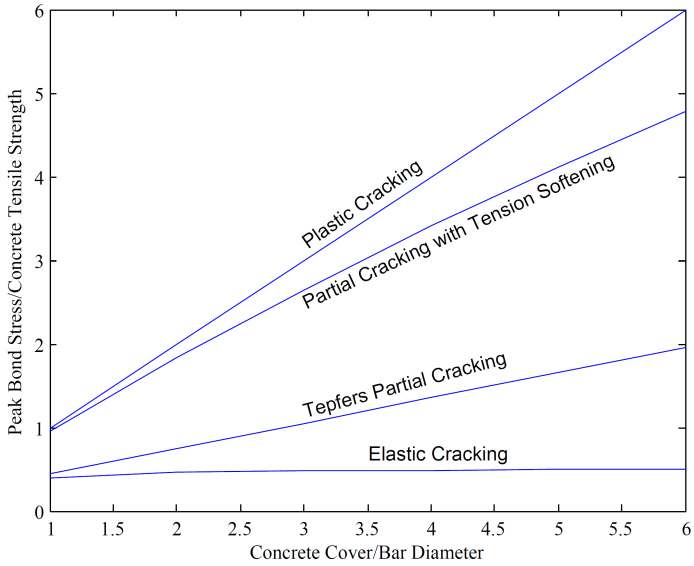

Figure 7.20: Comparison of Peak Bond Stress with Tepfers Results

For passively confined bond-zone with confining reinforcement, the initial response is the same as that for an unconfined specimen: secondary cracking oriented at 45 degrees with respect to the bar axis, as shown from results in Chapter 6. However, as load increases, the radial stress in a passively confined bond-zone, due to activation of confining reinforcement (Equation 7.7) can reach the compression strength of the concrete. Bond stress will not increase linearly with the radial stress for two reasons. First, the development of bond strength under confinement is similar with shear behavior of bar surface concrete under confinement as the constrain of splitting from the confinement. Research on shear strength of confined concrete [161] under direct shear test shows that concrete shear stress increases with shear displacement, peak shear strength corresponds to shear plane displacement of approximately 0.05-0.08 inch (1-2 mm), after peak shear strength is the residual friction shear. Previous research [161] also shows the dilation of concrete and cleavage failure under lower confinement and shear failure for high confined concrete. Under high confinement, the dependence of shear strength on normal stress is nonlinear. Second, the interaction between bond shear stress and radial normal stress leads to varied concrete stress state near bond-zone. The bond-zone concrete stress state varies from initial pure shear state to compression and shear state to friction shear state. The angle α in Figure 7.14 (d) increases from 45 degree to almost 90 degree as load increases for confined specimen. This is also consistent with FE analyses in Chapter 5 and Chapter 6, where initial cracking is 45 degree to the bar axis and progressive cracking changes the direction to perpendicular to bar axis at peak load stage and parallel to bar axis at residual load stage which indicates shear friction behavior of concrete.

For typical RC structures, the bond-zone concrete is under passive confining pressure. The radial stress induced by hoop stress from confining reinforcing bar is included in Equation 7.7. Figure 7.21 shows the bond stress versus radial displacement for specimen SE with different levels of confining reinforcement. In Figure 7.21, the high confinement case represents the case of a two inch thick aluminum tube confining concrete cylinder, which is

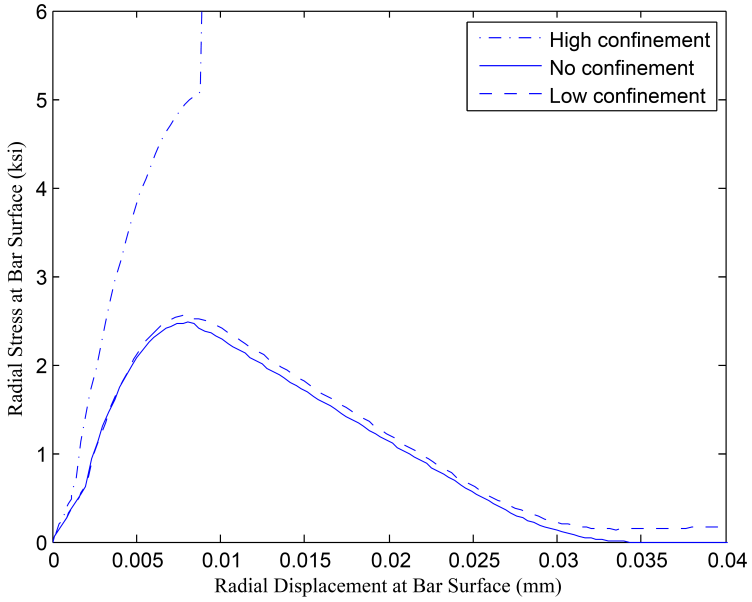

Figure 7.21: Bond Radial Stress versus Radial Displacement under Different Reinforcing Bar Confinement

specimen SA tested by researchers at UW, Low confinement case has 0.059 inch diameter spiral with pitch spacing of one inch, located at a radius of 1.5 inches with the six inches diameter concrete cylinder, this represents specimen SE tested by researchers at UW. Equation 7.21 suggests that the radial stress can reach infinity if the confinement is high enough or if active confinement pressure is applied. However, this radial stress should follow the compression strength of concrete material under similar confinement conditions.

7.5.6 Relationship Between Radial Deformation and Bar Slip

With radial stress versus radial displacement response defined, bond stress can be derived using equation 7.15 and bar slip can be derived by assuming a relationship between radial displacement and bar slip, the angle β in Figure 7.18. The angle β can be estimated from FE analyses of bond test specimens. Figures 7.22 shows relationship between radial expansion and bar slip determined from FE analyses of three specimens with high confinement

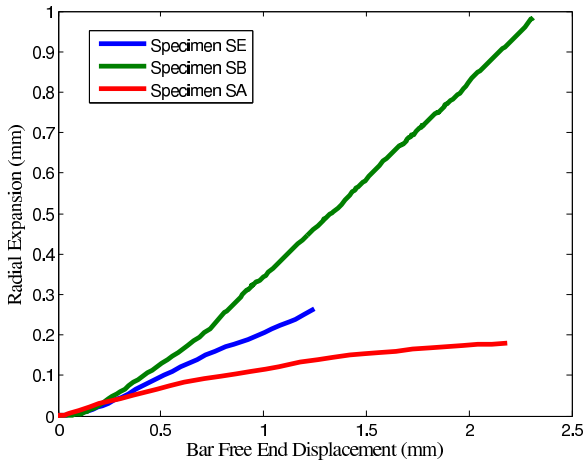

Figure 7.22: Average Radial Expansion versus Bar Slip for Three Specimens

(Specimen SA), no confinement (Specimen SB) and moderate confinement (Specimen SE). At the initial load level, the ratio of radial displacement to bar slip is small, as cracking has not occurred. As bar slip increases with load, the ratio of radial expansion to bar slip increases. For the unconfined specimen SB, this ratio is approximately 0.5 and remains constant through the load history. For the confined specimens SA and SE, this ratio begins to decrease once peak bond strength is achieved. This behavior is consistent with global observation that unconfined specimen has splitting failure, but confined specimen has pull-through failure. For specimen SE, the average ratio of radial displacement over bar slip is approximately 0.2 and for specimen SA, the average ratio is approximately 0.1.

7.5.7 Bond Stress as a Function of Bar Slip

In summary, bond stress as a function of bar slip is defined by following equations:

$$\tau 1 = \frac{1}{tan(\alpha)}\sigma_{rb} + \frac{1}{tan(\alpha)} f(\delta sin\alpha)\ splitting\ control \tag{7.16}$$

$$\tau 2 = tan(\phi)\sigma_{rb} + c\ confined\ shear\ control \tag{7.17}$$

$$\tau = min(\tau 1, \tau 2) \tag{7.18}$$

$$\sigma_{rb} = \frac{1}{R_b}(\int_{R_b}^{r_0} f_{ct}(1 - \frac{f_{ct}W_b}{2G_t}\frac{u_r E_c - f_{ct} r}{u_r E_c - f_{ct} R_b})dr + \epsilon_s E_s A_s + f_{ct}\frac{R_c^2 - r_0^2}{R_c^2 + r_0^2} r_0) \tag{7.19}$$

In above equations, the bond stress is controlled either by longitudinal splitting or confined shear (assuming linear Mohr-Coulomb model here). The parameters, ϕ and c, for the linear Mohr-Coulomb model can be assumed with the procedure in Chapter 5, as 14 degree and $5f_{ct}$ respectively. Table 7.2 shows the comparisons of peak bond stress and radial expansion between the analytical model and results from experimental tests and FE rib-scale modeling. Table 7.3 shows the comparisons of peak bond stress and bar slip at peak stress between the analytical model with results from experimental tests and FE rib-scale modeling. Specimen SB and SE are controlled by splitting failure, and specimen SA is controlled by pull-through type of shear failure. For specimens SB and SE, the analytical model results in smaller bond strength and radial deformation. This could be due to the linear tension softening model used, the Poisson effect which is ignored in the model, or other parameters. For specimen SA, the analytical model results in larger bond strength but much smaller radial deformation. This is due to linear Mohr-Coulomb model may over-estimate the shear strength. The smaller radial deformation may be due to the ignorance of Poisson effects. Further research is needed to test the analytical model with different constitutive model of concrete and accounts for the Poisson effect.

Table 7.2: Peak Bond Stress and Radial Expansion for Pull-out Test

	Specimen SE		Specimen SB		Specimen SA		Malvar Test	
	Peak Bond Sress (ksi)	Radial Ex-pan. (mm)	Peak Bond Sress (ksi)	Radial Ex-pan. (mm)	Peak Bond Sress (ksi)	Radial Ex-pan. (mm)	Peak Bond Sress (ksi)	Radial Ex-pan. (mm)
Experimental Test	3.84	0.2	2.71		3.96		2	0.1
FE Analysis	3.71	0.24	2.65	0.4	3.75	0.13		
Analytical Model	2.7	0.01	2.5	0.008	4.5	0.01	1.5	0.008

Table 7.3: Peak Bond Stress and Bar Slip for Pull-out Test

	Specimen SE		Specimen SB		Specimen SA		Malvar Test	
	Peak Bond Sress (ksi)	Bar Slip (mm)	Peak Bond Sress (ksi)	Bar Slip (mm)	Peak Bond Sress (ksi)	Bar Slip (mm)	Peak Bond Sress (ksi)	Bar Slip
Experimental Test	3.84	1	2.71	1	3.96	2	2	1
FE Analysis	3.71	1.2	2.65	0.8	3.75	1.3		
Analytical Model	2.7	0.05	2.5	0.016	4.5	0.1	1.5	0.04

7.6 Summary

This chapter summarizes bond behavior and bond mechanisms as understood from previous research, analyses of X-ray CT images of bond test specimens and high resolution FE analyses. For pull-out tests, the global behavior composes an initial linear increase in bond stress with bar slip, a nonlinear stage of bond stress versus bar slip associate with local cracking, loss of bond strength and residual strength at large slip levels. For unconfined or moderately confined pull-out tests, the failure mechanism is development of splitting cracks; this is a brittle mechanism. For highly confined pull-out specimens, the failure mechanism is shearing of the concrete between ribs on the steel reinforcing bar. This is a more ductile mechanism than the tensile splitting developed in unconfined specimens. The global behavior of the uniform tension test is controlled by transverse cracking accompanied by local splitting near the transverse cracks.

To investigate local bond-zone damage, the maximum principal strain and minimum principal strain are used to quantify the cracking and crushing. For pull-out test considered, both image and FE analysis results showed the concrete damage near bond-zone and the major failure mechanism: longitudinal splitting. The FE analysis results show regular crack patterns near the concrete-steel interface; these crack patterns are not fully captured in the image data. For the uniform tension test, both image data and FE analyses show initiation of secondary cracking near bond-zone, development of major transverse cracking, and splitting near the transverse cracking. FE analyses show more regular cracking patterns than do image analysis data.

The radial deformation of the bond-zone is an important phenomenon that connects the global bond strength with local bond mechanism. The radial deformations developed from image and FE analyses are reasonably consistent and may be used to develop simplified bar-scale bond strength versus deformation models.

As part of this study, a simplified bar-scale model is developed based on the improved understanding of bond-zone response derived from image and FE analysis results. In this model, the relationship between bond stress and radial stress, the relationship between the radial stress and radial deformation, and the relationship between bond stress and bar slip are defined to reflect the bond response mechanisms observed from previous research, image analyses and high-resolution rib-scale FE models.

Chapter 8

Conclusions and Future Work

The research presented here applied computer vision and finite element analysis methods to investigate bond behavior in RC structures. The investigation analyzed X-ray CT images of bond test specimens using a state-of-the-art motion estimation algorithm and analyzed bond test specimens using high-resolution nonlinear finite element analysis. Results of the images analyses include three-dimensional displacement data for bond test specimens; such data have not been generated previously , as they cannot be generated using traditional experimental techniques. The results of nonlinear FE analyses advance understanding of local bond behavior and the correspondence between local damage and global bond strength as well as the accuracy and limitations of different approaches for modeling bond. The research activities are summarized below with major findings and conclusions identified.

8.1 X-ray CT Image Analyses

X-ray CT images of two typical bond test specimens, a pull-out test specimen and a uniform tension test specimen, were analyzed to investigate local damage and global behavior. First, a basic threshold segmentation was used on the gray-scale images of the uniform tension test specimen to extract qualitative cracking patterns. The development of three types of cracks in bond-zone were identified: major transverse cracks, in-plane secondary cracks and splitting cracks. Next, a more rigorous motion estimation algorithm was tested and applied to the bond images. The motion estimation algorithm captured the rigid motion of the specimen, large deformations, and local cracking. The accuracy of the resulting displacement field is about 10% for large deformations and cracks. Fine cracks that are less than 1 pixel width were not accurately detected due to either the image resolution or limitation of the algorithm. Following are summaries of research activities and significant results and conclusions addressing various aspects of bond-zone response.

Crack Propagation (Chapter 3) was investigated for a uniform tension test specimen using a basic image processing technique: threshold segmentation. Four sets of images for load levels of 0, 2400, 6000 and 8400 lbs were analyzed. Since load-displacement response of the uniform tension specimen is monotonically increasing, these load levels do not correspond to specific events in the load history. At the 2400 lb load level, the initiation of transverse cracking was observed; crack initiated at the crack initiators at the outer surface of the concrete cylinder but did not extend to the center of the cylinder. At the 6000 lb load level, major transverse cracking was fully developed and cracks traversed the entire cross-section of the concrete cylinder. At the 8400 lb load level, 1) small conical secondary cracks were observed close to the exposed transverse crack surface, 2) an additional transverse crack has initiated at the concrete-steel interface but not propagated through the outer surface of the cylinder, and 3) the concrete close to the primary transverse cracks was beginning to split into three pieces, though splitting cracks that initiated at the concrete-steel interface had not propagated through the outer surface. The three type of crack patterns observed via image segmentation are consistent with observations by previous researchers using destructive methods [65, 73, 108].

The Bond-zone Displacement Field (Chapter 4) was calculated by the motion estimation algorithm for 3D images generated for an uniform tension test specimen and a pull-out test specimen. Given two images at different load steps of a specimen, the motion estimation algorithm seeks the displacement field that minimizes the difference in the gray scale intensity, gradient of the gray scale intensity and gradient of the displacement field as the global objective. Minimization of the objective function requires solution of a system of nonlinear partial differential equations. The nonlinear partial differential equations are solved by spatial discretization and temporal iterations. A domain decomposition implementation was applied on the uniform tension specimen which has high-resolution and large image size. Displacement between two adjacent sequence of 3D images were calculated for both specimens. The calculated displacement field include both rigid motion and deforma-

tion of the specimen. The significance of the calculated displacement is that it has avoided the disadvantages and disruption of using traditional instrumental measurement. The displacements calculated are also full displacement field instead of the isolated locations with traditional instruments. The motion algorithm had been tested on accuracy of capturing rigid motion and displacement discontinuity such as cracks in concrete. The accuracy on continuous displacement including rigid motion and large deformation is within 10%. Higher accuracy can be achieved with more iterations with smaller time steps. The accuracy on discontinuous cracking displacement is proportional to the crack width. Cracks with width less than 1 pixel will have as high as 50% errors.

3D Deformation and Strain Fields (Chapter 4) were calculated from the estimated displacement field data. Deformations of interest to this study were the bond-zone bar slip with respect to concrete and the radial deformation of the concrete surrouding the embedded bar; these are difficult to measure using traditional experimental test procedures and instrumentation. Concrete cracks were identified based on maximum principal strain exceeding the cracking strain of concrete. Crack patterns identified in the pull-out specimen and uniform tension specimen are consistent with segmentation results and previous experimental observations. In addition, quantitative crack width could be calculated from the displacement and strain data.

8.2 Finite Element Modeling

High-resolution Rib-scale FE Model (Chapter 5 and 6) of the bond-zone was developed to investigate local behavior and damage patterns. The model employs a nonlinear concrete material model and geometric contact between concrete and steel to simulate the bond behavior using MSC.marc software. Concrete was assumed to be a homogeneous material and was modeled using Drucker-Prager model with tensile cracking and softening. To simulate load transfer between concrete and steel, the bar rib geometry was explicitly modeled, and the mechanical interaction between concrete and reinforcing bar ribs was sim-

ulated via geometric contact analysis. The concrete and steel bar with ribs were treated as two separate contact bodies. The initial adhesion was ignored to emphasize the mechanical bond behavior. The high-resolution model was evaluated to assess the impact of different assumptions about concrete material properties and numerical solution parameters. 2D axisymmetric model and 3D model were created and the analysis results were compared. Ultimately, analysis results were compared with laboratory test data. The comparisons between analysis and lab test results show that the contact model has good performance on representing the load displacement response and failure mode of different specimens. The significance of this rib-scale model is not only its ability to predict the global bond strength, but also provide full 3D deformation field in bond-zone, and local damage such as cracking and crushing.

Local Bond-zone Response through Load History: The FE model was applied first to investigate local bond-behavior for the pull-out tests. Results using the rib-scale 2D and 3D contact models show secondary conical cracking and yielding of concrete in front of the steel ribs at very low load level (approximately 5% of peak load), with damage initiating at the loaded end of the anchorage and propagating towards the free end of the bar. Lab test [108] and the analysis results show that the global load displacement curve exhibits high nonlinearity at approximately 80% of peak load. At this load level, longitudinal splitting extended from bond interface to the out surface of concrete after the in-plane conical cracking was developed. For both unconfined and moderately confined specimens, the peak bond strength is reached when the splitting cracks propagate through the outer cylinder surface. Post-peak strength loss is associated with the fully developed splitting propagating along the bar axis. For well-confined specimens, the initial response is similar to unconfined specimens. As load increases, splitting cracks are limited to the concrete-steel interface, and the peak bond strength is achieved when concrete in front of ribs experiences extensive yielding and starts crushing. The post-peak strength loss is associated with shear-through of the concrete between the bar ribs.

The FE model was applied to also investigate the response of an uniform tension test specimen. For the uniform tension test specimen, the initial concrete cracking and yielding in front of bar ribs is similar to that observed in pull-out test simulations, here, initial cracking and yielding start at the two loaded ends of the bar, and propagate toward the middle of the specimen. As load increases, major transverse cracks, perpendicular to the axis of the bar, propagate from the concrete-steel interface to the outer surface of the specimen. These cracks appear first at two locations that are approximately one-third of the specimen length. As load increases, additional transverse cracks appear between previous cracks. After the concrete cross-section is exposed at the location of a fully developed transverse crack, longitudinal splitting cracks can be observed and new secondary conical cracks near the transverse crack was observed. In the uniform tension test, splitting cracks are limited to near the major transverse cracks in the vicinity of the concrete-steel interface without propagating through the cross-section of the specimen.

Parameters Affecting Bond Strength: Both concrete tensile and compressive strength have impact to the bond strength. The relation was similar with previous research that the bond strength is proportional to the square root of the concrete strength. Analyses also show that confinement has influence on bond peak strength and residual strength but not initial stiffness unless at high active pressure in which case the initial stiffness is larger.

2D Model or 3D Model: Use of a 2D axisymmetric model to simulate the response of an unconfined specimen leads to more ductile behavior than 3D model results, as the splitting cracks are not locally represented by discrete elements but are smeared along the entire hoop direction. For moderate to high confinement, results obtained using a 2D axisymmetric model or full 3D model are similar, as spitting is controlled.

Evaluation of Other Approaches for Modeling the Bond-zone: Results show that rib-scale models can provide high-resolution data characterizing bond-zone behavior. However, in modeling reinforced concrete *structures*, the computational demand of rib-scale modeling may be prohibitive and the data provided by rib-scale modeling unnecessary;

thus, bar-scale models or other simplified modeling approaches are typically used. These approaches were investigated with the following results: Using continuum elements to fully represent the volume of the bar results in a load-displacement response that is the closest to that simulated using a 3D rib-scale model and to lab test results. Using a truss element instead of continuum element to model the steel bar results in mesh sensitivity of the solution due to the truss element fails to represent the geometry of the steel bars. In general, bar-scale models smear the local bond-zone damage along the bar axis, in the layer of concrete elements surrounding the bar. Cracking and crushing of concrete near the concrete-steel interface are not explicitly represented. However, by appropriately modeling bar element such as using continuum element and concrete materials such as modeling cracks and yielding, a global response close to actual bond performance could be achieved.

8.3 Analytical Model of Bond-zone Response

Based on the understanding of local bond-zone mechanisms from previous research of analytical and laboratory results, as well as image and FE analyses in current study, a simplified analytical model frame work was proposed. The simplified model uses Timoshenko's elastic thick-wall solution to derive the bond stress as a function of radial displacement. Concrete tension softening model is used to analyze longitudinal splitting, and concrete compression model (linear Mohr-Coulomb) is used to analyze bond strength under high confinement. The relationship between radial displacement and bar-slip under different confining levels are recommended based on results of FE analysis. The analytical results of bond strength, radial deformation, and bar slip at the peak strength are compared with results from previous research, experimental data and FE analysis in this study. The model results are reasonably consistent with previous research by Tepfers [147], but large differences exists between the model results and data from experiments [107, 108] and FE analyses in this study.

8.4 Recommendations for Future Work

Image Analysis: X-ray CT images of bond test specimens provide both visual and quantitative information for bond response. The motion estimation method implemented in this study exhibited very good performance capturing displacement field of bond specimens, with the limitation that the method does not accurately identify fine cracks less than one pixel. This limitation is due to the fact that the algorithm seeks to minimize the gradient of the displacement field. Thus, the displacement field across the fine cracks is smoothed. However, as the algorithm takes pixel as calculation unit, this limitation is insignificant when the cracks across a number of pixels with higher resolution images. Given the current image resolution, improvements in motion estimation to provide better calculation of crack width can be achieved by using discrete displacement field [3, 142] or adaptive smoothing of the flow field [135] to reserve the cracking discontinuity.

FE Modeling: In general, the 3D reference model provided accurate simulation of observed load-displacement response, local and global damage patterns. The use of linear Mohr-Coulomb model with tension softening for concrete has best performance when modeling unconfined specimen with full 3D models. However, further research could improve the concrete material models. Specifically, to enable accurate simulation of the response of unconfined specimens using 2D axisymmetric model, it is necessary to modify the concrete constitutive model to account for the fact that the effective length, over which cracking is smeared, is different for in-plane cracking and out-of-plane longitudinal splitting. For specimens with moderate to significant confinement, the use of linear Mohr-Coulomb model and associate flow rule over-predicted confined concrete compressive strength due to the use of linear proportion between compressive strength and hydraulic pressure. This could be improved by using a nonlinear Mohr-Coulomb model and non-associated flow rule. Further research could also be conducted to improve the solution procedure to obtain better converged post-peak response.

The Analytical Model: As certain differences exist between the analytical model

results and data from experiments and FE analyses, future work is needed to investigate the reasons for the differences.

Bibliography

[1] ACI 446.3R-97. *Finite Element Analysis of Fracture in Concrete Structures: State-of-the-Art*. 1997.

[2] M. D. Abramoff and M. A. Viergever. Computation and visualization of three-dimensional soft tissue motion in the orbit. *IEEE Transactions on Medical Imaging*, 21(4):296–304, 2002.

[3] T. Amiaz and N. Kiryati. Piecewise-smooth optical flow via level sets. *Internaltional Journal of Computer Vision*, 68(2):111–124, 2006.

[4] A. Ammouche, D. Breysse, H. Hornain, O. Didry, and J. Marchand. A new image analysis technique for the quantitative assessment of microcracks in cement-based materials. *Cement and Concrete Research*, 30:25–35, 2000.

[5] S. Baker, D. Scharstein, J. P. Lewis, S. Roth, M. J. Black, and R. Szeliski. *A Database and Evaluation Methodology for Optical Flow*. Microsoft Research Technical Report, 2009.

[6] S. Balakrishnan and D.W. Murray. Concrete constitutive model for NLFE analysis of structures. *Journal of Structural Engineering*, 114(7):1449–1466, 1988.

[7] J. Barron. 3D optical flow in gated mri cardiac datasets. *Imaging Beyond the Pinhole Camera*, K. Daniilidis and R. Klette (eds.)(Springer):331–344, 2006.

[8] J. Barron, D. J. Fleet, and S. S. Beauchemin. Systems and experiment of optical flow techniques. *International Journal of Computer Vision*, 12(1):43–77, 1994.

[9] K. Bathe, J. Walczak, A. Welch, and N. Mistry. Nonlinear analysis of concrete structures. *Computers & Structures*, 32(3):563–590, 1989.

[10] Z.P. Bazant and M. Jirasek. Size effect in pullout tests. *Journal of Engineering Mechanics*, 128(11):1119–1149, 2002.

[11] Z.P. Bazant and S. Sener. Size effect in pullout tests. *ACI Materials Journal*, 85(5):347–351, 1989.

[12] M. Berry. *Finite Element Modeling of Reinforced Concrete Beam-Column Bridge Connections*. PhD Dissertation, University of Washington, 2006.

[13] A. Bigaj. *Bond Behavior of Deformed Bars in NSC and HSC: Experimental Study*. Delft University of Technology, Report no. 25.5-95-11, 1995.

[14] M. J. Black. *The robust incremental optical flow*. Yale University, 1992.

[15] M. J. Black and P. Anandan. The robust estimation of multiple motions: Parametric and piecewise-smooth flow fields. *Journal of Biomechanics*, 63(1):75–104, 1996.

[16] S. K. Boyd and Ralph. Muller. Surface meshing for automated finite element model generation from 3D image data. *Journal of Biomechanics*, 39(7):1287–1295, 2006.

[17] B. B. Broms. Crack width and crack spacing in reinforced concrete members. *ACI Journal*, pages 1237–1256, 1965.

[18] B. B. Broms. Technique for investigation of internal cracks in reinforced concrete members. *ACI Journal, Proceedings*, 62(1):35–44, 1965.

[19] C. J. Brown, D. Darwin, and S. L. McCabe. *Finite element fracture analysis of steel-concrete bond, SM Report no. 36*. Department of Civil Engineering, Univerity of Kansas, Lawrence, KS, 1993.

[20] T. Brox. *From Pixels to Regions: Partial Differential Equations in Image Analysis*. Saarland University, Saarbrucken, Germany, 2005.

[21] T. Brox, A. Bruhn, N. Papenberg, and J. Weickert. High accuracy optical flow estimation based on a theory for warping. *In Proc. 8th European Conference on Computer Vision* , 4:25–36, 2004.

[22] A. Bruhn. *Variational Optic Flow Computation Accurate Modelling and Efficient Numerics*. PhD Dissertation, Saarland University, Saarbrucken, Germany, 2006.

[23] A. Bruhn, J. Weickert, F. Feddern, T. Kohlberger, and C. Schnrr. Variational optical flow computation in real time. *IEEE Transactions on Image Processing*, 14(5):608–615, 2005.

[24] O. Buyukozturk. Nonlinear analysis of reinforced concrete structures. *Computers & Structures*, 7:149–156, 1977.

[25] O. Buyukozturk. Imaging of concrete structures. *NDT & E International*, 31(4):233–243, 1998.

[26] O. Buyukozturk, H.A. Nilson, and O.F. Slate. Stress-strain response and fracture of a concrete model in biaxial loading. *ACI Journal*, 68(8):590–599, 1971.

[27] O. Buyukozturk and S. S. Syed. Constitutive modeling of concrete in finite element analysis. *Computers & Structures*, 21(3):581–610, 1985.

[28] O. Buyukozturk and T. Tseng. Concrete in biaxial cyclic compression. *Journal of Structural Engineering*, 110(3):461–475, 1984.

[29] J. Cairns and K. Jones. An evaluation of the bond-splitting action of ribbed bars. *ACI Material Journal*, 93(1):10–19, 1996.

[30] Q. Cal, J.M. Robberts, and B.W.J. Van Rensburg. Cracking in concrete using smeared cracking finite element modeling. *South African Journal of Science*, 102(11/12):548–556, 2006.

[31] J. Canny. A computational approach to edge detection. *IEEE Transactions on Pattern Analysis and Machine Intelligenc*, 8:679–698, 1986.

[32] M. Cervera and M. Chiumenti. Mesh objective tensile cracking via a local continuum damage model and a crack tracking technique. *Computer Methods in Applied Mechanics and Engineering*, 196:304–320, 2006.

[33] C. C. Chang and X. H. Xiao. Three-dimensional structural translation and rotation measurement using monocular videogrammet. *Journal of Engineering Mechanics*, 2009.

[34] L. Chen, Y. Shao, H. Jan, C. Huang, and Y. Tien. Measuring system for cracks in concrete using multitemporal images. *Journal of Surveying Engineering*, 132(2): , 2006.

[35] Z. Chen and T. C. Hutchinson. Application of PDE methods for image-based concrete surface damage detection. *Proc. of SPIE*, page , 2007.

[36] Y. Cheng. Mean shift, mode seeking, and clustering. *IEEE Transactions on Pattern Analysis and Machine Intelligence*, 17(8):790–799, 1995.

[37] MSC Corporation. *MSC.Marc software users manual*. 2005.

[38] J. V. Cox and L. R. Herrmann. Development of a plasticity bond model for steel reinforcement. *Mech. of Cohes.-Frict. Mater.*, 3(2):155–180, 1998.

[39] J. V. Cox and L. R. Herrmann. Validation of a plasticity bond model for steel reinforcement. *Mech. of Cohes.-Frict. Mater.*, 4(4):361–389, 1999.

[40] J. V. Cox and H. Yu. Radial elastic stiffness associated with bond between steel bars and concrete. *ACI Structural Journal*, 98(1):16–26, 2001.

[41] M. A. Crisfield. snap-through and snap-back response in concrete structures and

the dangers of under-integration. *International Journal for Numerical Methods in Engineering*, 22(3):751–767, 1986.

[42] S. Das and M. Hadi. Non-linear finite element analysis of reinforced concrete members using MSC/NASTRAN. *1996 MSC World Users Conference* , page , 1996.

[43] R. de Borst. Stability and uniqueness in numerical modeling of concrete structures. *IABSE Rep.*, 54:161–176, 1987.

[44] R. de Borst and M. A. Gutierrez. Computation of post-bifurcation and post-failure behavior of strain-softening solids. *Computers & Structures*, 25(2):211, 1987.

[45] R. de Borst and M. A. Gutierrez. A unified framework for concrete damage and fracture models including size effects. *International Journal of Fracture*, 95:261–277, 1999.

[46] A. K. De Groot, G. M. A. Kusters, and T. Monnier. Numerical modeling of bond-slip behavior. *Heron, I.B.B.C. Institute TNO, Delft, Netherlands*, 26(1b):, 1981.

[47] J. A. den Uijl and A. J. Bigaj. A bond model for ribbed bars based on concrete confinement. *HERON*, 41(3):201–226, 1996.

[48] J. M. Desir, M. R. B. Romdhane, F. J. Ulm, and E. M. R. Fairbairn. Steel-concrete interface: revisiting constitutive and numerical modeling. *Computers & Structures*, 71(5):489–503, 1999.

[49] J. J. Dongarra, I.S. Duff, D. C. Sorensen, and H. A. Van der Vorst. *Solving Linear Systems on Vector and Shared Memory Computers*. Society for Industry and Applied Mathematics, 1991.

[50] R Eligehausen, E. P. Popov, and V. V. Bertero. *Local bond stress-slip relationships of deformed bars under general ized excitations*. University of California, Report no. UCB/EERC-83/23 of the National Science Foundation, 1983.

[51] L. E. Elsgolc. *Calculus of Variation*. Pergamon Press, 1961.

[52] S. K. Esche, G. L. Kinzel, and T. Altan. Issues in convergence improvement for non-linear finite element programs. *International Journal for Numerical Methods in Engineering*, 40:4577–4594, 1997.

[53] P. H. Feenstra. *Computational Aspects of Biaxial Stress in Plain and Reinforced Concrete*. PhD dissertation, Delft University of Technology, 1993.

[54] P.H. Feenstra, R. de Borst, and J.G. Rots. Numerical study on crack dilatancy. i: models and stability analysis; ii: application. *Journal of Engineering Mechanics*, 117(4):733–769, 1992.

[55] P.M. Fergusson. Bond-stress the state of the art. *ACI Journal*, pages 1161–1188, 1966.

[56] B. P. Flannery, H. W. Deckman, W. G. Roberge, and K. L. Damico. Three-dimensional x-ray microtomography. *Science, New Series*, 237(4821):1439–1444, 1987.

[57] D. J. Fleet and Y. Weiss. Optical flow estimation. *Mathematical Models in Computer Vision: The Hand Book*, 15:1–24, 2005.

[58] O. S. Floyd and S. Olsefski. X-ray study of internal structure and microcracking of concrete. *Journal of the American Concrete Institute*, pages 575–588, 1963.

[59] S.J. Foster and H. Dabbagh. A smeared-fixed crack model for fe analysis of RC membranes incorporating aggregate interlock. *Advances in structural engineering*, 9:91–102, 2006.

[60] P. G. Gambarova and E. Giuriani. Discussion of fracture mechanics of bond in reinforced concrete, by ingraffea et al. *J. Struct. Engng.*, 111(5):1161–1164, 1984.

[61] P.G. Gambarova, G.P. Rosati, and B. Zasso. Steel-to-concrete bond after concrete

splitting: Constitutive laws and interface deterioration. *Materials and Structures*, 22(131):347–356, 1989.

[62] P.G. Gambarova, G.P. Rosati, and B. Zasso. Steel-to-concrete bond after concrete splitting: Test results. *Materials and Structures*, 22(127):35–47, 1989.

[63] E.J. Garboczi. Three-dimensional mathematical analysis of particle shape using x-ray tomography and spherical harmonics: Application to aggregates used in concrete. *Cement and Concrete Research*, 32:1621–1638, 2002.

[64] G. Golub and J.M. Ortega. *Scientific Computing: an Introduction with Parallel Computing*. Academic Press, Inc, 1993.

[65] Y. Goto. Cracks formed in concrete around deformed tension bars. *ACI Journal, Proceedings*, 68(4):244–251, 1971.

[66] S. Govindjee, G.J. Kay, and J.C. Simo. Anisotropic modelling and numerical simulation of brittle damage in concrete. *International Journal for Numerical Methods in Engineering*, 38(21):3611–3633, 1995.

[67] B.S. Hamad. Comparative bond strength of coated and uncoated bars with different rib geometries. *ACI Materials Journal*, 92(6):579–590, 1995.

[68] N.M. Hawkins, I.J. Lin, and F.L. Jeang. Comparative bond strength of coated and uncoated bars with different rib geometries. *Bond in Concrete. P. Bartos (editor). Applied Science Publishers Ltd., London*, pages 151–161, 1982.

[69] B. Horn and B. Schunck. Determining optical flow. *Artificial Intelligence*, 17:185–203, 1981.

[70] J. Houde. Study of force-displacement relationships for the finite element analysis of reinforced concrete, report no. 73-2. *Department of Civil Engineering and Applied Mechanics, McGill University, Quebec, Montreal, Canada*, pages 12–14, 1973.

[71] S.S. Hsieh, E.C. Ting, and W.F. Chen. Study of force-displacement relationships for the finite element analysis of reinforced concrete, report no. 73-2. *International Journal of Solids and Structures*, 18(3):181–197, 1982.

[72] T.C. Hsu and F.O. Slate. Tensile bond strength between coarse aggregate and cement past or mortar. *ACI Journal, Proceedings*, 60(4):465–486, 1963.

[73] S. Hungspreug. *Local Bond Between a Steel Bar and Concrete Under High Intensity Cyclic Loading*. Ph.D. Dissertation, Cornell University, Ithaca, NY, 1981.

[74] A. R. Ingraffea, W. H. Gerstle, P. Gergely, and V. Saouma. Fracture mechanics of bond in reinforced concrete. *J. Struct. Engng. ASCE*, 110(4):871–890, 1984.

[75] A. R. Ingraffea and V. Saouma. Numerical modeling of discrete crack propagation in reinforced and plain concrete. *Fracture Mechanics of Concrete: Structural Application and Numerical Calculation,G. C. Sih and A. Ditommaso, eds., Martinus Nijhoff Publishers, Dordrecht*, pages 171–225, 1985.

[76] E.M. Kalmoun, H. Kostler, and U. Rude. 3D optical flow computation using a parallel variational multigrid scheme with application to cardiac c-arm ct motion. *Image and Vision Computing*, 25(9):1482–1494, 2007.

[77] M. Kass, A. Witkin, and D. Terzopoulos. Snakes: Active contour models. *International Journal of Computer Vision*, 1:321–331, 1988.

[78] M. Kawagai, A. Sando, and N. Takano. Image-based multi-scale modeling strategy for complex and heterogeneous porous microstructures by mesh superposition method. *Modelling Simul. Mater. Sci. Eng*, 14(1):53–69, 2006.

[79] P. Kettil and N. E. Wiberg. Simulation of failure of structures using dynamics and optimization techniques. *Computers & Structures*, 82:815–828, 2004.

[80] A. H. Khalil, T. Fawzy, and S. Taher. New special finite elements for modeling reinforcement and steel-concrete interface. *Engineering Computations, ABI/INFORM Global*, 16(5):871–890, 1984.

[81] T. Kohlberger, C. Schnrr, A. Bruhn, and J. Weickert. Parallel variational motion estimation by domain decomposition and cluster computing. *ECCV2004*, pages 205–216, 2004.

[82] D. Krajcinovic and G.U. Fonseka. The continuous damage theory of brittle materials: Part 1 - general theory. *ASME Journal of Applied Mechanics*, 48:809–815, 1981.

[83] H. Kupper, H. Hilsdorf, and H. Rusch. Behavior of concrete under biaxial stress. *Journal of Engineering Mechanics Division, ASCE 16199, EM4*, pages 852–866, 1973.

[84] H. G. Kwakt and F. C. Filippuu. Nonlinear fe analysis of r/c structures under monotonic loads. *Computers & Structures*, 65(1):1–16, 1997.

[85] A.K.H. Kwan, Z.M. Wang, and H.C. Chan. Microscopic study of concrete ii: nonlinear finite element analysis. *Computers & Structures*, 70:545–556, 1999.

[86] N.E. Landis, N.E. Nagy, and T.D. Keane. Microtomographic measurements of internal damage in portland-cement-based composites. *Journal of Aerospace Engineering*, 10(1):1–6, 1997.

[87] J. Lee and G.L. Fenves. *Numerical Implementation of Plastic-Damage Model for Concrete under Cyclic Loading: Application to Concrete Dam.* Report UCB/SEMM-94/03, Department of Civil Engineering, University of California, Berkeley, CA, 1994.

[88] J. Lemaitre. Coupled elasto-plasticity and damage constitutive equations. *Computer Methods in applied Mechanics and Engineering*, 51:31–49, 1985.

[89] R. Leon. *Bond and Development of Reinforcement: A tribute to Dr. Peter Gergely. Special Publication 180.* Farmington Hills, MI: ACI International, 1998.

[90] S. Lettow, J. Ozbolt, R. Eligehausen, and U. Mayer. Bond of RC members using nonlinear 3D FE analysis. *Fracture Mechanics of Concrete Structures*, pages 861–868, 2004.

[91] M. Li and P. Vitanyi. *An Introduction to Kolmogorov Complexity and Its Applications*. New York: Springer-verlag, 1993.

[92] W. E. Lorensen and H. E. Cline. Marching cubes: a high resolution 3D surface construction algorithm. *ACM Computer Graphics (Proceedings of SIGGRAPH 87)*, 21(4):163–169, 1987.

[93] A. Losberg and P.A. Olsson. Bond failure of defomred reinforcing bars based on the longitudinal splitting effect the bars. *ACI Journal*, pages 5–18, 1979.

[94] L. N. Lowes, J. P. Moehle, and S. Govindjee. Concrete-steel bond model for use in finite element modeling of reinforced concrete structures. *ACI structural journal*, 101(4):501–511, 2004.

[95] L.N. Lowes. *Finite Element Modeling of Reinforced Concrete Beam-Column Bridge Connections*. PhD Dissertation, University of California Berkeley , 1998.

[96] L.N. Lowes. *An X-Ray Tomography Investigation of Bond in Reinforced Concrete*. Research Report, University of Washington, Seattle, 2009.

[97] J. Lubliner, J.and Oliver, S. Oller, and E. Oate. A plastic-damage model for concrete. *International Journal of Solids and Structures*, 25(3):299–326, 1989.

[98] J.J. Lubliner. *Plasticity Theory*. New York: Macmillan Publishing Company, 1990.

[99] T. Lucas, B. D.and Kanade. An iterative image registration technique with an application to stereo vision. *In Proc. Seventh International Joint Conference on Artificial Intelligence, Vancouver, Canada*, pages 674–679, 1981.

[100] B. M. Luccioni and D. E. Lpez. Bond-slip in reinforced concrete elements. *Journal of Structural Engineering*, 131(11):1690–1698, 2005.

[101] K. Lundgren and K. Gylltoft. A model for the bond between concrete and reinforcement. *Magazine of Concrete Research*, 52(1):53–63, 2000.

[102] L.A. Lutz. Analysis of stresses in concrete near a reinforcing bar due to bond and transverse cracking. *ACI Journal*, pages 778–787, 1970.

[103] L.A. Lutz and P. Gergely. Mechanics of bond and slip of deformed bars in concrete. *ACI Journal*, pages 711–721, 1967.

[104] L.A. Lutz, P. Gergely, and G. Winter. *The Mechanics of Bond and Slip of Deformed Reinforcing Steel in Concrete*. Structural Engineering Report No. 66/05. Cornell University, 1966.

[105] E. Maire, A. Fazekas, and S. Youssef. X-ray tomography applied to the characterization of cellular materials related finite element modeling problems. *Composites Science and Technology*, 63(16):2431–2443, 2003.

[106] L. J. Malvar and G.E. Warren. Fracture energy for 3-point bent tests on single-edge-noteched beams. *Experimental Mechanics*, 28(3):266–272, 1988.

[107] L. J. Malvar and G.E. Warren. Bond of reinforcement under controlled confinement. *ACI Materials Journal*, 89(6):593–601, 1992.

[108] J. Martin. *An Experimental Investigation of Bond in Reinforced Concrete*. MSCE Thesis, University of Washington, Seattle, WA, 2006.

[109] H. Matthies and G. Strang. The solution of nonlinear finite element equations. *International Journal for Numerical Methods in Engineering*, 14:1613–1626, 1979.

[110] P.K. Mehta and P.J.M. Monteiro. *Concrete: Structure, Properties, and Methods*. Englewood Cliffs: Prentice-Hall, Inc., 1993.

[111] M. S. Mirza and J. Houde. Study of bond stress-slip relationships in reinforced concrete. *ACI Journal, Proceedings*, 76(1):19–46, 1979.

[112] F. C. Monteiro and A. Campilho. Region and graph-based motion segmentation. *ICIAR 2008*, pages 609–618, 2008.

[113] G. Nagai and T. Yamada. Three dimensional element modeling for concrete materials using digital image and embedded discontinuous element. *International Journal for Multiscale Computational Engineering*, 4(4):461–474, 2006.

[114] C.V. Nielsen and N. Bicanic. Radial fictitious cracking of thick-walled cylinder due to bar pull-out. *Magazine of Concrete Research*, 54(3):215–221, 2002.

[115] A. H. Nilson. Internal measurement of bond slip. *ACI Journal, Proceedings*, 69(7):439–441, 1971.

[116] J. Oliver. A consistent characteristic length for smeared cracking models. *International Journal for Numerical Methods in Engineering*, 28:461–474, 1989.

[117] M. Ortiz and E.P. Popov. Plain concrete as a composite. *Mechanics of Materials*, 1(1):139–150, 1982.

[118] N.S. Ottosen. Failure criterion of concrete. *ASCE Journal of Engineering Mechanics*, 103(EM4):527–535, 1977.

[119] J. Ozbolt and Z. P. Bazant. Numerical smeared fracture analysis: nonlocal microcrack interaction approach. *International Journal for Numerical Methods in Engineering*, 39:635–661, 1996.

[120] J. Ozbolt and R. Eligehausen. Numerical simulation of cycling bond-slip behavior. *Bond in Concrete, Proc. Int. Conf., CEB*, pages 1227–1233, 1992.

[121] J. Ozbolt, Y. J. Li, and I. Kozar. Microplane model for concrete with relaxed kinematic constraint. *International Journal of Solids and Structures*, 38:2683–2711, 2001.

[122] T.W. Pfeiler, D.S. Lalush, and E.G. Loboa. Semiautomated finite element mesh generation methods for a long bone. *Computer Methods and Programs in Biomedicine*, 85:196–202, 2007.

[123] S. Pietruszczak, J. Jiang, and F. A. Mirza. An elastoplastic constitutive model for concrete. *Computers & Structures*, 24(7):705–722, 1988.

[124] S. Pietruszczak and G. XU. Brittle response of concrete as a localization problem. *International Journal of Solids and Structures*, 32(11):1517–1533, 1995.

[125] ST. Pietruszczak and Z. Mroz. Finite element analysis of deformation of strain-softening materials. *International Journal for Numerical Methods in Engineering*, 17:327–334, 1981.

[126] G. F. Pla-Rucki and M. O. Eberhard. Imaging of reinforced concrete: state-of-the-art review. *Journal of Infrastructure Systems*, 1(2):134–141, 1995.

[127] M. Plos and K. Gylltoft. Nonlinear fe analysis of rc bridge frame corners based on fracture mechanics. *Journal of Bridge Engineering*, 3(4):204–210, 1998.

[128] S. Popovics. A numerical approach to the complete stress strain curve for concrete. *Cement and Concrete Research*, 3(5):583–599, 1973.

[129] G. Rehm and R. Eligehausen. Bond of ribbed bars under high cycle repeated loads. *ACI Structural Journal*, 76(2):297–309, 1979.

[130] H. W. Reinhardt, J. Blaauwendraad, and E. Vos. Prediction of bond between steel and concrete by numerical analysis. *Mater. Struct.*, 17(100):311–320, 1984.

[131] H.W. Reinhardt, H.A.W. Cornelissen, and D.A. Hordijk. Tensile tests and failure analysis of concrete. *Journal of Structural Engineering ASCE*, 112(11):2462–2477, 1986.

[132] L. Resende and J.B. Martin. A progressive damage continuum model for granular materials. *Computer Methods in Applied Mechanics and Engineering*, 42:1–18, 1984.

[133] J. G. Rots. *Computational Modeling of Concrete Fracture*. Ph.D. Dissertation, Delft University of Technology, Delft , 1988.

[134] H. M. Salem and K. Maekawa. Pre- and postyield finite element method simulation of bond of ribbed reinforcing bars. *Journal of Structural Engineering*, 130(4):671–680, 2004.

[135] P. Sand and S. Teller. Particle video: Long-range motion estimation using point trajectories. *IEEE Conference on Computer Vision and Pattern Recognition*, page , 2006.

[136] B. J. Schunck and Horn B.K. P. Determining optical flow. *Artificial Intelligence*, 17:185–203, 1981.

[137] H. Shima, L.L. Chou, and H. Okamura. Bond characteristics in post-yield range of deformed bars. *Concrete Library of JSCE*, 10:113–124, 1987.

[138] H. Shima, L.L. Chou, and H. Okamura. Micro and macro models for bond in reinforced concrete. *Journal of the Faculty of Engineering, University of Tokyo*, 39(2):133–194, 1987.

[139] J.C. Simo and T.J.R. Hughes. *Computational Inelasticity*. New York: Springer Verla , 1998.

[140] S.K. Sinha. Automated condition assessment of buried pipeline using computer vision techniques. *IE(I) Journal-CP*, 85:38–43, 2004.

[141] C. K. Soh, S.P. Chiew, and Y.X. Dong. Concrete-steel bond under repeated loading. *Magazine of Concrete Research* , 54(1):35–46, 2002.

[142] T. Sprague. *An X-Ray Tomography Investigation of Bond in Reinforced Concrete*. MSCE Thesis, University of Washington, Seattle, WA , 2006.

[143] S. Tanathong. *Object Oriented Change Detection of Buildings After a Disaster*. ASPRS, 2009.

[144] J. A. Tanner. *Experimental Determination of Bond Slip in Reinforced Concrete*. MS thesis, Cornell University, Ithaca, N.Y., 2006.

[145] T.P. Tassios. *Properties of Bond Between Concrete and Steel under Load Cycles Idealizing Seismic Actions*. Comit Euro-International De Bton, Bulletin No. 131, 1979.

[146] M. A. Taylor and B. B. Broms. Shear bond strength between coarse aggregate and cement paste or mortar. *ACI JOURNAL, Proceedings* , 61(8):939–958, 1964.

[147] R. Tepfers. Cracking of concrete cover along anchored deformed reinforcing bar. *Magazine of Concrete Research*, 31(106):3–12, 1979.

[148] R. Tepfers. Bond stress along lapped reinforcing bar. *Magazine of Concrete Research*, 32(112):135–142, 1980.

[149] R. Tepfers and P.A. Olsson. Ring test for evaluation of bond properties of reinforcing bars. *Bond in Concrete. Proceedings of the International Conference Riga, Latvia. CEB*, pages 1.89–1.99, 1992.

[150] D. Tikhomirov and E. Stein. Finite element computations of anisotropic continuum damage in reinforced concrete. *Computers & Structures*, 79:2249–2260, 2001.

[151] S. Timoshenko. *Strength of Materials, Part II, 3rd edition*. New York, 1966.

[152] K.C. Valanis. On the uniqueness of solution of the initial value problem in softening materials. *Journal of Applied Mechanics*, 52:649–653, 1985.

[153] J.G.M. Van Mier. Fracture of concrete under complex stress. *Heron*, 31(3): , 1986.

[154] S. Viwathanatepa, E. P. Popov, and V.V. Bertero. *Effects of generalized loadings on bond of reinforced bars embedded in confined concrete blocks*. Earthquake Engineering Research Center,Report No. EERC 76-2, University of California, Berkeley , 1976.

[155] H. Wang. An analytical model of bond strength associated with splitting of concrete cover. *Engineering Structures*, 31:968–975, 2009.

[156] X. Wang and X. Liu. A strain-softening model for steel-concrete bond. *Cement and Concrete Research*, 33:1669–1673, 2003.

[157] Z.M. Wang, A.K.H. Kwan, and H.C. Chan. Microscopic study of concrete I: generation of random aggregate structure and finite element mesh. *Computers & Structures*, 70:533–544, 1999.

[158] P. Watstein and R. G. Mathey. Width of cracks in concrete at the surface of reinforcing steel evaluated by means of tensile bond specimens. *ACI Journal, Proceedings* , 56(1):47–56, 1999.

[159] Website. `http://vision.middlebury.edu/flow/`.

[160] A. Wedel, T. Pock, T. Braun, U. Franke, and D. Cremers. Duality TV-L1 flow with fundamental matrix prior. *IEEE IVCNZ*, pages 1–6, 2008.

[161] R.C.K. Wong, S.K.Y. Ma, R.H.C. Wong, and K.T. Chau. Shear strength components of concrete under direct shearing. *Cement and Concrete Research*, 37:1248–1256, 2007.

[162] B. Yao and D. W. Murray. *Finite Element Analysis of Distributed Discrete Concrete Cracking*. Structural Engineering Report No. 179, University of Alberta, Department of Civil Engineering , 1992.

[163] B. Yao and D. W. Murray. Width of cracks in concrete at the surface of reinforcing

steel evaluated by means of tensile bond specimens. *ASCE Journal of Structural Engineering* , 119(10):2813–2834, 1993.

[164] S. Youssef, E. Maire, and R. Gaertner. Finite element modeling of the actual structure of cellular materials determined by x-ray tomography. *Acta Materialia*, 53:719–730, 2005.

[165] R. C. Yu and G. Ruiz. Explicit finite element modeling of static crack propagation in reinforced concrete. *Int. J. Fract.* , 141:357–372, 2006.

[166] Z.Q. Yue, S. Chen, and L.G. Tham. Finite element modeling of geomaterials using digital image processing. *Computers and Geotechnics*, 30:375397, 2003.

[167] C. Zach, T. Pock, and H. Bischof. A duality based approach for realtime TV-L1 optical flow. *DAGM 2007*, 2007.

[168] S. G. Zachariah, J. E. Sanders, and G. M. Turkiyyah. Automated hexahedral mesh generation from biomedical image data: Applications in limb prosthetics. *IEEE Transactions on Rehabilitation Engineering* , 4(2):91–102, 1996.

[169] T. Zhang. *Identification of structural changes from volumetric image sequence*. PhD dissertation, Rensselaer Polytechnic Institute, 2004.

[170] Y. Zhang and C. Bajaj. Adaptive and quality quadrilateral/hexahedral meshing from volumetric data. *Computer Methods in Applied Mechanics and Engineering*, 195(9-12):942–960, 2006.

[171] J. Zhu and J. S. Popovics. *Non-contact NDT of Concrete Structures Using Air Coupled Sensors*. Research Report, University of Illinois, Urbana Champaign, 2008.

Vita

Jingjuan (Jane) Li finished her study for Bachelor of Science degree in Civil Engineering and Minor certificate in Computer Science Engineering in 1993 from Dalian University of Technology, China. She finished graduate study for Master of Science degree in Structural Engineering in 1996 from the same school, with the thesis titled "Investigation of rigid connection feasibility between main girder supporting the cables and approaching multi-cell box girder for Jinma Cable-stayed bridge". After that, she had been working as a consulting engineer at China Airport Construction Corporation, where she had accumulated rich experience in reinforced and prestressed concrete bridge design. In 2003, she began to study transportation engineering in Washington State University, where she finished with Master of Science degree in Geotechnical/transportation engineering in 2005 with the thesis titled "A methodology to generate traffic input for NCHRP 1-37A Pavement Design Guide". She had worked as a bridge consulting engineer in Parsons Brinckerhoff Inc from 2005 to 2006. Then she decided to study for her PhD degree in Structural Engineering at the University of Washington in 2006. She finished her PhD study in May 2010 with the dissertation titled "An investigation of behavior and modeling of bond for reinforced concrete". Her research interests include computational mechanics, computer vision, structural health monitoring and bridge engineering.